frontiers | Research Topics

Bridging the gap in neuroscience and neurotherapeutics: From fundamental research to clinical translational applications

Edited by
Na Li, Haojie Mao, Jing Teng and Zhou Zhou

Published in
Frontiers in Neuroscience

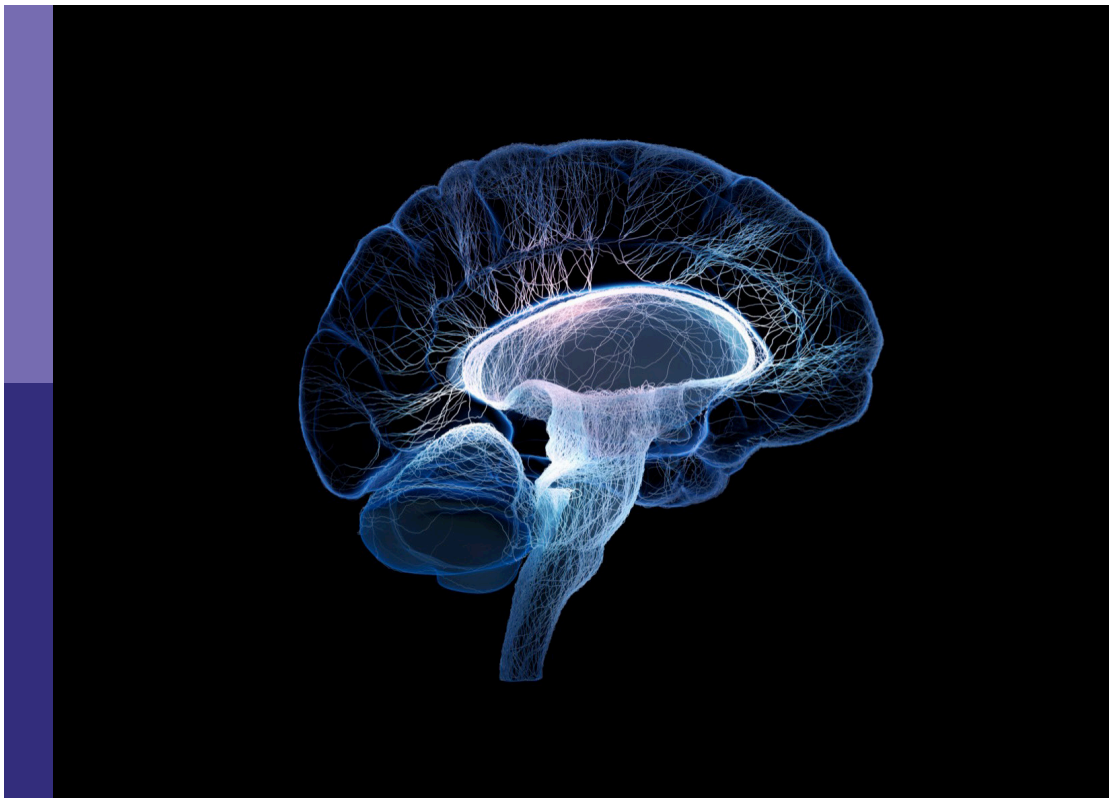

ISSN 1664-8714
ISBN 978-2-8325-4033-6
DOI 10.3389/978-2-8325-4033-6

About Frontiers

Frontiers is more than just an open access publisher of scholarly articles: it is a pioneering approach to the world of academia, radically improving the way scholarly research is managed. The grand vision of Frontiers is a world where all people have an equal opportunity to seek, share and generate knowledge. Frontiers provides immediate and permanent online open access to all its publications, but this alone is not enough to realize our grand goals.

Frontiers journal series

The Frontiers journal series is a multi-tier and interdisciplinary set of open-access, online journals, promising a paradigm shift from the current review, selection and dissemination processes in academic publishing. All Frontiers journals are driven by researchers for researchers; therefore, they constitute a service to the scholarly community. At the same time, the *Frontiers journal series* operates on a revolutionary invention, the tiered publishing system, initially addressing specific communities of scholars, and gradually climbing up to broader public understanding, thus serving the interests of the lay society, too.

Dedication to quality

Each Frontiers article is a landmark of the highest quality, thanks to genuinely collaborative interactions between authors and review editors, who include some of the world's best academicians. Research must be certified by peers before entering a stream of knowledge that may eventually reach the public - and shape society; therefore, Frontiers only applies the most rigorous and unbiased reviews. Frontiers revolutionizes research publishing by freely delivering the most outstanding research, evaluated with no bias from both the academic and social point of view. By applying the most advanced information technologies, Frontiers is catapulting scholarly publishing into a new generation.

What are Frontiers Research Topics?

Frontiers Research Topics are very popular trademarks of the *Frontiers journals series*: they are collections of at least ten articles, all centered on a particular subject. With their unique mix of varied contributions from Original Research to Review Articles, Frontiers Research Topics unify the most influential researchers, the latest key findings and historical advances in a hot research area.

Find out more on how to host your own Frontiers Research Topic or contribute to one as an author by contacting the Frontiers editorial office: frontiersin.org/about/contact

Bridging the gap in neuroscience and neurotherapeutics: From fundamental research to clinical translational applications

Topic editors

Na Li — Central South University, China
Haojie Mao — Western University, Canada
Jing Teng — North China Electric Power University, China
Zhou Zhou — Royal Institute of Technology, Sweden

Citation

Li, N., Mao, H., Teng, J., Zhou, Z., eds. (2023). *Bridging the gap in neuroscience and neurotherapeutics: From fundamental research to clinical translational applications*. Lausanne: Frontiers Media SA. doi: 10.3389/978-2-8325-4033-6

Table of contents

frontiers | Frontiers in Neuroscience

TYPE Mini Review
PUBLISHED 29 November 2022
DOI 10.3389/fnins.2022.1055601

OPEN ACCESS

EDITED BY
Jing Teng,
North China Electric Power University, China

REVIEWED BY
Hyunsoo Shawn Je,
Duke-NUS Medical School, Singapore
Na Li,
Central South University, China

*CORRESPONDENCE
Jin Yu
yj20200330@163.com

†These authors have contributed equally to this work and share first authorship

SPECIALTY SECTION
This article was submitted to Translational Neuroscience, a section of the journal Frontiers in Neuroscience

RECEIVED 28 September 2022
ACCEPTED 02 November 2022
PUBLISHED 29 November 2022

CITATION
Yu J, Wang K and Zheng D (2022) Brain organoids for addressing COVID-19 challenge.
Front. Neurosci. 16:1055601.
doi: 10.3389/fnins.2022.1055601

Brain organoids for addressing COVID-19 challenge

Jin Yu[1*†], Kailun Wang[2†] and Dalin Zheng[1†]

[1]Department of Hematology, Panzhihua Central Hospital, Panzhihua, Sichuan, China, [2]Department of Emergency, Panzhihua Central Hospital, Panzhihua, Sichuan, China

COVID-19 is a systemic disease involving multiple organs, and clinically, patients have symptoms of neurological damage to varying degrees. However, we do not have a clear understanding of the relationship between neurological manifestations and viral infection due to the limitations of current *in vitro* study models. Brain organoids, formed by the differentiation of stem cells under 3D culture conditions, can mimic the structure of tiny cell clusters with neurodevelopmental features in different patients. The paper reviewed the history of brain organoids development, the study of the mechanism of viral infection, the inflammatory response associated with neurological damage, the detection of antiviral drugs, and combined microarray technology to affirm the status of the brain organoid models in the study of COVID-19. In addition, our study continuously improved the model in combination with emerging technologies, to lay a theoretical foundation for clinical application and academic research.

KEYWORDS

brain organoids, COVID-19, organoids-on-a-chips, translational medicine, 3D culture

Introduction

The pandemic of COVID-19 has resulted in 635,538,583 confirmed cases and 6,594,050 deaths worldwide as of 31 October 2022, according to the World Health Organization.[1] Almost 30–40% of patients have predominantly neurological symptoms such as headaches, strokes, and hyposmia (Gasmi et al., 2021). The construction of preclinical models to obtain first-hand information on possible mechanisms of viral infection between COVID-19 and neurological manifestations is of great urgency.

Common models for pathogen research include common two-dimensional (2D) cell and animal models. The models for COVID-19 include A549, Calu-3, Human neural progenitor cells-based 2D cells and mouse-based rodents, and even non-human primates such as rhesus monkeys, which may be efficient in studying possible mechanisms of viral infection and treatment (Blanco et al., 2020; Zhou et al., 2020). The 2D unit, which is the main model for current studies, also has some non-negligible

1 https://worldometers.info/coronavirus

problems. (1) Vulnerability to disturbances in the signal dynamics in the petri dish, which is detrimental to nerve cell growth. (2) Human nerve cells can show characteristic changes such as myelin formation and electrophysiology, while 2D cells lack these properties (Dehaene and Spelke, 2015). (3) 2D cultures emphasize individual cells, whereas the advanced functions of the brain are achieved through synaptic connections, and the regulatory functions of various glial cells cannot be presented in 2D cultures (Silbereis et al., 2016); Animal models are more widely used in the study of neurological disorders and altered consciousness, but again, there are some problems. (1) Not only has the human cerebral cortex evolved many more neurons than other mammals, but it has also formed functional structures such as the sulcus gyrus. More importantly, it has thinking activities not found in lower species (Herculano, 2009); (2) some medications may cause severe neurological damage and even death in patients due to drug accumulation during diseases treatment, but the aforementioned phenomena were not observed in preclinical animal models (Giandomenico and Lancaster, 2017). Given the above limitations of the models, we had to look for new *in vitro* research models, and therefore, we focused on organoids.

An organoid is an organ-like structure formed by the aggregation of stem cells in three-dimensional (three-dimensional, 3D) culture, containing cell types specific to the source organ that can reproduce a variety of functions such as secretion, filtration and even partial neural activity, according to the source organ function. Therefore, it displays the physiological functional structure of real organs *in vitro*, which then has great potential for replacing cell and animal testing (Sato et al., 2009; Lancaster et al., 2013; Lancaster and Knoblich, 2014). In the surge of COVID-19, organoids are contributing to host-pathogen interactions, to the study of differences in viral tropism of individual cells, and the kinetics of viral replication, especially in neurological infections, as organovir states "we want to bring organoids for virology to the next level.[2]" Therefore, brain organoids play an essential role in the molecular pathology of virus-invading cells and the development of therapeutic drugs, and related research is in full swing (**Table 1**).

As a disease involving multiple systems throughout the body, a single brain organoid only statically reflects the pathological changes following direct viral action on specific cells. Moreover, since the human body is a dynamic and balanced system integrating multiple organs and a physiological microenvironment, how to combine the organ-like model of viral infection with existing equipment to realize the interaction between each organ and the microenvironment to study COVID-19 remains a concern. Therefore, we introduced the organoid-on-chips technology, which is a micro-physiological system built on a chip with microfluidics as its core, through the cross-fertilization of physics, chemistry, biology, materials science, engineering, micro-electro-mechanics and medicine, and other multidisciplinary science and technology fields (Reardon, 2015; Park et al., 2019). Organoid-on-chips technology is included in organ-on-chips technology, which replaces 2D cells with organoids and uses microfluidics to construct a unified whole *in vitro* to represent multiple organoids, biofluids, mechanical signals, and functional tissue interfaces (Wang et al., 2022). The use of this model allows for a more comprehensive understanding of the association between viruses and neurological manifestations based on existing findings, providing a new platform for discovering potential targets and developing effective treatments.

The chronicles of brain organoids

Research on brain organoids dates back to 1907 when Harrison (1907) discovered that isolated sponge cells had the potential to spontaneously re-form organoids. Over the next century, many teams gradually progressed through 2D to 3D culture of embryoid and potential stem cells (potential stem cells, PSC) from experimental animals until a ROCK inhibitor sustaining human embryonic stem cells (human embryonic stem cells, hESC) passaging allowed hESC to survive through multiple passages (Martin, 1981; Thomson et al., 1998; Watanabe et al., 2005, 2007). Yoshiki, by adjusting the initial conditions of patterning factors and then the tissue will order folding and assembly spontaneously, generated a mammalian brain without external instructions in the Petri dish, unveiling the possibility for a variety of other systems to be studied while demonstrating the organoid as an *in vitro* model (Eiraku et al., 2008). Since then, many teams have continued to improve on culture protocol construction, culture identification, drug efficacy and toxicology testing, making organoids a hot spot in basic life science research, clinical disease simulation and new drug development (Eiraku et al., 2011; Lancaster et al., 2013; Sakaguchi et al., 2015; Watanabe et al., 2017; Mansour et al., 2018; Tao et al., 2018; Pellegrini et al., 2020; Popova et al., 2021).

The pathogenesis of COVID-19 in brain organoids

COVID-19 is an infection induced by the synaptic protein on the envelope of the severe acute respiratory syndrome virus 2 (The severe acute respiratory syndrome virus 2, SARS-CoV-2), which enters the host cells along with receptors/co-receptors on the surface of the host cell membrane and other cofactors. Angiotensin-Converting Enzyme 2 (Angiotensin-Converting Enzyme 2, ACE2), transmembrane serine protease 2 (transmembrane serine protease 2, TMPRSS2), neomycin trichothecene 1 (neomycin trichothecene 1, NRP1) and

2 https://organovir.com

TABLE 1 Applications of brain organoids in virus.

Brain regions	Cell types	Patterning factors	Age of organoids when assayed	Virus type used	Infection details	References
Dorsal /ventral forebrain	Hipsc/ESC	Y27632, CHIR99021, SB431542, GM-CSF, A-83-01,LDN193189,dorsomorphin,WNT3A, IWR1e,XAV-939,SHH,SAG,NT3	35 days	ZIKV-MR776	Infected microglia-containing organoids are indicated by the significant morphological abnormalities and cell detachment.	Xu et al., 2021
Cerebral cortex(early-stage)	Human H9 ES (WA09)	bFGF,Noggin,BMP-4,VEGF, hLIF, Y27632, CHIR99021, SB431542, GM-CSF, Cyc A/SNH,BDNF,GDNF.	10 days	ZIKV-H/PF/2013	Organoids incubated with a virus inoculum are exhibited in time-dependent growth attenuation and significantly smaller	Krenn et al., 2021
Cerebral cortex	Hipsc	bFGF,Noggin,BMP-4,VEGF, hLIF, Y27632, CHIR99021, SB431542, GM-CSF, Cyc A/SNH,BDNF,GDNF.	14 days	ZIKV-H/PF/2013	Brain organoids are inoculated with ZIKV to induce a prominent change in organoid structure.	Pettke et al., 2020
Cerebral cortex	Hips	human recombinant FGF and EGF,	14 days	HIV-1 strain NLYU2	Both infected and uninfected microglia continued to infltrate into the hBORGs	Dos Reis et al., 2020
Cerebral cortex	Hipsc	bFGF, Y27632	15 days	HSV-1 strain F	Cerebral organoids are infected with different titer of HSV-1 in the culture medium for three day.	Qiao et al., 2020
Neocortical /forebrain	hiPSC lines (73 -56010 -01 SA and 73 –56010 -02)	bFGF, Y27632, CHIR99021, SB431542, LDN193189	12 weeks	HSV -1 strain KOS	Brain organoids are infected for 2 h, and then the inoculum is removed.	Abrahamson et al., 2020
Neocortical /forebrain	iPSCs	FGF,EGF, Y27632, CHIR99021, SB431542, LDN193189	12 weeks	HCMV strain TB40/E	The inocula of cerebral organoids are removed after 2h and then analyzed at days 3 and 5 post infection	Sison et al., 2019
ventricular/ subventricular zone	AG14048 iPSCs	bFGF,Noggin,BMP-4,VEGF, hLIF, Y27632, CHIR99021, SB431542, GM-CSF, Cyc A/SNH,BDNF,GDNF.	>9 weeks	HCMV strains Towne	Brain organoids are exposed to virus for 24 h, and then medium is replaced.	Brown et al., 2019
Forebrain	HNSC.100	bFGF,Noggin,BMP-4,VEGF, hLIF, Y27632, CHIR99021, SB431542, GM-CSF, Cyc A/SNH,BDNF,GDNF.	>6 weeks	DENV-1 (Hawaiian strain)	Direct injection of the virus strain	Yoon et al., 2017

ZIKA, zika virus; HIV, human immunodeficiency virus; HSV, herpes simplex virus; HCMV, human cytomegalovirus; HIPSC, human induced pluripotent stem cells.

10.3389/fnins.2022.1055601

furin/furin-like proteases are common receptor components, and the broad spectrum of ACE2 receptor hosts establishes its status as the primary receptor for neurological infections (Liu Z. R. et al., 2020).

The mechanism of COVID-19 based on ACE2 receptor in brain organoids

When comparing the distribution of ACE2 in different *in vitro* models, the expression of ACE2 in neurons and astrocytes in brain organoid was significantly higher than that in 2d cultures, so a rational choice of *in vitro* models is a prerequisite for achieving the reliability of the study results. COVID-19 selectively infects astrocytes and radial glial progenitor cells in brain organoids, but there are also differences in infection rates between the two: nearly 50% in the former compared to 30% in the latter (Chen et al., 2020). In addition to the above-mentioned cells, it has been suggested that the virus is more plexiform cellophilic, but the detailed mechanism relies on Jacob et al. (2020) showing infection rates of up to 20% in choroid plexus-like organs with COVID-19 are accompanied by a large number of transcribed genes de-regulated. Genes related to cytokines and vascular remodeling were upregulated, whereas genes related to ion channels and intercellular junctions were downregulated. Similarly, Pellegrini and Lancaster (2021) further found that IL-6 produced by the virus through intrinsic immunity and C3 and C4 production by the complement system led to both studies. Both results suggested that ACE2-expressing choroid plexus epithelial cells are the main pathogenic mechanism of viral infection in brain organoids as the blood-brain barrier is disrupted by the recruitment of inflammatory factors (Sungnak et al., 2020).

However, ACE2 expression is lower in the neuronal cells, which make up the majority of brain cells, and the virus has a different proclivity for these cells (Qi et al., 2020). Some studies pointed out that the virus does not infect neurons, but several studies also concluded that the virus affects the upregulation of metabolism-related pathways such as cell division and the formation of a hypoxic environment at the foci of infection; or causes stress and direct damage to neurons by altering the distribution of Tau proteins in neurons and hyperphosphorylation (Song et al., 2020; McMahon et al., 2021); The above studies mentioned that viral infection interferes with metabolic processes, leading to changes in the microenvironment between normal and infected cells. The aforementioned studies suggest that viral infection interferes with metabolic processes, thereby affecting the survival of pericytes which constitute the neurovascular brain. Interestingly, viral mRNA may be 50-fold higher in pericyte-containing organoids, which act as a center of viral replication. In contrast, in controls without pericytes, no SARS-CoV-2 fragments are detected, which may be related to the fact that pericytes promote astrocyte maturation and mediate viral infection of cells (Ramani et al., 2020). Furthermore, it has been proposed that infection causes corresponding neurological symptoms such as headache and dizziness by rapidly decreasing the number of excitatory synapses of cortical neurons in brain organoids (Wang L. et al., 2021). In addition to the ACE2-mediated direct infection of neuronal cells described above, the nasal cavity, consisting of the sieve plate and olfactory epithelium, establishes a contact with the nerve center, and the severe acute respiratory syndrome virus infection of the nervous system via this pathway also provides new inspiration, that is, whether COVID-19 can also invade the nervous system along this pathway? (Baig et al., 2020) The expression level of ACE2, the key to viral invasion, correlates with the time of organoid culture. Bullen et al. (2021) notes that brain ACE2 expression was highest in organoids at 9 weeks, while McMahon et al. (2021) found that organoids cultured *in vitro* for 180 days had viral titers that could be diluted to 10^2 PFU due to the wide distribution of ACE2 and that the amount of ACE2 was not constant. As the virus replicates in neuronal cells, ACE2 expression increases accordingly, which warns us that ACE2 mRNA levels do not represent ACE2 protein expression (Wang L. et al., 2021); it is worth mentioning that ACE2 expression levels also change if patients have comorbidities such as chronic diseases like hypertension and neurodegenerative diseases like Alzheimer's disease (Cantuti et al., 2020).

The mechanism of COVID-19 based on other receptor in brain organoids

Most of the aforementioned studies on nerve cell infection by COVID-19 have focused on ACE2, which is less expressed in olfactory cells. And the higher viral infection may be attributed to the high expression of the NRP1 co-receptor, which promotes viral interaction with a small number of ACE2 receptors to enhance viral entry into host cells when ACE2, TMPRSS2, and NRP1 are present together, but does not promote infection when only NRP1 is expressed. Meanwhile, the role of NRP1 depends on florin cleavage of the viral S protein to form a specific c-terminal sequence that promotes viral invasion of neuronal cells (Andrews et al., 2021). Similarly, in human cortical organoids, no significant ACE2 expression was observed in astrocytes, while in virus-infected cells, CD147 and DPP4 co-receptor expression were significantly higher in virus-infected cells, and the rate of viral infection also varied with the amount of co-receptor expression. Interestingly, co-receptors also induce an inflammatory gliosis-like injury (Wang et al., 2020). It has also been suggested that T lymphocytes with low levels of ACE2 expression are also susceptible to infection, which may be associated with CD147 receptor molecule-mediated endocytosis on the surface of T cells. Further studies are still

needed to address whether it is another potential target for viral invasion (Blanco et al., 2020).

The mechanism of inflammation of COVID-19 in brain organoids

There is also controversy regarding the neuroinflammation induced by viral infection via the aforementioned receptors (or targets). Some studies have pointed out that infection does not cause the production of neuroinflammation such as interferon (interferon, IFN; McMahon et al., 2021). But others have pointed out that low levels of IFN I and III with elevated chemokines and high expression of IL-6 are key to the development of neuroinflammatory symptoms, even more importantly, infected astrocytes are involved in neuroinflammation through upregulation of inflammation-related genes such as IFIT1, IFI44, and ISG15, and that genotoxic stress activation leads to nearly 20% apoptosis (Ramani et al., 2020). Inflammatory factors such as IL-1β, IL-6, chemokine ligand 5, and chemokine ligand 10 are significantly upregulated, compromising the integrity of the blood-brain barrier (blood-brain barrier, BBB). Local hypoxia produces an inflammatory response, which in turn lowers the threshold for tissue damage and thus exacerbates neurological damage, and these findings further expand our understanding of the pathogenic mechanisms of COVID-19 (Blanco et al., 2020).

Screening therapeutic regimens of brain organoids in COVID-19

With an understanding of the pathogenesis of COVID-19, drug selection and vaccine development become particularly important in treatment and prevention. We all know that antiviral drugs generally take 8–12 years to develop, and even after hitting the market, they can be withdrawn at any time due to issues of efficiency, quality, targeting, and safety issues; Vaccines involve phase IV clinical trials and require constant adaptation to cope with the high variability of the virus, and as Feinberg says, "This is a world where we're going to see infectious diseases we've never seen before, and we need to get really good at developing vaccines against them quickly.[3]" And the time to market for vaccines is usually longer than for drugs, taking about 8–18 years. The urgent need to develop antiviral drugs and vaccines that use brain-based organs continues to be explained by the wide range of people involved in COVID-19, the high mortality rate, and the poor prognosis.

Given that ACE2 is a major molecule mediating infection, Monteil et al. (2020) attempted to inhibit viral infection by blocking the ACE2 receptor, and they used human recombinant soluble ACE2 (hrsACE2, human recombinant soluble ACE2) to treat virus-infected vascular and kidney organoids. They found that the rate of virus infection in vascular organoids was reduced by about 5-fold before and after the use of hrsACE2, while the effect was even more dramatic in renal organoids, even decreasing by nearly 1,000-fold. Since ACE2 is widely distributed in multiple tissues, including the brain, can hrsACE2 achieve the same anti-infective effect in infected brain organoids? In addition, in brain organoids with TMPRSS2 receptor expression, the serine protease inhibitor Camostat Mesilate, blocks viral S protein-mediated infection (Hoffmann et al., 2020). The EK1 peptide, an inhibitor of stinging proteins, inhibits endocytosis mediated by the binding of viral stinging proteins to cellular receptors at 40 μM, thereby inhibiting viral infection by interfering with the cell fusion process (Blanco et al., 2020). Not only are there drugs targeting each receptor molecule but the monoclonal antibody tocilizumab to ACE2 is also very effective and inhibits viral infection of the organoid even at 100-fold dilution (Song et al., 2020). Lv et al. (2021) found that using SARS-CoV-2 infected lung and small intestine organoids, including imatinib, mescaline, quinacrine hydrochloride and chloroquine, could inhibit virus invasion. Moreover, the effective concentration of mycophenolic acid in the four drugs could even be as low as 0.15 μM, and the animal model also verified the experimental results, enlightening us whether SARS-CoV-2 can first infect the lung, then there was a relay station for virus replication and transmission, and eventually led to brain infection through blood circulation remains to be further investigated. Sofosbuvir, an Food and Drug Administration-approved anti-hepatitis C drug, was used to prevent infection-induced neurotoxic changes because of its high homology to SARS-CoV-2 in terms of base arrangement. Mesci et al. (2020) chose 20 μm of Sofosbuvir to treat brain organoids infected with the virus and found that the drug significantly reduced virus replication and nerve cell death in brain organoids.

The applications of COVID-19 in brain organoid-on-a-chip

Brain organoids reproduce, to some extent, some of the structures and functions of the human nervous system, but the lack of vascular endothelial cells and immune cells exposes us to the deficiencies of this model in simulating the host's inability to initiate intrinsic and adaptive immune response after the pathogenic attack; simultaneously, the formation of neuronal networks in the brain is dependent on the regulation of physicochemical factors, and most existing protocols include chemical signals such as neurotrophic factors and hormones sequentially to induce nerve cell differentiation, migration and maturation, and eventually brain organogenesis (Yu et al., 2022).

3 https://www.statnews.com

Without including physical signals in the culture. This may result in problems such as difficulties in the simulation and control of organoid tissues whose structure and function are not equivalent to the source tissue's physical signals, including mechanical, electromagnetic, and optical signals. Additionally, because of challenges with modeling and control, organoids are often only maintained in static culture systems, even though both the growth of nerve cells and the production of myelin depend on the presence of physical signals (Ryan et al., 2021). However, more importantly, fluids are crucial in order to meet the high metabolic demands during organoid culture and to avoid inefficient ways of oxygen uptake and nutrient supply in static culture systems, such as passive diffusion of nutrient supply only. In a study of COVID-19 infection of the intestine, the expression of ACE2 increased significantly with the combination of physical signals such as fluid shear and mechanical peristalsis, laying the model basis for further studies (Bein et al., 2021).

The organic combination of developmental biology, bioengineering, and 3D stem cell culture technology to form a micro-processed cell culture device, the organ chip, depends on how to introduce and precisely regulate the physicochemical factors at the right time during each stage of model construction. Therefore, the existing organoid models can have a high match with the source tissues. It simplifies the major anatomical structures of the target organ and takes the corresponding cells for co-culture with novel materials and a controlled microfluidic environment, forming a model with high fidelity. The model is widely used, especially in alveolar epithelial cells, endothelial cells, fluid, air-fluid interface, and air sac structures on both sides that deform with respiratory movements together constitute the lung organ- on-a-chip, and then infection with the COVID-19 can better simulate the virus transmission process along the respiratory tract (Thacker et al., 2021). Since organoids composed of multiple cells produce coordinated mechanical activity in terms of traction and fluid shear that is significantly different from that of organoids formed by individual cells on chip. Combining organoids containing multiple differentiated cells with microfluidic systems to form organoids on a chip allows the construction of *in vitro* models with more significant advantages (Guo et al., 2021; Zhang et al., 2021).

For the current status of the COVID-19 pandemic, organoid microarrays have become the first choice in studying the potential pathogenesis of the virus. The lung respiratory membrane and blood-brain barrier communicate through the microfluidic chip. Interestingly, unlike the virus that directly infects brain organoids to destroy the integrity of the BBB, in this experiment, the virus first infects alveolar organoids on the chip and activates immune cells in the lung to trigger systemic inflammation, leading to brain endothelial damage and BBB dysfunction, validating the theory that COVID-19 is a multisystem infection. At the same time, this study mimics pathological changes in the viral host after infection at the organ level, which is difficult to achieve in other *in vitro* models (Wang P. et al., 2021). Moreover, even CD4 + T cells in the intestine of necrotizing enterocolitis (NEC, necrotizing enterocolitis) mice induce NEC-associated brain injury by releasing IFN-γ in brain organoids via blood circulation (Zhou et al., 2021). All these studies showed the obvious limitations of single brain organoids in studying systemic diseases, highlighting the need for multi-class organ microfluidic chips as an experimental research vehicle (**Figure 1**).

Challenges and future prospect

Traditional *in vitro* models such as 2D cells and experimental animals have been more successful in the study of pathogens. However, for infections where 2D cells cannot mimic host-pathogen interactions and the host spectrum is limited to humans and cannot be performed in animal models, organoids have leaped to be a better choice under their homology with the source host and their high genetic and phenotypic match. Current studies on COVID-19 infected organoids have focused on the lung, especially when screening drugs using this model, not only have clinical therapeutic doses of certain drugs failed to achieve inhibition of viral infection in lung organoids but even shown experimentally from experiments in 2D cellular and animal models (Si et al., 2021). Although some patients with clinically significant neurological symptoms of COVID-19, most of whom patients exhibit neuroinflammation caused by a storm of inflammatory factors. Building a research system targeting brain organoids to demonstrate infection-induced immune responses and interactions between multiple organs to address these questions. The formation of a brain-organoid-on-a-chip, an automated platform by co-culture with mesenchymal and immune cells and other advanced approaches, in addition to fluidly connecting different organs into a whole, inspired us to build a "multi organoids-on-chips" to achieve the goal of immune response and the study of COVID-19 from a multi-organoids level (Skardal et al., 2017). In February 2022, the U.S. FDA formally approved the cold agglutinin syndrome drug Enjaymo for autoimmune demyelinating diseases based on preclinical efficacy data from human organoids, demonstrating that we can achieve the goal of "old drugs, new uses" by relying only on organoid models and providing clinical efficacy evidence for new drug indications.[4] In addition to studying infection mechanisms and treatment options, the brain organoids on a chip can also be used to study the long-term effects of environmental factors such as nicotine that predispose to neurological disorders (Wang et al., 2018). And the use of organoid microarrays in vaccine research includes a significant

4 https://www.pharmacytimes.com

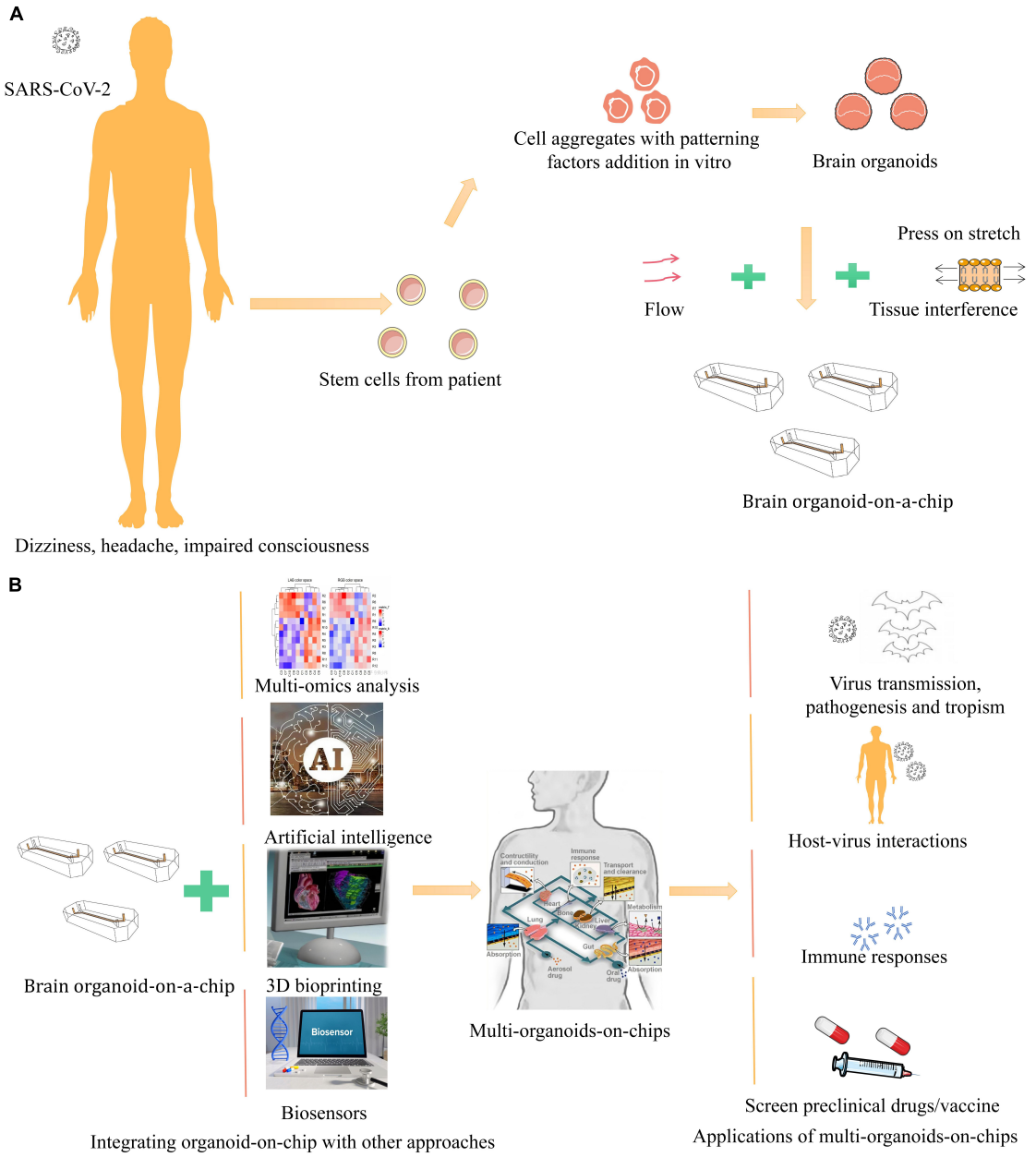

FIGURE 1
Schematic illustration of *in vitro* human organoid models for COVID-19 research. **(A)** COVID-19, clinically presents a wide spectrum of neurological complications, such as dizziness, headache, impaired consciousness (Blanco et al., 2020). Brain organoids are derived from human stem cells and aggregated with patterning factors addition *in vitro* (Chen et al., 2021). With fluid flow, stretch, and tissue interface to mimic cellular microenvironment on a bioengineered microfluidic cell culture device, recapitulating the brain organoid-on-a-chip (Park et al., 2019). **(B)** Integrating brain organoid and other organoids with other approaches like multi-omics, biosensors, 3D bioprinting, and artificial intelligence to generate multi-organoid-on-chips to provide new pathway for virus, which physiologically relevant model systems can be applied to study SARS-CoV-2 virus transmission, pathogenesis and tropism, host-virus interactions, immune responses, and screen preclinical drugs and vaccine (Sang et al., 2021; Wang et al., 2022).

increase in B-cell differentiation and specific IgG antibody production in tonsil organoids infected with live attenuated influenza vaccine and triple vaccine against measles, mumps, and rubella (Wagar et al., 2021); In contrast, lymphoid follicle organoids formed by B and T lymphocytes in human blood are similar to tonsil organoids in terms of cytokine secretion and immunoglobulin production after influenza vaccination. And with the addition of antigen-presenting cells, they can also be used to test immune responses induced by vaccines and adjuvants (Goyal et al., 2021). To research viral and

vaccine effectiveness in real-time and combat the formation of mutant virus strains, brain organoid microarrays are therefore a valuable tool.

In terms of the current problems with brain organoids, the duration of brain organoids culture varies from weeks to months, with material selection, culture protocols, virus titers, and duration of infection effects varying between research teams (Yi et al., 2020; Zhu et al., 2022). Moreover, the affinity of viruses for brain organoids varies depending on the growth stage, and most organoids formed during culture are currently used only for studies related to the early stages of neurodevelopment, whereas the extended culture time allows brain organoids to have a broader scope of application, especially in the study of pathogenic infections, degenerative diseases. In addition, brain damage caused by mid-to late-stage chronic diseases, and the communication between nerve cells and the connections established at each synapse is also crucial for the reproduction of functions (Sidhaye and Knoblich, 2020). How to mimic viral recruitment of immune cells and initiate immune responses to clear viruses when combined with other pathogens to form a complex infection. And the use of specific hydrogels instead of animal-derived matrix gels can reduce the variability introduced by the compositions and batches (Liu H. T. et al., 2020). Since culture protocols vary from lab to lab and the culture period and size of organoids vary, it is also possible to separate organoids of a certain size by setting traps on microcolumn arrays to obtain uniformly sized organoids (Zhu et al., 2017). Currently, technologies such as multi-omics analysis, artificial intelligence, 3D bioprinting and biosensor provide new ways to efficiently study virus-induced diseases, and the combination of brain organoids with these approaches ultimately allows for study the virus transmission, host-virus interaction, immune responses, and the development of new therapies and vaccines (Yin et al., 2021). It is believed that with the improvement of culture technology and further research on viruses, organoid models can continuously provide new clinical ideas in the field of pathogen research, which is expected to solve the bottlenecks and troubles of clinical diseases and provide better application prospects for the development of academic research and translational medicine.

Author contributions

JY and KW: conceptualization. KW and DZ: investigation. KW: resources. DZ: supervision. JY and DZ: writing—original draft. JY: writing—review and editing. All authors contributed to the article and approved the submitted version.

Conflict of interest

The authors declare that the research was conducted in the absence of any commercial or financial relationships that could be construed as a potential conflict of interest.

Publisher's note

All claims expressed in this article are solely those of the authors and do not necessarily represent those of their affiliated organizations, or those of the publisher, the editors and the reviewers. Any product that may be evaluated in this article, or claim that may be made by its manufacturer, is not guaranteed or endorsed by the publisher.

References

Abrahamson, E. E., Zheng, W. X., Muralidaran, V., Ikonomovic, M. D., Bloom, D. C., Nimgaonkar, V. L., et al. (2020). Modeling Aβ42 Accumulation in Response to Herpes Simplex Virus 1 Infection: 2D or 3D? *J. Virol.* 95, e02219–20. doi: 10.1128/JVI.02219-20

Andrews, M. G., Mukhtar, T., Eze, U. C., Simoneau, C. R., Perez, Y. T., Mostajo, R. M. A., et al. (2021). Tropism of SARS-CoV-2 for Developing Human Cortical Astrocytes. *BioRxiv* [Preprint]. . doi: 10.1101/2021.01.17.427024

Baig, A. M., Khaleeq, A., Ali, U., and Syeda, H. (2020). Evidence of the COVID-19 Virus Targeting the CNS: Tissue Distribution, Host-Virus Interaction, and Proposed Neurotropic Mechanisms. *ACS Chem. Neurosci.* 11, 995–998.

Bein, A., Kim, S. M., Goyal, G., Cao, W. J., Fadel, C., and Naziripour, A. (2021). Enteric Coronavirus Infection and Treatment Modeled With an Immunocompetent Human Intestine-On-A-Chip. *Front. Pharmacol.* 12:718484. doi: 10.3389/fphar.2021.718484

Blanco, M. D., Nilsson, P. B. E., Uhl, S., Hoagland, D., Møller, R., et al. (2020). Imbalanced Host Response to SARS-CoV-2 Drives Development of COVID-19. *Cell* 181, 1036–1045.e9. doi: 10.1016/j.cell.2020.04.026

Brown, R. M., Rana, P. S. J. B., Jaeger, H. K., O'Dowd, J. M., Balemba, O. B., and Fortunato, E. A. (2019). Human Cytomegalovirus Compromises Development of Cerebral Organoids. *J. Virol.* 93, e00957–19. doi: 10.1128/JVI.00957-19

Bullen, K., Hogberg, H. T., Bahadirli-Talbott, A., Bishai, W. R., Hartung, T., Keuthan, C. (2021). Infectability of human BrainSphere neurons suggests neurotropism of SARS-CoV-2. *ALTEX* 37, 665–671. doi: 10.14573/altex.2006111

Cantuti, C. L., Ojha, R., and Pedro, L. D. (2020). Neuropilin-1 facilitates SARS-CoV-2 cell entry and infectivity. *Science* 370, 856–860.

Chen, K. G., Park, K., and Spence, J. R. (2021). Studying SARS-CoV-2 infectivity and therapeutic responses with complex organoids. *Nat. Cell Biol.* 23, 822–833.

Chen, R., Wang, K., Yu, J., Howard, D., French, L., Chen, Z., et al. (2020). The spatial and cell-type distribution of SARS-CoV-2 receptor ACE2 in human and mouse brain. *BioRxiv* [Preprint]. doi: 10.1101/2020.04.07.030650

Dehaene, L. G., and Spelke, E. S. (2015). The infancy of the human brain. *Neuron* 88, 93–109.

Dos Reis, R. S., Sant, S., Keeney, H., Wagner, M. C. E., and Ayyavoo, V. (2020). Modeling HIV-1 neuropathogenesis using three-dimensional human brain organoids (hBORGs) with HIV-1 infected microglia. *Sci. Rep.* 10:15209. doi: 10.1038/s41598-020-72214-0

Eiraku, M., Takata, N., Ishibashi, H., Kawada, M., Sakakura, E., Okuda, S., et al. (2011). Self-organizing optic-cup morphogenesis in three-dimensional culture. *Nature* 472, 51–56. doi: 10.1038/nature09941

Eiraku, M., Watanabe, K., Matsuo, T. M., Kawada, M., Yonemura, S., Matsumura, M., et al. (2008). Self-organized formation of polarized cortical tissues from ESCs and its active manipulation by extrinsic signals. *Cell Stem Cell* 3, 519–532. doi: 10.1016/j.stem.2008.09.002

Gasmi, A., Tippairote, T., Mujawdiya, P. K., Gasmi, B. A., Menzel, A., Dadar, M., et al. (2021). Neurological Involvements of SARS-CoV2 Infection. *Mol. Neurobiol.* 58, 944–949.

Giandomenico, S. L., and Lancaster, M. A. (2017). Probing human brain evolution and development in organoids. *Curr. Opin. Cell Biol.* 44, 36–43. doi: 10.1016/j.ceb.2017.01.001

Goyal, G., Mahajan, G., Gilboa, T., et al. (2021). Lymphoid follicle formation and human vaccination responses recapitulated in an organ-on-a-chip. *BioRxiv* [Preprint]. doi: 10.1101/806505

Guo, Y. Q., Luo, R. H., Wang, Y. Q., Deng, P. W., Song, T. Z., and Zhang, M. (2021). SARS-CoV-2 induced intestinal responses with a biomimetic human gut-on-chip. *Sci. Bull.* 66, 783–793. doi: 10.1016/j.scib.2020.11.015

Harrison, R. G. (1907). Observations on the living developing nerve fifibre. *Proc. Soc. Exp. Biol.* 4:140.

Herculano, H. S. (2009). The human brain in numbers: A linearly scaled-up primate brain. *Front. Hum. Neurosci.* 3:31. doi: 10.3389/neuro.09.031.2009

Hoffmann, M., Kleine, W. H., Krüger, N., Herrler, T., and Erichsen, S. (2020). SARS-CoV-2 Cell Entry Depends on ACE2 and TMPRSS2 and Is Blocked by a Clinically Proven Protease Inhibitor. *Cell* 181, 271–280.e8.

Jacob, F. P., Sarshan, W. K., Samuel, Z., Haowen, Z., Feng, C., Beatrice, C., et al. (2020). Human Pluripotent Stem Cell-Derived Neural Cells and Brain Organoids Reveal SARS-CoV-2 Neurotropism. *BioRxiv* [Preprint]. doi: 10.1101/2020.07.28.225151

Krenn, V., Bosone, C., Burkard, T. R., Spanier, J., Kalinke, U., Calistri, A., et al. (2021). Organoid modeling of Zika and herpes simplex virus 1 infections reveals virus-specific responses leading to microcephaly. *Cell Stem Cell* 28, 1362–1379.e7. doi: 10.1016/j.stem.2021.03.004

Lancaster, M. A., and Knoblich, J. A. (2014). Organogenesis in a dish: Modeling development and disease using organoid technologies. *Science* 345:1247125. doi: 10.1126/science.1247125

Lancaster, M. A., Renner, M., Martin, C. A., Wenzel, D., Bicknell, L. S., Hurles, M. E., et al. (2013). Cerebral organoids model human brain development and microcephaly. *Nature* 501, 373–379. doi: 10.1038/nature12517

Liu, H. T., Wang, Y. Q., Wang, H., Zhao, M. Q., Tao, T. T., Zhang, X., et al. (2020). A Droplet Microfluidic System to Fabricate Hybrid Capsules Enabling Stem Cell Organoid Engineering. *Adv. Sci.* 7:1903739. doi: 10.1002/advs.201903739

Liu, Z. R., Chu, R. L., Gong, L., Su, B., and Wu, J. B. (2020). The assessment of transmission efficiency and latent infection period in asymptomatic carriers of SARS-CoV-2 infection. *Int. J. Infect. Dis.* 99, 325–327. doi: 10.1016/j.ijid.2020.06.036

Lv, T., Meng, F. L., Yu, M., Huang, H. H., Lin, X. H., and Zhao, B. (2021). Defense of COVID-19 by Human Organoids. *Phenomics* 1, 113–128.

Mansour, A. A., Gonçalves, J. T., Bloyd, C. W., Li, H., Fernandes, S., Quang, D., et al. (2018). An in vivo model of functional and vascularized human brain organoids. *Nat. Biotechnol.* 36, 432–441. doi: 10.1038/nbt.4127

Martin, G. R. (1981). Isolation of a pluripotent cell line from early mouse embryos cultured in medium conditioned by teratocarcinoma stem cells. *Proc. Natl. Acad. Sci. U S A.* 78, 7634–7638. doi: 10.1073/pnas.78.12.7634

McMahon, C. S., Hilary, G., Michal, C., and Ricardo, H. J. (2021). SARS-CoV-2 targets glial cells in human cortical organoids. *Stem Cell Rep.* 16, 1156–1164. doi: 10.1016/j.stemcr.2021.01.016

Mesci, P., Macia, A., Saleh, A., Martin, S. L., and Snethlage, C. (2020). Sofosbuvir protects human brain organoids against SARS-CoV-2. *BioRxiv* [Preprint]. doi: 10.1101/2020.05.30.125856

Monteil, V., Kwon, H., Prado, P., Hagelkrüys, A., Wimmer, R. A., Stahl, M., et al. (2020). Inhibition of SARS-CoV-2 Infections in Engineered Human Tissues Using Clinical-Grade Soluble Human ACE2. *Cell* 181, 905–913.e7. doi: 10.1016/j.cell.2020.04.004

Park, S. E., Georgescu, A., and Huh, D. (2019). Organoids-on-a-chip. *Science* 364, 960–965. doi: 10.1126/science.aaw7894

Pellegrini, L., and Lancaster, M. A. (2021). Modeling neurodegeneration with mutant-tau organoids. *Cell* 184, 4377–4379. doi: 10.1016/j.cell.2021.07.031

Pellegrini, L., Bonfio, C., Chadwick, J., Begum, F., Skehel, M., and Lancaster, M. A. (2020). Human CNS barrier-forming organoids with cerebrospinal fluid production. *Science* 369:eaaz5626. doi: 10.1126/science.aaz5626

Pettke, A., Tampere, M., Pronk, R., Wallner, O., Falk, A., Warpman, B. U., et al. (2020). Broadly Active Antiviral Compounds Disturb Zika Virus Progeny Release Rescuing Virus-Induced Toxicity in Brain Organoids. *Viruses* 13:37. doi: 10.3390/v13010037

Popova, G., Soliman, S. S., Kim, C. N., Keefe, M. G., Hennick, K. M., Jain, S., et al. (2021). Human microglia states are conserved across experimental models and regulate neural stem cell responses in chimeric organoids. *Cell Stem Cell* 28, 2153–2166. doi: 10.1016/j.stem.2021.08.015

Qi, F., Qian, S., Zhang, S., and Zhang, Z. (2020). Single cell RNA sequencing of 13 human tissues identify cell types and receptors of human coronaviruses. *Biochem. Biophys. Res. Commun.* 526, 135–140.

Qiao, H. W., Guo, M. J., Shang, J., Zhao, W., Wang, Z. Y., and Liu, N. (2020). Herpes simplex virus type 1 infection leads to neurodevelopmental disorder-associated neuropathological changes. *PLoS Pathog.* 16:e1008899. doi: 10.1371/journal.ppat.1008899

Ramani, A., Müller, L., Osterman, P. N., Gabriel, E., Abida, I. P., Müller, S. A., et al. (2020). SARS-CoV-2 targets neurons of 3D human brain organoids. *EMBO J.* 39:e106230.

Reardon, S. (2015). 'Organs-on-chips' go mainstream. *Nature* 523:266. doi: 10.1038/523266a

Ryan, C., Doulgkeroglou, M. N., and Zeugolis, D. I. (2021). Electric field stimulation for tissue engineering applications. *BMC Biomed. Eng.* 3:1. doi: 10.1186/s42490-020-00046-0

Sakaguchi, H., Kadoshima, T., Soen, M., Narii, N., Ishida, Y., Ohgushi, M., et al. (2015). Generation of functional hippocampal neurons from self-organizing human embryonic stem cell-derived dorsomedial telencephalic tissue. *Nat. Commun.* 6:8896. doi: 10.1038/ncomms9896

Sang, Y., Miller, L. C., Nelli, R. K., Giménez-Lirola, L. G., et al. (2021). Studying SARS-CoV-2 infectivity and therapeutic responses with complex organoids. *Nat. Cell Biol.* 23, 822–833. doi: 10.3389/fmicb.2021.725074

Sato, T., Vries, R. G., Snippert, H. J., van de, W. M., Barker, N., Stange, D. E., et al. (2009). Single Lgr5 stem cells build crypt-villus structures in vitro without a mesenchymal niche. *Nature* 459, 262–265. doi: 10.1038/nature07935

Si, L. L., Bai, H. Q., Rodas, M., Cao, W. J., Oh, C. Y., Jiang, A., et al. (2021). A human-airway-on-a-chip for the rapid identification of candidate antiviral therapeutics and prophylactics. *Nat. Biomed. Eng.* 5, 815–829. doi: 10.1038/s41551-021-00718-9

Sidhaye, J., and Knoblich, J. (2020). Brain organoids: An ensemble of bioassays to investigate human neurodevelopment and disease. *Cell Death Differ.* 28, 52–67. doi: 10.1038/s41418-020-0566-4

Silbereis, J. C., Pochareddy, S., Zhu, Y., Li, M. F., and Sestan, N. (2016). The Cellular and Molecular Landscapes of the Developing Human Central Nervous System. *Neuron* 89, 248–268.

Sison, S. L., O'Brien, B. S., Johnson, A. J., Seminary, E. R., Terhune, S. S., and Ebert, A. D. (2019). Human Cytomegalovirus Disruption of Calcium Signaling in Neural Progenitor Cells and Organoids. *J. Virol.* 93, e00954–19. doi: 10.1128/JVI.00954-19

Skardal, A., Murphy, S. V., Devarasetty, M., Mead, I., Kang, H. W., Seol, Y. J., et al. (2017). Multi-tissue interactions in an integrated three-tissue organ-on-a-chip platform. *Sci. Rep.* 7:8837. doi: 10.1038/s41598-017-08879-x

Song, E., Zhang, C. I., Benjamin, L., Peiwen, W. M., Orr, E. L., Dai, F. M., et al. (2020). Neuroinvasive potential of SARS-CoV-2 revealed in a human brain organoid model. *BioRxiv* [Preprint]. doi: 10.1101/2020.06.25.169946

Sungnak, W., Huang, N., Bécavin, C., Berg, M., Queen, R., Litvinukova, M., et al. (2020). SARS-CoV-2 entry factors are highly expressed in nasal epithelial cells together with innate immune genes. *Nat. Med.* 26, 681–687. doi: 10.1038/s41591-020-0868-6

Tao, C. L., Liu, Y. T., Sun, R., Zhang, B., Qi, L., Shivakoti, S., et al. (2018). Differentiation and Characterization of Excitatory and Inhibitory Synapses by Cryo-electron Tomography and Correlative Microscopy. *J. Neurosci.* 38, 1493–1510. doi: 10.1523/JNEUROSCI.1548-17.2017

Thacker, V. V., Sharma, K., Dhar, N., Mancini, G. F., Sordet, D. J., and McKinney, J. D. (2021). Rapid endotheliitis and vascular damage characterize SARS-CoV-2 infection in a human lung-on-chip model. *EMBO Rep.* 22:e52744. doi: 10.15252/embr.202152744

Thomson, J. A., Itskovitz, E. J., Shapiro, S. S., Waknitz, M. A., Swiergiel, J. J., Marshall, V. S., et al. (1998). Embryonic stem cell lines derived from human blastocysts. *Science* 282, 1145–1147. doi: 10.1126/science.282.5391.1145

Wagar, L. E., Salahudeen, A., Constantz, C. M., Wendel, B. S., Lyons, M. M., Mallajosyula, V., et al. (2021). Modeling human adaptive immune responses with tonsil organoids. *Nat. Med.* 27, 125–135.

Wang, L., Sievert, D., Clark, A. E., Lee, S. M., Federman, H., Gastfriend, B. D., et al. (2021). A human three-dimensional neural-perivascular 'assembloid' promotes astrocytic development and enables modeling of SARS-CoV-2 neuropathology. *Nat. Med.* 27, 1600–1606. doi: 10.1038/s41591-021-01443-1

Wang, P., Jin, L., Wu, Y. S., Duan, Z. L., Chen, W. W., et al. (2021). SARS-CoV-2 causes human BBB injury and neuroinflammation indirectly in a linked organ chip platform. *BioRxiv* [Preprint]. . doi: 10.1101/2021.10.05.463205

Wang, X. L., Hu, G. W., Xia, S., Sun, Z. P., Liu, Z. Z., Xie, Y. H., et al. (2020). SARS-CoV-2 infects T lymphocytes through its spike protein-mediated membrane fusion. *Cell. Mol. Immunol.* 17:894. doi: 10.1038/s41423-020-0424-9

Wang, Y. Q., Wang, L., Zhu, Y. J., and Qin, J. H. (2018). Human brain organoid-on-a-chip to model prenatal nicotine exposure. *Lab Chip* 18, 851–860.

Wang, Y. Q., Wang, P., and Qin, J. H. (2022). Human Organoids and Organs-on-Chips for Addressing COVID-19 Challenges. *Adv. Sci.* 9:e2105187. doi: 10.1002/advs.202105187

Watanabe, K., Kamiya, D., Nishiyama, A., Katayama, T., Nozaki, S., Kawasaki, H., et al. (2005). Directed differentiation of telencephalic precursors from embryonic stem cells. *Nat. Neurosci.* 8, 288–296.

Watanabe, K., Ueno, M., Kamiya, D., Nishiyama, A., Matsumura, M., Wataya, T., et al. (2007). A ROCK inhibitor permits survival of dissociated human embryonic stem cells. *Nat. Biotechnol.* 25, 681–686. doi: 10.1038/nbt1310

Watanabe, M., Buth, J. E., Vishlaghi, N., de la, T. U. L., Taxidis, J., Khakh, B. S., et al. (2017). Self-Organized Cerebral Organoids with Human-Specific Features Predict Effective Drugs to Combat Zika Virus Infection. *Cell Rep.* 21, 517–532. doi: 10.1016/j.celrep.2017.09.047

Xu, R. J., Boreland, A. J., Li, X. X., Erickson, C., Jin, M. M., Atkins, C., et al. (2021). Developing human pluripotent stem cell-based cerebral organoids with a controllable microglia ratio for modeling brain development and pathology. *Stem Cell Rep.* 16, 1923–1937. doi: 10.1016/j.stemcr.2021.06.011

Yi, S. A., Nam, K. H., Yun, J. Y., Gim, D. M., Joe, D., Kim, Y. H., et al. (2020). Infection of Brain Organoids and 2D Cortical Neurons with SARS-CoV-2 Pseudovirus. *Viruses* 12:1004. doi: 10.3390/v12091004

Yin, Y., Liu, P. Y., Shi, Y., and Li, P. (2021). Single-Cell Sequencing and Organoids: A Powerful Combination for Modelling Organ Development and Diseases. *Rev. Physiol. Biochem. Pharmacol.* 179, 189–210. doi: 10.1007/112_2020_47

Yoon, K. J., Song, G., Qian, X. Y., Pan, J. B., Xu, D., Rho, H. S., et al. (2017). Zika-Virus-Encoded NS2A Disrupts Mammalian Cortical Neurogenesis by Degrading Adherens Junction Proteins. *Cell Stem Cell* 21, 349–358.e6. doi: 10.1016/j.stem.2017.07.014

Yu, X. Y., Meng, X. T., Pei, Z., Wang, G. Q., Liu, R. R., Qi, M. G., et al. (2022). Physiological Electric Field: A Potential Construction Regulator of Human Brain Organoids. *Int. J. Mol. Sci.* 23:3877. doi: 10.3390/ijms23073877

Zhang, M., Wang, P., Luo, R. H., Wang, Y. Q., Li, Z. Y., Guo, Y. Q., et al. (2021). Biomimetic Human Disease Model of SARS-CoV-2-Induced Lung Injury and Immune Responses on Organ Chip System. *Adv. Sci.* 8:2002928. doi: 10.1002/advs.202002928

Zhou, P., Yang, X. L., Wang, X. G., Hu, B., Zhang, L., and Zhang, W. (2020). A pneumonia outbreak associated with a new coronavirus of probable bat origin. *Nature* 579, 270–273.

Zhou, Q. J., Niño, D. F., Yamaguchi, Y., Wang, S. X., Fulton, W., Jia, H. P., et al. (2021). Necrotizing enterocolitis induces T lymphocyte–mediated injury in the developing mammalian brain. *Sci. Transl. Med.* 13:eaay6621. doi: 10.1126/scitranslmed.aay6621

Zhu, L. L., Fan, Y. H., Huang, X. M., Chen, T., Xu, X. D., Xu, F., et al. (2022). Patent bibliometric analysis for global trend of organoid technologies in the past decade. *IScience* 25:104728. doi: 10.1016/j.isci.2022.104728

Zhu, Y. J., Wang, L., Yu, H., Yin, F. C., Wang, Y. Q., Liu, H. T., et al. (2017). In situ generation of human brain organoids on a micropillar array. *Lab Chip* 17, 2941–2950.

frontiers | Frontiers in Neuroscience

TYPE Original Research
PUBLISHED 07 December 2022
DOI 10.3389/fnins.2022.1041015

OPEN ACCESS

EDITED BY
Zhou Zhou,
Royal Institute of Technology, Sweden

REVIEWED BY
Coen Zandvoort,
University of Oxford, United Kingdom
Francesco Lacquaniti,
University of Rome Tor Vergata, Italy

*CORRESPONDENCE
Claudia A. Angeli
claudia.angeli@louisville.edu

SPECIALTY SECTION
This article was submitted to Translational Neuroscience, a section of the journal Frontiers in Neuroscience

RECEIVED 10 September 2022
ACCEPTED 16 November 2022
PUBLISHED 07 December 2022

CITATION
Sun SY, Giszter SF, Harkema SJ and Angeli CA (2022) Modular organization of locomotor networks in people with severe spinal cord injury.
Front. Neurosci. 16:1041015.
doi: 10.3389/fnins.2022.1041015

Modular organization of locomotor networks in people with severe spinal cord injury

Soo Yeon Sun[1], Simon F. Giszter[2,3], Susan J. Harkema[4,5,6] and Claudia A. Angeli[4,6,7]*

[1]Department of Physical Therapy, Alvernia University, Reading, PA, United States, [2]Department of Neurobiology and Anatomy, College of Medicine, Drexel University, Philadelphia, PA, United States, [3]School of Biomedical Engineering, Science and Health Systems, Drexel University, Philadelphia, PA, United States, [4]Kentucky Spinal Cord Injury Research Center, University of Louisville, Louisville, KY, United States, [5]Department of Neurological Surgery, University of Louisville, Louisville, KY, United States, [6]Frazier Rehab Institute, University of Louisville Health, Louisville, KY, United States, [7]Department of Bioengineering, University of Louisville, Louisville, KY, United States

Introduction: Previous studies support modular organization of locomotor circuitry contributing to the activation of muscles in a spatially and temporally organized manner during locomotion. Human spinal circuitry may reorganize after spinal cord injury; however, it is unclear if reorganization of spinal circuitry post-injury affects the modular organization. Here we characterize the modular synergy organization of locomotor muscle activity expressed during assisted stepping in subjects with complete and incomplete spinal cord injury (SCI) of varying chronicity, before any explicit training regimen. We also investigated whether the synergy characteristics changed in two subjects who achieved independent walking after training with spinal cord epidural stimulation.

Methods: To capture synergy structures during stepping, individuals with SCI were stepped on a body-weight supported treadmill with manual facilitation, while electromyography (EMGs) were recorded from bilateral leg muscles. EMGs were analyzed using non-negative matrix factorization (NMF) and independent component analysis (ICA) to identify synergy patterns. Synergy patterns from the SCI subjects were compared across different clinical characteristics and to non-disabled subjects (NDs).

Results: Results for both NMF and ICA indicated that the subjects with SCI were similar among themselves, but expressed a greater variability in the number of synergies for criterion variance capture compared to NDs, and weaker correlation to NDs. ICA yielded a greater number of muscle synergies than NMF. Further, the clinical characteristics of SCI subjects and chronicity did not predict any significant differences in the spatial synergy structures despite any neuroplastic changes. Further, post-training synergies did not become closer to ND synergies in two individuals.

Discussion: These findings suggest fundamental differences between motor modules expressed in SCIs and NDs, as well as a striking level of spatial and temporal synergy stability in motor modules in the SCI population, absent the application of specific interventions.

KEYWORDS

spinal cord injury, locomotion, synergy modules, locomotor networks, electromyography, spinal cord electrical stimulation

Introduction

Locomotion requires complex coordination of muscles in the body. It is a general consensus that the central nervous system (CNS) often controls the coordination by activating groups of muscles via networks of interneurons in the spinal cord, rather than controlling each of the muscles individually (Bernstein, 1967; Lundberg et al., 1987; Bizzi et al., 1995, 2000; McCrea and Rybak, 2008; Giszter, 2015). It has been suggested that descending signals combined with reflexes and local excitatory and inhibitory interactions of spinal circuitry dynamically select appropriate muscle synergies and behavior from the available repertoire (McCrea, 1992; Kargo and Giszter, 2000; Hart and Giszter, 2004; Cappellini et al., 2006; Krouchev et al., 2006; Ivanenko et al., 2007, 2013; Dominici et al., 2011; Fox et al., 2013; Yang et al., 2019; Sylos-Labini et al., 2020). Spinal interneurons that organize synergy patterns have been identified in frogs, mice and primates (Hart and Giszter, 2010; Takei and Seki, 2010; Levine et al., 2014; Takei et al., 2017), and intraspinal stimulation similarly revealed modular recruitment in animal models (Bizzi et al., 1991; Giszter et al., 1993; Mussa-Ivaldi et al., 1994; Tresch and Bizzi, 1999; Caggiano et al., 2016; Yaron et al., 2020). Further, modular organization of the spinal network is likely determined early in development and refined with experience (Dominici et al., 2011; Yang et al., 2019). Combined, these studies support modular organization of the spinal networks across species.

Muscle synergies are observed during locomotion in healthy individuals and following CNS injury. It is reported that people with complete and incomplete spinal cord injury (SCI) exhibited muscle synergies during treadmill walking (Ivanenko et al., 2013). The patterns of muscle weighting from individuals with motor-incomplete SCI resembled the normal pattern; however, the patterns from individuals with motor-complete SCI did not, indicating that the severity of the injury impacted the weighting in synergies (Ivanenko et al., 2013). In ambulatory individuals with incomplete SCI, fewer synergy modules and altered patterns of synergies were identified both in adults (Hayes et al., 2014; Perez-Nombela et al., 2017) and in pediatric populations (Fox et al., 2013), compared to non-disabled individuals. Danner et al. (2015) reported that step-like, synergistic electromyography (EMG) patterns in the leg muscles were induced by unpatterned epidural electrical stimulation in individuals with motor-complete SCI while supine, suggesting modular organization of the spinal circuitry can be expressed in this population even with unusual or altered feedback. In people post-stroke, fewer synergy modules were identified during walking as a result of merging of the modules observed in non-disabled individuals (Clark et al., 2010). These studies investigated the organization of modules when some supraspinal inputs are partially or completely lost after CNS injury. However, we know rather little about the synergies exhibited by the residual spinal locomotor circuitry (which is known to undergo anatomical and functional reorganization in both humans (Hiersemenzel et al., 2000; Schindler-Ivens and Shields, 2000; Beauparlant et al., 2013; Tseng and Shields, 2013) and animal models (de Leon et al., 1998, 1999; Rossignol et al., 1999, 2008; Pearson, 2000; Rossignol, 2006; Cote et al., 2012; Houle and Côté, 2013; Takeoka et al., 2014; Asboth et al., 2018), after motor-complete severe SCI, and with varying chronicity and neurological injury level. Interestingly, in rats, complete spinal transection occurring at different ages (neonate vs. adult) affords similar synergy patterns, that are nonetheless slightly different from intact adult synergy patterns, despite different experience and influences of descending pathways (Yang et al., 2019).

To better understand the modular organization of the locomotor network in the absence of voluntary stepping ability and its changes following the recovery of walking in humans, we here characterize the modular structure of the locomotor network expressed by the human spinal cord after SCI, and relate the modular structures to healthy patterns. We also explore if chronicity of the injury that allows extensive neuroplastic changes of the spinal circuitry affects the modular organization of the locomotor circuitry. Further, we examine whether clinical characteristics, such as the severity and neurological level of SCI, affect the modular organization. Finally, we asked whether and how the synergy characteristics changed when the subjects achieved walking after locomotor training with spinal cord epidural stimulation (scES, n = 2). Using non-negative matrix factorization (NMF) and independent component analysis (ICA), we investigate synergy

profiles of leg muscle activity observed during stepping with manual facilitation and body weight support in people with SCI and non-disabled individuals. Our study provides information regarding the spatial and temporal profile of muscle synergies in a large sampling of people with SCI with varying clinical characteristics, prior to any systematic locomotor training, and demonstrates several consistent synergy structures despite these variations. Further, we show that the training with neuromodulation (scES) does not lead to the normalization of synergy patterns in the absence of neuromodulation, even though the individuals achieved independent walking with scES.

Materials and methods

Subjects

Eighty individuals were included in this study, consisting of two groups: 73 individuals with SCI (SCI group) and 7 non-disabled individuals (ND group). The SCI group (age 33.94 ± 12.92 years, YSI 4.30 ± 4.34 years, median YSI 3.0 years, IQR = 3.07 years) included 54 individuals with no motor function below the lesion (AIS A n = 34, AIS B n = 20), and 19 with an impaired motor function below the lesion (AIS C n = 13, AIS D n = 6). **Table 1** and **Supplementary Table 1** summarize the demographic and clinical characteristics of the subjects in the SCI group. All individuals in the SCI group were non-ambulatory, except 2 AIS D participants (D11 and D43) who ambulated with a walker. Removing these 2 ambulatory subjects from the data analysis did not affect any of the statistical findings presented here, and their modular patterns were similar to non-ambulatory subjects. We also present the data from two subjects (B23 and B30) who achieved independent walking in the presence of epidural stimulation following locomotor training with task-specific stimulation. The ND group (age 26.84 ± 3.57 years) had no diagnosis of neural injury and served as a control group to understand the characteristics of the modular organization of locomotor circuitry in the absence of spinal cord injury. The experimental protocol was approved by Institutional Review Board at the University of Louisville.

Data collection

Both ND and SCI groups stepped on the treadmill using partial body weight support. During stepping, surface EMG was recorded at 2,000 Hz using a custom-written LabView program (National Instruments, Austin, TX). EMGs from the soleus (SOL), medial gastrocnemius (MG), tibialis anterior (TA), medial hamstring (MH), vastus lateral (VL), rectus femoris (RF), and adductor magnus (AD) muscles were recorded bilaterally using bipolar surface electrodes with fixed inter-electrode distance (Motion Lab Systems, Baton Rouge, LA). Vertical ground reaction force (70 SCIs, 7 NDs) or foot switch data (3 SCIs) were also collected and used to identify the swing and stance phases of the step cycle. For post-training data (n = 2), the EMG data without epidural stimulation during treadmill walking with minimal assistance and body weight support were analyzed. Individuals in the ND group walked on the treadmill at varying speeds with body weight load (BWL), and EMGs during 1.07-1.34 meters/second (m/s) with 100% BWL were included in the analysis of the motor module. Individuals in the SCI group stepped on a body-weight supported treadmill with manual facilitation. Manual facilitation provided stepping-related sensory cues and helped optimize body kinematics. Step speed and percentage BWL were selected for each subject to produce the optimal kinematic pattern and muscle activation with manual facilitation. Foot switches with four sensors on each side were attached to the shoe insole to detect foot contact with the treadmill during stepping. Vertical ground reaction force data were acquired at a frequency of 100 Hz from the treadmill instrumented with pressure sensors (Zebris Medical GmbH, Germany).

Data processing and analysis of motor module

Each channel of EMG signals was high-pass filtered at 40 Hz using a zero-lag fourth-order Butterworth filter, demeaned and rectified. The EMG signals were then low-pass filtered at 4 Hz using a zero lag, fourth-order Butterworth filter (Clark et al., 2010). Subsequently, the EMG from each muscle was normalized to its peak value from the gait cycle and time-interpolated over individual gait cycles on a time base with 100 points (Chvatal and Ting, 2012; Hayes et al., 2014) in order to allow comparisons between subjects. Motor modules were calculated based on the EMG traces of concatenated steps of ≥10 step cycles to capture step-to-step variability (Clark et al., 2010). In NDs, 10-19 steps were analyzed (13.29 ± 3.64 steps), and in SCIs, 10-34 steps were analyzed (18.03 ± 6.07 steps). After the EMG processing, motor modules during stepping were extracted separately for left and right leg muscles in each subject using three analysis methods: spatially-fixed non-negative matrix factorization (SF-NMF), temporally-fixed non-negative matrix factorization (TF-NMF), and independent component analysis (ICA). The number of modules required to account for ≥90% of the total variability in the EMG (VAF) was identified using each analysis (Clark et al., 2010).

Non-negative matrix factorization (NMF)

For both SF- and TF-NMF, the number of modules required to account for ≥90% of the total variability in the EMG (total VAF) was identified in each subject (Clark et al., 2010) using a custom-written MATLAB program. SF-NMF analysis was used to test the hypothesis that muscle synergies during stepping have

TABLE 1 Clinical characteristics of SCI subjects.

	Age (years)	Gender	YSI	NLI
AIS A (N = 34)	33.94 ± 11.72	26 male, 8 female	5.23 ± 5.59	Cervical = 16, Thoracic = 18
AIS B (N = 20)	32.30 ± 11.61	16 male, 4 female	3.26 ± 1.83	Cervical = 14, Thoracic = 5Lumbar = 1
AIS C (N = 13)	34.46 ± 13.30	9 male, 4 female	4.13 ± 2.93	Cervical = 9, Thoracic = 4
AIS D (N = 6)	41.00 ± 18.84	4 male, female	2.88 ± 3.26	Cervical = 4, Thoracic = 2

YSI, years since injury, NLI, neurological level of injury.

fixed spatial patterns and varying temporal patterns (Safavynia and Ting, 2012). To identify spatially-fixed synergy patterns, the EMG data were structured in m x t matrices, where m is the number of muscles recorded from each leg, and t is the concatenated steps (100 points per cycle x number of step cycles). Then, the NMF algorithm was applied to the matrix, which generated spatially-fixed muscle weightings W (m x n matrix) and temporally-varying muscle recruitment pattern C ($n \times t$ matrix).

TF-NMF analysis yielded motor module descriptions used to explore the hypothesis that muscle synergies during stepping have fixed temporal patterns and varying spatial patterns (Safavynia and Ting, 2012). To identify temporally-fixed synergy patterns, the EMG data were structured in s x r matrices, where s is the number of time points, and r is the number of muscles x step cycles. When the NMF algorithm was applied to the matrix, temporally-fixed muscle recruitment pattern C (s $\times$ n matrix) and spatially-varying muscle weightings W (n x r matrix) were generated (Ivanenko et al., 2003; Safavynia and Ting, 2012).

Independent component analysis (ICA)

Independent component analysis was used to extract mutually independent synergy components from EMG data (Bell and Sejnowski, 1995; Hart and Giszter, 2004; Dominici et al., 2011; Yang et al., 2019). The value of ICA is to detect weakly excited synergies using information rather than variance (Yang et al., 2019). As many components as input muscles are extracted on the basis of minimal information of components. However, ICA is very sensitive to information content and the original sampling and filtering of EMG. It has been very effective with intramuscular recordings (Kargo and Nitz, 2003; Hart and Giszter, 2004; Krouchev et al., 2006; Yang et al., 2019) though often also effective in surface EMG (Cappellini et al., 2006). Here, we tested ICA to explore if it added valuable information to the variance-based analyses. ICA always provides as many modules as muscles, which can then be examined for variance contributions. ICA was performed using the code from Giszter lab (adapted from Makeig's EEGlab; (McCrea, 1992; Makeig et al., 1997; Cappellini et al., 2006; Krouchev et al., 2006; Ivanenko et al., 2013; Yang et al., 2019). To be consistent with the synergy selection criterion in NMF analyses, the number of motor modules was identified based on the cumulative VAF $\geq$ 90%. In addition, to find a breakpoint or an "elbow" in the ICA VAF, a piecewise linear regression was performed using a piecewise regression function in OriginPro (Version 2021, OriginLab Corporation, Northampton, MA, USA).

Grouping of motor modules

The temporal and spatial characteristics of motor modules in NDs and SCIs were examined by grouping motor modules from each participant. Modules were grouped based on the muscle weighting and recruitment patterns with a high correlation coefficient (Pearson $r \geq 0.7$). We did not set the ND patterns as a reference due to the possibility that the common synergy patterns in SCIs differ from those of NDs. Modules identified by SF-NMF were grouped based on the correlation of spatial patterns, whereas modules from TF-NMF were grouped based on the correlation of temporal patterns.

Analysis of post-training data

In the individuals who achieved voluntary walking post-training, we further compared their pre-training and post-training (no stimulation) data. Six out of 7 muscles (RF, VL, MH, TA, MG, and SOL) were in common between pre-training data and post-training data. Therefore, 7 AIS B participants were randomly selected to define muscle synergies for non-ambulatory SCIs using NMF analyses (SF and TF-NMF). Further, muscle synergies from 6 muscles were defined in all NDs (n = 7) using NMF analyses. We quantified the similarity of the sets of synergies in pre- and post-training in 2 subjects with those of NDs and a cohort of AIS B SCI individuals in free order, by calculating an inner product column similarity measure using the matcorr and matperm function in MATLAB (from EEGlab; (Makeig et al., 1997; Godlove et al., 2016; Yang et al., 2019). Ratios of the correlation for each pre- and post-training module were calculated by dividing its correlation to ND group mean synergy by its correlation to SCI group mean synergy. The ratio of greater than 1 indicates that the module exhibits greater similarity to the NDs than to the SCIs, and less than 1 indicates the module exhibits greater similarity to the SCIs than to the NDs.

Statistical analysis

For descriptive and inferential statistics, the clinical characteristics, such as NLI and chronicity of injury (YSI),

were further categorized to determine the effects of clinical characteristics on the number and profile of motor modules. NLI was categorized into upper cervical (C1-C4), lower cervical (C5-C8), upper thoracic (T1-T6), and lower thoracic (T7-T12) lesions. Categorization of thoracic lesions was based on the potential impact of the autonomic dysfunction present in subjects with T6 injury and above on the modular organization and spinal plasticity. A subject with a lumbar lesion (n = 1) was not categorized. YSI was categorized into 5 subgroups: $\leq$ 1 year, 1-2 years, 2-5 years, 5-10 years, and $\geq$ 10 years. to compare the effects of chronicity of the injury on motor modules. Group differences in the number of modules across synergy extraction methods in the SCIs were analyzed using a 3-way ANOVA or MANOVA (SPSS, Version 26.0. IBM Corp., Armonk, NY). A repeated-measures ANOVA was used to compare the number of modules identified by the 3 analyses. Wilcoxon signed-rank test and paired t-test were used to compare the number of modules found bilaterally in NDs and SCIs, respectively. The significance level was set at 0.05, and *post hoc* comparisons were performed using Bonferroni correction. The comparisons of the muscle weighting and recruitment patterns among individuals were conducted using a Pearson correlation. Data are presented as mean $\pm$ standard deviation (SD).

Results

We analyzed data recorded from non-disabled individuals (NDs, N = 7) and SCI subjects (SCIs, N = 73; clinical characteristics in **Table 1** and **Supplementary Figure 1**). Of those SCIs, 71 were non-ambulatory, while 2 American Spinal Injury Association Impairment Scale (AIS) D subjects were ambulatory with a walker. None were subject to any in-house locomotor training prior to the testing. Consistent with previous findings, subjects with motor-complete and incomplete SCI showed patterns of rhythmic leg muscle activity during stepping with manual facilitation (Dietz et al., 1995; Dobkin et al., 1995), allowing extraction of muscle synergies (**Supplementary Figure 1**). Fifty-one SCI subjects demonstrated irregular activity or inactivity in at least one muscle during stepping. Note that in both NMF and ICA these "noise patterns" were segregated by the synergy separation algorithms and account for the fractions of ungrouped synergies excluded. They are thus not a confound in our data. In addition, individuals with SCI showed greater step-to-step variability in vertical ground reaction force during stepping. The standard deviation of vertical ground reaction force was 5.21 $\pm$ 3.58% BWL on average (range 1.74-30.18%) in SCIs, whereas in NDs, the standard deviation of vertical ground reaction force was 3.35 $\pm$ 0.83% BWL on average (range 2.01-4.85%).

Characteristics of stepping in individuals with SCI

We first examined if there was a specific set of step parameters that produced optimal stepping patterns with manual facilitation in individuals with SCI, and if the parameters differed depending on the clinical characteristics. The step speed and% body weight load (% BWL) were related to categorizations by AIS, years since injury (YSI), and neurological level of injury (NLI), and are shown in **Supplementary Figure 2**. A three-way MANOVA using AIS, YSI, and NLI indicated a significant interaction among the three factors on speed and% BWL, $F(4, 74) = 3.71$ $p = 0.008$. However, neither of the clinical characteristics individually had a significant effect on the step speed and% BWL (AIS $p = 0.08$; YSI $p = 0.08$; NLI $p = 0.39$). *Post hoc* analysis using Kruskal-Wallis tests also indicated that the AIS, YSI, and NLI had no significant effects on speed or % BWL in our subjects (all $p > 0.1$).

Number of motor modules from SF-NMF, TF-NMF, and ICA

We used spatially-fixed NMF (SF-NMF), temporally-fixed NMF (TF-NMF), and ICA to extract synergy patterns. These yielded varying numbers of motor modules to reliably reconstruct $\geq$90% variances accounted for (VAF) in the stepping EMG patterns in the NDs and SCIs. In all ND subjects, the SF-NMF and TF-NMF resulted in 3 modules to explain $\geq$90% VAF in each leg (**Figures 1A,B**), whereas the ICA identified 4-6 modules to explain $\geq$90% VAF (**Figure 1C**). Four modules were identified in 1 leg, 5 modules in 4 legs (4 individuals), and 6 modules in 9 legs (6 individuals). A repeated-measures ANOVA indicated that different modular analyses resulted in a significant difference in the number of modules in NDs detected, $F(2, 26) = 221$, $p < 0.001$ (**Figure 1D**). *Post hoc* comparison indicated that the number of modules from ICA was significantly greater than those from SF and TF-NMF analyses (*Bonferroni* $p < 0.001$; **Figure 1D**).

The number of motor modules was also compared between left and right legs to examine potential laterality or "sidedness" revealed by the analysis of motor modules. While all 7 NDs had the same number of modules bilaterally from both SF-NMF and TF-NMF (**Figures 1E,F**, respectively), in ICA, only 43% had the same number of modules bilaterally (**Figure 1G**). However, the number of motor modules extracted from ICA was not statistically different bilaterally (Wilcoxon signed rank test, $Z = 0.80$, $p = 0.38$).

Subjects in the SCI group exhibited a wider range of the number of motor modules, compared to NDs, needed to explain $\geq$90% VAF in all analyses. SF-NMF analysis led

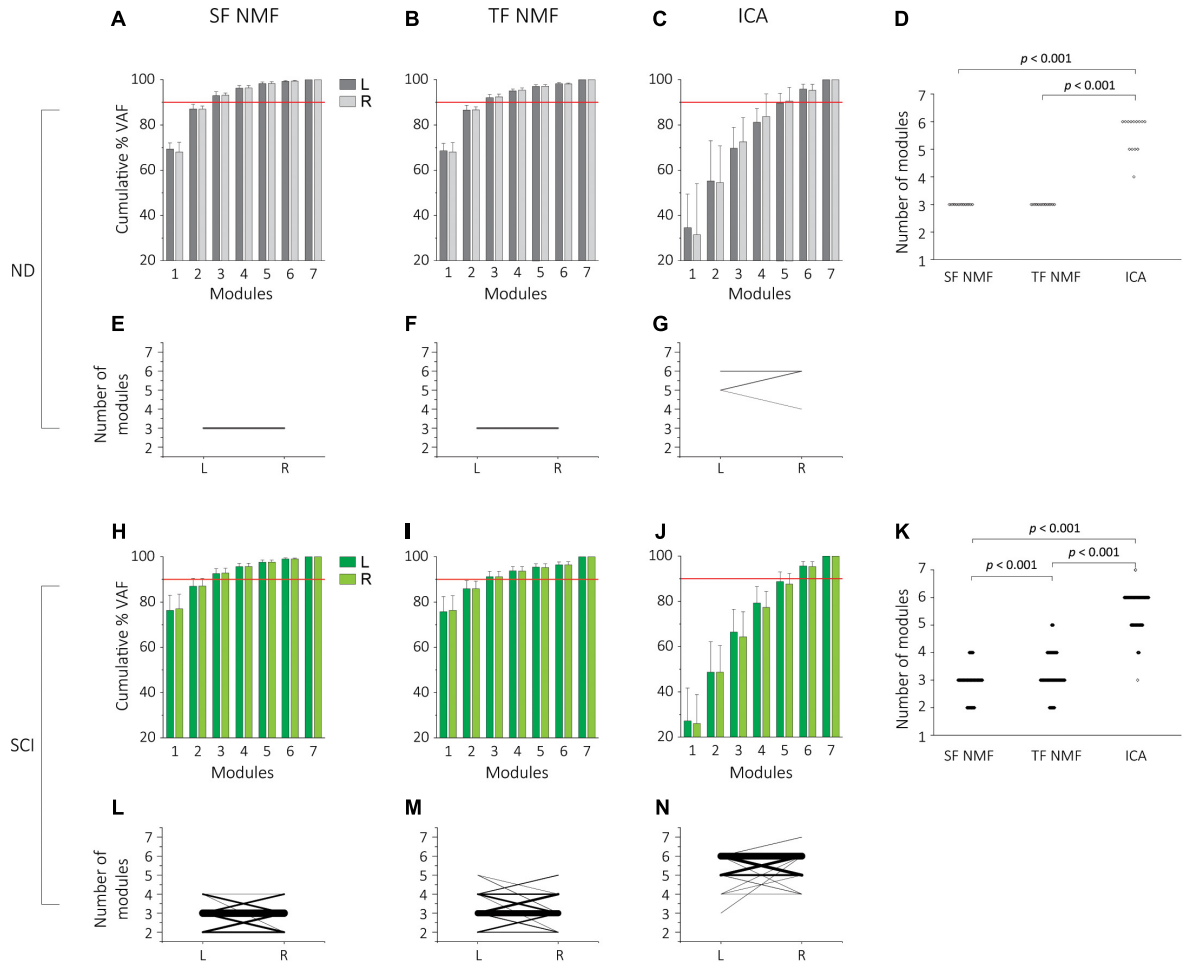

FIGURE 1
Cumulative percentage variability accounted for (%VAF) and the number of modules extracted by SF-NMF, TF-NMF, and ICA in NDs and SCIs. **(A–G)** indicates VAF and the number of modules in NDs (N = 7, 14 legs), and **(H,N)** indicates SCI data (N = 73, 146 legs). **(A–C)** %VAF (group mean + SD) for left (L) and right (R) legs from SF-NMF **(A)**, TF-NMF **(B)**, and ICA **(C)** in NDs. The horizontal red line indicates 90%. ICA required a greater number of modules to explain 90% VAF in EMGs. **(D)** Comparison of the number of modules explaining ≥90% VAF in the EMG all three analyses in NDs (left and right pooled). Each dot indicates an individual data point. SF- and TF-NMF identified 3 modules in all NDs, whereas ICA identified 4 modules in 1 leg (1 individual), 5 modules in 4 legs (4 individuals), 6 modules in 9 legs (6 individuals). ICA yielded a significantly greater number of modules compared to SF and TF-NMF to explain ≥90% VAF in NDs ($p < 0.001$). **(E-G)** The number of left and right modules in NDs, identified by SF-NMF **(E)**, TF-NMF **(F)**, and ICA **(G)**. Each line represents left-right pair for each subject. Thicker lines represent a greater prevalence of the pair. All subjects had 3 modules bilaterally from SF- and TF-NMF, whereas only 3 ND subjects had the same number of modules (Bizzi et al., 2000) bilaterally in ICA. The number of modules between left and right legs was not statistically different. **(H-J)**%VAF (group mean + SD) for left (L) and right (R) legs from SF-NMF **(H)**, TF-NMF **(I)**, and ICA **(J)** in SCIs. Similar to the NDs, ICA required a greater number of modules to explain 90% VAF in SCIs. **(K)** Comparison of the number of modules explaining ≥ 90% VAF in the EMG all three analyses in SCIs. SF-NMF yielded 2 modules in 32 legs (25 individuals), 3 modules in 97 legs (64 individuals), and 4 modules in 17 legs (16 individuals). TF-NMF yielded 2 modules in 19 legs (15 individuals), 3 modules in 85 legs (56 individuals), 4 modules in 35 legs (29 individuals), and 5 modules in 7 legs (7 individuals). ICA yielded 3 modules in 1 leg (1 individual), 4 modules in 7 legs (6 individuals), 5 modules in 44 legs (36 individuals), 6 modules in 92 legs (61 individuals) and 7 modules in 2 legs (2 individuals). ICA resulted in a significantly greater number of modules than SF- and TF-NMF in SCIs, and TF-NMF resulted in a greater number of modules than SF-NMF ($p < 0.001$). **(L-N)** The number of left and right modules in SCIs, identified by SF-NMF **(L)**, TF-NMF **(M)**, and ICA **(N)**. Each line represents left-right pair for each subject, and thicker lines represent a greater frequency of the pair. The number of modules between left and right legs was not statistically different.

to 2-4 modules (mean 2.90 ± 0.57, Figure 1H), and TF-NMF led to 2-5 modules (mean 3.21 ± 0.73; Figure 1I). SF-NMF identified 2 modules in 34% of SCIs, 3 modules in 88%, and 4 modules in 22%. In TF-NMF, 2 modules were found 21% of SCIs, 3 modules in 77%, 4 modules in 40%, and 5 modules in 10%. Similar to the NDs, the ICA in the SCIs indicated a greater number of modules, resulting in 3-7 modules (mean 5.59 ± 0.64; Figure 1J). Three modules were identified in 1% of SCIs, 4 modules in 8%, 5 modules in 49%, 6 modules in 84%, and 7 modules in 3%. A repeated-measures ANOVA again indicated that different modular analyses resulted in a significantly

different number of modules in SCIs, $F(2,286) = 1382.40$, $p < 0.001$ (Figure 1K). *Post hoc* comparison indicated that the number of modules from all 3 analyses was significantly different from each other (*Bonferroni* $p < 0.001$; Figure 1K). Results from NDs and SCIs together indicated that the ICA resulted in a greater number of modules compared to SF- and TF-NMF. This was consistent with ICA capturing weaker activated modules in the information-based analyses and likely richer drive structure, but the reduced number of recorded muscles and the surface EMG signal properties made these highly granular ICA results less informative than in other studies. Thus, subsequent analyses described here are focused on NMF.

The cumulative percentage VAF (% VAF) from SF- and TF-NMF demonstrated a clear "elbow" or breakpoint to determine the number of motor modules both in the NDs (Figures 1A,B) and SCIs (Figures 1H,I); however, cumulative% VAF found from ICA did not show the same characteristics (Figures 1C,J), and breakpoints were relatively poorly defined. Fuller and detailed comparison of NMF and ICA method for these data are in Supplementary material (Supplementary Results).

While some bilateral asymmetry is usually assumed *a priori* in SCIs, we directly compared the number of modules for the left and right leg in SCIs (Figures 1L–N). Forty-one SCI (56%) in SF-NMF, 37 SCIs (51%) in TF-NMF, and 39 SCIs (53%) in ICA had the same number of modules bilaterally. Paired *t*-tests indicated no significant laterality and associated bilateral asymmetry in the number of modules in the SCIs ($df = 72$, $t = 0.17$, $p = 0.87$ for SF-NMF; $df = 72$, $t = -0.3$, $p = 0.77$ for TF-NMF; $df = 72$, $t = -0.29$, $p = 0.77$ for ICA).

While the results of the left-right comparison indicated no sidedness, significant bilateral asymmetry may be present in the NDs and SCIs, absent systematic laterality, if the population sidedness was randomly sorted. Thus, we sorted the legs in each subject by fewer vs. more modules, i.e., regardless of the left or right, and tested if bilateral asymmetry was present and statistically significant in NDs and SCIs. When the number of modules between legs that had fewer vs. more modules was compared, there was no asymmetry in NDs ($Z = 1.80$, $p = 0.13$). However, in the SCI group, results indeed indicated significant bilateral asymmetry for SF-NMF (paired *t*-test, $t = -7.31$, $d.f. = 72$, $p < 0.001$) and for TF-NMF ($t = -7.71$, $d.f. = 72$, $p < 0.001$). Similarly, in ICA, there was also a significant bilateral asymmetry in SCIs ($t = -6.95$, $d.f. = 72$, $p < 0.001$). Thus, SCI resulted in significant bilateral asymmetry in the spinal circuitry that led to significant differences in motor modules between sides during stepping, but no laterality was observable. Lack of any systematic laterality allowed pooling of left and right legs into a single group for several of the subsequent analyses examining muscle weightings (spatial) and recruitment (temporal) patterns of motor modules.

Clinical characteristics do not determine the number of motor modules

We examined if the clinical characteristics, including AIS, NLI, and YSI influenced the number of motor modules in individuals with SCI. Supplementary Figure 4 represents the percentage distribution of each number of modules across AIS (Supplementary Figure 4A), NLI (upper and lower cervical or thoracic level; Supplementary Figure 4B), and YSI ($\leq$ 1 year, 1-2 years, 2-5 years, 5-10 years, $\geq$ 10 years; Supplementary Figure 4C), respectively. Three-way MANOVAs tested the effects of clinical characteristics on the left and right number of modules (separately) assessed from each of the analyses. Results for SF-NMF indicated no significant interaction among the three clinical characteristics, $F(4, 74) = 0.86$, $p = 0.50$, nor were main effects significant, $F(6, 74) = 1.44$, $p = 0.21$; $F(8, 74) = 0.95$, $p = 0.49$; $F(8, 74) = 1.34$, $p = 0.23$, respectively. Results for TF-NMF and ICA were similar, indicating that there were no significant interactions and no main effects of the clinical characteristics on the number of left and right modules, similar to the finding of clinical characteristics being unrelated to functional measures of %BWL and walking speed.

Characteristics of motor modules identified by SF-NMF in NDs and SCIs

Spatially-fixed non-negative matrix factorization identified 3 modules in NDs and 2-4 modules in SCIs. In NDs, all the synergy patterns had a within-group correlation coefficient of $\geq$0.7 when cross-correlated and grouped; therefore, no patterns were excluded. However, in SCIs, 88.2-92.2% of the spatial pattern showed a correlation coefficient of $\geq$0.7. Further details on the excluded patterns are found in Supplementary material (Supplementary Results).

The spatial and temporal patterns obtained from SF-NMF are presented in Figure 2. Spatial (synergy muscle weight) matching of modules extracted by SF-NMF resulted in a low variance in spatial patterns but greater variance in temporal patterns. Even though most muscles were active in more than 1 module, they were predominantly active in one module, as indicated by their weightings in the spatial pattern. We classified SCI subjects' leg modularity by the number of modules capturing 90% VAF and examined the resulting groups of synergies in 2-module, 3-module, and 4-module patterns. In NDs, only 3-module patterns were identified.

In the 3-module pattern for NDs, Module 1 (M1) was characterized by SOL and MG activity during the mid-late stance, Module 2 (M2) was characterized by TA, VL, RF, and AD activity during the early stance and early and late swing, and Module 3 (M3) was characterized by MH, VL, and AD activity during the swing-to-stance transition (Figure 2A).

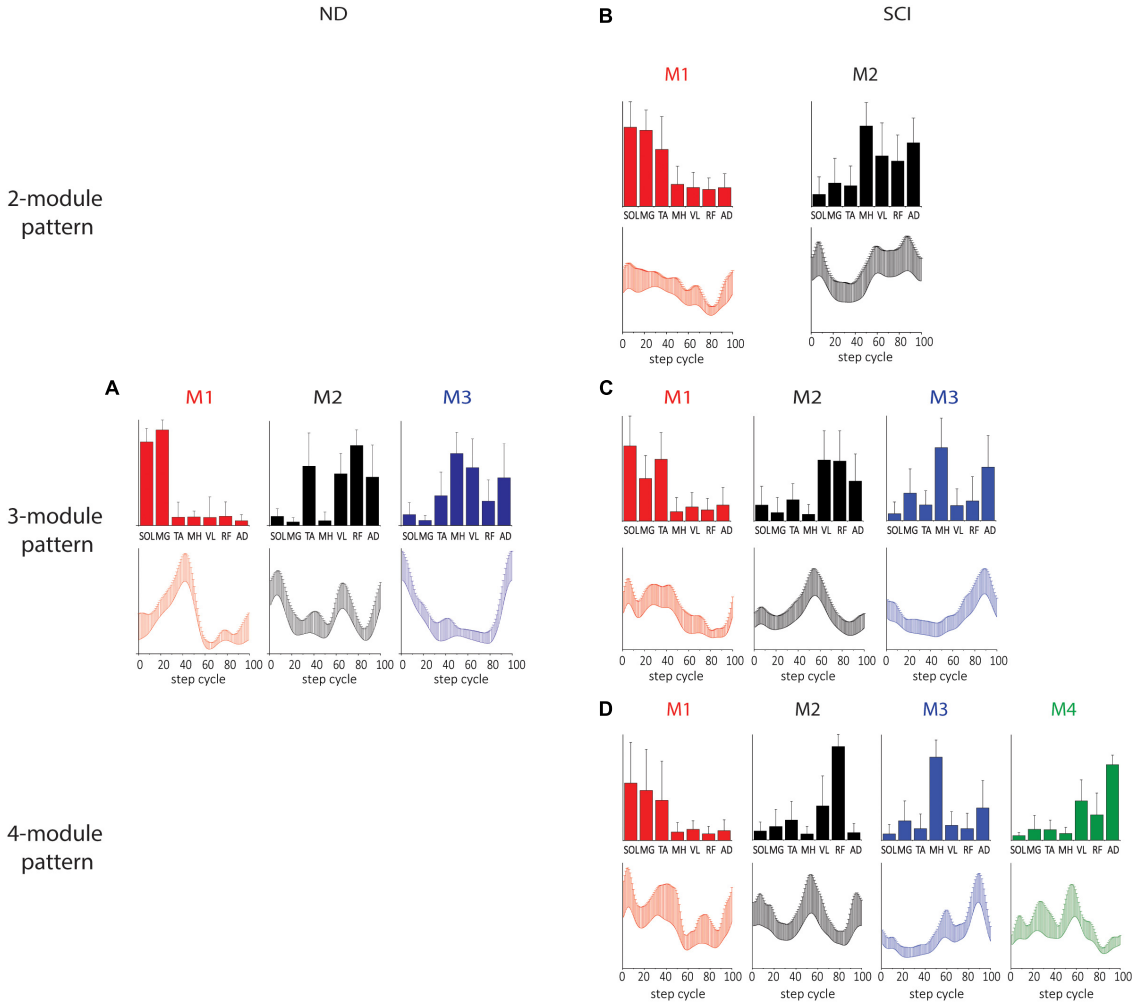

FIGURE 2
Spatial and temporal pattern identified by SF-NMF in NDs and SCIs. **(A)** ND 3-module pattern. **(B–D)** SCI 2-, 3-, and 4-module patterns. The correlations between the ND and SCI 3-module patterns were weak to moderate. Pearson r for M1 was 0.60 for the spatial patterns and 0.65 for the temporal patterns. For M2, Pearson r was 0.78 for spatial patterns and 0.03 for temporal patterns. For M3, Pearson r was 0.61 and 0.35 for spatial and temporal patterns, respectively. Bar graphs for spatial patterns indicate the group mean + SD. Temporal patterns are also indicated by group mean + SD. SOL, soleus; MG, medial gastrocnemius; TA, tibialis anterior; MH, medial hamstring; VL, vastus lateralis; RF, rectus femoris; AD, adductor.

In SCIs, all spatial and temporal profiles of motor modules looked somewhat different from those of NDs. In SCI 2-module patterns, each module was predominantly tied to stance or swing, with M1 active during the stance comprising SOL, MG, and TA activity and M2 active during the early stance and swing phases comprising MH, VL, RF, and AD activity (Figure 2B). In SCI 3-module patterns, while the spatial and temporal patterns of M1 appeared similar to the 2-module M1, we found that M2 and M3 diverged from the spatial pattern of the 2-module M2. During late stance in M2 in this case, VL and RF were active (M2), while MH and AD were active in M3 in late swing (M3; Figure 2C). In the SCI 4-module pattern (Figure 2D), the spatial and temporal patterns of M1, M2, and M3 appeared similar to those in the SCI 3-module patterns, and an M4 pattern appeared to have diverged from the 3-module M2. The correlation between the 3-module patterns of the NDs and SCIs was moderate (see Figure 2 legend for details). The differences in the temporal and spatial patterns between NDs and SCIs here indicate clear differences of synergy, e.g., coactivation of antagonistic ankle muscles during the stance phase occurs in the SCIs.

Characteristics of motor modules identified by TF-NMF in NDs and SCIs

Temporal matching in the modules extracted by TF-NMF resulted in a lower variance in temporal patterns and a greater

variance in spatial patterns. Only 3 modules were identified by TF-NMF in all NDs. M1 was active during the mid-late stance with SOL and MG activity, M2 was active during the early swing and swing-to-stance transition with TA, MH, VL, RF, and AD activity, and M3 was active during the early stance and early and late swing phases with TA activity (**Figure 3A**).

Modules identified by TF-NMF in SCIs further revealed differences in the modular organization, also identifying more (Lundberg et al., 1987; Bizzi et al., 1995, 2000; McCrea and Rybak, 2008) module patterns (**Figures 3B–D**). In correlating temporal patterns, 88.6-91.4% of temporal patterns showed a correlation coefficient of $\geq$0.7 (further details in **Supplementary material** (**Supplementary Results**). In 2-module patterns, while temporal patterns indicated a synergy during stance (M1) and swing phase (M2), the associated spatial patterns did not show any clear distinction in muscle activation for each (**Figure 3B**). In 3-module patterns, M1 was characterized by SOL and MG activity during the early-mid stance, M2 by VL, RF, and AD activity during the stance-to-swing transition, and M3 by MH and AD activity during late swing (**Figure 3C**). The correlation coefficients between the ND and SCI 3-module patterns were only weak to moderate. In 4-module patterns, M1 and M4 appeared to have diverged from the M1 in 2- and 3-module temporal patterns (**Figure 3D**). In 5-module patterns, while temporal patterns indicated peaks in different phases of stepping, spatial patterns again lacked clear distinctions in muscle activity (**Figure 3E**). Interestingly, in 4- and 5-module patterns, the M1 temporal patterns resembled the M1 of NDs, although the spatial pattern from TF-NMF did not show any similarity.

Correlation of motor modules identified by SF- and TF-NMF

In order to investigate if different strategies of identifying synergy patterns lead to different patterns of motor modules, we examined (for both SF- and TF-NMF analyses) the correlations between the within-method average temporal and spatial patterns of motor modules in NDs. M1 and M2 identified by both the two analyses in ND demonstrated a high correlation among subjects. For M1 of SF-NMF and TF-NMF, Pearson r for both temporal and spatial patterns were 1.00, and for M2, Pearson r for the spatial patterns was 0.78, and the temporal patterns 0.80. However, for M3, the correlation was weak; the correlation coefficient for the spatial patterns was 0.16, and the temporal patterns 0.42. These results indicate that while M1 and M2 in NDs were commonly identified as synergy patterns during stepping regardless of whether the spatial or temporal pattern was fixed, the patterns of M3 were more specific to the analysis method in ND.

We next compared correlations between the SF-NMF and TF-NMF methods. In SCIs, temporal and spatial patterns derived from SF-NMF and TF-NMF were compared within each of the 2-, 3-, and 4-module groups. In the SCI 2-module patterns, both M1 and M2 were highly correlated between SF- and TF-NMF methods. The correlation for M1 spatial patterns was 0.79, and temporal patterns 0.88. The correlation for M2 spatial patterns was 0.75, and temporal patterns 0.92. The SCI 3-module patterns also showed a high correlation between SF and TF-NMF. In M1, the correlation for spatial patterns was 0.97, and the temporal pattern was 1.00. The correlations for M2 spatial and temporal patterns were 0.97 and 0.96, respectively. Further, the correlation for M3 spatial patterns was 0.86, and temporal patterns 0.95. In SCI 4-module patterns, the correlation for M1 spatial patterns was 0.63, and temporal patterns 0.55. The correlation for M2 spatial patterns was 0.78, and temporal patterns 0.75. For M3, the correlation for the spatial patterns was 0.98, and the temporal pattern was 0.96. However, for M4, the correlation for the spatial and temporal patterns was −0.24 and −0.18, respectively. These results in the SCI group suggest that the modules identified in 2- and 3-module patterns were reliably identified regardless of whether the spatial or temporal pattern was fixed. However, the M4 pattern identified in the richer, 4-module pattern in SCI was more specific to the analysis method. The data as a whole support repeatable synergies and activation patterns across individuals in the untreated SCI population.

Characteristics of motor modules across clinical characteristics using three modules

While the number and shape of synergy modules extracted based on $\geq$90% VAF criterion provided valuable information on the characteristics of the modular organization of stepping circuitry in NDs and SCIs, the variations in module number resulting made it difficult to compare the motor modules across all SCI subjects. Thus, we proceeded to run a version of the NMF analysis using a 3-modules analysis on all subjects. This allowed us to further examine the effects of NLI, AIS, and chronicity of injury on the characteristics of motor modules.

The spatial and temporal patterns identified by the added 3-module SF- and TF-NMF analyses were mostly similar across AIS (SF-NMF modules in **Figure 4**, TF-NMF modules in **Supplementary Figure 6**). The majority of the spatial and temporal profiles of each AIS subgroup also demonstrated moderate to strong correlation with each other (**Supplementary Table 2**). Results also indicated that the spatial and temporal profiles of the subgroups showed a weak or (for temporal) even negative correlation to ND synergies, except in spatial patterns of M1 and M2 from SF-NMF (cf. **Figures 2A**, **3A**, **4** and **Table 2**) and temporal pattern of M3 from TF-NMF (cf. **Figures 2A**, **3A**

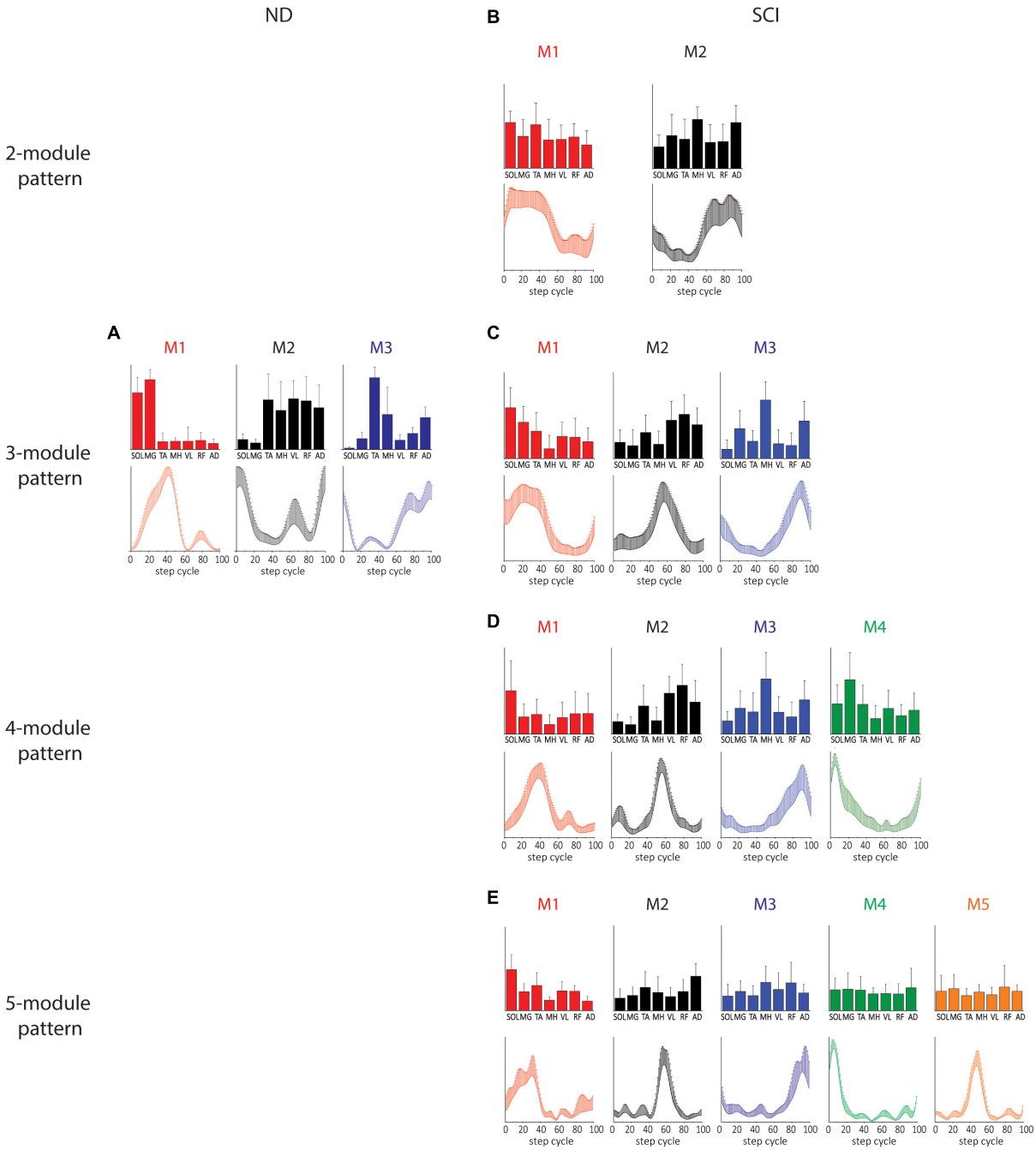

FIGURE 3
Spatial and temporal patterns identified by TF-NMF in NDs and SCIs. **(A)** ND 3-module pattern. **(B–E)** SCI 2-, 3-, 4-, and 5-module patterns. The correlations between the ND and SCI ND 3-module patterns were: for M1, temporal pattern $r = 0.79$ and spatial pattern $r = 0.82$; for M2, temporal pattern $r = -0.30$ and spatial pattern $r = 0.75$; for M3, temporal pattern $r = 0.83$ and spatial pattern $r = 0.25$.

and Supplementary Figure 6, Supplementary Table 2). Further, the correlations of the patterns between NDs and AIS C and D subjects were similar to the correlations between NDs and ASI A and B subjects, indicating functional supraspinal control of leg muscles does not lead to stepping synergy patterns that better resemble those of NDs.

The spatial and temporal patterns from SF-NMF and TF-NMF were also mostly similar across SCIs with different NLI (Figure 5 and Supplementary Figure 7) and varying chronicity of SCI (Supplementary Figure 8). The majority of comparisons between modules across neurological levels of injury (Supplementary Table 3) and chronicity

TABLE 2 Correlation of SF-NMF 3-module patterns among ND and AIS groups.

	Correlation of spatial patterns					Correlation of temporal patterns			
M1	**ND**	**AIS A**	**AIS B**	**AIS C**	**M1**	**ND**	**AIS A**	**AIS B**	**AIS C**
AIS A	**0.81***				AIS A	−0.28*			
AIS B	**0.85***	0.61			AIS B	0.61*	0.49*		
AIS C	**0.77***	0.68	**0.94***		AIS C	0.50*	0.64*	**0.93***	
AIS D	**0.91***	**0.78***	**0.94***	**0.87***	AIS D	0.55*	0.54*	**0.92***	**0.97***
M2					**M2**				
AIS A	**0.82***				AIS A	0.13			
AIS B	0.69	0.61			AIS B	**0.81***	0.58*		
AIS C	**0.91***	**0.92***	0.49		AIS C	0.10	**0.97***	0.50*	
AIS D	0.68	**0.90***	0.24	**0.91***	AIS D	−0.38*	**0.76***	0.11	**0.73***
M3					**M3**				
AIS A	0.63				AIS A	0.27*			
AIS B	0.58	**0.99***			AIS B	0.43*	**0.97***		
AIS C	0.58	**0.99***	**1.00***		AIS C	0.11	**0.94***	**0.92***	
AIS D	0.51	**0.88***	**0.92***	**0.92***	AIS D	0.24*	**0.87***	**0.80***	**0.78***

Bold text indicates a strong correlation ($r \geq 0.7$). Asterisk indicates statistical significance ($p < 0.05$).

(Supplementary Table 4) indicated strong correlations in spatial and temporal patterns among the subgroups of SCIs, but weak correlations to those of NDs. These findings indicate that the plasticity occurring in the spinal cord circuitry after SCI and the NLI do not strongly affect the modular structure expressed in pattern generation during stepping in this SCI population.

Characteristics of motor modules using 6 muscles in NDs and SCIs

Two subjects (B23 and B30) achieved independent walking in the presence of scES following locomotor training with task-specific stimulation. In order to examine synergy patterns in those two subjects with 6 EMGs (RF, VL, MH, TA, MG, and SOL) collected post-training, we performed the NMF analysis with 6 muscles in the non-ambulatory AIS B SCI subjects ($n = 7$, randomly selected) and NDs ($n = 7$). The number of motor modules extracted from 6 muscles varied from 2 to 4 in NDs and SCIs. In NDs, SF-NMF resulted in 2 modules (2 legs in 2 individuals) and 3 modules (12 legs in 7 individuals, Figures 6, 7 ND group), whereas TF-NMF resulted in 3 modules to explain ≥90% VAF in all individuals (14 legs). The spatial and temporal patterns of three-module synergy were consistent with those extracted from 7 muscles. In SCIs (7 AIS B subjects), SF-NMF yielded 3 modules in 6 individuals (11 legs' data) and 2 modules in 2 individuals (3 legs' data; Figures 6, 7, SCI group), and TF-NMF yielded 3 modules in all individuals (12 legs' data), 2 modules in 2 individuals (2 legs' data, 1 in each individual).

Characteristics of motor modules post-training in two successfully rehabilitated AIS B individuals

Post-training, the subject B23 walked on the treadmill at 0.13 m/s and 70% BWL, and B30 walked at 0.72 m/s and 65% BWL, respectively. Twelve concatenated steps from B23 and 36 steps from B30 were analyzed. The number of motor modules was mostly similar pre-training and post-training in both subjects. For B23, SF-NMF using 6 muscles led to 3 modules to explain ≥ 90% VAF pre- and post-training, and TF-NMF led to 4 modules pre- and post-training both legs. For B30, SF-NMF yielded 2 modules to explain ≥ 90% VAF pre- and post-training, and TF-NMF produced 3 modules pre-training and 2 modules post-training for both legs.

Training changed both temporal and spatial synergy patterns. In B23, despite the consistency in the number of modules to explain ≥ 90% VAF pre- and post-training, temporal and spatial patterns of muscle synergies changed (Figures 6, 7). Further, bilateral symmetry increased both for the spatial and temporal patterns. For example, pre-training, Pearson r for the left-right spatial pattern correlation of the three-module patterns ranged 0.15-0.86, and temporal correlation ranged 0.32-0.81 from SF-NMF. Post-training, Pearson r for left-right spatial pattern correlation ranged 0.88-0.92, and temporal pattern correlation ranged 0.75-0.95. In B30, temporal and spatial patterns obtained from SF-NMF were similar pre- and post-training. However, the patterns from TF-NMF had a reduction in motor modules. Bilateral symmetry remained

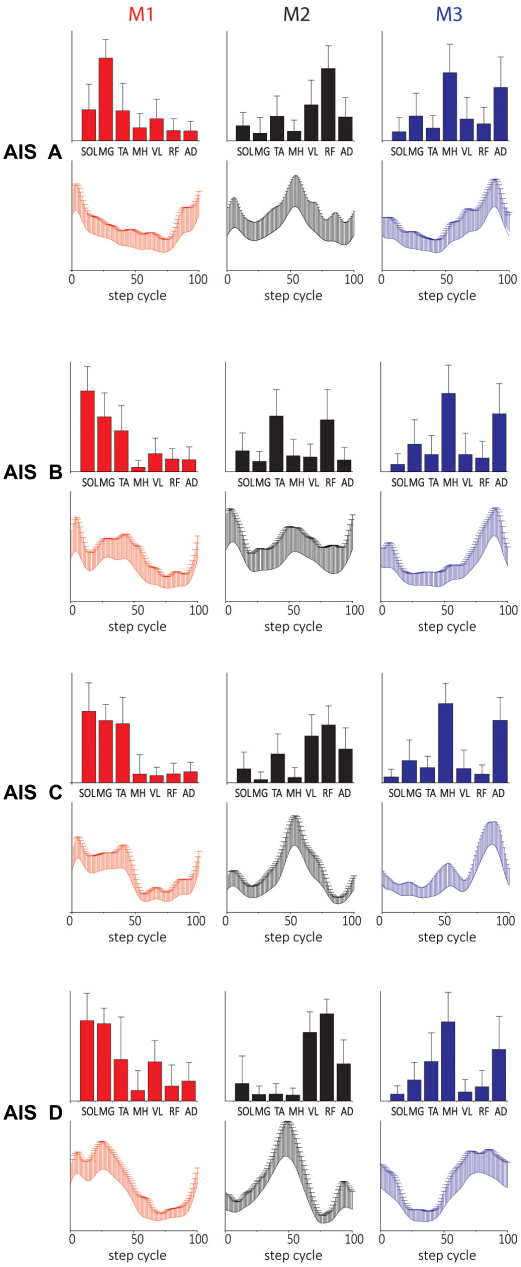

FIGURE 4
Three-(fixed) modules extracted from SF-NMF sorted by AIS. Each panel shows spatially-fixed synergy patterns during stepping categorized by AIS grade (group mean + SD). The patterns were generally well correlated across AIS categories. See **Table 2** for details on correlation.

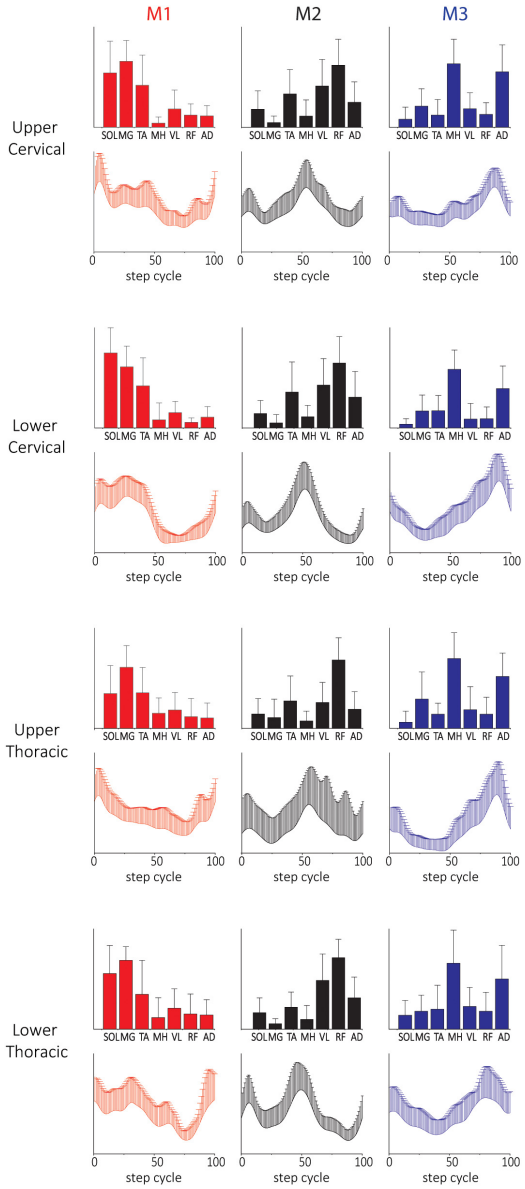

FIGURE 5
Three-(fixed) modules extracted from SF-NMF sorted by NLI. Each panel shows spatially-fixed synergy patterns grouped by NLI (group mean + SD). The patterns were generally well correlated across NLI categories. See **Supplementary Table 3** for details on correlations.

consistently high in B30 pre- and post-training. Pre-training, Pearson r for the left-right spatial pattern correlation of the two-module pattern was 0.99 and 1, and temporal correlation was 0.93 and 0.96 from SF-NMF. Post-training, Pearson r for left-right spatial pattern correlation was 0.97 and 1, and temporal pattern correlation was 0.93 and 0.94. While some of the motor modules changed, the synergy patterns did not exhibit greater similarity to the ND patterns (**Figures 6**, **7**, scatterplots on the bottom), indicating that the recovery of walking function is not dependent on normalized synergy patterns.

Discussion

In this study, we have characterized the modular structure of the locomotor network that the spinal cord is capable of

producing. We identified modularity in response to the step-related sensory feedback received during assisted stepping in subjects with severe SCI, and able-bodied locomotion (NDs). We also compared clinical characteristics, such as AIS, NLI, and YSI to modular control of locomotion and constituent muscle synergies. In addition, we analyzed the changes in synergy patterns in two individuals who achieved independent walking overground with scES, following step training with epidural stimulation (Angeli et al., 2018). Synergy patterns identified by ICA in SCIs mostly presented as single muscle-level synergies, and the NMF analyses were better suited to identify consistent synergy structure for the surface EMGs collected here. Our results indicated that the numbers of synergy patterns identified in SCIs were more variable than those in NDs. Further, neither the severity of the injury, the expected strength of supraspinal inputs, nor the post-injury time available for neuroplastic changes of the spinal circuitry was related to differences in the synergy structures in the SCIs. The synergy modules extracted by SF- and TF-NMF were largely similar within each group (NDs, SCIs). We demonstrated a highly consistent 3-module synergy pattern capturing $\geq$90% VAF in the ND group in NMF analyses within which M1 and M2 were highly similar but M3 could show more variation with analysis method (SF vs. TF). The SCI synergy characteristics are discussed in detail below. Lastly, our results in two successfully rehabilitated individuals indicated no discernable patterns that were consistent between them, indicating that the recovery of walking function with epidural stimulation is not dependent on the normalization of the spinal generated synergy patterns. This may be due to the fact that independent walking is only achieved during the combination of epidural stimulation and the subject's intention to walk, and thus may depend highly on neuromodulation and supraspinal controls. Nonetheless, small changes observed in the synergy patterns without stimulation indicate that the interneuronal network that generates synergy patterns in the lumbosacral spinal cord undergoes some changes during the locomotor training and scES, and these changes may also contribute to the recovery.

In the SCI group, SF- and TF-NMF identified 2-5 modules required for $\geq$90% VAF capture in stepping EMG. Subjects with 2-module synergy patterns, showed a peak of each during the stance or swing phase, similar to the patterns identified during stepping in neonates (Dominici et al., 2011). This resemblance suggests that the expression of the 2-module pattern may be related a collapse of synergies to a de-differentiated pattern caused by insufficient supraspinal control of the locomotor circuitry and compromised propriospinal and proprioceptive control. The spatial and temporal profiles of 3-, 4- and 5-module patterns showed some correlation between healthy modules and SCI modules, but also the SCI coactivation of antagonistic muscles (e.g., SOL, MG, and TA). When taken together, the data suggest that following SCI, even non-collapsed motor modules are expressed differently in some way from healthy modules. These findings further illustrate that the modular control of the locomotor circuitry either reverts to a more primitive structure as suggested by Yang, Logan (Yang et al., 2019), or else alternatively becomes tuned to or reorganized by the feedback controllers or specific biomechanical task requirements following SCI. For example, while commonly considered maladaptive, the coactivation of ankle muscles shown during stepping may be advantageous for tasks such as transfers or limb stabilization in SCIs (Lee et al., 2020).

Interestingly, we found that the synergy structures remained largely stable across AIS, YSI, and NLI. Ivanenko et al. (2003) reported that the motor modules identified from subjects with AIS C and D exhibited greater similarities to modules of NDs. This is inconsistent with our findings, as in 3-module patterns, spatial and temporal patterns of AIS C and D subjects showed a stronger correlation with those of AIS A and B subjects, rather than with those of NDs. This inconsistency may be due to the fact that the subjects in Ivanenko et al. (2003) underwent daily sessions of body weight-supported treadmill training for 1-3 months prior to the recording of leg muscle activity. In contrast, our subjects were untrained in any specific way prior to testing, except for the data from two participants (B23 and B30) presented after training. The training sessions might have helped guide the Ivanenko's SCI subjects to achieve synergy patterns closer to the healthy modules in AIS C and D subjects (Ivanenko et al., 2003). Further, our results of post-training synergies in two subjects indicate that the synergies sometimes do not strongly correlate with either SCIs or NDs (B23) or else change little and still correlate more to SCI (B30). These results suggest that the propriospinal contribution to the activation of synergies in these subjects post-training with scES is not adequate to normalize the synergy patterns even though the circuitry is capable of generating independent walking when additional excitation is provided to the spinal cord below the lesion. Alternatively, or in addition, it may be that specific supraspinal input is required for the generation of synergies similar to the NDs. Our new data also suggest that the step training combined with neuromodulation in spinal cord injured subjects may re-organize spinal circuitry differently compared to the locomotor training alone.

Our data suggest that AIS is not predictive of the modular control of the locomotor circuitry in response to afferent inputs following SCI. While AIS classification is a widely used diagnostic and classification tool in individuals with SCI, here and elsewhere, it is limited in capturing physiological and functional changes and classifying residual functions and potential for recovery following SCI (Steeves et al., 2007; Krishna et al., 2014; Kirshblum et al., 2021). Further, examining YSI also indicated stronger correlations among groups with different time frames since the injury, suggesting a striking level of stability in motor modules and in the core locomotor circuitry in SCIs over time, despite the reorganization of the spinal cord circuitry clearly occurring after injury (de Leon et al., 1998, 1999; Rossignol et al., 1999, 2008; Hiersemenzel et al., 2000; Pearson,

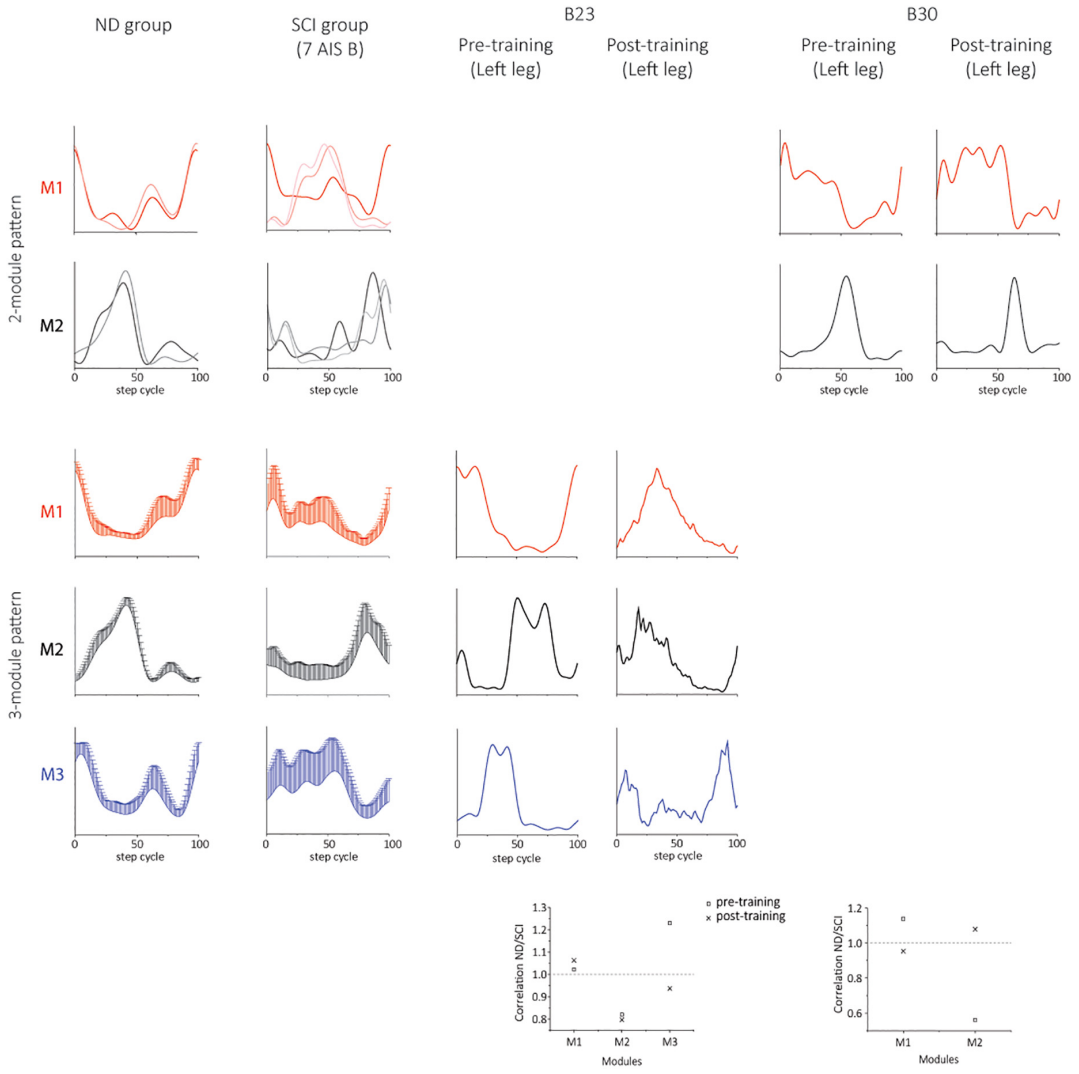

FIGURE 6
Temporal synergy patterns from SF-NMF using 6 muscles in NDs, SCIs, and two successfully rehabilitated individuals (B23 and B30). Each panel shows temporal patterns from SF-NMF grouped by the number of modules that explain ≥90% variance in the EMG from 6 muscles of each leg. In the 2-module patterns of ND and SCI groups, each line represents a temporal synergy pattern from a leg. The 3-module patterns of ND and SCI groups represent group mean + SD. The scatterplots on the bottom represent the ratio of the maximum absolute correlation of each module. The ratio of greater than 1 indicates that the module exhibits greater similarity to the NDs than to the SCIs. See section "Materials and methods" for further details.

2000; Schindler-Ivens and Shields, 2000; Rossignol, 2006; Cote et al., 2012; Beauparlant et al., 2013; Houle and Côté, 2013; Tseng and Shields, 2013; Takeoka et al., 2014; Asboth et al., 2018) and regardless of rehabilitation status. This is consistent with findings in the rodent SCI model (Yang et al., 2019), but it contrasts with the previous findings in people post-stroke during upper extremity tasks (Cheung et al., 2012). There, synergy patterns of upper extremity muscles were directly related to the chronicity of stroke (Cheung et al., 2012). Further, a strong correlation among patterns of NLI categories also indicated that the modular control of leg muscles is not strongly influenced by the level of disruption of intersegmental coupling between arms and legs (Bergmans et al., 1973; Miller et al., 1975; English and Lennard, 1982; Muzii et al., 1984; Wannier et al., 2001; Donker et al., 2002). This result also indicates that the autonomic dysfunction present in subjects with T6 injury or above does not influence the modular control nor the plasticity of the locomotor circuitry modularity expression following injury.

Populations with different neuropathologies possess different impairments of modular control of locomotor circuitry. Types of descending inputs lost or disrupted may affect the manifestation of motor modules differently. Individuals post-stroke showed a reduced number and

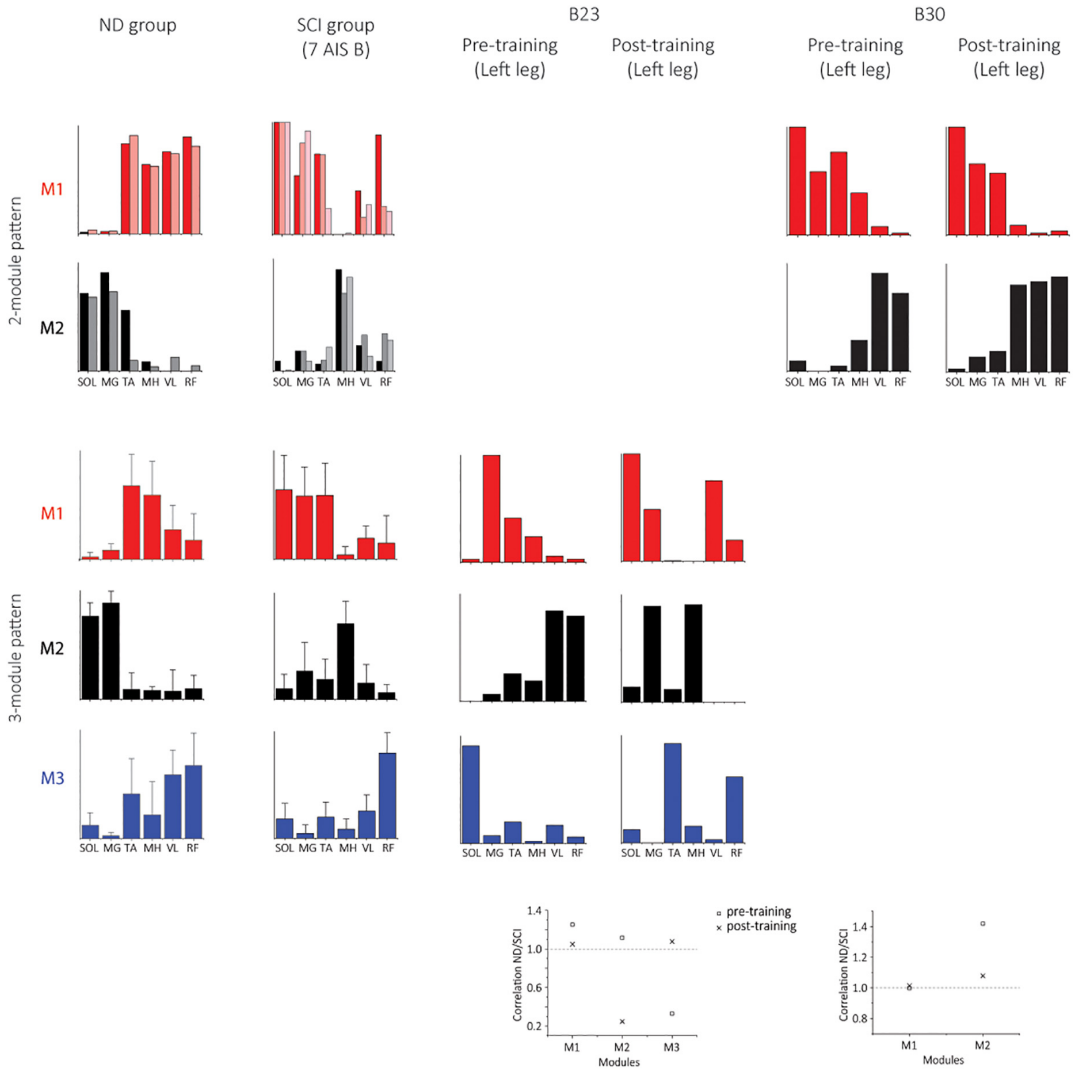

FIGURE 7
Spatial synergy patterns from SF-NMF using 6 muscles in NDs, SCIs, and two successfully rehabilitated individuals (B23 and B30). Each panel shows spatial patterns from SF-NMF grouped by the number of modules that explain ≥90% variance. In the 2-module patterns of the ND and SCI groups, each bar represents a spatial synergy pattern from a leg. The 3-module patterns of ND and SCI groups represent group mean + SD. The scatterplots on the bottom represent the ratio of the maximum absolute correlation of each module between the ND and SCI group mean synergies (2- or 3-modules) in B23 (3 modules) or B30 (2 modules). The ratio of greater than 1 indicates that the module exhibits greater similarity to the NDs than to the SCIs.

complexity of modules (Clark et al., 2010; Kautz et al., 2011; Routson et al., 2014) due to merging of motor modules (Clark et al., 2010), suggesting that cortical lesion leads to the inability to independently activate each module (Clark et al., 2010; Safavynia et al., 2011). Similarly, in people with Parkinson's disease, fewer motor modules were identified compared to healthy subjects, and temporal patterns were altered while some spatial synergy patterns were unaffected (Rodriguez et al., 2013). Individuals with cerebellar lesions showed similar numbers of modules to healthy subjects with an altered duration of muscle activation in the temporal pattern (Martino et al., 2015). While some of our results showed similarities to the previous findings regarding fewer motor modules compared to healthy subjects (Fox et al., 2013; Hayes et al., 2014; Danner et al., 2015; Perez-Nombela et al., 2017), we also identified similar and greater complexities in motor modules in some SCI subjects. These differences may be attributable to the ambulatory capabilities of individuals with SCI tested and the conditions in which the locomotor patterns were induced. The supraspinal control of the locomotor circuitry and the use of assistive devices may together contribute to a constrained and simplified modular expression (Fox et al., 2013; Hayes et al., 2014; Perez-Nombela et al., 2017). The varying number of motor modules, as well as altered temporal and spatial

patterns in the SCI subjects in our study, suggests that the loss of supraspinal inputs in the SCI subjects has extensive effects on spinal rhythm and pattern generation circuitry, and that these deficits of the modular control are not easily characterized by the commonly used clinical characteristics such as YSI, AIS, and NLI.

Our results on laterality illustrated that there was asymmetry in the number of modules, but, unsurprisingly, no inherent sidedness. While exploring bilateral symmetry of synergy patterns was not within the scope of this study, the rhythm and pattern generation between the two sides are clearly not independent of each other based on simulation and experimental investigations of the locomotor central pattern generator (Lanuza et al., 2004; Rybak et al., 2006, 2015; Crone et al., 2008; McCrea and Rybak, 2008; Dougherty et al., 2013; Hagglund et al., 2013; MacLellan et al., 2014; Ha and Dougherty, 2018; Dougherty and Ha, 2019). Further, greater bilateral symmetry in post-training synergies in one of the subjects (B30) may indicate that the recovery of bilateral symmetry is associated with the recovery of walking with neuromodulation. Future work may explore whether and how the synergy characteristics expressed on one side influence the synergy characteristics on the other side in the SCI stepping systems.

In SCI subjects, despite findings from Ivanenko et al. (2003), it is still unclear whether rehabilitation strategies can improve the modular control of locomotor circuitry across the range of SCI population and/or lead to modular characteristics more similar to NDs. Our data here, when combined with the earlier Ivanenko study, suggest that treatment modalities and rehabilitation combinations may have major impacts on this. Post-stroke, both merging and fractionation of muscle synergies during walking were observed over the course of therapy (Hashiguchi et al., 2016), and both spatial and temporal patterns of modularity can become similar to the healthy pattern after gait training (Routson et al., 2013). In SCI rats, electrical stimulation of motoneuron pools that mimics the spatiotemporal activation of muscle synergies seen during locomotion in healthy rats could improve weight-bearing ability and quality of locomotion (Wenger et al., 2016). As innovative techniques such as epidural and transcutaneous electrical stimulation combined with gait training and pharmacotherapy develop, it will be crucial to further investigate how these neuromodulatory techniques impact modular control of locomotor circuitry and generation of synergy patterns. It is of particular interest whether features of spinal-generated modular patterns, e.g., the number of modules or specific synergy patterns, serve as constraints or predictors for functional improvement.

There are two competing ways to think of the origins of synergies in locomotion: In the first locomotion synergies are relatively fluid and may be emergent from the combined influences of load and kinematic feedback systems of spinal cord operating as an ensemble under, or separated from descending control; in the second locomotion synergies may be evolutionarily pre-determined and have spinal structural bases, but be actively adjusted or augmented through reflex and descending control in voluntary tasks. Given the range of SCI subjects tested pre-training, we believe our data are consistent with a common core infrastructure of synergies, expressed in all SCI subjects despite their wide variations in condition. However, it remains conceivable that if the complex and technically difficult experiment were to be performed in which the initial untrained SCI kinematics and loading in stepping were somehow precisely matched to some variant of identical ND kinematics and loading, the patterns in stepping and the synergy production of each would converge to identical outputs. In the absence of such a technical tour de force experiment, we favor the hypothesis of a common synergy infrastructure in spinal cord across all SCI subjects, modified in intact individuals through voluntary and other descending controls of spinal cord. It is noteworthy that both perspectives on synergy origins expect that some SCI subjects will achieve good stepping and weight support after extensive training, as described in Grasso et al. (2004) where detailed kinematics and EMG analyses were combined with the modular EMG organization presented in Ivanenko et al. (2003). Presumably, this training outcome must build on and further engage the consistent synergy patterns described here in the non-ambulatory initial conditions.

The purpose of manual facilitation during stepping was to provide stepping-related sensory feedback that provides excitation to the spinal circuitry that is otherwise silent, and to optimize body kinematics. Further, in the SCIs, step speed and percent BWL were selected for each subject to produce the optimal stepping pattern and muscle activation with manual facilitation. However, the excitation that the selected step speed and BWL provided to the spinal cord may not be identical to the excitation in NDs, who did not require manual facilitation during stepping.

In conclusion, we demonstrated that SCI synergy patterns expressed were mostly stable across different severities of injury, strength of supraspinal inputs (AIS grade), and length of time, and also largely similar among SCI subjects, though differing from NDs. Further, the recovery of walking function following spinal cord epidural stimulation and locomotor training does not lead to the normalization of synergy patterns during stepping without the scES in two AIS B subjects. We believe that our findings provide a basis for future investigations of neural and biomechanical mechanisms underlying the modular organization of locomotor circuitry and constraints on plastic changes, and gait symmetry during training in people with SCI. In addition, the consistent synergy patterns in the SCI subjects and their variations from healthy patterns must impact the design and assessment of future rehabilitation strategies.

Data availability statement

The raw data supporting the conclusions of this article will be made available by the authors, without undue reservation.

Ethics statement

The studies involving human participants were reviewed and approved by the Institutional Review Board at the University of Louisville. The patients/participants provided their written informed consent to participate in this study.

Author contributions

SYS and CAA designed research. SJH and CAA collected the data. SYS, SFG, and CAA analyzed the data. SFG helped design and data analysis. SYS, SFG, and CAA wrote the manuscript. All authors contributed to the article and approved the submitted version.

Funding

This work was funded by National Institutes of Health (MPI P01 NS016333 to SJH, MPI R01 NS049209 to SJH, P30 RR031159 to SJH, MPI R01NS104194 to SFG), this work was also funded by the Leona M. and Harry B. Helmsley Charitable Trust, and the Craig H. Neilsen Foundation.

Acknowledgments

We are indebted to our research participants for their courage, dedication, motivation, and perseverance that made these research findings possible.

Conflict of interest

The authors declare that the research was conducted in the absence of any commercial or financial relationships that could be construed as a potential conflict of interest.

Publisher's note

Supplementary material

The Supplementary Material for this article can be found online at: https://www.frontiersin.org/articles/10.3389/fnins.2022.1041015/full#supplementary-material

References

Angeli, C. A., Boakye, M., Morton, R. A., Vogt, J., Benton, K., Chen, Y., et al. (2018). Re covery of over-ground walking after chronic motor complete spinal cord injury. *NEJM* 379, 1244–1250. doi: 10.1056/NEJMoa1803588

Asboth, L., Friedli, L., Beauparlant, J., Martinez-Gonzalez, C., Anil, S., Rey, E., et al. (2018). Cortico–reticulo–spinal circuit reorganization enables functional recovery after severe spinal cord contusion. *Nat. Neurosci.* 21, 576–588. doi: 10.1038/s41593-018-0093-5

Beauparlant, J., van den Brand, R., Barraud, Q., Friedli, L., Musienko, P., Dietz, V., et al. (2013). Undirected compensatory plasticity contributes to neuronal dysfunction after severe spinal cord injury. *Brain* 136, 3347–3361. doi: 10.1093/brain/awt204

Bell, A. J., and Sejnowski, T. J. (1995). An information-maximization approach to blind separation and blind deconvolution. *Neural Comput.* 7, 1129–1159.

Bergmans, J., Miller, S., and Reitsma, D. J. (1973). Influence of L-DOPA on transmission in long ascending propriospinal pathways in the cat. *Brain Res.* 62, 155–167. doi: 10.1016/0006-8993(73)90625-2

Bernstein, N. A. (1967). *The co-ordination and regulation of movements*. Oxford: Pergamon Press.

Bizzi, E., Giszter, S. F., Loeb, E., Mussa-Ivaldi, F. A., and Saltiel, P. (1995). Modular organization of motor behavior in the frog's spinal cord. *Trends Neurosci.* 18, 442–446. doi: 10.1016/0166-2236(95)94494-P

Bizzi, E., Mussa-Ivaldi, F., and Giszter, S. (1991). Computations underlying the execution of movement: A biological perspective. *Science* 253, 287–291. doi: 10.1126/science.1857964

Bizzi, E., Tresch, M. C., Saltiel, P., and d'Avella, A. (2000). New perspectives on spinal motor systems. *Nat. Rev. Neurosci.* 1, 101–108. doi: 10.1038/35039000

Caggiano, V., Cheung, V. C. K., and Bizzi, E. (2016). An optogenetic demonstration of motor modularity in the mammalian spinal cord. *Sci. Rep.* 6:35185. doi: 10.1038/srep35185

Cappellini, G., Ivanenko, Y. P., Poppele, R. E., and Lacquaniti, F. (2006). Motor patterns in human walking and running. *J. Neurophysiol.* 95, 3426–3437. doi: 10.1152/jn.00081.2006

Cheung, V. C. K., Turolla, A., Agostini, M., Silvoni, S., Bennis, C., Kasi, P., et al. (2012). Muscle synergy patterns as physiological markers of motor cortical damage. *PNAS* 109, 14652–14656. doi: 10.1073/pnas.1212056109

Chvatal, S. A., and Ting, L. H. (2012). Voluntary and reactive recruitment of locomotor muscle synergies during perturbed walking. *J. Neurosci.* 32, 12237–12250. doi: 10.1523/JNEUROSCI.6344-11.2012

Clark, D. J., Ting, L. H., Zajac, F. E., Neptune, R. R., and Kautz, S. A. (2010). Merging of healthy motor modules predicts reduced locomotor performance and muscle coordination complexity post-stroke. *J. Neurophysiol.* 103, 844–857. doi: 10.1152/jn.00825.2009

Cote, M. P., Detloff, M. R., Wade, R. E. Jr., Lemay, M. A., and Houle, J. D. (2012). Plasticity in ascending long propriospinal and descending supraspinal pathways in chronic cervical spinal cord injured rats. *Front. Physiol.* 3:330. doi: 10.3389/fphys.2012.00330

Crone, S. A., Quinlan, K. A., Zagoraiou, L., Droho, S., Restrepo, C. E., Lundfald, L., et al. (2008). Genetic ablation of V2a ipsilateral interneurons disrupts left-right locomotor coordination in mammalian spinal cord. *Neuron* 60, 70–83. doi: 10.1016/j.neuron.2008.08.009

Danner, S. M., Hofstoetter, U. S., Freundl, B., Binder, H., Mayr, W., Rattay, F., et al. (2015). Human spinal locomotor control is based on flexibly organized burst generators. *Brain* 138(Pt 3), 577–588. doi: 10.1093/brain/awu372

de Leon, R. D., Hodgson, J. A., Roy, R. R., and Edgerton, V. R. (1998). Locomotor capacity attributable to step training versus spontaneous recovery after spinalization in adult cats. *J. Neurophysiol.* 79, 1329–1340. doi: 10.1152/jn.1998.79.3.1329

de Leon, R. D., Tamaki, H., Hodgson, J. A., Roy, R. R., and Edgerton, V. R. (1999). Hindlimb locomotor and postural training modulates glycinergic inhibition in the spinal cord of the adult spinal cat. *J. Neurophysiol.* 82, 359–369. doi: 10.1152/jn.1999.82.1.359

Dietz, V., Colombo, G., Jensen, L., and Baumgartner, L. (1995). Locomotor capacity of spinal cord in paraplegic patients. *Ann. Neurol.* 37, 574–582. doi: 10.1002/ana.410370506

Dobkin, B. H., Harkema, S., Requejo, P., and Edgerton, V. R. (1995). Modulation of locomotor-like EMG activity in subjects with complete and incomplete spinal cord injury. *J. Neurol. Rehabil.* 9, 183–190.

Dominici, N., Ivanenko, Y. P., Cappellini, G., d'Avella, A., Mondì, V., Cicchese, M., et al. (2011). Locomotor primitives in newborn babies and their development. *Science* 334, 997–999. doi: 10.1126/science.1210617

Donker, S. F., Mulder, T., Nienhuis, B., and Duysens, J. (2002). Adaptations in arm movements for added mass to wrist or ankle during walking. *Exp. Brain Res.* 146, 26–31. doi: 10.1007/s00221-002-1145-2

Dougherty, K. J., and Ha, N. T. (2019). The rhythm section: An update on spinal interneurons setting the beat for mammalian locomotion. *Curr. Opin. Physiol.* 8, 84–93. doi: 10.1016/j.cophys.2019.01.004

Dougherty, K. J., Zagoraiou, L., Satoh, D., Rozani, I., Doobar, S., Arber, S., et al. (2013). Locomotor rhythm generation linked to the output of spinal shox2 excitatory interneurons. *Neuron* 80, 920–933. doi: 10.1016/j.neuron.2013.08.015

English, A. W., and Lennard, P. R. (1982). Interlimb coordination during stepping in the cat: In-phase stepping and gait transitions. *Brain Res.* 245, 353–364. doi: 10.1016/0006-8993(82)90818-6

Fox, E. J., Tester, N. J., Kautz, S. A., Howland, D. R., Clark, D. J., Garvan, C., et al. (2013). Modular control of varied locomotor tasks in children with incomplete spinal cord injuries. *J. Neurophysiol.* 110, 1415–1425. doi: 10.1152/jn.00676.2012

Giszter, S. F. (2015). Motor primitives new data and future questions. *Curr. Opin. Neurobiol.* 33, 156–165. doi: 10.1016/j.conb.2015.04.004

Giszter, S. F., Mussa-Ivaldi, F. A., and Bizzi, E. (1993). Convergent force fields organized in the frog's spinal cord. *J. Neurosci.* 13, 467–491. doi: 10.1523/JNEUROSCI.13-02-00467.1993

Godlove, J., Gulati, T., Dichter, B., Chang, E., and Ganguly, K. (2016). Muscle synergies after stroke are correlated with perilesional high gamma. *Ann. Clin. Transl. Neurol.* 3, 956–961. doi: 10.1002/acn3.368

Grasso, R., Ivanenko, Y. P., Zago, M., Molinari, M., Scivoletto, G., Castellano, V., et al. (2004). Distributed plasticity of locomotor pattern generators in spinal cord injured patients. *Brain* 127(Pt 5), 1019–1034. doi: 10.1093/brain/awh115

Ha, N. T., and Dougherty, K. J. (2018). Spinal Shox2 interneuron interconnectivity related to function and development. *Elife* 7:e42519. doi: 10.7554/eLife.42519

Hagglund, M., Dougherty, K. J., Borgius, L., Itohara, S., Iwasato, T., and Kiehn, O. (2013). Optogenetic dissection reveals multiple rhythmogenic modules underlying locomotion. *Proc. Natl. Acad. Sci. U.S.A.* 110, 11589–11594. doi: 10.1073/pnas.1304365110

Hart, C. B., and Giszter, S. F. (2004). Modular premotor drives and unit bursts as primitives for frog motor behaviors. *J. Neurosci.* 24, 5269–5282. doi: 10.1523/JNEUROSCI.5626-03.2004

Hart, C. B., and Giszter, S. F. (2010). A neural basis for motor primitives in the spinal cord. *J. Neurosci.* 30, 1322–1336. doi: 10.1523/JNEUROSCI.5894-08.2010

Hashiguchi, Y., Ohata, K., Kitatani, R., Yamakami, N., Sakuma, K., Osako, S., et al. (2016). Merging and fractionation of muscle synergy indicate the recovery process in patients with hemiplegia: The first study of patients after subacute stroke. *Neural Plast.* 2016, 1–7. doi: 10.1155/2016/5282957

Hayes, H. B., Chvatal, S. A., French, M. A., Ting, L. H., and Trumbower, R. D. (2014). Neuromuscular constraints on muscle coordination during overground walking in persons with chronic incomplete spinal cord injury. *Clin. Neurophysiol.* 125, 2024–2035. doi: 10.1016/j.clinph.2014.02.001

Hiersemenzel, L. P., Curt, A., and Dietz, V. (2000). From spinal shock to spasticity: Neuronal adaptations to a spinal cord injury. *Neurology* 54, 1574–1582. doi: 10.1212/WNL.54.8.1574

Houle, J. D., and Côté, M.-P. (2013). Axon regeneration and exercise-dependent plasticity after spinal cord injury. *Ann. N. Y. Acad. Sci.* 1279, 154–163. doi: 10.1111/nyas.12052

Ivanenko, Y. P., Cappellini, G., Dominici, N., Poppele, R. E., and Lacquaniti, F. (2007). Modular control of limb movements during human locomotion. *J. Neurosci.* 27, 11149–11161. doi: 10.1523/JNEUROSCI.2644-07.2007

Ivanenko, Y. P., Cappellini, G., Solopova, I. A., Grishin, A. A., Maclellan, M. J., Poppele, R. E., et al. (2013). Plasticity and modular control of locomotor patterns in neurological disorders with motor deficits. *Front. Comput. Neurosci.* 7:123. doi: 10.3389/fncom.2013.00123

Ivanenko, Y. P., Grasso, R., Zago, M., Molinari, M., Scivoletto, G., Castellano, V., et al. (2003). Temporal components of the motor patterns expressed by the human spinal cord reflect foot kinematics. *J. Neurophysiol.* 90, 3555–3565. doi: 10.1152/jn.00223.2003

Kargo, W. J., and Giszter, S. F. (2000). Rapid correction of aimed movements by summation of force-field primitives. *.J. Neurosci.* 20, 409–426. doi: 10.1523/JNEUROSCI.20-01-00409.2000

Kargo, W. J., and Nitz, D. A. (2003). Early skill learning is expressed through selection and tuning of cortically represented muscle synergies. *J. Neurosci.* 23, 11255–11269. doi: 10.1523/JNEUROSCI.23-35-11255.2003

Kautz, S. A., Bowden, M. G., Clark, D. J., and Neptune, R. R. (2011). Comparison of motor control deficits during treadmill and overground walking poststroke. *Neurorehabil. Neural Repair* 25, 756–765. doi: 10.1177/1545968311407515

Kirshblum, S., Snider, B., Eren, F., and Guest, J. (2021). Characterizing natural recovery after traumatic spinal cord injury. *J. Neurotrauma* 38, 1267–1284. doi: 10.1089/neu.2020.7473

Krishna, V., Andrews, H., Varma, A., Mintzer, J., Kindy, M. S., and Guest, J. (2014). Spinal cord injury: How can we improve the classification and quantification of its severity and prognosis? *J. Neurotrauma* 31, 215–227. doi: 10.1089/neu.2013.2982

Krouchev, N., Kalaska, J. F., and Drew, T. (2006). Sequential activation of muscle synergies during locomotion in the intact cat as revealed by cluster analysis and direct decomposition. *J. Neurophysiol.* 96, 1991–2010. doi: 10.1152/jn.00241.2006

Lanuza, G. M., Gosgnach, S., Pierani, A., Jessell, T. M., and Goulding, M. (2004). Genetic identification of spinal interneurons that coordinate left-right locomotor activity necessary for walking movements. *Neuron* 42, 375–386. doi: 10.1016/s0896-6273(04)00249-1

Lee, S. S. M., Lam, T., Pauhl, K., and Wakeling, J. M. (2020). Quantifying muscle coactivation in individuals with incomplete spinal cord injury using wavelets. *Clin. Biomech.* 73, 101–107. doi: 10.1016/j.clinbiomech.2020.01.001

Levine, A. J., Hinckley, C. A., Hilde, K. L., Driscoll, S. P., Poon, T. H., Montgomery, J. M., et al. (2014). Identification of a cellular node for motor control pathways. *Nat. Neurosci.* 17:586. doi: 10.1038/nn.3675

Lundberg, A., Malmgren, K., and Schomburg, E. D. (1987). Reflex pathways from group II muscle afferents. 2. Functional characteristics of reflex pathways to alpha-motoneurones. *Exp. Brain. Res.* 65, 282–293. doi: 10.1007/BF00236300

MacLellan, M. J., Ivanenko, Y. P., Massaad, F., Bruijn, S. M., Duysens, J., and Lacquaniti, F. (2014). Muscle activation patterns are bilaterally linked during split-belt treadmill walking in humans. *J. Neurophysiol.* 111, 1541–1552. doi: 10.1152/jn.00437.2013

Makeig, S., Jung, T. P., Bell, A. J., Ghahremani, D., and Sejnowski, T. J. (1997). Blind separation of auditory event-related brain responses into independent components. *PNAS* 94, 10979–10984. doi: 10.1073/pnas.94.20.10979

Martino, G., Ivanenko, Y. P., D'Avella, A., Serrao, M., Ranavolo, A., Draicchio, F., et al. (2015). Neuromuscular adjustments of gait associated with unstable conditions. *J. Neurophysiol.* 114, 2867–2882. doi: 10.1152/jn.00029.2015

McCrea, D. (1992). Can sense be made of spinal interneuron circuits? *Behav. Brain Sci.* 15:633.

McCrea, D. A., and Rybak, I. A. (2008). Organization of mammalian locomotor rhythm and pattern generation. *Brain Res. Rev.* 57, 134–146. doi: 10.1016/j.brainresrev.2007.08.006

Miller, S., van der Burg, J., and van der Meché, F. G. A. (1975). Coordination of movements of the hindlimbs and forelimbs in different forms of locomotion in

normal and decerebrate cats. *Brain Res.* 91, 217–237. doi: 10.1016/0006-8993(75)90544-2

Mussa-Ivaldi, F. A., Giszter, S. F., and Bizzi, E. (1994). Linear combinations of primitives in vertebrate motor control. *PNAS* 91, 7534–7538. doi: 10.1073/pnas.91.16.7534

Muzii, R. A., Warburg, C. L., and Gentile, A. M. (1984). Coordination of the upper and lower extremities. *Hum. Mov. Sci.* 3, 337–354. doi: 10.1016/0167-9457(84)90014-9

Pearson, K. G. (2000). Neural adaptation in the generation of rhythmic behavior. *Annu. Rev. Physiol.* 62, 723–753. doi: 10.1146/annurev.physiol.62.1.723

Perez-Nombela, S., Barroso, F., Torricelli, D., de Los Reyes-Guzman, A., Del-Ama, A. J., Gomez-Soriano, J., et al. (2017). Modular control of gait after incomplete spinal cord injury: Differences between sides. *Spinal Cord* 55, 79–86. doi: 10.1038/sc.2016.99

Rodriguez, K. L., Roemmich, R. T., Cam, B., Fregly, B. J., and Hass, C. J. (2013). Persons with Parkinson's disease exhibit decreased neuromuscular complexity during gait. *Clin. Neurophysiol.* 124, 1390–1397. doi: 10.1016/j.clinph.2013.02.006

Rossignol, S. (2006). Plasticity of connections underlying locomotor recovery after central and/or peripheral lesions in the adult mammals. *Philos. Trans. R. Soc. Lond. B Biol. Sci.* 361, 1647–1671. doi: 10.1098/rstb.2006.1889

Rossignol, S., Barrière, G., Frigon, A., Barthélemy, D., Bouyer, L., Provencher, J., et al. (2008). Plasticity of locomotor sensorimotor interactions after peripheral and/or spinal lesions. *Brain Res. Rev.* 57, 228–240. doi: 10.1016/j.brainresrev.2007.06.019

Rossignol, S., Drew, T., Brustein, E., and Jiang, W. (1999). Locomotor performance and adaptation after partial or complete spinal cord lesions in the cat. *Prog. Brain Res.* 123, 349–365. doi: 10.1016/S0079-6123(08)62870-8

Routson, R. L., Clark, D. J., Bowden, M. G., Kautz, S. A., and Neptune, R. R. (2013). The influence of locomotor rehabilitation on module quality and post-stroke hemiparetic walking performance. *Gait Posture* 38, 511–517. doi: 10.1016/j.gaitpost.2013.01.020

Routson, R. L., Kautz, S. A., and Neptune, R. R. (2014). Modular organization across changing task demands in healthy and poststroke gait. *Physiol. Rep.* 2:e12055. doi: 10.14814/phy2.12055

Rybak, I. A., Dougherty, K. J., and Shevtsova, N. A. (2015). Organization of the mammalian locomotor CPG: Review of computational model and circuit architectures based on genetically identified spinal interneurons. *eNeuro* 2:0069-15. doi: 10.1523/ENEURO.0069-15.2015

Rybak, I. A., Shevtsova, N. A., Lafreniere-Roula, M., and McCrea, D. A. (2006). Modelling spinal circuitry involved in locomotor pattern generation: Insights from deletions during fictive locomotion. *J. Physiol.* 577(Pt 2), 617–639. doi: 10.1113/jphysiol.2006.118703

Safavynia, S. A., and Ting, L. H. (2012). Task-level feedback can explain temporal recruitment of spatially fixed muscle synergies throughout postural perturbations. *J. Neurophysiol.* 107, 159–177. doi: 10.1152/jn.00653.2011

Safavynia, S. A., Torres-Oviedo, G., and Ting, L. H. (2011). Muscle synergies: Implications for clinical evaluation and rehabilitation of movement. *Top. Spinal Cord Inj. Rehabil.* 17, 16–24. doi: 10.1310/sci1701-16

Schindler-Ivens, S., and Shields, R. K. (2000). Low frequency depression of H-reflexes in humans with acute and chronic spinal-cord injury. *Exp. Brain Res.* 133, 233–241. doi: 10.1007/s002210000377

Steeves, J. D., Lammertse, D., Curt, A., Fawcett, J. W., Tuszynski, M. H., Ditunno, J. F., et al. (2007). Guidelines for the conduct of clinical trials for spinal cord injury (SCI) as developed by the ICCP panel: Clinical trial outcome measures. *Spinal Cord* 45, 206–221. doi: 10.1038/sj.sc.3102008

Sylos-Labini, F., La Scaleia, V., Cappellini, G., Fabiano, A., Picone, S., Keshishian, E. S., et al. (2020). Distinct locomotor precursors in newborn babies. *PNAS* 117, 9604–9612. doi: 10.1073/pnas.1920984117

Takei, T., and Seki, K. (2010). Spinal interneurons facilitate coactivation of hand muscles during a precision grip task in monkeys. *J. Neurosci.* 30, 17041–17050. doi: 10.1523/JNEUROSCI.4297-10.2010

Takei, T., Confais, J., Tomatsu, S., Oya, T., and Seki, K. (2017). Neural basis for hand muscle synergies in the primate spinal cord. *PNAS* 114, 8643–8648. doi: 10.1073/pnas.1704328114

Takeoka, A., Vollenweider, I., Courtine, G., and Arber, S. (2014). Muscle spindle feedback directs locomotor recovery and circuit reorganization after spinal cord injury. *Cell* 159, 1626–1639. doi: 10.1016/j.cell.2014.11.019

Tresch, M. C., and Bizzi, E. (1999). Responses to spinal microstimulation in the chronically spinalized rat and their relationship to spinal systems activated by low threshold cutaneous stimulation. *Exp. Brain Res.* 129, 401–416. doi: 10.1007/s002210050908

Tseng, S.-C., and Shields, R. K. (2013). Limb compressive load does not inhibit post activation depression of soleus H-reflex in indiviudals with chronic spinal cord injury. *Clin. Neurophysiol.* 124, 982–990. doi: 10.1016/j.clinph.2012.10.020

Wannier, T., Bastiaanse, C., Colombo, G., and Dietz, V. (2001). Arm to leg coordination in humans during walking, creeping and swimming activities. *Exp. Brain Res.* 141, 375–379. doi: 10.1007/s002210100875

Wenger, N., Moraud, E. M., Gandar, J., Musienko, P., Capogrosso, M., Baud, L., et al. (2016). Spatiotemporal neuromodulation therapies engaging muscle synergies improve motor control after spinal cord injury. *Nat. Med.* 22, 138–145. doi: 10.1038/nm.4025

Yang, Q., Logan, D., and Giszter, S. F. (2019). Motor primitives are determined in early development and are then robustly conserved into adulthood. *Proc. Natl. Acad. Sci. U.S.A.* 116, 12025–12034. doi: 10.1073/pnas.1821455116

Yaron, A., Kowalski, D., Yaguchi, H., Takei, T., and Seki, K. (2020). Forelimb force direction and magnitude independently controlled by spinal modules in the macaque. *PNAS* 117, 27655–27666. doi: 10.1073/pnas.1919253117

frontiers | Frontiers in Neuroscience

TYPE Original Research
PUBLISHED 20 December 2022
DOI 10.3389/fnins.2022.1082867

OPEN ACCESS

EDITED BY
Jing Teng,
North China Electric Power University, China

REVIEWED BY
Yande Ren,
The Affiliated Hospital of Qingdao University, China
Zhenghua Zhang,
Gansu Provincial Cancer Hospital, China
Jianbing Zhang,
Shanghai General Hospital, China

*CORRESPONDENCE
Yujie Feng
fengyujie@smail.xtu.edu.cn
Yixin Lu
luyixinh2020@sr.gxmu.edu.cn

†These authors have contributed equally to this work

SPECIALTY SECTION
This article was submitted to Translational Neuroscience, a section of the journal Frontiers in Neuroscience

RECEIVED 28 October 2022
ACCEPTED 02 December 2022
PUBLISHED 20 December 2022

CITATION
Zuo Z, Liu W, Zeng Y, Fan X, Li L, Chen J, Zhou X, Jiang Y, Yang X, Feng Y and Lu Y (2022) Multiparametric magnetic resonance imaging-derived deep learning network to determine ferroptosis-related gene signatures in gliomas.
Front. Neurosci. 16:1082867.
doi: 10.3389/fnins.2022.1082867

Multiparametric magnetic resonance imaging-derived deep learning network to determine ferroptosis-related gene signatures in gliomas

Zhichao Zuo[1†], Wen Liu[2†], Ying Zeng[1†], Xiaohong Fan[3], Li Li[4], Jing Chen[5], Xiao Zhou[1], Yihong Jiang[1], Xiuqi Yang[1], Yujie Feng[3*] and Yixin Lu[6*]

[1]Department of Radiology, Xiangtan Central Hospital, Xiangtan, Hunan, China, [2]Department of Radiology, The Third Xiangya Hospital, Central South University, Changsha, Hunan, China, [3]The School of Mathematics and Computational Science, Xiangtan University, Xiangtan, Hunan, China, [4]Department of Radiology, Hunan Children's Hospital, University of South China, Changsha, Hunan, China, [5]Department of Radiology, The Affiliated Hospital of Southwest Medical University, Luzhou, Sichuan, China, [6]Medical Imaging Department, Guangxi Medical University Cancer Hospital, Nanning, Guangxi, China

Introduction: Ferroptosis-related gene (FRG) signature is important for assessing novel therapeutic approaches and prognosis in glioma. We trained a deep learning network for determining FRG signatures using multiparametric magnetic resonance imaging (MRI).

Methods: FRGs of patients with glioma were acquired from public databases. FRG-related risk score stratifying prognosis was developed from The Cancer Genome Atlas (TCGA) and validated using the Chinese Glioma Genome Atlas. Multiparametric MRI-derived glioma images and the corresponding genomic information were obtained for 122 cases from TCGA and The Cancer Imaging Archive. The deep learning network was trained using 3D-Resnet, and threefold cross-validation was performed to evaluate the predictive performance.

Results: The FRG-related risk score was associated with poor clinicopathological features and had a high predictive value for glioma prognosis. Based on the FRG-related risk score, patients with glioma were successfully classified into two subgroups (28 and 94 in the high- and low-risk groups, respectively). The deep learning networks TC (enhancing tumor and non-enhancing portion of the tumor core) mask achieved an average cross-validation accuracy of 0.842 and an average AUC of 0.781, while the deep learning networks WT (whole tumor and peritumoral edema) mask achieved an average cross-validation accuracy of 0.825 and an average AUC of 0.781.

Discussion: Our findings indicate that FRG signature is a prognostic indicator of glioma. In addition, we developed a deep learning network

that has high classification accuracy in automatically determining FRG signatures, which may be an important step toward the clinical translation of novel therapeutic approaches and prognosis of glioma.

KEYWORDS

glioma, ferroptosis, prognosis, MRI, deep learning network

1 Introduction

Glioma, the most common primary brain tumor in adults, is highly invasive and resistant to various combination therapies such as surgery, radiotherapy, and chemotherapy (Zhou et al., 2022). In particular, glioblastoma multiforme, which is the most malignant type of central nervous system (CNS) tumor, has a median survival <16 months, and this has not improved substantially with modern medical advances (Ma et al., 2018). Glioma recurrence, progression, and metastasis are the three primary challenges that lead to treatment failure. Previous studies have shown that glioma, as a highly complex and heterogeneous tumor, involves multiple pathways, the immune microenvironment, and metabolic reprogramming during its development and progression (Gao et al., 2022). Recently, molecular markers related to the prognosis and treatment of gliomas have been actively explored. For example, isocitrate dehydrogenase (IDH) and 1P/19q have been confirmed to be associated with the prognosis of glioma. In addition, there are new drugs targeting epidermal growth factor receptor (EGFR) and mammalian target of rapamycin (mTOR) for the treatment of gliomas (Deluche et al., 2019; Heinzen et al., 2019; Hu et al., 2022). Unfortunately, there are still many gaps in the prognostic assessment and treatment of gliomas; therefore, the identification of new markers remains imperative.

Ferroptosis is a form of regulated cell death triggered by lipid peroxidation that differs from other genetic, biochemical, and morphological forms of cell death (Dixon et al., 2012). The mechanism of ferroptosis involves several redox-inducing compounds (e.g., erastin and RSL3) and ferroptosis inhibitors (e.g., ferrostatin-1 and liproxstatin-1). Importantly, some cancer cells that are resistant to compounds targeting traditional cell death processes are susceptible to RSL3- and erastin-induced ferroptosis, indicating that ferroptosis induction may be an encouraging therapeutic strategy for gliomas (Hangauer et al., 2017). Previous studies have indicated that ferroptosis-related gene (FRG) signatures are associated with tumor immune features and have potential for prognosis prediction and immunotherapy assessment in gliomas (Hu et al., 2021; Wan et al., 2021). Thus, it is crucial to accurately predict FRG-related risk to plan an effective curative treatment.

Convolutional neural networks (CNNs) are a form of deep learning widely applied for image processing and cover an extensive range of disciplines, such as molecular profiles and genomic mutations in gliomas (Liu et al., 2021). Even though several hurdles exist for clinical implementation (Chang K. et al., 2018; Chang P. et al., 2018), these image signal intensity-based CNNs did not enable the incorporation of information from the tumor 3D voxel, which may cause data leakage problems. Moreover, the existing methodologies require extensive manual preprocessing, presegmentation, or multicontrast acquisitions, which limit their clinical merits. To mitigate these limitations, in the present study, we developed a fully automated and highly accurate deep learning 3D network and further performed this non-invasive method to determine the FRGs signature.

2 Materials and methods

2.1 Data collection

mRNA expression data and clinical information in glioma from three public databases (Ceccarelli et al., 2016), The Cancer Genome Atlas (TCGA),[1] Chinese Glioma Genome Atlas (CGGA),[2] and Genotype-Tissue Expression (GTEx),[3] were used in this study. After data filtration, five available datasets, namely CGGA_693, CGGA_325, TCGA_LGG, TCGA_GBM, and GTEx, were chosen for further analyses. Among these datasets, TCGA_LGG and TCGA_GBM were assigned to the training cohort, whereas CGGA-693 and CGGA-325 were assigned to the validation cohort. Differential gene expression (DGE) analysis was conducted based on the GTEx dataset.

Gene transcription levels were normalized as fragments per kilobase million (FPKM) and further transformed to log2 (FPKM+1) for downstream analysis. A batch correction per subclass was applied using R packages "limma" and "sva." A total of 323 ferroptosis-related genes, including drivers, suppressors,

1 https://tcga-data.nci.nih.gov
2 http://www.cgga.org.cn/
3 http://xenabrowser.net

and marker regulators, were obtained from the FerrDb database (Zhou and Bao, 2020)[4].

2.2 Construction of the FRG-related risk score

DGE analysis was conducted using the R package "limma" between tumor and normal tissue samples, and FDR < 0.05 and $|\log FC| > 1$ was set as the threshold. Univariate Cox regression was used for the analysis of independent prognostic factors, and $P < 0.05$ was set as the significance threshold. The intersection of the genes, based on the results of DGE and univariate Cox regression analyses, was mapped using the R package "Venn" and described as FRGs for further analysis.

The defined FRGs were subjected to least absolute shrinkage and selection operator (LASSO) Cox regression, which is a classical dimension-reduction approach to screen for independent prognostic factors. The FRG-related risk score was constructed based on the LASSO weighting coefficients of the final selected genes using the following formula:

$$\sum_{i=1}^{n} (Coef_i \times x_i),$$

where $Coef_i$ represents the coefficients and x_i is the FPKM value of each FRG.

2.3 FRG-related risk score stratification

We used the R package "survminer" to classify the FRG-related risk scores into low- and high-risk groups. The survival rate differences among the stratified groups were compared using Kaplan–Meier (KM) analysis along with log-rank tests. Time-dependent receiver operating characteristic (tROC) curves were used to assess the efficiency of the FRG-related risk score in prognostic prediction.

To compare the clinicopathological and molecular characteristics between the low- and high-risk groups, Chi-square or Student's *t*-tests were used. Statistical significance was set at $P < 0.05$.

2.4 Gene ontology and Kyoto encyclopedia of genes and genomes

A functional annotation of differentially expressed genes was used to visualize gene ontology (GO) and Kyoto Encyclopedia of Genes and Genomes (KEGG) results using the R package "ClusterProfiler," to further explore their functional correlation.

4 http://www.zhounan.org/ferrdb/current/

2.5 Imaging acquisition and preprocessing

This study used multiparametric magnetic resonance (MR) images obtained from The Cancer Imaging Archive (TCIA) (Bakas et al., 2017).[5] Preoperative MR images of each patient with glioma were obtained from T1-weighted (T1WI), T2-weighted (T2WI), fluid-attenuated inversion recovery (FLAIR), and T1 contrast-enhanced (T1CE) images.

A total of 122 patient samples were analyzed, representing all matched cases (according to shared barcodes) of glioma in TCGA and TCIA, of which 28 and 94 were partitioned into the high-risk and low-risk groups, respectively. The multiparametric MR images were preprocessed using the Cancer Imaging Phenomics Toolkit open-source software (CaPTk v.1.9.0) (Pati et al., 2020).[6] The acquired Digital Imaging and Communications in Medicine (DICOM) images were converted to Neuroimaging Informatics Technology Initiative (NIfTI) images and reoriented to the right-most, anterior-most, inferior-most (RAI) coordinate system. Based on the SRI atlas, it was coregistered and resampled to a spatial resolution of 1 mm × 1 mm × 1 mm (Rohlfing et al., 2010). The anatomical images were bias-corrected and skull-stripped after high-resolution reconstruction. After removing the outlier pixels that did not fall in the 99.9% percentile of the image histogram, the intensities of the images were converted into a background range of 0–255. Automated segmentation was performed using the DeepMedic module (Kamnitsas et al., 2017) and was approved or adjusted when necessary by a board-certified neuroradiologist (Lu) through CaPTk to determine the tumoral subregions of the TC (enhancing tumor and non-enhancing portion of the tumor core) and WT (whole tumor and peritumoral edema) (**Figure 1**).

2.6 Network details

We used the network architecture shown in **Figure 2**, a classification network trained on T1WI, T1CE, T2WI, and FLAIR based on TC and WT mask images, respectively. It is a CNN classifier for predicting high- and low-risk FRG-related signatures. The network framework is derived from the classical ResNet50, which contains an initial part (stage0), a residual learning part (stage1–stage4), and a fully connected part (AvgPool3d+Reshape+FC).

The residual learning part (stage1–stage4) comprises three, four, six, and three residual blocks, respectively. The residual blocks employed here are the Conv Block (Block1) and Identity Block (Block2). The Conv Block has inconsistent input

5 https://wiki.cancerimagingarchive.net

6 https://www.cbica.upenn.edu/captk

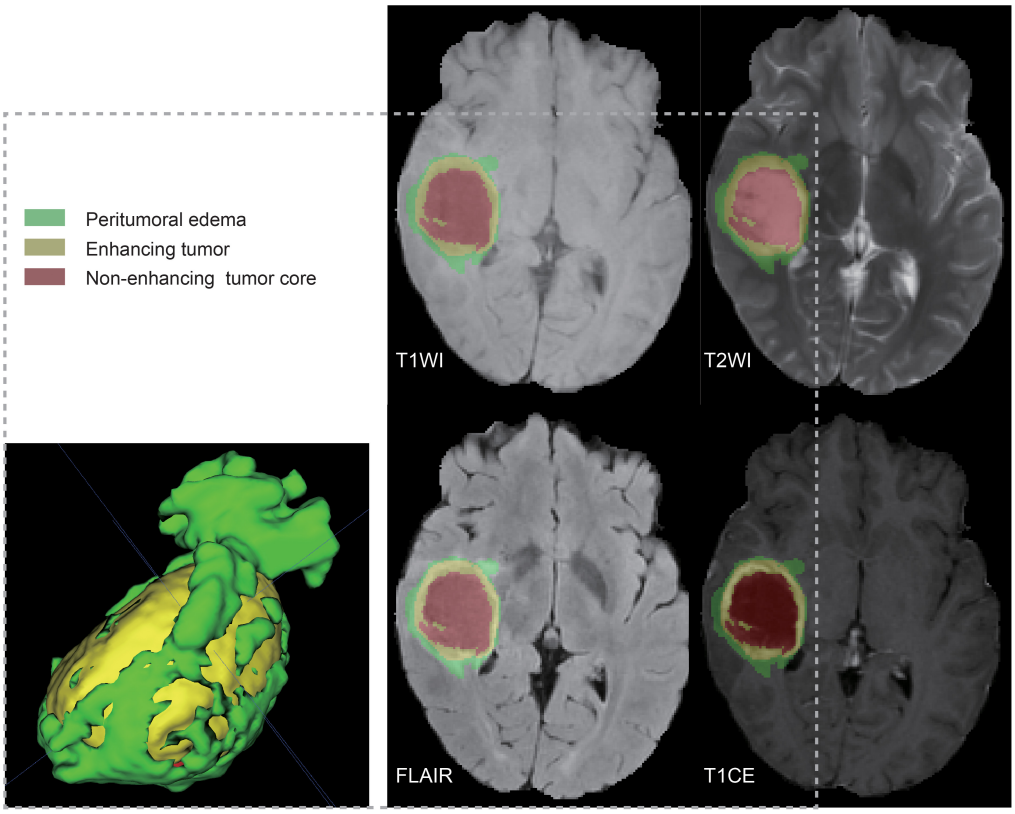

FIGURE 1
Ground truth whole-tumor masks. Red voxels represent non-enhancing tumor core; yellow voxels, enhancing tumor; and green voxels, peritumoral edema.

and output dimensions, requiring the addition of a 1 × 1 convolution and Batch Normalization (BN) at the location of the shortcut path to stretch the channels and make the dimensions consistent before the summation operation. The Identity Block (Block2) has consistent input and output dimensions, allowing for straightforward addition. The output of the residual learning part was transformed into data dimensions by AvgPool3d and reshape operations and used as the input of the FC.

2.6.1 Network implementation and cross-validation

To ensure the reliability of the network implementation, threefold cross-validation was performed on data from 122 patients (28 high-risk and 94 low-risk groups), and the dataset was randomly divided into threefolds. The data from these threefolds were alternated between the two training sets and one validation set to obtain three prediction models, and the average performance of these three models was calculated. The input images were T1WI, T1CE, T2WI, and FLAIR images cropped by the TC/WT mask to obtain the data with 96 × 96 × 96 pixels. During network training, we performed random flip operations on the input images for data enhancement. The Cross Entropy Loss was chosen as the loss function of the network. The network learning rate was set to 10^{-4}, the batch size was 8, and the maximum number of epochs was 70. Our pipeline was written in Pytorch, and all experiments were performed on a workstation with an Intel Xeon CPU E5-2630 and NVIDIA Tesla V100 GPU.

2.7 Network assessment

The diagnostic efficiency was assessed by receiver operating characteristic (ROC) using all predictions across folds of the cross-validation, and the area under the curve (AUC), accuracy (ACC), sensitivity, and specificity were calculated. Besides, we used the precision, recall, and F1 score to assess the signature classification performance of the FRGs. The F1 score was calculated by combining the precision and recall.

3 Results

3.1 Landscape of FRGs

A flowchart describing our study's analytical procedure is presented (**Supplementary Figure 1**). The TCGA cohort

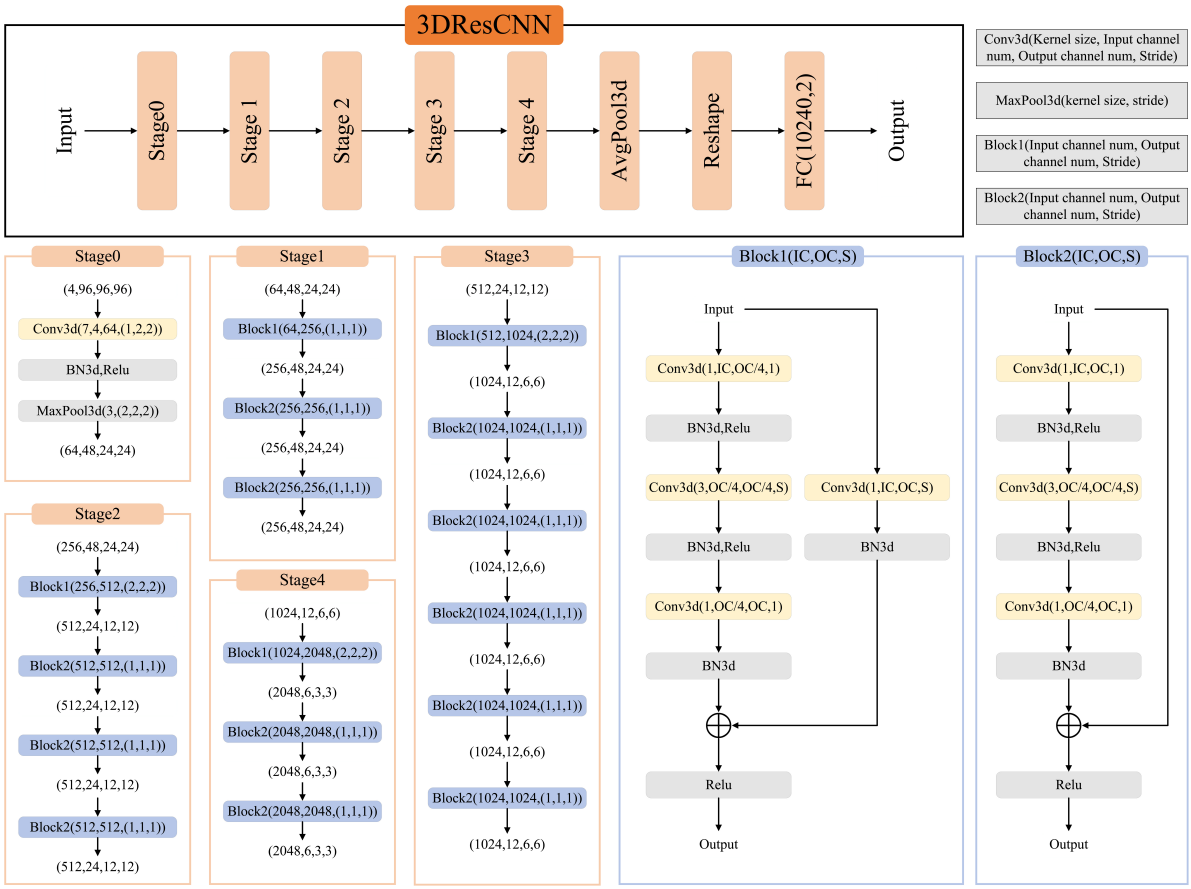

FIGURE 2
The network framework for FRGs signature prediction.

containing 270 ferroptosis-related genes was obtained after removing some of the low-expression ferroptosis-related genes. After DGE analysis between tumor and normal tissue samples, 99 genes were retained (Figure 3). In addition, Cox regression analysis identified 221 genes as independent prognostic factors. Taking the intersection of predicted genes, 80 genes described as FRGs, including 53 up-regulated genes and 27 down-regulated genes, were enrolled (Supplementary Figure 2). Upregulation and downregulation of gene expression were also plotted as heatmaps and compared with the corresponding control (Figure 4).

Least absolute shrinkage and selection operator Cox regression analysis was conducted on 80 FRGs and identified 23 genes associated with the prognosis of glioma: 12 driven genes (*NOX1*, *NCOA4*, *ALOX12*, *ALOX15B*, *ZEB1*, *HMOX1*, *TGFBR1*, *IDH1*, *PEX12*, *MYCN*, *SMG9*, and *SLC39A7*) and 12 suppressor genes (*SCD*, *NFS1*, *SQSTM1*, *CD44*, *RRM2*, *GDF15*, *PARP4*, *PARP14*, *KIF20A*, *ETV4*, *LCN2*, and *HMOX1*), among which *HMOX1* is both a driver and a suppressor gene. The LASSO coefficient profiles of candidate genes are shown in Figure 5. The FRG-related risk score was calculated according to the LASSO weighting coefficients of the final selected genes.

3.2 FRG-related risk score in prognosis

We determined the optimal cut-off using the "surv_cutpoint" function of the "survminer" R package (Supplementary Figure 3). Patients with FRG-related risk scores were further divided into high- and low-risk groups (Supplementary Figure 4).

Kaplan–Meier survival analysis showed that the survival probability was significantly worse in the high-risk group than in the low-risk group in the training and validation cohorts ($P < 0.001$) (Figure 6). tROC curve analysis showed that the development of the risk score in the present study exhibited good predictive effectiveness, which was indicated by 0.899, 0.917, and 0.930 for 1-, 2-, and 3-year AUC, respectively, in the training cohort and 0.765, 0.834, and 0.826 for 1-, 2-, and 3-year AUC, respectively, in the validation cohort (Figure 7).

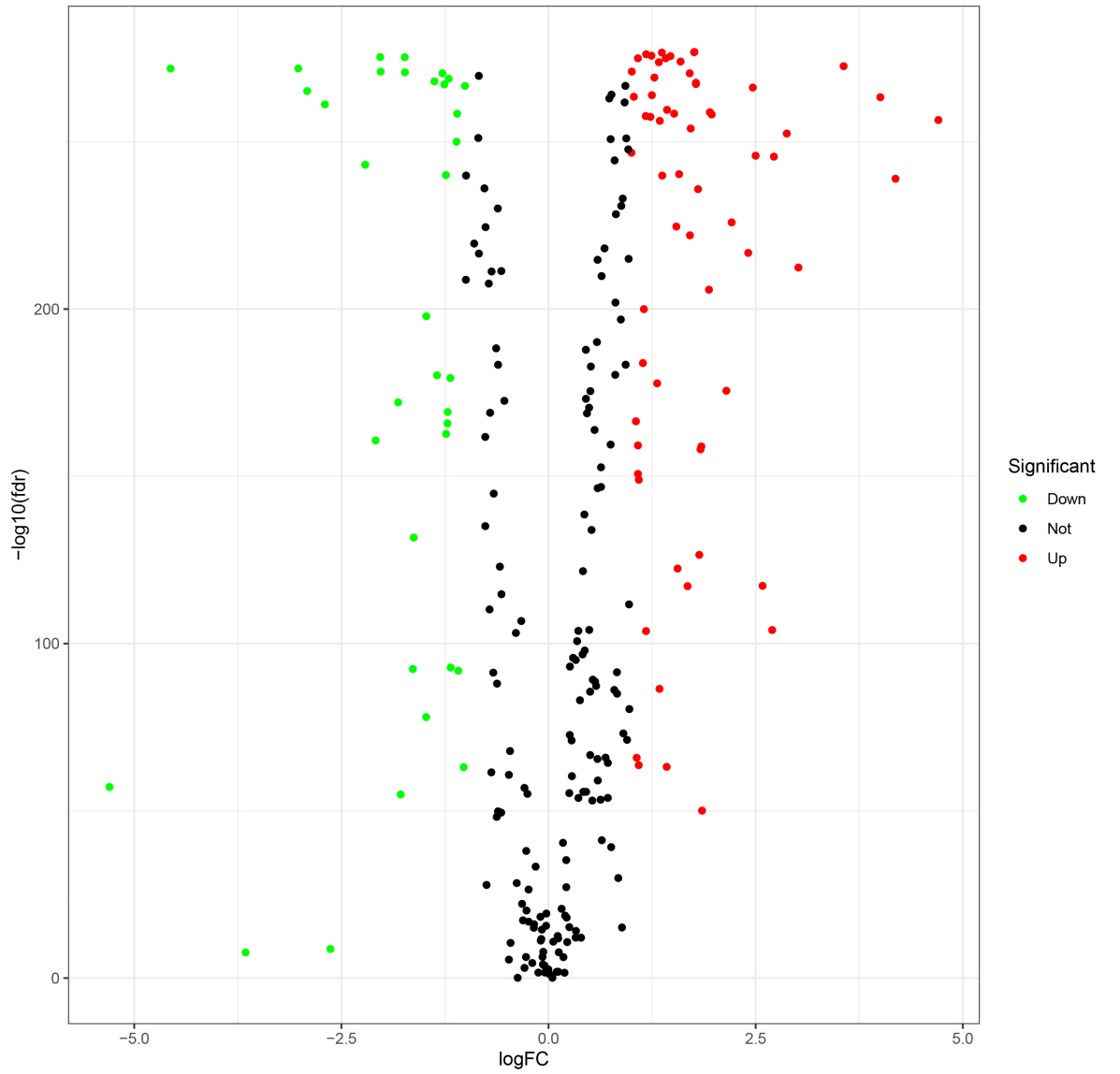

FIGURE 3
Volcano plot of differential gene expression analysis between tumor and normal tissues.

3.3 Association of FRG-related risk score with clinicopathological and molecular characteristics

There were significant differences in FRG-related risk scores among patients in age ($P < 0.001$), grade ($P < 0.001$), IDH status ($P < 0.001$), MGMT promoter ($P < 0.001$), and 1p/19q codeletion ($P < 0.001$), but no significant differences were observed in sex ($P = 0.912$) (Figure 8).

In addition, patients in the high-risk group had higher grade, older age, wild-type IDH, 1p/19q non-codeletion, and MGMT promoter unmethylation ($P < 0.001$), but had no significant differences in sex (Table 1).

3.4 Analysis of biological properties and pathways related to the gene signatures

Gene ontology and KEGG analyses were used to annotate the intersection genes after risk differential analysis, (Figure 9). The biological processes (BPs) involved included the following: Cellular iron ion homeostasis, iron ion homeostasis, cellular transition metal ion homeostasis, transition metal ion homeostasis, response to metal ion, response to iron ion, regulation of protein serine/threonine kinase activity, cellular response to metal ion, cellular response to chemical stress, and cellular response to inorganic substance (Figure 9A). The

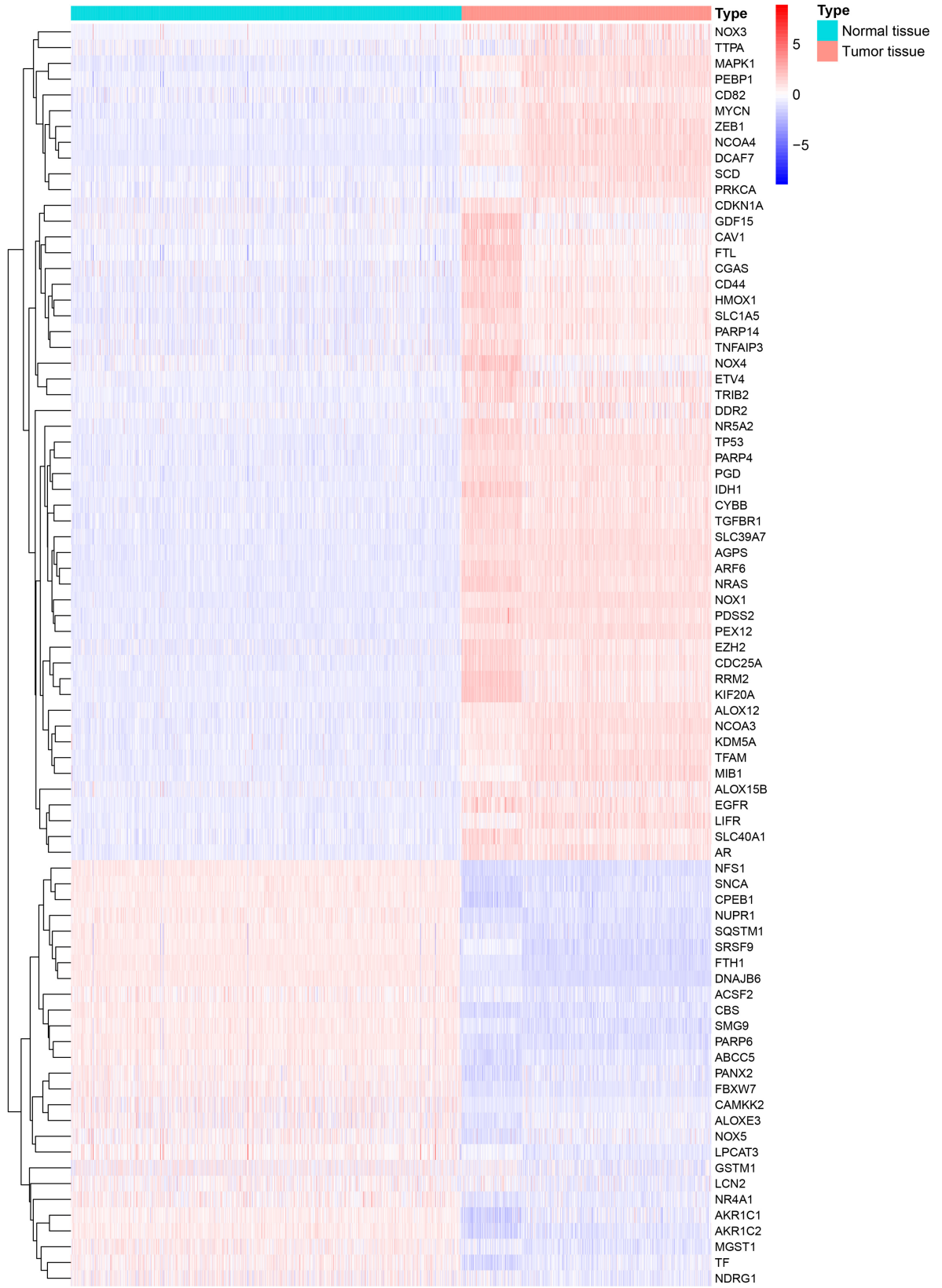

FIGURE 4
Heatmap generated and displayed as log twofold change.

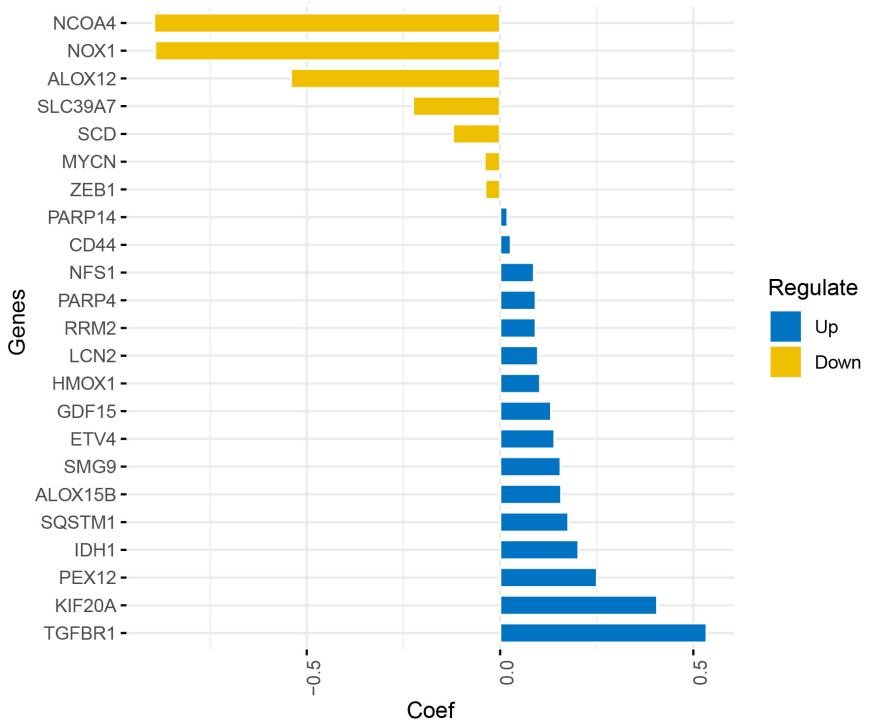

FIGURE 5
Least absolute shrinkage and selection operator coefficient profile of the candidate genes.

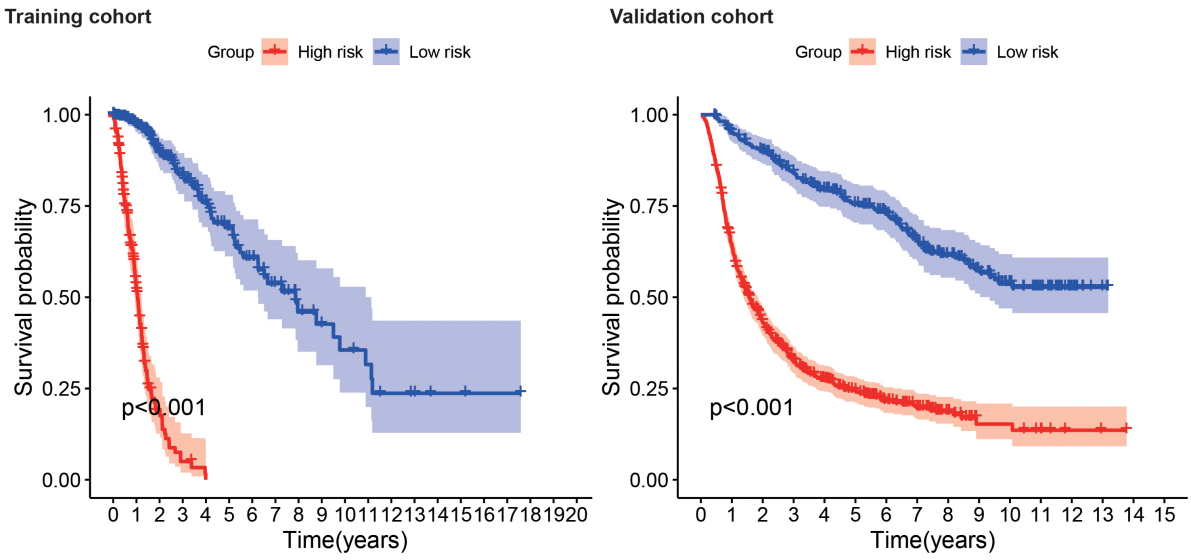

FIGURE 6
Survival analysis shows survival probability curves in the training and validation cohort.

most abundant cellular component (CC) terminology included autolysosome, secondary lysosome, basal plasma membrane, basal part of cell, secretory granule membrane, and endocytic vesicle membrane (Figure 9A). The most abundant molecule function (MF) terms were ferric iron binding, ferrous iron binding, iron ion binding (Figure 9A). KEGG pathway analysis revealed that ferroptosis, Mineral absorption, HIF-1 signaling pathway, MicroRNAs in cancer, Hepatocellular carcinoma, and Glutathione metabolism were the most abundant pathways (Figure 9B).

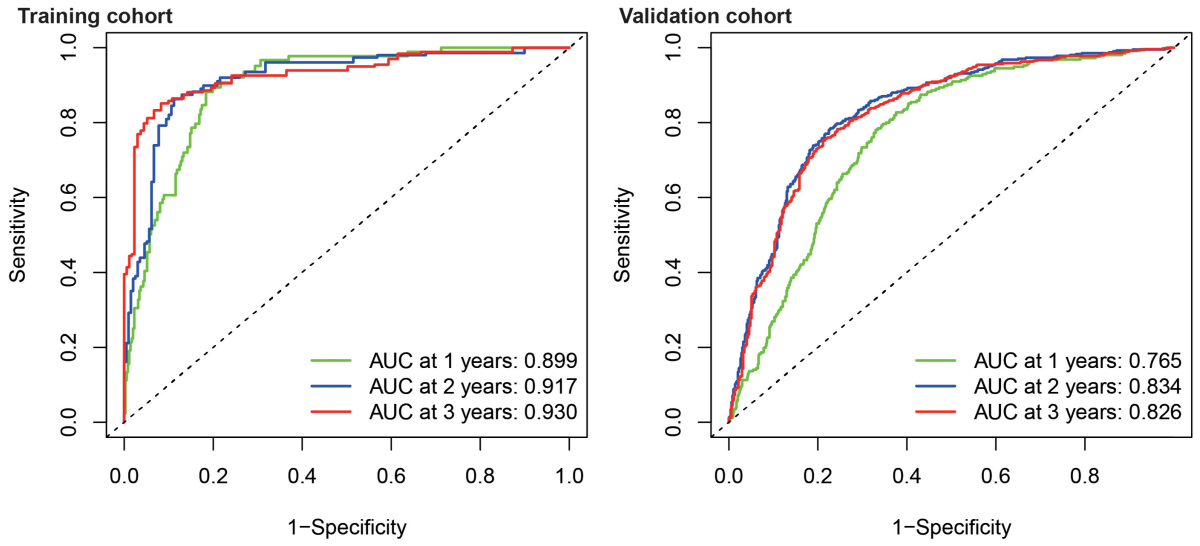

FIGURE 7
Time-dependent receiver operating characteristic analysis showed the AUC of FRGs for 1, 2, and 3 years in the training and validation cohort.

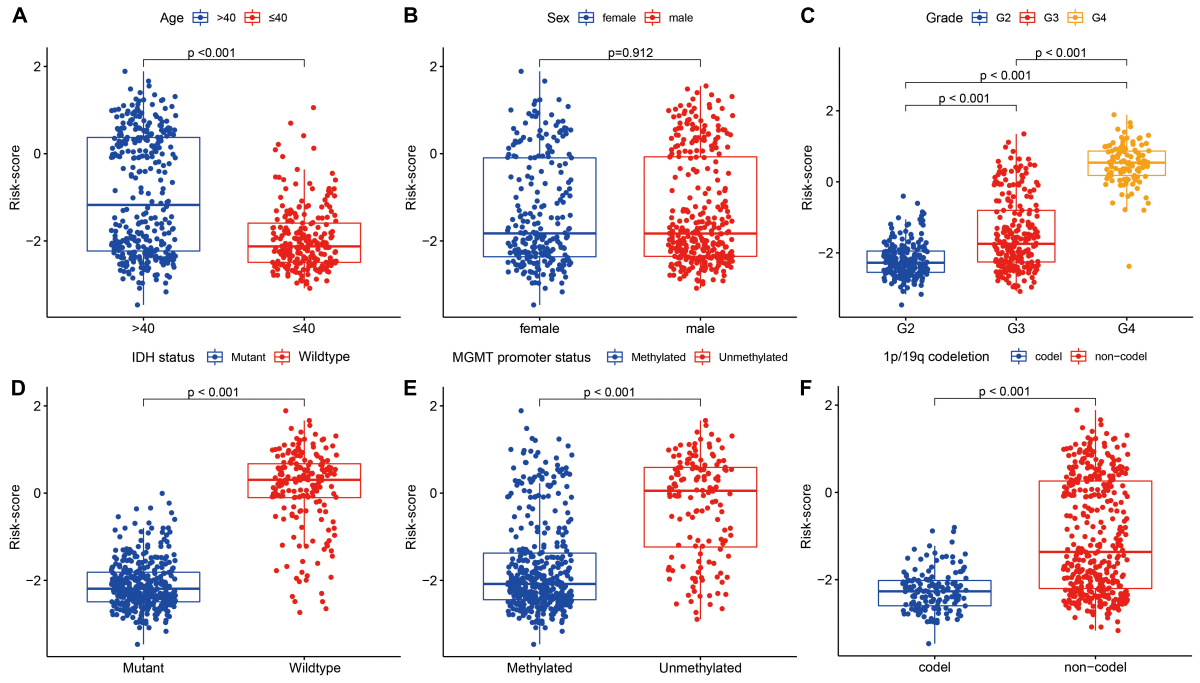

FIGURE 8
Association between the FRGs and other clinicopathological characteristics (**A**, age; **B**, sex; **C**, grade; **D**, IDH status; **E**, MGMT promoter status; and **F**, 1p/19q codeletion) in the training cohort.

3.5 Network performance in determining FRG signatures

The cross-validation average ACC of 3DResCNN (network (TC-mask)) reached 0.842 (0.900, 0.850, and 0.775 for Fold1, Fold2, and Fold3, respectively), the average F1 score was 0.843 (0.900, 0.844, and 0.784 for Fold1, Fold2, and Fold3, respectively), and the average AUC was 0.781 (0.827, 0.767, and 0.750 for Fold1, Fold2, and Fold3, respectively).

The cross-validation average ACC of 3DResCNN [network (WT-mask)] reached 0.825 (0.925, 0.800 and 0.750 for Fold1, Fold2, Fold3, respectively), the average F1 score was 0.830

TABLE 1 Characteristics of patients in low- and high-risk groups in the training cohort.

Characteristic	High-risk (*N* = 145)	Low-risk (*N* = 418)	*P*-value
Grade:			<0.001
G2	0 (0.00%)	212 (50.7%)	
G3	40 (27.6%)	196 (46.9%)	
G4	105 (72.4%)	10 (2.39%)	
Age (year)	61.0 (53.0, 70.0)	39.0 (32.0, 51.0)	<0.001
Sex:			0.912
Female	61 (42.1%)	180 (43.1%)	
Male	84 (57.9%)	238 (56.9%)	
IDH status:			<0.001
Mutant	1 (0.69%)	369 (88.3%)	
Wildtype	144 (99.3%)	49 (11.7%)	
1p/19q codeletion:			<0.001
Codel	0 (0.00%)	149 (35.6%)	
Non-codel	145 (100%)	269 (64.4%)	
MGMT promoter:			<0.001
Methylated	63 (43.4%)	356 (85.2%)	
Un-methylated	82 (56.6%)	62 (14.8%)	

(0.923, 0.810 and 0.757 for Fold1, Fold2, Fold3, respectively), and the average AUC was 0.781 (0.842, 0.800, and 0.700 for Fold1, Fold2, Fold3, respectively). The specific results of 3DResCNN in terms of the threefold respective and average metrics are shown in Table 2.

The network (TC mask) showed a similar performance to the network (WT mask), and the summary ROC curves for the network (TC mask and WT mask) are shown in Supplementary Figure 5.

4 Discussion

Evidence suggests that ferroptosis plays a crucial role in tumor initiation, progression, and evolution (Dixon et al., 2012). Several investigations have indicated that the risk score generated by ferroptosis is associated with the clinicopathological features of gliomas, which can independently predict patient prognosis (Zhuo et al., 2020; Hu et al., 2021; Wan et al., 2021). In addition, ferroptosis may affect immune cell infiltration in the glioma microenvironment (Hu et al., 2021; Wan et al., 2021). Bioimaging is an essential tool for the non-invasive diagnosis of gliomas. Indeed, combined with multiple imaging modalities, multiparametric MR imaging enables effective expansion of the feature pool, which would provide more information. Previous studies have indicated that multiparametric MR-based deep learning has diagnostic performance in the differentiation of glioma mimicking encephalitis (Wu et al., 2021), classification of IDH mutation status (Bangalore Yogananda et al., 2020), discrimination of pseudoprogression and true progression (Lee et al., 2020), and determination of molecular subtype in gliomas (Li et al., 2022). For these reasons, we developed a deep learning 3D network

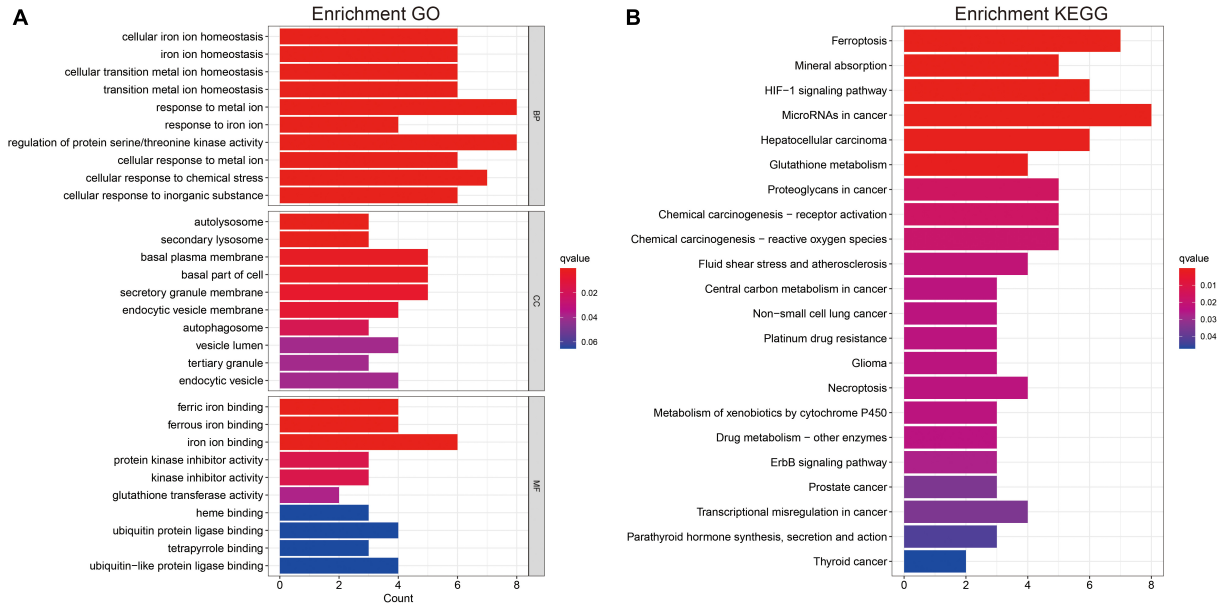

FIGURE 9
Gene ontology and KEGG analysis **(A,B)**. Functional annotation of FRGs using GO terms and the KEGG pathway.

TABLE 2 Network performance in determining FRG signatures.

Metrics	AUC	ACC	F1	Sensitivity	Specificity
TC-mask					
Fold1	0.827	0.900	0.900	0.714	0.939
Fold2	0.767	0.850	0.844	0.600	0.933
Fold3	0.750	0.775	0.784	0.700	0.800
Average	0.781	0.842	0.843	0.671	0.891
WT-mask					
Fold1	0.842	0.925	0.923	0.714	0.970
Fold2	0.800	0.800	0.810	0.800	0.800
Fold3	0.700	0.750	0.757	0.600	0.800
Average	0.781	0.825	0.830	0.705	0.857

and further applied this non-invasive method to assess FRG signatures.

The results of GO and KEGG analysis showed the main enrichment pathways of intersection genes in this study. Considering the genetic diversity, 23 FRGs were finally incorporated into prognostic signatures based on LASSO Cox analysis. Our results indicated that the expression of FRGs was associated with poor clinicopathological features, and the FRG-related risk score had a high predictive value for glioma prognosis, which is consistent with previous literature (Zhuo et al., 2020; Hu et al., 2021; Wan et al., 2021). According to the FRG-related risk score, patients with glioma were successfully classified into high- and low-risk groups, which contributed to prognosis stratification.

To our knowledge, this is the first study to demonstrate the application of multiparametric MRI-derived deep learning network for determining FRG signatures in gliomas. CNNs are the cornerstone of deep learning methods, which remain more efficient in image annotation than classical hand-engineered selections, such as color, geometrical, and texture features (Korfiatis and Erickson, 2019). In the present study, we used 3DRESCNN (ResNet50) to predict FRG-related risk signatures and used multiparametric MRI imaging (T1WI, T1CE, T2WI, and FLAIR images) as network inputs. The network (TC or WT mask) achieved highly satisfactory prediction efficiency, with ACCs of 84.2 and 82.5%, respectively. In reviewing these multiparametric MRI images, there were no specific imaging features, indicating that the deep learning network provided additional information that could not be interpreted manually. The TC mask represented an enhancing tumor and non-enhancing portion of the tumor core, and the WT mask represented the whole tumor and peritumoral edema. WT mask and TC mask demonstrated similar performances, indicating that peritumoral edema did not enhance the diagnostic effectiveness for determining the FRG signatures.

Despite the satisfactory results, the present study has several limitations. First, we developed a multiparametric MRI-derived deep learning network, whereas diffusion-weighted MRI images were not available. Second, training deep learning models usually requires large amounts of data (Choy et al., 2018), whereas the cases for training are limited. Despite the application of data augmentation for CNNs, because of their high complexity and the use of 3DCNN in this study, the amount of data is too small, easily leading to poor network training and performance. Third, owing to the relatively large number of low-risk FRG-related signatures, this type of quantitative imbalance has a significant negative impact on the training of the CNN classifier, which affects both the convergence of the training phase and analysis of the test set results, as well as the threefold validation.

5 Conclusion

In conclusion, we developed a multiparametric MRI-derived deep learning network with high accuracy for automatically determining FRG signatures. This study represents an important technological milestone using MR imaging to evaluate genetic diversity, prognosis conditions, and drug-targeted genes for gliomas.

Data availability statement

Publicly available datasets for this study can be found in the Cancer Genome Atlas (TCGA, https://tcga-data.nci.nih.gov), Chinese Glioma Genome Atlas (CGGA, http://www.cgga.org.cn/), Genotype-Tissue Expression (GTEx, http://xenabrowser.net), FerrDb database (http://www.zhounan.org/ferrdb/current/), and The Cancer Imaging Archive (TCIA, https://wiki.cancerimagingarchive.net).

Ethics statement

Ethical review and approval was not required for the study on human participants in accordance with the local legislation and institutional requirements. Written informed consent for participation was not required for this study in accordance with the national legislation and the institutional requirements.

Author contributions

ZZ, WL, and YZ: conceptualization. XF, YJ, and XY: methodology. ZZ, XF, YJ, and XY: software and project administration. ZZ: validation and formal analysis. LL and JC: investigation. XZ, YJ, and XY: resources. LL: data curation. ZZ,

YJ, and XY: writing—original draft preparation. WL: writing—review and editing, visualization, and supervision. XF and YF: funding acquisition. All authors contributed to the article and approved the submitted version.

Funding

This study has received funding by the Postgraduate Scientific Research Innovation Project of Hunan Province (grant nos. CX20220633 and CX20210598) and Postgraduate Scientific Research Innovation Project of Xiangtan University (grant nos. XDCX2022Y060 and XDCX2021B097), China.

Acknowledgments

We would like to thank Editage (www.editage.com) for English language editing.

Conflict of interest

The authors declare that the research was conducted in the absence of any commercial or financial relationships that could be construed as a potential conflict of interest.

Publisher's note

Supplementary material

The Supplementary Material for this article can be found online at: https://www.frontiersin.org/articles/10.3389/fnins.2022.1082867/full#supplementary-material

SUPPLEMENTARY FIGURE 1
Flow chart.

SUPPLEMENTARY FIGURE 2
Venn diagram shows overlaps between genes conducted by univariate Cox regression analysis and DEGs.

SUPPLEMENTARY FIGURE 3
Based on the surv_cutpoint function in the survminer R package, the cut-off value of risk-score was determined to be −0.1.

SUPPLEMENTARY FIGURE 4
Distribution of risk-score **(top)**; survival time **(bottom)**.

SUPPLEMENTARY FIGURE 5
Summary ROC curves for the network (TC-mask and WT mask).

References

Bakas, S., Akbari, H., Sotiras, A., Bilello, M., Rozycki, M., Kirby, J. S., et al. (2017). Advancing the cancer genome atlas glioma MRI collections with expert segmentation labels and radiomic features. *Sci. Data.* 4:170117. doi: 10.1038/sdata.2017.117

Bangalore Yogananda, C. G., Shah, B. R., Vejdani-Jahromi, M., Nalawade, S. S., Murugesan, G. K., Yu, F. F., et al. (2020). A novel fully automated MRI-based deep-learning method for classification of IDH mutation status in brain gliomas. *Neurol. Oncol.* 22, 402–411. doi: 10.1093/neuonc/noz199

Ceccarelli, M., Barthel, F. P., Malta, T. M., Sabedot, T. S., Salama, S. R., Murray, B. A., et al. (2016). Molecular profiling reveals biologically discrete subsets and pathways of progression in diffuse glioma. *Cell* 164, 550–563. doi: 10.1016/j.cell.2015.12.028

Chang, K., Bai, H. X., Zhou, H., Su, C., Bi, W. L., Agbodza, E., et al. (2018). Residual convolutional neural network for the determination of idh status in low- and high-grade gliomas from MR imaging. *Clin. Cancer Res.* 24, 1073–1081. doi: 10.1158/1078-0432.ccr-17-2236

Chang, P., Grinband, J., Weinberg, B. D., Bardis, M., Khy, M., Cadena, G., et al. (2018). Deep-learning convolutional neural networks accurately classify genetic mutations in gliomas. *AJNR Am. J. Neuro. Radiol.* 39, 1201–1207. doi: 10.3174/ajnr.A5667

Choy, G., Khalilzadeh, O., Michalski, M., Do, S., Samir, A. E., Pianykh, O. S., et al. (2018). Current applications and future impact of machine learning in radiology. *Radiology* 288, 318–328. doi: 10.1148/radiol.2018171820

Deluche, E., Bessette, B., Durand, S., Caire, F., Rigau, V., Robert, S., et al. (2019). CHI3L1, NTRK2, 1p/19q and IDH status predicts prognosis in glioma. *Cancers* 11:544. doi: 10.3390/cancers11040544

Dixon, S. J., Lemberg, K. M., Lamprecht, M. R., Skouta, R., Zaitsev, E. M., Gleason, C. E., et al. (2012). Ferroptosis: An iron-dependent form of nonapoptotic cell death. *Cell* 149, 1060–1072. doi: 10.1016/j.cell.2012.03.042

Gao, X., Zhao, J., Jia, L., and Zhang, Q. (2022). Remarkable immune and clinical value of novel ferroptosis-related genes in glioma. *Sci. Rep.* 12:12854. doi: 10.1038/s41598-022-17308-7

Hangauer, M. J., Viswanathan, V. S., Ryan, M. J., Bole, D., Eaton, J. K., Matov, A., et al. (2017). Drug-tolerant persister cancer cells are vulnerable to GPX4 inhibition. *Nature* 551, 247–250. doi: 10.1038/nature24297

Heinzen, D., Divé, I., Lorenz, N. I., Luger, A. L., Steinbach, J. P., and Ronellenfitsch, M. W. (2019). Second generation mTOR inhibitors as a double-edged sword in malignant glioma treatment. *Int. J. Mol. Sci.* 20:4474. doi: 10.3390/ijms20184474

Hu, C., Leche, C. A. II, Kiyatkin, A., Yu, Z., Stayrook, S. E., Ferguson, K. M., et al. (2022). Glioblastoma mutations alter EGFR dimer structure to prevent ligand bias. *Nature* 602, 518–522. doi: 10.1038/s41586-021-04393-3

Hu, Y., Tu, Z., Lei, K., Huang, K., and Zhu, X. (2021). Ferroptosis-related gene signature correlates with the tumor immune features and predicts the prognosis of glioma patients. *Biosci. Rep.* 41:BSR20211640. doi: 10.1042/bsr20211640

Kamnitsas, K., Ledig, C., Newcombe, V. F. J., Simpson, J. P., Kane, A. D., Menon, D. K., et al. (2017). Efficient multi-scale 3D CNN with fully connected CRF for accurate brain lesion segmentation. *Med. Image Anal.* 36, 61–78. doi: 10.1016/j.media.2016.10.004

Korfiatis, P., and Erickson, B. (2019). Deep learning can see the unseeable: Predicting molecular markers from MRI of brain gliomas. *Clin. Radiol.* 74, 367–373. doi: 10.1016/j.crad.2019.01.028

Lee, J., Wang, N., Turk, S., Mohammed, S., Lobo, R., Kim, J., et al. (2020). Discriminating pseudoprogression and true progression in diffuse infiltrating glioma using multi-parametric MRI data through deep learning. *Sci. Rep.* 10:20331. doi: 10.1038/s41598-020-77389-0

Li, Y., Wei, D., Liu, X., Fan, X., Wang, K., Li, S., et al. (2022). Molecular subtyping of diffuse gliomas using magnetic resonance imaging: Comparison

and correlation between radiomics and deep learning. *Eur. Radiol.* 32, 747–758. doi: 10.1007/s00330-021-08237-6

Liu, D., Chen, J., Hu, X., Yang, K., Liu, Y., Hu, G., et al. (2021). Imaging-genomics in glioblastoma: Combining molecular and imaging signatures. *Front. Oncol.* 11:699265. doi: 10.3389/fonc.2021.699265

Ma, Q., Long, W., Xing, C., Chu, J., Luo, M., Wang, H. Y., et al. (2018). Cancer stem cells and immunosuppressive microenvironment in glioma. *Front. Immunol.* 9:2924. doi: 10.3389/fimmu.2018.02924

Pati, S., Singh, A., Rathore, S., Gastounioti, A., Bergman, M., Ngo, P., et al. (2020). The cancer imaging phenomics toolkit (CaPTk): Technical overview. *Brainlesion* 11993, 380–394. doi: 10.1007/978-3-030-46643-5_38

Rohlfing, T., Zahr, N. M., Sullivan, E. V., and Pfefferbaum, A. (2010). The SRI24 multichannel atlas of normal adult human brain structure. *Hum. Brain Mapp.* 31, 798–819. doi: 10.1002/hbm.20906

Wan, R. J., Peng, W., Xia, Q. X., Zhou, H. H., and Mao, X. Y. (2021). Ferroptosis-related gene signature predicts prognosis and immunotherapy in glioma. *CNS Neurosci. Ther.* 27, 973–986. doi: 10.1111/cns.13654

Wu, W., Li, J., Ye, J., Wang, Q., Zhang, W., and Xu, S. (2021). Differentiation of glioma mimicking encephalitis and encephalitis using multiparametric MR-based deep learning. *Front. Oncol.* 11:639062. doi: 10.3389/fonc.2021.639062

Zhou, N., and Bao, J. (2020). FerrDb: A manually curated resource for regulators and markers of ferroptosis and ferroptosis-disease associations. *Database* 2020:baaa021. doi: 10.1093/database/baaa021

Zhou, Y., Fang, C., Xu, H., Yuan, L., Liu, Y., Wang, X., et al. (2022). Ferroptosis in glioma treatment: Current situation, prospects and drug applications. *Front. Oncol.* 12:989896. doi: 10.3389/fonc.2022.989896

Zhuo, S., Chen, Z., Yang, Y., Zhang, J., Tang, J., and Yang, K. (2020). Clinical and biological significances of a ferroptosis-related gene signature in glioma. *Front. Oncol.* 10:590861. doi: 10.3389/fonc.2020.590861

frontiers | Frontiers in Neuroscience

TYPE Original Research
PUBLISHED 25 January 2023
DOI 10.3389/fnins.2023.1077858

OPEN ACCESS

EDITED BY
Na Li,
Central South University, China

REVIEWED BY
Zhou Zhou,
Royal Institute of Technology, Sweden
Jie Zhu,
Wuxi Clinical College of Anhui Medical University, China
Junhui Chen,
Renmin Hospital of Wuhan University, China
Xiaojie Shi,
Haining Branch of the First Affiliated Hospital of Zhejiang University, China
Junfeng Feng,
Shanghai Jiao Tong University, China

*CORRESPONDENCE
Guanjun Wang
✉ hainingwwwhk@163.com
Rongcai Jiang
✉ jiang116216@163.com

†These authors have contributed equally to this work

SPECIALTY SECTION
This article was submitted to Translational Neuroscience, a section of the journal Frontiers in Neuroscience

RECEIVED 23 October 2022
ACCEPTED 09 January 2023
PUBLISHED 25 January 2023

CITATION
Chen W, Yao C, Li S, Huang H, Zhu Z, Chen R, Su W, Huang X, Xu L, Sun K, Song J, Jiang R and Wang G (2023) Cognitive impairment in diffuse axonal injury patients with favorable outcome. *Front. Neurosci.* 17:1077858. doi: 10.3389/fnins.2023.1077858

Cognitive impairment in diffuse axonal injury patients with favorable outcome

Weiliang Chen[1†], Chunyu Yao[1†], Shengwen Li[2†], Hongguang Huang[3], Zujian Zhu[1], Rui Chen[1], Wen Su[1], Xiao Huang[1], Lisheng Xu[1], Kaijie Sun[1], Jiannan Song[1], Rongcai Jiang[4]* and Guanjun Wang[1]*

[1]Department of Neurosurgery, Haining People's Hospital, Jiaxing, Zhejiang, China, [2]The Second Department of Orthopaedics, Haining People's Hospital, Haining, Zhejiang, China, [3]Department of Neurosurgery, The First Affiliated Hospital of Zhejiang University Medical College, Hangzhou, Zhejiang, China, [4]Department of Neurosurgery, Tianjin Medical University General Hospital, Tianjin, China

Background and purpose: Traumatic brain injury (TBI), especially the severe TBI are often followed by persistent cognitive sequalae, including decision-making difficulties, reduced neural processing speed and memory deficits. Diffuse axonal injury (DAI) is classified as one of the severe types of TBI. Part of DAI patients are marginalized from social life due to cognitive impairment, even if they are rated as favorable outcome. The purpose of this study was to elucidate the specific type and severity of cognitive impairment in DAI patients with favorable outcome.

Methods: The neurocognition of 46 DAI patients with favorable outcome was evaluated by the Chinese version of the Montreal Cognitive Assessment Basic (MoCA-BC), and the differences in the domains of cognitive impairment caused by different grades of DAI were analyzed after data conversion of scores of nine cognitive domains of MoCA-BC by Pearson correlation analysis.

Results: Among the 46 DAI patients with favorable outcome, eight had normal cognitive function (MoCA-BC $\geq$ 26), and 38 had cognitive impairment (MoCA-BC $<$ 26). The MoCA-BC scores were positively correlated with pupillary light reflex (r = 0.361, p = 0.014), admission Glasgow Coma Scale (GCS) (r = 0.402, p = 0.006), and years of education (r = 0.581, $p < 0.001$). Return of consciousness (r = −0.753, $p < 0.001$), Marshall CT (r = −0.328, p = 0.026), age (r = −0.654, $p < 0.001$), and DAI grade (r = −0.403, p = 0.006) were found to be negatively correlated with the MoCA-BC scores. In patients with DAI grade 1, the actually deducted scores (Ads) of memory (r = 0.838, $p < 0.001$), abstraction (r = 0.843, $p < 0.001$), and calculation (r = 0.782, $p < 0.001$) were most related to the Ads of MoCA-BC. The Ads of nine cognitive domains and MoCA-BC were all proved to be correlated, among patients with DAI grade 2. However, In the DAI grade 3 patients, the highest correlation with the Ads of MoCA-BC were the Ads of memory (r = 0.904, $p < 0.001$), calculation (r = 0.799, p = 0.006), orientation (r = 0.801, p = 0.005), and executive function (r = 0.869, p = 0.001).

Conclusion: DAI patients with favorable outcome may still be plagued by cognitive impairment, and different grades of DAI cause different domains of cognitive impairment.

KEYWORDS

diffuse axonal injury, cognitive impairment, outcome, Montreal cognitive assessment, cognitive domain

Introduction

DAI is caused by acceleration-deceleration or rotational forces on brain tissues, resulting in axonal shear injuries and delayed axonal disconnection, categorized as a special type of traumatic brain injury (TBI) (Mu et al., 2021; Zhou et al., 2021; Chen et al., 2022; Kim et al., 2022). A total of 20–38% of TBI patients with DAI were followed up with unfavorable outcome (Extended Glasgow Outcome Scale, GOSE 1–4) (Humble et al., 2018; Lohani et al., 2020), but over 85% suffered from persistent cognitive impairment (Macruz et al., 2022; RaukolaLindblom et al., 2022). Significant differences appeared in the incidence of unfavorable outcome and cognitive impairment, reflecting that part of DAI patients classified as favorable outcome were still plagued by cognitive impairment and could not return to normal social life. However, at present, the prevalence and specificity of cognitive impairment in diffuse axonal injury patients with favorable outcome remain unclear.

"Neurocognition" is defined as a collection of interrelated domains such as executive function (EF), language and perceptual motor function, calculation, complex attention, memory, and visuoperception (George et al., 2018; Holguin et al., 2022; RaukolaLindblom et al., 2022). Found that the Finnish KAT test is a valuable tool to detect cognitive-linguistic deficits by comparing the cognitive function of 48 adults with moderate to severe DAI and 27 healthy controls. The Hopkins Language Learning Test (HVLT), Trail Making Test (TMT), and Rey–Osterrieth Complex Figure test were used to assess neuropsychological results in 25 DAI patients at 6 and 12 months post-traumatic, revealed that patients' episodic verbal memory, attention, and executive function were improved at 6 and 12 months after the trauma (Macruz et al., 2022). All of the above test methods could only evaluate certain domains of Neurocognition, and the Montreal Cognitive Assessment (MoCA) (Nasreddine et al., 2005) was considered to be a more appropriate scale to comprehensively assess cognitive function after traumatic brain injury, subarachnoid hemorrhage, stroke and Alzheimer's disease (Cornea et al., 2022; Holguin et al., 2022; Wang et al., 2022). MoCA and resting-state perfusion magnetic resonance imaging were performed in 40 patients with acute mild TBI and 40 healthy controls within 14 days following injury to elucidate the relationship between cerebral blood flow connectivity differences and cognitive outcomes in the acute phase after mild TBI (Duan et al., 2022). Further more, a study from Shanghai Huashan Hospital confirmed that the Chinese version of the Montreal Cognitive Assessment Basic (MoCA-BC), as a reliable cognitive screening test across all education levels, has the advantages of high acceptance and good reliability, and is more suitable than MoCA for Chinese elderly adults with low years of education (Chen et al., 2016).

The favorable outcome (GOSE 5–8) can not be used as the final prognostic indicator because a large part of DAI patients is still troubled by cognitive impairment at several months after TBI (George et al., 2018). We hypothesized that DAI patients with favorable outcomes still have cognitive impairment in different domains. To test this hypothesis, we analyzed the functional status of nine cognitive domains in patients with DAI at 6 months after injury.

Materials and methods

Participants

Patients with DAI diagnosed by magnetic resonance imaging (MRI) within 30 days after injury were screened in this retrospective observational study between January 2019 and December 2021. Neuropsychological of DAI patients were assessed by MoCA-BC at 6 months after TBI. This data collection site was approved by the local Institutional Review Board, and written informed consent was obtained from all participants or their representatives.

The inclusion criteria were the following: TBI patients' age between 18 and 70 years, diagnosed as DAI by clinical MRI scan within 30 days after injury, 6-month GOSE score $\geq$5, years of education $\geq$4. The exclusion criteria were the following: Progressive brain illness (Dementia, Parkinson disease, multiple sclerosis, seizure disorder, and brain tumor) (2/8), history of brain surgery or stroke without full recovery (1/8), Unable to complete or cooperate with the cognitive function test (speech disorder or mental illness) (5/8).

Parameters

Demographic and clinical characteristics were collected during hospitalization, including age, sex, causes of trauma (road traffic accident, fall, and others), years of education, admission GCS score, pupillary light reflex (none, unilateral or bilateral), Marshall CT classification (evaluated on a scale from 1 to 6) from the first head CT scan, time of the return of consciousness.

Diagnosis and grading of DAI

The clinical MRI was performed with a 1.5T scanner (Siemens Symphony, ATim) within 30 days after injury. DAI were defined as TBI patients with lesions in gray-white matter junction of the cerebrum, corpus callosum, or brain stem with T2-weighted imaging (T2WI), T2-weighted fluid attenuated inversion recovery (T2 FLAIR), and diffusion-weighted imaging (DWI) in magnetic resonance imaging (MRI) (Subash et al., 2020; Yue et al., 2020). These lesions were defined as having hypointense focus presented on T2WI (hemorrhagic DAI), or hyperintense focus presented on DWI, T2 FLAIR, and T2WI (non-hemorrhagic DAI) (Rutman et al., 2017; Benjamini et al., 2021). The MRI and CT images were independently analyzed by two experienced neuroradiologists, who had access to patient clinical information but were blinded to the cognitive function.

The presence of DAI in the hemispheres or cerebellum was recorded as DAI grade 1, in the corpus callosum with or without lesions of grade 1 as DAI grade 2, and in the brainstem with or without lesions of grade 1 and/or 2 as DAI grade 3. Patients without DAI were assigned to grade 0 (Adams et al., 1989; **Figure 1**).

Extended Glasgow outcome scale

GOSE was used to quantify 6-month outcome as favorable outcome (GOSE 5–8; no or moderate disability) or unfavorable

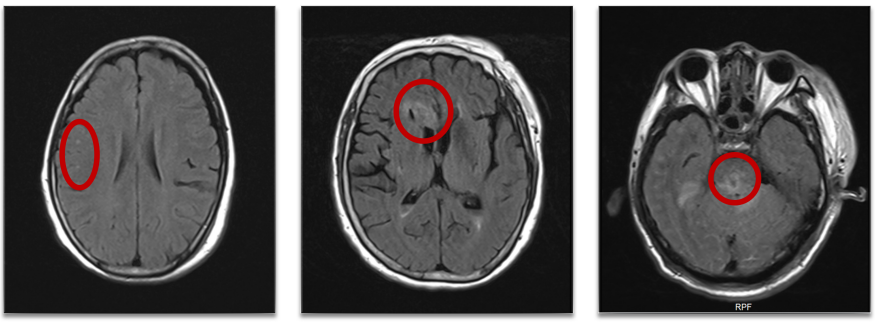

FIGURE 1
DAI grade 1: Lesions in the hemispheres, DAI grade 2: Lesions in the corpus callosum, DAI grade 3: Lesions in the brainstem (as shown in the red circle). DAI, Diffuse axonal injury.

outcome (GOSE 1–4; severe disability or death). GOSE was divided into eight levels (Wilson et al., 1998; **Table 1**).

Neuropsychological assessment

The MoCA-BC was translated from the original English version with subtle linguistic and cultural modifications and regarded as an effective cognitive test for Chinese elderly adults with low years of education (Chen et al., 2016; Huang et al., 2018). The MoCA-BC assesses nine cognitive domains including executive function, language, orientation, calculation, abstraction, memory, visuoperception, naming, and attention. It takes about 10 min to complete the test, with a maximum score of 30 points. More than 26 points was regarded as normal and with a lower score indicating greater cognitive impairment (Zhang et al., 2019). Each patient's test was performed by trained staff in a quiet environment at 6 months after injury.

Data conversion

The scores of nine cognitive domains of MoCA-BC were all converted into the actually deducted scores (Ads), because the study focused on analyzing the negative impact of cognitive function (Rainer et al., 2006). The specific conversion method was to subtract the total score of each cognitive domain from the actual score of this domain, that is, the negative value of the score deducted from each domain, for example, if the patient's orientation score was four, then his a Ads of orientation was four minus six (the total score of orientation), which equals to negative two points.

TABLE 1 Extended Glasgow Outcome Scale.

Unfavorable outcome	Favorable outcome
1: Death	5: Moderately disabled, qualified for low-level work
2: Plant state	6: Moderately disabled, resuming the previous job but requiring some adjustments
3: Severely disabled and totally dependent on others for daily activities	7: Good recovery, and accompanied by minor physical and mental deficits
4: Severely disabled and can do some daily activities with the help of others	8: Great recovery

Statistical analysis

All statistical analyses were performed using GraphPad Prism 8 (GraphPad Software, San Diego, CA, USA). A value of $p < 0.05$ with a two-tailed test was considered statistically significant. Categorical data are presented as frequency or percentage and compared by Fisher exact test. Continuous data are presented as the median and interquartile range (IQR) and were compared by the Mann–Whitney *U*-test. Pearson correlation analysis was employed to show the association of potential risk factors with neurocognition and the Ads of nine cognitive domains with MoCA-BC after data conversion in different grades of DAI patients, and presented in the form of a forestplot.

Results

Demographic and clinical characteristics of subjects

A total of 79 DAI patients diagnosed by clinical MRI within 30 days after injury were enrolled during the study period. At 6 months after injury, 54 patients met all the criteria for inclusion, eight patients were excluded due to the exclusion criteria, and a total of 46 DAI patients with favorable outcome were analyzed. Among them, eight had normal cognitive function (MoCA-BC $\geq$ 26) and 38 had cognitive impairment (MoCA-BC $<$ 26). Comparing the two groups of DAI patients with 6-month favorable outcome with or without cognitive impairment, it was found that there were significant statistical differences in patients' age, years of education, and time to return of consciousness ($p = 0.003$, $p = 0.009$, and $p < 0.001$). But surprisingly, there were no significant statistical differences in pupillary light reflex, admission GCS, Marshall CT score, and DAI grade (**Table 2**).

Relationship between risk factors and MoCA-BC scores

Pearson correlation analysis was employed to define the relationship of potential risk factors with the scores of MoCA-BC (Figure 2). The following four factors were found to be negatively correlated with the MoCA-BC scores: Return of consciousness ($r = -0.753$, $p < 0.001$), Marshall CT ($r = -0.328$, $p = 0.026$), age ($r = -0.654$, $p < 0.001$), and DAI grade ($r = -0.403$, $p = 0.006$). The MoCA-BC scores were positively correlated with pupillary light reflex ($r = 0.361$, $p = 0.014$), admission GCS ($r = 0.402$, $p = 0.006$) and years of education ($r = 0.581$, $p < 0.001$), Non-significant correlations were observed between sex, causes of trauma and the MoCA-BC scores.

Cognitive impairment in different grades of DAI patients

Moreover, to identify the association of cognitive impairment and each cognitive domain, Pearson correlation analysis was performed between the Ads of nine cognitive domains and MoCA-BC after data conversion in different grades of DAI patients (Figure 3). In patients with DAI grade 1, the Ads of memory ($r = 0.838$, $p < 0.001$), abstraction ($r = 0.843$, $p < 0.001$), and calculation ($r = 0.782$, $p < 0.001$) were most related to the Ads of MoCA-BC. The Ads of nine cognitive domains and MoCA-BC were all proved to be correlated, among patients with DAI grade 2. However, in the DAI grade 3 patients, the highest correlation with the Ads of MoCA-BC were the Ads of memory ($r = 0.904$, $p < 0.001$), calculation ($r = 0.799$, $p = 0.006$), orientation ($r = 0.801$, $p = 0.005$), and executive function ($r = 0.869$, $p = 0.001$). The whole correlation analysis results can be found in Supplementary Table 1.

TABLE 2 Demographic and clinical characteristics of eligible patients with or without cognitive impairment.

Variables	MoCA-BC		*P*-value
	≥26 (*n* = 8)	<26 (*n* = 38)	
Male, *n* (%)	7 (87.5)	22 (57.9)	0.226
Age (years), median (IQR)	29.5 (25.8–35.8)	61 (47–65)	0.003*
Cause of trauma, *n* (%)			
Road traffic accident	5 (62.5)	24 (63.2)	>0.999
Fall	1 (12.5)	13 (34.2)	0.403
Others	2 (25)	1 (2.6)	0.074
Pupillary light reflex, *n* (%)			
None pupillary light reflex	0 (0)	7 (18.4)	0.325
Unilateral pupillary light reflex	1 (12.5)	8 (21.1)	>0.999
Bilateral pupillary light reflex	7 (87.5)	23 (60.5)	0.230
GCS, median (IQR)	13 (9–14.3)	7 (6–11)	0.051
Marshall CT score, median (IQR)	2.5 (2–3.5)	4 (3–5)	0.133
Education (years) (IQR)	12 (11.5–14.5)	6 (6–9)	0.009*
Return of consciousness (days) (IQR)	2 (1–5.8)	19 (9.3–28.3)	<0.001*
DAI grade 1 *n* (%)	6 (75)	18 (47.4)	0.247
DAI grade 2 *n* (%)	2 (25)	10 (26.3)	>0.999
DAI grade 3 *n* (%)	0 (0)	10 (26.3)	0.171

MoCA-BC, the Chinese version of the Montreal Cognitive Assessment Basic; GCS, Glasgow Coma Scale; DAI, Diffuse axonal injury; IQR, 25th percentile–75th percentile. *Represents a significant difference between the two groups.

Discussion

This retrospective study indicated that 82.6% (38/46) of DAI patients with 6-month GOSE ≥5 were still plagued by cognitive impairment, and the major domains of cognitive impairment caused by different grades of DAI were also distinctive.

More than 50 million people are suffering from TBI each year worldwide, and most TBI patients are diagnosed by clinical MRI with some degree of DAI, especially severe TBI among them (Jiang et al., 2019; Lammy, 2020). DAI manifests in the form of focal axonal shear injuries and axonal breakage, so patients with DAI are more likely to have long-term sequelae or serious neurological deficits, even death (Lang et al., 2021; Palmieri et al., 2021).

GOSE or GOS are usually used by neurosurgeons to evaluate the prognosis of patients with DAI, but these assessment methods are not detailed and comprehensive, because previous studies have found that the rate of cognitive impairment is much higher than that of unfavorable outcome (Humble et al., 2018; Lohani et al., 2020; Macruz et al., 2022; RaukolaLindblom et al., 2022). In our study, MoCA-BC was performed to evaluate the cognitive function of 46 patients with DAI who were classified as favorable outcome, and 38 patients were found to have some degree of cognitive impairment. By comparing the two groups of patients with or without cognitive impairment in the present study, it was concluded that there were significant differences in age, education and return of consciousness, but there were no significant differences in admission GCS, Marshall CT score, pupillary light reflex and DAI grades.

In (Macruz et al., 2022) article, admission GCS and Marshall CT score had significant impact on cognitive function. Outcome was better in patients with DAI grade 1 and DAI grade 2 than in patients with DAI grade 3 (Skandsen et al., 2010; Moe et al., 2020). Have confirmed that age, GCS score, pupillary dilatation, traumatic axonal injury (TAI) grade on clinical MRI were significant predictors for poor outcome. Some of the results in our research were not consistent with the recent literature, which may be due to the deviation caused by the insufficient sample size.

Followed the long-term functional outcome of 134 patients with DAI and found independent prognostic factors were age, return of consciousness ≤7 days, pupillary reaction and DAI grade (van Eijck et al., 2018). Education level has been considered to be the strongest non-cognitive factor influencing performance on the MoCA (Chen et al., 2016). Analysis of 228 patients with TBI showed that education status was correlated with MoCA scores: Those patients with higher level of education had significant association with higher MoCA scores ($p = 0.012$) (Panwar et al., 2019). Marshall CT score, pupillary light reflex, duration of coma and admission GCS were predictors of clinical outcome in DAI (Palmieri et al., 2021; Xie et al., 2021; Chen et al., 2022). In the present study we also confirmed that return of consciousness, Marshall CT score, age and DAI grade have a negative correlation with cognitive function in DAI patients with 6-month GOSE 5–8. The more sensitive the pupillary light reflex, the higher the admission GCS and the longer the education, the better the long-term cognitive function of DAI patients. The correlation of these

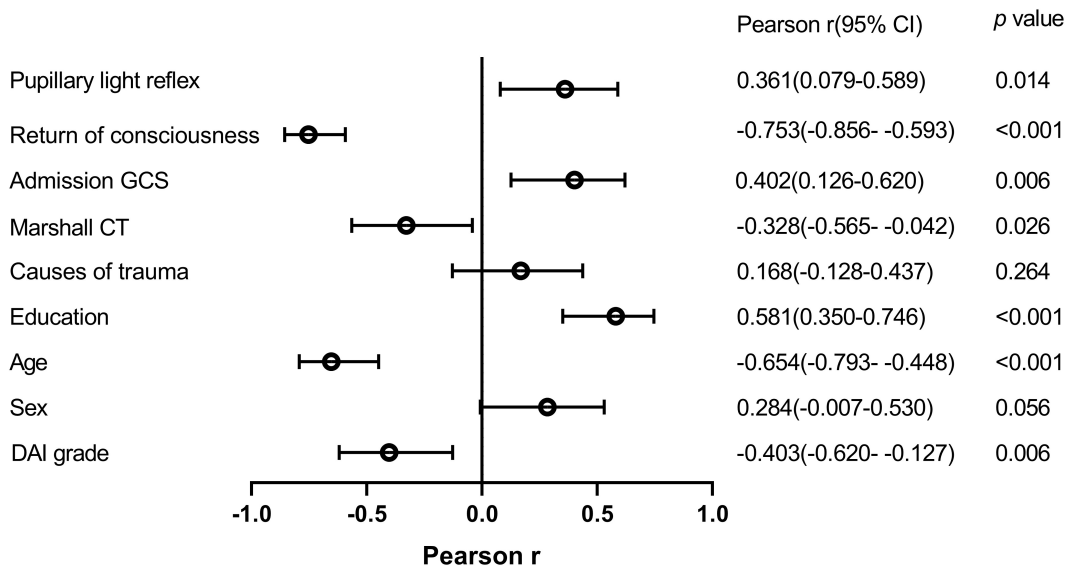

FIGURE 2
Relationship between potential risk factors and MoCA-BC scores. MoCA-BC, the Chinese version of the Montreal Cognitive Assessment Basic; GCS, Glasgow Coma Scale.

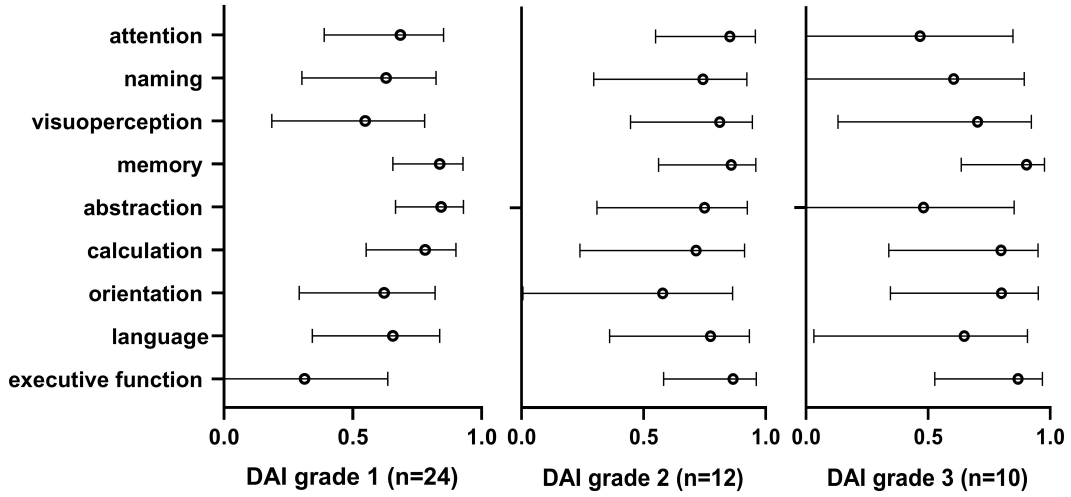

FIGURE 3
Pearson correlation analysis was performed between the Ads of nine cognitive domains and MoCA-BC after data conversion in different grades of DAI patients. MoCA-BC, the Chinese version of the Montreal Cognitive Assessment Basic; DAI, Diffuse axonal injury.

risk factors was basically consistent for the cognitive function of TBI patients and DAI patients with favorable outcome.

Severe cognitive impairment and physical disability were caused by lateral hypothalamus and medial hypothalamus damage during DAI (Wang et al., 2021). HVLT, TMT, and Rey–Osterrieth Complex Figure test were performed by Macruz et al. (2022) to reveal the impairment and recovery of episodic verbal memory, attention, and executive function of DAI patients. Further, scholars found that cognitive impairment was associated with brain tissue lesions displayed on MRI (Yue et al., 2020). Twenty-four patients with moderate or severe DAI were evaluated at 2, 6, and 12 months post-injury (Stewan et al., 2018) found out that microhaemorrhage load (MHL) was correlated only with white matter volume (WMV) reduction, executive function and episodic verbal memory were not correlated with MHL, but were, in part, correlated with WMV and total brain volume reduction. Not only severe TBI, but repetitive mild brain injury impair cognitive abilities and increase risk of neurodegenerative disorders in humans (Sai et al., 2020). So far, the persistent cognitive sequelae of patients suffering from DAI have been identified by the current studies, but the specificity of the impairment of nine cognitive domains caused by different grades of DAI have not been noticed by scholars. In our study, according to the diagnostic results of clinical MRI, DAI was divided into three grades for hierarchical interpretation. Finally, it was found that different degrees of DAI lead to significant differences in the domains of cognitive impairment. The decline of cognitive function in patients with DAI grade 1 was mainly caused by dysfunction in the three cognitive domains of memory, abstraction and calculation. But for patients with DAI grade 2, after the damage of the important structure

(corpus callosum) connecting the left and right sides of the brain (Shah et al., 2021; Lewis et al., 2022), the cognitive impairment was most widely distributed, and none of the nine cognitive domains was immune. Patients with DAI grade 3 suffered from brainstem (the bridge of morphological and functional connection between telencephalon, diencephalon, cerebellum, and spinal cord) (Henson et al., 2020; Paton, 2020) injury, showing cognitive impairment dominated by memory, calculation and orientation and executive function dysfunction.

There are several limitations in our present study. First, insufficient sample size may lead to deviation and compromise the statistical power. Second, taking 6-month GOSE score $\geq$5 as the inclusion criteria may exclude some DAI patients who are classified as unfavorable outcome but can cooperate with the cognitive function test, thus affecting the final cognitive domain analysis results. Third, MoCA-BC was translated according to Chinese culture and may not be suitable for people in other countries.

Conclusion

Our current research has revealed that DAI patients with favorable outcome may still be plagued by cognitive impairment. Different grades of DAI cause different domains of cognitive impairment, which requires neurosurgeons to provide patients with targeted cognitive rehabilitation programs.

Data availability statement

The original contributions presented in this study are included in the article/**Supplementary material**, further inquiries can be directed to the corresponding authors.

Ethics statement

The studies involving human participants were reviewed and approved by the Institutional Review Board of Haining People's Hospital. The patients/participants provided their written informed consent to participate in this study.

Author contributions

WC, CY, SL, JS, GW, and RJ: conceptualization and writing – review and editing. HH, ZZ, WS, and RC: data curation. XH and LX: formal analysis. LX, KS, JS, WC, CY, and HH: investigation. WC, SL, RJ, and GW: methodology. RJ and GW: supervision. HH and ZZ: visualization. WC and CY: writing – original draft. All authors contributed to the article and approved the submitted version.

Conflict of interest

The authors declare that the research was conducted in the absence of any commercial or financial relationships that could be construed as a potential conflict of interest.

Publisher's note

All claims expressed in this article are solely those of the authors and do not necessarily represent those of their affiliated organizations, or those of the publisher, the editors and the reviewers. Any product that may be evaluated in this article, or claim that may be made by its manufacturer, is not guaranteed or endorsed by the publisher.

Supplementary material

The Supplementary Material for this article can be found online at: https://www.frontiersin.org/articles/10.3389/fnins.2023.1077858/full#supplementary-material

References

Adams, J. H., Doyle, D., Ford, I., Gennarelli, T. A., Graham, D. I., and McLellan, D. R. (1989). Diffuse axonal injury in head injury: Definition, diagnosis and grading. *Histopathology* 15, 49–59. doi: 10.1111/j.1365-2559.1989.tb03040.x

Benjamini, D., Iacono, D., Komlosh, M. E., Perl, D. P., Brody, D. L., and Basser, P. J. (2021). Diffuse axonal injury has a characteristic multidimensional MRI signature in the human brain. *Brain* 144, 800–816. doi: 10.1093/brain/awaa447

Chen, K., Xu, Y., Chu, A., Ding, D., Liang, X., Nasreddine, Z. S., et al. (2016). Validation of the Chinese version of montreal cognitive assessment basic for screening mild cognitive impairment. *J. Am. Geriat. Soc.* 64, e285–e290. doi: 10.1111/jgs.14530

Chen, W., Wang, G., Yao, C., Zhu, Z., Chen, R., Su, W., et al. (2022). The ratio of serum neuron-specific enolase level to admission glasgow coma scale score is associated with diffuse axonal injury in patients with moderate to severe traumatic brain injury. *Front. Neurol.* 13:887818. doi: 10.3389/fneur.2022.887818

Cornea, A., Simu, M., and Rosca, E. C. (2022). Montreal cognitive assessment for evaluating cognitive impairment in subarachnoid hemorrhage: A systematic review. *J. Clin. Med.* 11:4679. doi: 10.3390/jcm11164679

Duan, M., Liu, Y., Li, F., Lu, L., and Chen, Y. (2022). Cerebral blood flow network differences correlated with cognitive impairment in mild traumatic brain injury. *Front. Neurosci.* 16:969971. doi: 10.3389/fnins.2022.969971

George, S., David, K. M., Emmanuel, A. S., John, D. P., and Barbara, J. S. (2018). Personalised treatments for traumatic brain injury: Cognitive, emotional and motivational targets. *Psychol. Med.* 48, 1397–1399. doi: 10.17863/CAM.25958

Henson, J. W., Benkers, T., and McCormick, C. (2020). Brainstem ischemic syndrome in juvenile NF2. *Neurol. Genet.* 6:e446. doi: 10.1212/NXG.0000000000000446

Holguin, J. A., Margetis, J. L., Narayan, A., Yoneoka, G. M., and Irimia, A. (2022). Vascular cognitive impairment after mild stroke: Connectomic insights, neuroimaging, and knowledge translation. *Front. Neurosci.* 16:905979. doi: 10.3389/fnins.2022.905979

Huang, L., Chen, K., Lin, B., Tang, L., Zhao, Q., Lv, Y., et al. (2018). Chinese version of montreal cognitive assessment basic for discrimination among different severities of Alzheimer's disease. *Neuropsych. Dis. Treat.* 14, 2133–2140. doi: 10.2147/NDT.S174293

Humble, S. S., Wilson, L. D., Wang, L., Long, D. A., Smith, M. A., Siktberg, J. C., et al. (2018). Prognosis of diffuse axonal injury with traumatic brain injury. *J. Trauma Acute Care Surg.* 85, 155–159. doi: 10.1097/TA.0000000000001852

Jiang, J. Y., Gao, G. Y., Feng, J. F., Mao, Q., Chen, L. G., Yang, X. F., et al. (2019). Traumatic brain injury in China. *Lancet Neurol.* 18, 286–295. doi: 10.1016/S1474-4422(18)30469-1

Kim, M., Hong, S. K., Jeon, S. R., Roh, S. W., and Lee, S. (2022). Treatment outcome and risk factors associated with diffuse axonal injury in patients with moderate to severe head injury. *Turk Neurosurg.* 32, 6–15. doi: 10.5137/1019-5149.JTN.28132-19.4

Lammy, S. (2020). Management of traumatic brain injury in China versus Europe. *Lancet Neurol.* 19:886. doi: 10.1016/S1474-4422(20)30345-8

Lang, S. S., Kilbaugh, T., Friess, S., Sotardi, S., Kim, C. T., Mazandi, V., et al. (2021). Trajectory of long-term outcome in severe pediatric diffuse axonal injury: An exploratory study. *Front. Neurol.* 12:704576. doi: 10.3389/fneur.2021.704576

Lewis, J. D., Acosta, H., Tuulari, J. J., Fonov, V. S., Collins, D. L., Scheinin, N. M., et al. (2022). Allometry in the corpus callosum in neonates: Sexual dimorphism. *Hum. Brain Mapp.* 43, 4609–4619. doi: 10.1002/hbm.25977

Lohani, S., Bhandari, S., Ranabhat, K., and Agrawal, P. (2020). Does diffuse axonal injury MRI grade really correlate with functional outcome? *World Neurosurg.* 135, e424–e426.

Macruz, F. B. D. C., Feltrin, F. S., Zaninotto, A., Guirado, V. M. D. P., Otaduy, M. C. G., Tsunemi, M. H., et al. (2022). Longitudinal assessment of magnetization transfer ratio, brain volume, and cognitive functions in diffuse axonal injury. *Brain Behav.* 12:e2490. doi: 10.1002/brb3.2490

Moe, H. K., Limandvik Myhr, J., Moen, K. G., Håberg, A. K., Skandsen, T., and Vik, A. (2020). Association of cause of injury and traumatic axonal injury: A clinical MRI study of moderate and severe traumatic brain injury. *J. Neurosurg.* 133, 1559–1567. doi: 10.3171/2019.6.JNS191040

Mu, J., Wang, T., Li, M., Guan, T., Guo, Y., Zhang, X., et al. (2021). Ketogenic diet protects myelin and axons in diffuse axonal injury. *Nutr. Neurosci.* 28, 1–14. doi: 10.1080/1028415X.2021.1875300

Nasreddine, Z. S., Phillips, N. A., Bedirian, V., Charbonneau, S., Whitehead, V., Collin, I., et al. (2005). The montreal cognitive assessment, MoCA: A brief screening tool for mild cognitive impairment. *J. Am. Geriatr. Soc.* 53, 695–699. doi: 10.1111/j.1532-5415.2005.53221.x

Palmieri, M., Frati, A., Santoro, A., Frati, P., Fineschi, V., and Pesce, A. (2021). Diffuse axonal injury: Clinical prognostic factors, molecular experimental models and the impact of the trauma related oxidative stress. An extensive review concerning milestones and advances. *Int. J. Mol. Sci.* 22:10865. doi: 10.3390/ijms221910865

Panwar, N., Purohit, D., Deo, S. V., and Joshi, M. (2019). Evaluation of extent and pattern of neurocognitive functions in mild and moderate traumatic brain injury patients by using montreal cognitive assessment (MoCA) score as a screening tool: An observational study from India. *Asian J. Psychiatr.* 41, 60–65. doi: 10.1016/j.ajp.2018.08.007

Paton, J. (2020). Clarity of the rhythmic brainstem. *J. Physiol.* 598, 2045–2046. doi: 10.1113/JP279732

Rainer, S., Kathrin, W., Thomas, G., Christoph, P., and von Cramon, D. (2006). Cognitive sequelae of diffuse axonal injury. *Arch. Neurol.* 63, 418–424. doi: 10.1001/archneur.63.3.418

RaukolaLindblom, M., Ljungqvist, L., Kurki, T., Tenovuo, O., and Laasonen, M. (2022). Cognitive-Linguistic outcome in moderate to severe diffuse axonal injury and association with fatigue. *Brain Injury* 35, 1674–1681. doi: 10.1080/02699052.2021.2012824

Rutman, A. M., Rapp, E. J., Hippe, D. S., Vu, B., and Mossa-Basha, M. (2017). T2*-weighted and diffusion magnetic resonance imaging differentiation of cerebral fat embolism from diffuse axonal injury. *J. Comput. Assist. Tomogr.* 41, 877–883. doi: 10.1097/RCT.0000000000000635

Sai, A. T., Zsolt, K. B., Nóra, B., Lili, V. N., Krisztina, A., Bálint, F., et al. (2020). Long-term cognitive impairment without diffuse axonal injury following repetitive mild traumatic brain injury in rats. *Behav. Brain Res.* 378:112268. doi: 10.1016/j.bbr.2019.112268

Shah, A., Jhawar, S., Goel, A., and Goel, A. (2021). Corpus callosum and its connections: A fiber dissection study. *World Neurosurg.* 151, e1024–e1035. doi: 10.1016/j.wneu.2021.05.047

Skandsen, T., Kvistad, K. A., Solheim, O., Strand, I. H., Folvik, M., and Vik, A. (2010). Prevalence and impact of diffuse axonal injury in patients with moderate and severe head injury: A cohort study of early magnetic resonance imaging findings and 1-year outcome. *J. Neurosurg.* 113, 556–563. doi: 10.3171/2009.9.JNS09626

Stewan, F. F., Zaninotto, A. L., Guirado, V. M. P., Macruz, F., Sakuno, D., Dalaqua, M., et al. (2018). Longitudinal changes in brain volumetry and cognitive functions after moderate and severe diffuse axonal injury. *Brain Injury* 32, 1208–1217. doi: 10.1080/02699052.2018.1494852

Subash, L., Shreeram, B., Kajan, R., and Prity, A. (2020). Does diffuse axonal injury MRI grade really correlate with functional outcome? *World Neurosurg.* 135, e424–e426.

van Eijck, M., van der Naalt, J., de Jongh, M., Schoonman, G., Oldenbeuving, A., Peluso, J., et al. (2018). Patients with diffuse axonal injury can recover to a favorable long-term functional and quality of life outcome. *J. Neurotrauma* 35, 2357–2364. doi: 10.1089/neu.2018.5650

Wang, G., Estrella, A., Hakim, O., Milazzo, P., Patel, S., Pintagro, C., et al. (2022). Mini-mental state examination and montreal cognitive assessment as tools for following cognitive changes in Alzheimer's disease neuroimaging initiative participants. *J. Alzheimer's Dis. JAD* 90, 263–270. 10.3233/JAD-220397 doi: :

Wang, Y., Zhou, F., Li, Y., Li, J., Kuang, H., Chen, Q., et al. (2021). Functional plasticity in lateral hypothalamus and its prediction of cognitive impairment in patients with diffuse axonal injury: Evidence from a resting-state functional connectivity study. *Neuro. Rep.* 32, 7588–7595. doi: 10.1097/WNR.0000000000001630

Wilson, J. T., Pettigrew, L. E., and Teasdale, G. M. (1998). Structured interviews for the glasgow outcome scale and the extended glasgow outcome scale: Guidelines for their use. *J. Neurotrauma* 15, 573–585. doi: 10.1089/neu.1998.15.573

Xie, Q., Huang, W., Shen, L., Wang, M., Liu, K., and Liu, F. (2021). The combination of neutrophil-to-lymphocyte ratio and admission GCS score is an independent predictor of clinical outcome in diffuse axonal injury. *World Neurosurg.* 152:248. doi: 10.1016/j.wneu.2021.05.060

Yue, J. K., Yuh, E., Stein, M., Winkler, E., Deng, H., Ore, C. L. D., et al. (2020). Diffuse axonal injury and cerebral contusions on MRI are associated with decreased functional outcome in CT-negative TBI: A TRACK-TBI pilot study. *Neurosurgery* 67 (Supplement_1). doi: 10.1093/neuros/nyaa447_442

Zhang, Y., Ding, Y., Chen, K., Liu, Y., Wei, C., Zhai, T., et al. (2019). The items in the Chinese version of the montreal cognitive assessment basic discriminate among different severities of Alzheimer's disease. *BMC Neurol.* 19:269. doi: 10.21203/rs.2.10497/v5

Zhou, Z., Li, X., Liu, Y., Fahlstedt, M., Georgiadis, M., Zhan, X., et al. (2021). Toward a comprehensive delineation of white matter tract-related deformation. *J. Neurotrauma* 38, 3260–3278. doi: 10.1089/neu.2021.0195

frontiers | Frontiers in Neuroscience

TYPE Original Research
PUBLISHED 30 January 2023
DOI 10.3389/fnins.2023.1061578

OPEN ACCESS

EDITED BY
Haojie Mao,
Western University, Canada

REVIEWED BY
Chase Francis,
University of South Carolina, United States
Libo Zhang,
Peking University, China
Chris Pierce,
Rutgers, The State University of New Jersey, United States
Paul Meyer,
University at Buffalo, United States

*CORRESPONDENCE
Yoonbae Oh
✉ oh.yoonbae@mayo.edu

SPECIALTY SECTION
This article was submitted to Translational Neuroscience, a section of the journal Frontiers in Neuroscience

RECEIVED 04 October 2022
ACCEPTED 09 January 2023
PUBLISHED 30 January 2023

CITATION
Yuen J, Goyal A, Rusheen AE, Kouzani AZ, Berk M, Kim JH, Tye SJ, Blaha CD, Bennet KE, Lee KH, Shin H and Oh Y (2023) High frequency deep brain stimulation can mitigate the acute effects of cocaine administration on tonic dopamine levels in the rat nucleus accumbens.
Front. Neurosci. 17:1061578.
doi: 10.3389/fnins.2023.1061578

High frequency deep brain stimulation can mitigate the acute effects of cocaine administration on tonic dopamine levels in the rat nucleus accumbens

Jason Yuen[1,2], Abhinav Goyal[1,3], Aaron E. Rusheen[1,3], Abbas Z. Kouzani[4], Michael Berk[2], Jee Hyun Kim[2], Susannah J. Tye[5], Charles D. Blaha[1], Kevin E. Bennet[1,6], Kendall H. Lee[1,7], Hojin Shin[1,7] and Yoonbae Oh[1,7]*

[1]Department of Neurologic Surgery, Mayo Clinic, Rochester, MN, United States, [2]The Institute for Mental and Physical Health and Clinical Translation (IMPACT), Barwon Health, Deakin University, Geelong, VIC, Australia, [3]Medical Scientist Training Program, Mayo Clinic, Rochester, MN, United States, [4]School of Engineering, Deakin University, Geelong, VIC, Australia, [5]Queensland Brain Institute, The University of Queensland, St Lucia, QLD, Australia, [6]Division of Engineering, Mayo Clinic, Rochester, MN, United States, [7]Department of Biomedical Engineering, Mayo Clinic, Rochester, MN, United States

Cocaine's addictive properties stem from its capacity to increase tonic extracellular dopamine levels in the nucleus accumbens (NAc). The ventral tegmental area (VTA) is a principal source of NAc dopamine. To investigate how high frequency stimulation (HFS) of the rodent VTA or nucleus accumbens core (NAcc) modulates the acute effects of cocaine administration on NAcc tonic dopamine levels multiple-cyclic square wave voltammetry (M-CSWV) was used. VTA HFS alone decreased NAcc tonic dopamine levels by 42%. NAcc HFS alone resulted in an initial decrease in tonic dopamine levels followed by a return to baseline. VTA or NAcc HFS following cocaine administration prevented the cocaine-induced increase in NAcc tonic dopamine. The present results suggest a possible underlying mechanism of NAc deep brain stimulation (DBS) in the treatment of substance use disorders (SUDs) and the possibility of treating SUD by abolishing dopamine release elicited by cocaine and other drugs of abuse by DBS in VTA, although further studies with chronic addiction models are required to confirm that. Furthermore, we demonstrated the use of M-CSWV can reliably measure tonic dopamine levels *in vivo* with both drug administration and DBS with minimal artifacts.

KEYWORDS

substance use disorder, deep brain stimulation, nucleus accumbens, ventral tegmental area, cocaine, tonic dopamine

1. Introduction

Despite the increasing interest and resources devoted to addiction research, there has been little improvement in the clinical care and prevalence of substance use disorder (SUD) (Substance Abuse and Mental Health Services Administration [SAMHSA], 2020). In the USA alone, management and treatment of SUD costs the healthcare, welfare, and justice systems hundreds of billion dollars annually (United States Department of Health and Human Services [USDHHS], 2016; Peacock et al., 2018). Despite the development of a variety of behavioral and

pharmacological therapeutic options, most SUDs patients do not get treatment, response rates are low, and relapse rates as high as 75–98% have been reported (Brandon et al., 2007; Saloner and Karthikeyan, 2015). To better manage these "treatment-refractory" patients, it is important to further our understanding in the pathophysiology of SUD. One such approach is to study the neurochemical dynamics in the central nervous system associated with drug administration, which has the potential to identify treatment targets.

Dopamine is an important neurotransmitter for neuropsychiatric diseases such as SUD, obsessive compulsive disorder, and Tourette's syndrome (Denys et al., 2004; Oliva and Wanat, 2016; Maia and Conceicao, 2018). Therefore, controlling the release of dopamine *via* neuromodulation, as has been done for neurological diseases such as Parkinson's disease, is potentially an effective strategy for the treatment of these pathologies. Indeed, previous attempts have been made to stimulate targets within the mesolimbic dopaminergic pathway as a means to rectify dysfunctional dopamine dynamics (Holtzheimer and Mayberg, 2011).

The ventral tegmental area (VTA) and substantia nigra pars compacta are major producers of dopamine in the mesolimbic dopaminergic pathway (Bjorklund and Dunnett, 2007). A major VTA projection target is the nucleus accumbens (NAc), which has been implicated in mediating important cognitive functions, such as reward and learning (see **Figure 1A**; Salgado and Kaplitt, 2015). In addition, over- and under-release of dopamine in the NAc are important pathophysiological conditions of neuropsychiatric diseases, such as SUD (Di Chiara, 2002). The NAc is one of the most studied deep brain stimulation (DBS) targets to modulate dopamine release in SUD in both preclinical models and human trials (Liu et al., 2008; Knapp et al., 2009; Henderson et al., 2010; Guo et al., 2013; Vassoler et al., 2013; Hamilton et al., 2015; Müller et al., 2016; Batra et al., 2017; Chen et al., 2019; Sildatke et al., 2020).

Nevertheless, the dimensions and resolution of contemporary *in vivo* measuring methods such as the use of microdialysis have limited the continuous measurement of dopamine as a useful biomarker for interventive therapy, until recently (Watson et al., 2006; Gu et al., 2015). Despite having the ability to unequivocally distinguish between different types of analytes, microdialysis probes have a relatively large dimension (~200 μm in diameter) and the temporal resolution is of the order of ≥ 1 min (Morelli et al., 1992; Di Chiara et al., 1993; Blaha et al., 1996; Chefer et al., 2009; Oh et al., 2018; Rusheen et al., 2020). In addition, microdialysis measurements cannot be made *in situ*, requiring drawing samples from the brain for subsequent laboratory identification. The trauma caused by the probe size and the relatively low temporal resolution means this method is likely to be inadequate to detect the rapid changes in dopamine levels involved in psychopathologies in the neural structures of interest (Blaha et al., 1996; Bungay et al., 2003; Borland et al., 2005). The requirement to extract brain dialysate samples makes microdialysis unsuitable as a technique for human therapy.

We recently reported a new technique known as multiple-cyclic square wave voltammetry (M-CSWV). This method is able to measure tonic extracellular dopamine levels with unprecedented temporal resolution (10 s) and minimal trauma to the neural tissue when used in combination with carbon fiber microelectrodes (CFM) (Oh et al., 2018). This technique uses dynamic background subtraction and capacitive background current modeling to eliminate large capacitive background currents generated by the applied voltammetric waveform. This allows tonic dopamine concentrations to be measured every 10 s, something not possible with conventional fast-scan cyclic voltammetry (FSCV). Our group has previously demonstrated that M-CSWV is able to record changes in tonic dopamine levels in response to cocaine administration (Yuen et al., 2021a).

NAc DBS has shown promising results for the treatment of SUD (Liu et al., 2008; Knapp et al., 2009; Henderson et al., 2010; Guo et al., 2013; Ma et al., 2013; Batra et al., 2017; Schippers et al., 2017; Yuen et al., 2022b). Here we hypothesized that the therapeutic effects of NAc DBS may be due to its ability to rapidly modulate tonic dopamine concentrations. DBS of the VTA, the main dopaminergic afferent to the NAc, may also achieve a similar effect. In the present study, M-CSWV was utilized to elucidate the effects of high frequency stimulation (HFS) of both the VTA and the NAc on tonic dopamine levels in the nucleus accumbens core (NAcc) with or without acute cocaine administration (Yuen et al., 2021a).

2. Materials and methods

2.1. Animal subjects

Male Sprague-Dawley rats (250–300 g; Envigo, IN, USA) were used for this study. Rats were kept in social housing in an association for assessment and accreditation of laboratory animal care international (AAALAC) accredited vivarium following a standard 12-h light/dark cycle at constant temperature (21°C) and humidity (45%) with *ad libitum* food and water. The present studies were approved by the Institutional Animal Care and Use Committee (IACUC), Mayo Clinic, Rochester. The NIH Guide for the care and use of laboratory animals guidelines (Department of Health and Human Services, NIH publication No. 86-23, revised 1985) were followed for all aspects of animal care.

2.2. Electrode fabrication

Carbon fiber microelectrodes were fabricated using an established standardized CFM design at Mayo Clinic (Chang et al., 2013; Oh et al., 2016). Each microelectrode involved isolating and inserting a single carbon fiber (AS4, diameter = 7 μm; Hexcel, Stamford, CT, USA) into a silica tubing (20 μm ID, 90 μm OD, 10 μm coat with polyimide; Polymicro Technologies, Phoenix, AZ, USA). The connection between the carbon fiber and the silica tubing was covered with epoxy resin. The silica tubing was then attached to a nitinol extension wire (Nitinol #1, an alloy of nickel and titanium; Fort Wayne Metals, IN, USA) by a silver-based conductive paste (Chang et al., 2013). The carbon fiber attached nitinol wire was insulated with polyimide tubing (0.0089″ ID, 0.0134″ OD, 0.00225″ WT; Vention Medical, Salem, NH, USA) up to the carbon fiber sensing segment. The exposed carbon fiber was trimmed under a dissecting microscope to a length of ~50 μm. Teflon-coated silver (Ag) wire (A-M systems, Inc., Sequim, WA, USA) was prepared as an Ag/AgCl counter-reference electrode by chlorinating the exposed tip in saline with a 9 V dry cell battery. CFMs were pretested in a flow cell prior to coating deposition with a PEDOT:Nafion deposition solution (Vreeland et al., 2015), which minimized the effect of biofouling *in vivo*.

2.3. Implantation of recording and stimulating electrodes

Each rat was anesthetized with urethane (1.5 g/kg i.p.; Sigma-Aldrich, St Louis, MO, USA) and administered buprenorphine (0.05–0.1 mg/kg s.c., Par Pharmaceutical, Chestnut Ridge, NY, USA) for analgesia. Following anesthesia, they were placed in a stereotaxic frame (David Kopf Instruments, Tujunga, CA, USA). Respiratory rate (RespiRAT, Intuitive Measurement Systems, AZ, USA) and hind-paw and tail pinch were used to monitor the physiological state and depth of anesthesia, respectively. Using a standard rat brain atlas (Paxinos and Watson, 2007), three trephine holes were drilled, the first for placement of a CFM into the NAcc (all coordinates from bregma: AP 1.2 mm, ML 2.0 mm, DV 6.5–7.5 mm from dura), the second for a stimulating electrode into the VTA (twisted bipolar stimulating electrode–Plastics One, MS 303/2, Roanoke, VA, USA, with the tips separated by ∼1 mm; AP −5.3 mm, ML 0.9 mm, DV 7.5–9 mm from dura), and a third for an Ag/AgCl into the contralateral cortex (**Figure 1**; Clark et al., 2010). For NAcc stimulation experiments, a bipolar concentric simulating electrode (MicroProbes, Gaithersburg, MD, USA) was implanted immediately posterior and medial to the CFM in the NAcc (∼0.3 mm apart).

2.4. Recordings and stimulation parameters

The depths of the stimulating electrode in the VTA and CFM in the NAcc were first adjusted to obtain a robust stimulation-evoked dopamine signal as measured by FSCV (−0.4 to 1.3 V sweep; 10 Hz; see **Supplementary Figure A1**). Stimulation parameters were biphasic pulses at 60 Hz, 0.2 ms pulse width, 0.2 mA, and 2 s duration. Stimulation and FSCV were both performed using the WINCS Harmoni system (Lee et al., 2017), a wireless stimulation and neurochemical sensing system.

Once the optimal electrode depths were identified, the system was switched to the M-CSWV sensing technique (see **Figure 1B**). After 60 min of stabilization, either VTA or NAc biphasic pulse stimulation was applied at 130 Hz (0.2 ms, 0.2 mA) continuously. The delivered stimulation was interleaved with the M-CSWV recording to minimize artifacts. Once the signal was restabilized to a new plateau (≥ 30 min), i.v. saline (1 ml/kg) was administered as a negative control while stimulation and recording continued. After 30 min, i.v. cocaine (2 mg/kg) was administered (infused over 1 min *via* cannula at tail vein; dissolved in 0.5 ml of normal saline). After another 30 min of observation, the stimulation was turned off. Post-stimulation, the animal was observed for another 30 min before being sacrificed using Fatal-Plus injection (pentobarbital 390 mg/ml; 10 ml).

2.5. Pharmacological confirmation

In a separate group of animals ($N = 5$), alpha-methyl-p-tyrosine (AMPT; 250 mg/kg, i.p.), a tyrosine hydroxylase inhibitor, was given to further confirm the recording of dopamine by M-CSWV. Tyrosine hydroxylase is the rate limiting enzyme of catecholamine biosynthesis, converting tyrosine into L-DOPA, the precursor to dopamine. Thus, AMPT administration, acting as a negative control, was expected to decrease the voltammetric signal if the signal indeed arose from dopamine.

2.6. Calibration of electrodes

After experimentation, changes in dopamine release in individual CFMs were calibrated *in vitro* with dopamine solutions of different known concentrations. This is in a similar fashion to previously described procedures in the literature (Oh et al., 2018).

2.7. Histological analysis

CFM and stimulation electrode trajectories were confirmed by histological analysis. Brains were removed from euthanized animals and immersed in 4% paraformaldehyde overnight for fixation. After fixation, 60 μm coronal sections were cut on a freezing microtome. The sections were stained with cresyl violet. The location of the stimulating and CFMs were identified under light microscopy (**Supplementary Material B**) based on (Paxinos and Watson, 2007).

2.8. Statistical analysis

Statistical analysis was performed using repeated measures one-way ANOVA and two-tailed paired *t*-tests in relevant *post hoc* analyses (PRISM 8, GraphPad). For comparison, the levels were all measured by averaging over 10 data points, i.e., 10 s. In cases where i.v. drug was administered, the 10 data points centered at peak within 10 min of injection.

After ANOVA tests were performed among the positive control, negative control, VTA stimulation and NAcc stimulation groups, paired *t*-tests were used to demonstrate sequential changes in the *post hoc* analysis. In the control experiments, pre-injection baseline tonic dopamine concentrations were compared to the post-saline levels, and the post-saline levels were compared with the post-cocaine peak levels. In the NAcc stimulation experiments (see **Figure 4**), the initial stabilized baseline levels before injection were compared with the trough levels (not seen during VTA experiments) during stimulation. Then, similarly, the new baselines were compared with the post-saline levels, and the post-saline levels were compared with the post-cocaine peak levels. In VTA stimulation experiments (see **Figure 5**), the initial baselines were compared with the new baselines during stimulation. The new baselines were compared with the post-saline levels, and these post-saline levels were compared with the post-cocaine levels. All error bars and shaded areas are represented as S.E.M. statistical significance was set at $p < 0.05$. Bonferroni correction was applied in cases with multiple comparisons.

3. Results and discussion

3.1. Control experiments

In the positive control experiments, after implanting the CFM at the optimal position within NAcc (see section "Materials and methods"), we elicited cocaine-induced dopamine changes by first administering i.v. saline and then i.v. cocaine, while tonic dopamine

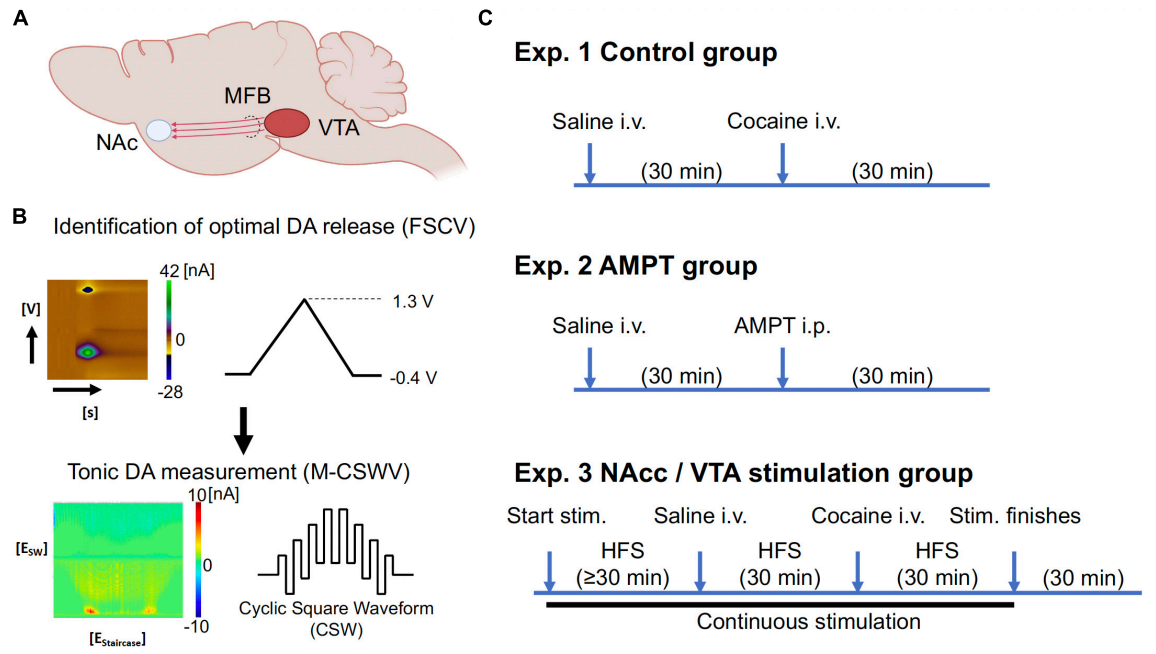

FIGURE 1
(A) Simplified diagram demonstrating some of the major dopaminergic projections from the VTA. **(B)** The optimal depths of electrodes in the VTA and nucleus accumbens core (NAcc) were first identified using FSCV (maximum dopamine evoked release; 60 Hz, 2 ms, 0.2 mA, 2 s duration; Supplementary Figure A1). The system was then switched to M-CSWV to record tonic dopamine levels in the NAcc. **(C)** Experimental set-up of tonic dopamine measurements. With the control and AMPT groups, no stimulation was given. Waiting time for AMPT group (250 mg/kg) was increased compared to the control group due to the different route of administration, with the expectation that i.p. injections would result in a slower onset of action than i.v. injections. The stimulation group consisted of the continuous high-frequency stimulation (130 Hz, 200 micro-sec, 0.2 mA), while saline (1 ml/kg) and cocaine (2 mg/kg) were given intravenously. Partly created with BioRender.com. *N* = 5/group (20 in total). AMPT, alpha-methyl-p-tyrosine; CFM, carbon fiber microelectrode; DA, dopamine; FSCV, fast-scan cyclic voltammetry; i.p., intraperitoneal; i.v., intravenous; stim., stimulation; M-CSWV, multiple-cyclic square wave voltammetry; MFB, medial forebrain bundle; NAc, nucleus accumbens; VTA, ventral tegmental area.

levels were recorded using M-CSWV. One-way ANOVA test among the three levels (baseline, saline, cocaine) showed significant differences (F = 17.95, p = 0.0047). In the *post hoc* analysis, as expected, saline administration did not evoke a statistically significant change in peak tonic dopamine concentration compared to pre-saline levels (N = 7 rats; paired t-test, p = 0.054; Figures 2A, B, blue). The dopamine levels were then observed to rapidly increase after acute i.v. cocaine administration [N = 7 rats; paired t-test, p = 0.022; change = +62.9 ± 14.9 nM (59%); time to peak = 6.8 ± 0.8 min; Figures 2A, B, red]. The pseudocolor plots of the peak dopamine concentration after saline administration (Figure 2C) and after cocaine administration (Figure 2D) showed clear differences in the magnitude of the dopamine oxidation current, indicating a much higher concentration present.

In the negative control experiments, AMPT, a tyrosine hydroxylase inhibitor, was applied intraperitoneally (i.p.) to reduce dopamine production. This was compared against i.p. saline. One-way ANOVA test among the three levels showed significant differences (F = 35.45, p = 0.0007). In the *post hoc* analysis, i.p. AMPT administration (250 mg/kg) did acutely reduce tonic NAcc dopamine concentrations over 30 min [N = 5; paired t-test, p = 0.004; change = −34.5 ± 5.7 nM (−27%); time to stable baseline = 25.3 ± 2.2 min; Figures 3A, B, red] but this was not observed in i.p. saline (N = 5; paired t-test, p = 0.513; Figures 3A, B, blue). This is further visualized by the pseudocolor plots, demonstrating a sharp decrease in dopamine oxidation current after 30 min of AMPT (Figure 3D), compared to after 30 min of saline (Figure 3C).

3.2. NAcc HFS reduces tonic NAcc dopamine levels and attenuates the effects of cocaine

Here, saline and cocaine administration was repeated on the background of NAcc stimulation (starting at least 30 min before saline administration and continued until 30 min after cocaine administration). With one-way ANOVA test, there were significant differences among the six different levels (control, trough during stimulation, new baseline during stimulation, level-post-saline, level-post-cocaine, post-stimulation) (F = 11.31, p = 0.010). With further *post hoc* analysis, NAcc HFS elicited an initial decrease in tonic dopamine concentration [N = 5; paired t-test, p = 0.011; change = −28.3 ± 6.3 nM (−20%); Figures 4A, C], followed by a relatively rapid return to baseline. Pseudocolor plots demonstrate a significant marked decrease in dopamine oxidation current during NAcc HFS (Figure 4E) compared to pre-stimulation baseline (Figure 4D).

Next, i.v. saline was administered (1 ml/kg) with continuous HFS, and, as before, did not significantly affect NAcc tonic dopamine concentrations over 30 min (N = 5; paired t-test, p = 0.131; Figures 4B, F). Thereafter, surprisingly, with continuous HFS of the NAcc, the cocaine-induced increases in tonic dopamine concentrations seen before were eliminated when i.v. cocaine was given, no longer leading to an increase compared to pre-cocaine levels (N = 5; paired t-test, p = 0.739; Figures 4B, F).

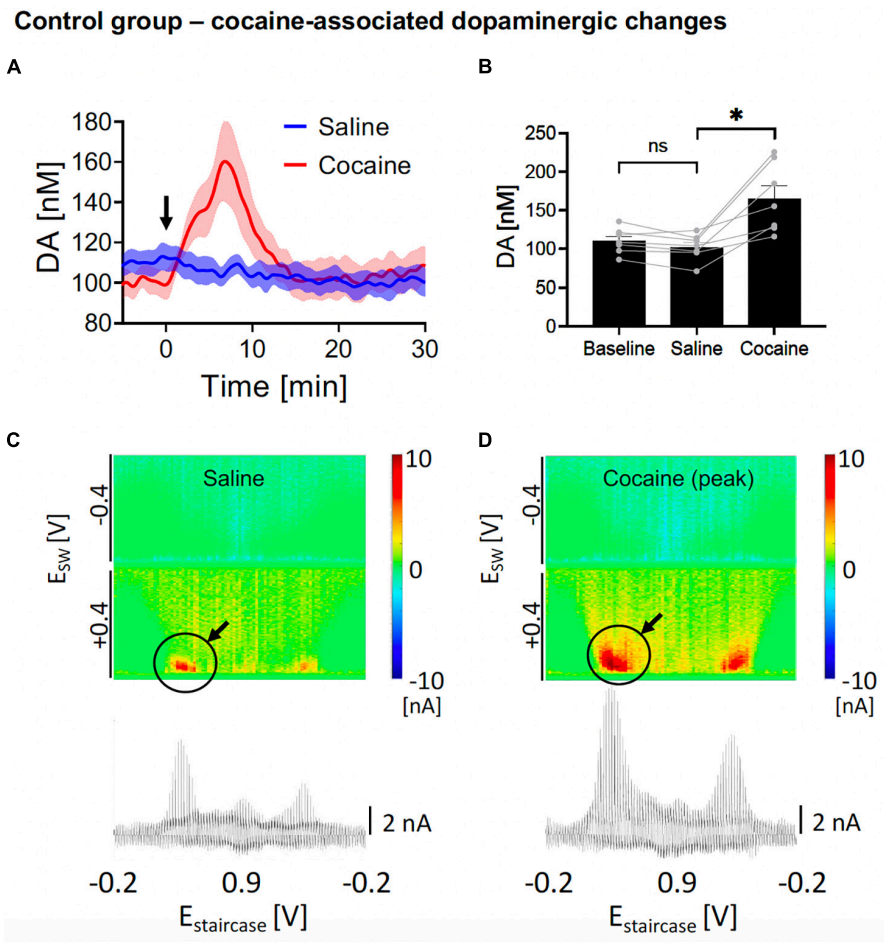

FIGURE 2
Changes in nucleus accumbens core (NAcc) tonic dopamine concentrations after saline and cocaine. **(A)** Rapid increase in dopamine was seen after i.v. cocaine administration (2 mg/kg) compared to i.v. saline (1 ml/kg). Arrow denotes time of drug administration. **(B)** Saline did not significantly alter tonic dopamine levels (−8.0 ± 3.4 nM, N = 7 rats, p = 0.054), whereas cocaine rapidly increased dopamine levels (+62.9 ± 14.9 nM, +62%, N = 7 rats, p = 0.006). Two out of seven of the sample had a stimulating electrode (turned off) adjacent to the recording electrode; both showed brisk increase in tonic dopamine levels with cocaine administration. *Denotes $p < 0.025$ (0.05/2, with Bonferroni correction, given there are two t-tests here). **(C,D)** Representative color plots and voltammograms after saline and cocaine administration, respectively.

3.3. VTA HFS reduces tonic NAcc dopamine levels and attenuates the effects of cocaine

Here, saline and cocaine administration was repeated on the background of VTA stimulation (starting at least 30 min before saline administration and continued until 30 min after cocaine administration). With one-way ANOVA test, there were significant differences among the five different levels (control, new baseline during stimulation, level post-saline, level-post-cocaine, post-stimulation) (F = 11.28, p = 0.011). With further *post hoc* analysis, VTA HFS elicited a decrease in tonic dopamine concentration which persisted over the 30 min [N = 5; paired t-test, p = 0.002; change = −47.3 ± 7.0 nM (−42%); Figures 5A, C]. Pseudocolor plots demonstrate a significant decrease in dopamine oxidation current during VTA HFS (Figure 5E) compared to pre-stimulation baseline (Figure 5D).

Next, i.v. saline was administered (1 ml/kg) with continuous HFS, and, as before, did not significantly affect NAcc tonic dopamine concentrations over 30 min (N = 5; paired t-test, p = 0.943; Figures 5B, F). Thereafter, with continuous HFS of the VTA, the cocaine-induced increases in tonic dopamine concentrations seen without stimulation were eliminated, no longer leading to a statistically significant increase compared to pre-cocaine (N = 5; paired t-test, p = 0.091; Figures 5B, F).

3.4. Interpretation

The present study demonstrated that cocaine-induced increases in tonic dopamine levels in the NAcc can be attenuated by HFS of the NAcc or of the VTA. In addition, VTA HFS resulted in a persistent suppression of NAcc tonic dopamine levels.

Interestingly, there was an initial trough in the dopamine levels at the start of NAcc HFS (Figure 4 and Supplementary Figure A3), followed by a return to baseline. Previous *ex vivo* voltammetry studies have shown that both electrical and optogenetic brief stimulation of dopaminergic terminals in the NAc can lead to local phasic release of dopamine (Melchior et al., 2015). Importantly, these studies have also shown that longer duration stimulations lead to lower magnitude stimulation-induced phasic release. Phasic dopamine

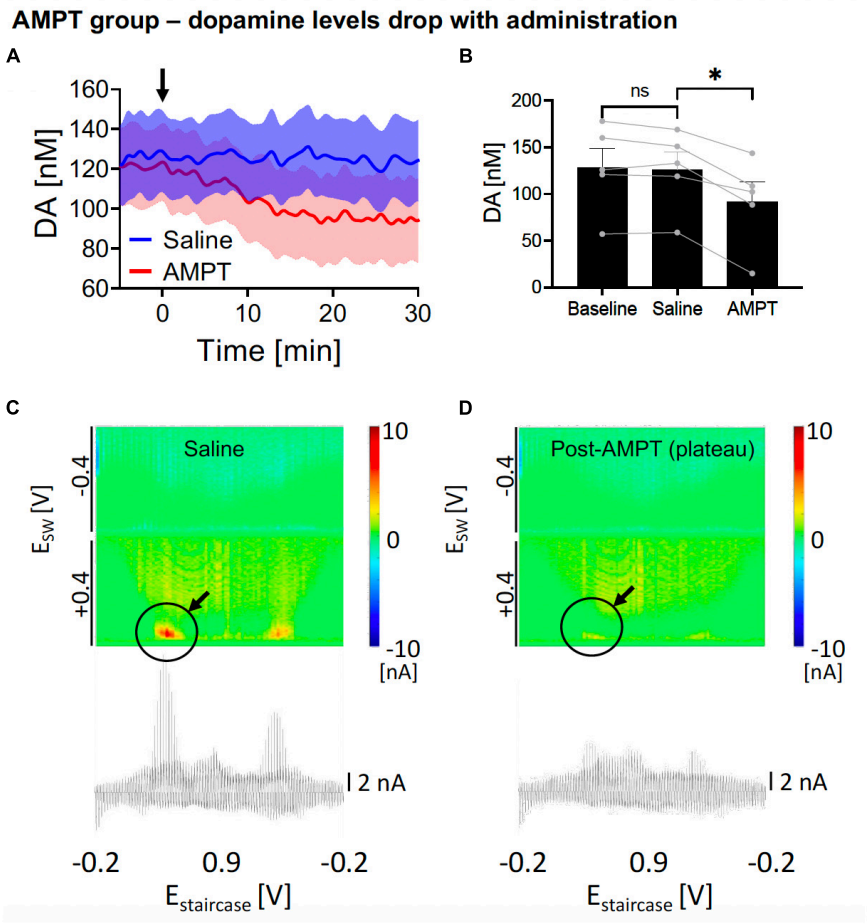

FIGURE 3
Changes in nucleus accumbens core (NAcc) tonic dopamine concentrations after saline and alpha-methyl-p-tyrosine (AMPT). **(A)** Gradual reduction in dopamine tonic levels was seen after i.p. AMPT administration (250 mg/kg) compared to i.v. saline (1 ml/kg). Arrow denotes time of drug administration. **(B)** Saline did not significantly alter tonic dopamine levels (−2.2 ± 3.1 nM, N = 5 rats, p = 0.513), whereas AMPT reduced dopamine levels (−34.5 ± 5.7 nM, −27%, N = 5 rats; p = 0.004). *Denotes $p < 0.025$ (0.05/2, with Bonferroni correction, given there are two t-tests here). **(C,D)** Representative color plots and voltammograms, after saline and AMPT administration, respectively.

release is measured on the order of seconds, whereas in the current study, the time resolution of M-CSWV was every 10 s. Therefore, it is possible that there may have been an initial phasic release of dopamine which was not detected by M-CSWV. This increase in dopamine may have then led to the activation of D2 autoreceptors in the VTA and NAcc, which reduced both the release of dopamine and excitability of dopamine neurons (Wieczorek and Kruk, 1995; Ford, 2014). Together with a depletion of presynaptic dopamine vesicular stores, this may have contributed to a decrease in the tonic levels of dopamine in the NAcc. One possibility is that as the D2 autoreceptor feedback became weaker, the tonic dopamine levels stabilized to an equilibrium. However, previous studies have shown the activation time of D2 autoreceptors is of the order of subseconds to seconds (Kennedy et al., 1992; Benoit-Marand et al., 2001); whereas in the present study, the troughs took ∼10 min to reach full reduction, implying there are likely other factors at play. Another possibility is back propagation of signals from NAc to VTA but this is yet to be confirmed.

Norepinephrine is a potential electroactive interferent that could affect dopamine measurements given their similarities in reduction-oxidation characteristics. However, previous microdialysis studies show that the NAcc, which we targeted, has a relatively low concentration of norepinephrine (McKittrick and Abercrombie, 2007).

Inhibition and activation of other local neurons (e.g., glutamatergic and GABAergic) are also possible, but it is difficult to ascertain how this may interact with the dopaminergic neurons in this case. A recent voltammetry study has shown that electrical stimulation leads to multi-synaptic modulation of dopamine release, as a gamma-aminobutyric acid (GABA) antagonist increased electrical stimulation-evoked release of dopamine, compared to optogenetic stimulation, which only targeted dopaminergic terminals (Melchior et al., 2015). In contrast, microdialysis studies have shown conflicting results. In naïve rodents, HFS of the NAc did not affect dopamine and glutamate levels but increased GABA levels (Varatharajan et al., 2015). Another study which specifically stimulated the NAcc also showed no changes in dopamine levels (Van Dijk et al., 2011). However, in rats treated with morphine, NAcc HFS reduced glutamate levels (Yan et al., 2013). In a depressed rat model, there were no changes in GABA or dopamine with NAc shell stimulation (Schumacher et al., 2020). Although microdialysis can measure multiple neurochemicals, most of these studies sampled at 30-min intervals, which would not capture the trough observed here.

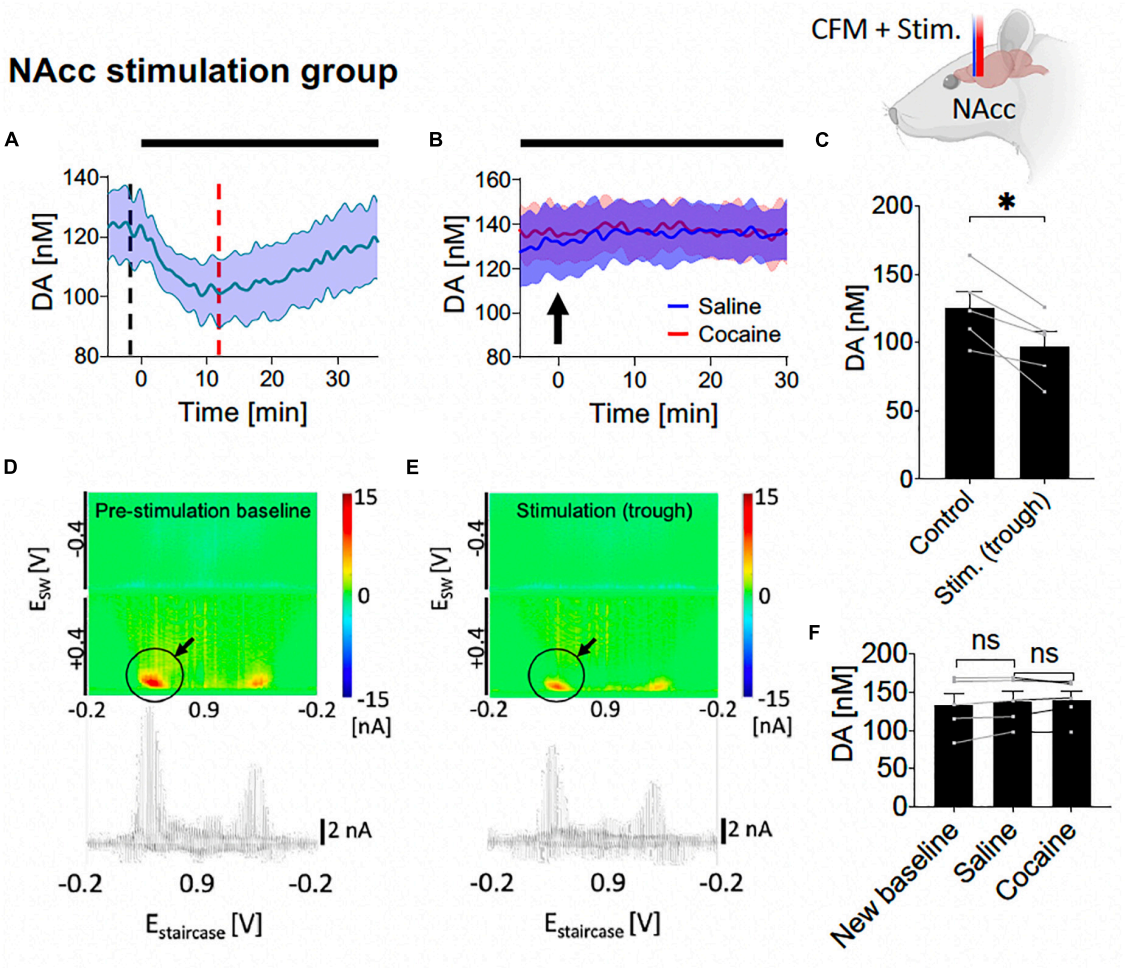

FIGURE 4
Tonic dopamine concentrations during nucleus accumbens core (NAcc) high frequency stimulation (HFS) and after cocaine administration. **(A,C)** Stimulation suppressed tonic dopamine levels (−28.3 ± 6.3 nM, −20%; N = 5 rats, p = 0.011). **(B,F)** Cocaine-induced increases in tonic dopamine levels were attenuated by stimulation to non-significant levels (new baseline vs. saline, −4.9 ± 2.6 nM, N = 5 rats, p = 0.131; saline vs. cocaine peak, 1.3 ± 3.5 nM, p = 0.739). Black bars represent stimulation period. Arrow denotes drug administration. *Denotes $p < 0.017$ (0.05/3, with Bonferroni correction, given there are three t-tests here); ns, non-statistically significant. **(D,E)** Representative color plots and voltammograms, corresponding to the time points marked by black and red dotted lines in panel **(A)**, respectively. Further trend in tonic dopamine levels after local HFS was stopped demonstrated no marked changes in levels (**Supplementary Figure A2**).

Both the NAcc (Liu et al., 2008; Knapp et al., 2009; Guo et al., 2013; Schippers et al., 2017) and shell (Knapp et al., 2009; Henderson et al., 2010; Ma et al., 2013; Batra et al., 2017) have been shown to be promising DBS targets for SUD for substances such as morphine, alcohol, heroin, and methamphetamine. The underlying treatment mechanism has not been fully understood. The present results suggest that one possibility is that accumbal dopamine extracellular levels are modulated by the local HFS, leading to suppression of the reward effect associated with cocaine-induced elevations in tonic dopamine levels (Schultz, 2016). Given its role as a monoamine reuptake inhibitor, cocaine normally increases dopaminergic concentration in the synapses (Sora et al., 2001). It is possible that local DBS may either alter cocaine activity at the local dopamine reuptake transporters and/or dopamine reserve, or it may reduce the ability of cocaine molecules to diffuse to these transporters due to factors such as vasoconstriction or tissue damage. Two out of seven of our control group were performed with a stimulating electrode adjacent to the recording electrode and both showed a brisk increase in tonic dopamine levels after cocaine administration, which makes tissue damage an unlikely explanation. The possibility that DBS can modify dopamine transporter (DAT) availability has been raised previously in Parkinson's disease patients (Lokkegaard et al., 2007; Loser et al., 2021).

Other possibilities may include down regulation of active dopaminergic transporters. The diminished response is consistent with a preclinical study where DBS of the NAc (shell) increased cocaine self-administration (Kallupi et al., 2021). This may be because the cocaine-associated effect is less marked with DBS and hence the animals would need to self-administer more to attain the same elevations in tonic dopamine levels. However, more experiments are required to confirm this hypothesis.

In contrast to NAc HFS, VTA HFS led to a decrease in NAcc dopamine levels that did not recover over the course of the experiment (**Figures 5A, D** and **Supplementary Figure A4**). There are at least two possible explanations for this phenomenon. First, continuous VTA HFS may have depleted presynaptic dopamine vesicular stores in the NAcc, which may have accounted for the initial peak observed immediately upon stimulation. In turn, this would lead

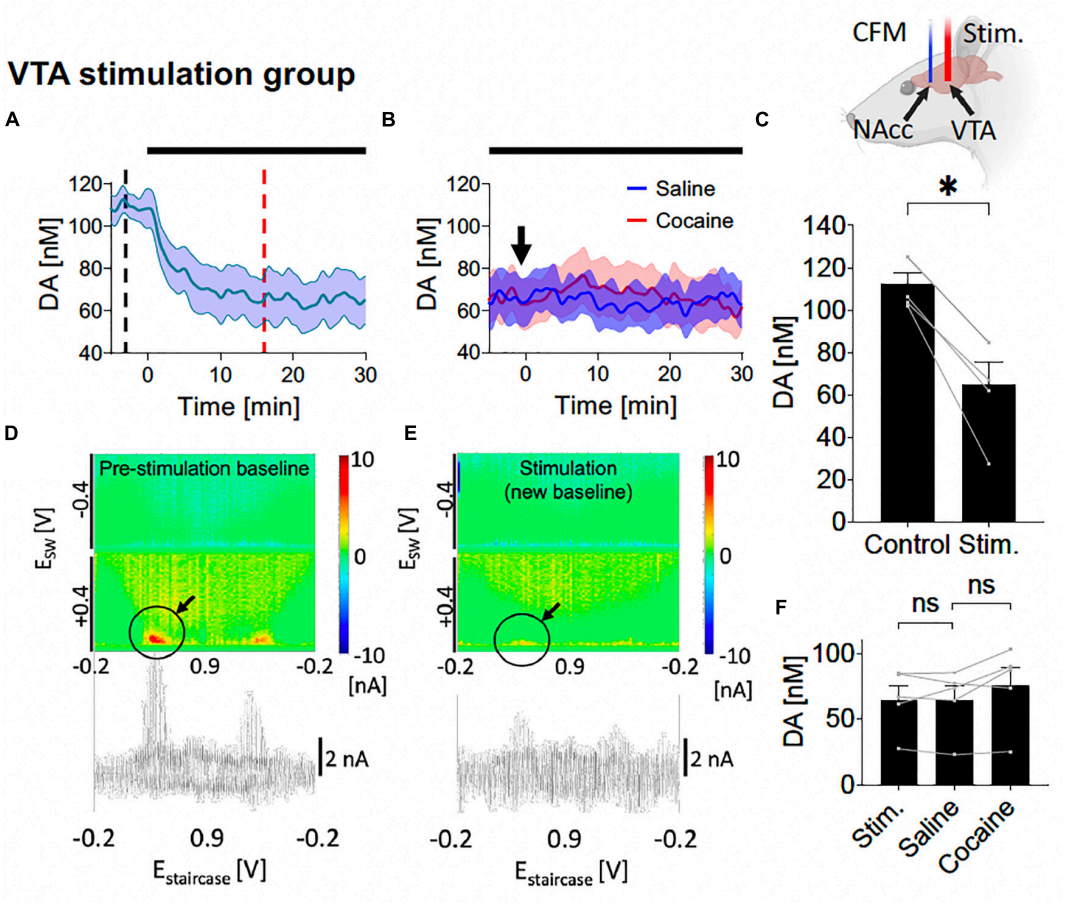

FIGURE 5
Tonic dopamine concentrations during ventral tegmental area (VTA) high frequency stimulation (HFS) and after cocaine administration. **(A,C)** Stimulation suppressed tonic dopamine levels (−47.3 ± 7.0 nM, −42%; p = 0.002). **(B,F)** Cocaine-induced increases in tonic dopamine levels were attenuated by stimulation to non-significant levels compared to the new baseline (+11.2 ± 5.0 nM, +17%; p = 0.091). Black bars represent stimulation period. Arrow denotes drug administration. *Denotes $p < 0.017$ (0.05/3, with Bonferroni correction, given there are three t-tests here); ns, non-statistically significant. **(D,E)** Representative color plots and voltammograms, corresponding to the time points marked by black and red dotted lines in panel **(A)**, respectively. Further trend in tonic dopamine levels after local HFS was stopped demonstrated no continued suppression in levels (**Supplementary Figure A5**). Representative color plot and voltammogram of new baseline after i.v. cocaine administration (2 mg/kg) during VTA stimulation is shown in **Supplementary Figure A6**.

to a reduced tonic level until vesicular stores could be replenished by dopamine synthesis. This is consistent with a previous study showing medial forebrain bundle (MFB) stimulation could reduce the dopamine level in the NAc to 70–80% of baseline during 2 h of stimulation (Bregman et al., 2015). Amperometry studies also showed that prolonged MFB stimulation can deplete presynaptic dopamine vesicular stores in the NAc (Fielding et al., 2013). As the mesolimbic dopaminergic pathway is contained within the MFB, it is likely that MFB stimulation would involve stimulating the VTA-NAc pathway. Second, dendritic release of dopamine in the VTA has been shown to activate autoinhibitory D2 receptors (De Jong et al., 2015), resulting in reduced terminal release of dopamine in the NAc. However, this effect is expected to be short-lived, as continuous VTA HFS would also be expected to deplete dopamine dendritic stores. One other speculative cause is that VTA HFS induced a depolarization block of dopaminergic axonal firing, which appeared sustained after stimulation was discontinued. Given the tonic dopamine levels did not recover, this suggests dopaminergic dynamics may be different between the VTA and NAc, possibly from different neurochemical and autoreceptor distribution and sensitivity.

Microdialysis studies have shown that extracellular dopamine release in the NAc is regulated by GABA (inhibitory), dopamine (inhibitory), glutamate (excitatory), and acetylcholine (facilitatory) receptors in the VTA (Westerink et al., 1996; Lester et al., 2010). It is possible that the electrical stimulation could lead to overfiring of GABA neurons within the VTA as well as suppression of glutamate neurons. Further pharmacological tests may potentially facilitate confirmation of this hypothesis.

Functional magnetic resonance imaging (fMRI) in rodent and in swine models have shown that electrical stimulation of the VTA not only induced dopamine release in the NAc (phasic release as detected by FSCV) but also led to increased blood-oxygen-level-dependent (BOLD) responses (Helbing et al., 2016; Settell et al., 2017). However, the latter appeared to be glutamate-dependent (Helbing et al., 2016). This suggests that the clinical effects of VTA DBS is likely to be much more complex and involves multiple other neurotransmitter systems besides dopamine.

In addition to SUD, NAc DBS has been of great interest for application to a number of neuropsychiatric diseases, such as depression (Yuen et al., 2021b), Tourette's syndrome

(Baldermann et al., 2016), and obsessive-compulsive disorder (Denys et al., 2010). It is unknown how DBS of the NAc and its surrounding structures, such as the anterior limb of internal capsule, may treat a range of diseases with such different clinical features. Nevertheless, studies have shown that dopamine plays a role in all these diseases. Thus, DBS may possibly modulate or even re-establish the dysregulated dopaminergic signaling, leading to symptomatic improvements and reversing neuroplasticity related changes (Denys et al., 2004; Buse et al., 2013; Tye et al., 2013).

Although the VTA is vital in the expression of a number of drug-related behaviors, such as behavioral sensitization (Oliva and Wanat, 2016), VTA DBS currently has a limited role in clinical practice. However, in a small case series, high-frequency VTA DBS appeared to be an effective treatment for medically refractory cluster headache (Akram et al., 2016). Given there is evidence that dopamine levels are elevated in circulating platelets of cluster headache (and migraine) patients (D'Andrea et al., 2006), it has been suggested that cluster headache may be a consequence of overactivity of the dopaminergic and autonomic systems (D'Andrea et al., 2019). Evidence of dysfunction of dopaminergic systems is further elucidated in a study where apomorphine, a non-selective dopamine D2 receptor agonist, was given to cluster headache patients that resulted in significantly lower evoked growth hormone release compared to healthy volunteers (Lepper et al., 2013).

Optogenetic studies have provided insight into the possible behavioral effects of VTA stimulation. One rodent study demonstrated continuous ("tonic") optogenetic stimulation of VTA dopaminergic neurons can reduce ethanol self-administration (Bass et al., 2013). In addition, other studies showed that optogenetic excitation and inhibition of VTA dopaminergic neurons can both inhibit and induce depression-like behavior, respectively (Tye et al., 2013). Although optogenetic and electrical stimulations have different underlying mechanisms of activation, one mouse study demonstrated they activate similar brain regions under certain conditions (Weidner et al., 2020).

Given the reduction in tonic dopamine levels and attenuation of the cocaine-induced response, VTA DBS may be helpful in not only treating SUD but also pathologies associated with hyperdopaminergic states such as mania, schizophrenia, and dopamine dysregulation syndrome, where excessive dopamine in the system may lead to excessive risk-taking behavior (Berk et al., 2007; Grace, 2016; Ashok et al., 2017). In addition, dopamine-containing cells in the VTA that comprise the mesolimbic dopaminergic projection are highly critical for the regulation of incentive motivation to natural and drug-related rewards (Blaha and Phillips, 1996; Schultz et al., 1997; Horvitz, 2000). In addition, by modifying the tonic level of dopamine here, it may be possible to replicate changes induced by different pharmacological agents and use it as a pathological model for other diseases such as depression. Likewise, given dopamine is also associated with non-drug reward, excessive depression of dopamine levels in a normal dopaminergic state may theoretically lead to anhedonia, anorexia, and/or depression. Therefore, one must be careful with implementing this form of intervention at the level of dopaminergic cells.

It should be noted the current study utilized anesthetized naïve rodent models with acute administration of cocaine. Larger animals and chronic addiction models will be necessary to verify the dopamine-attenuating effect of HFS. It would be useful to know the effects of HFS on models of SUD of other substances, especially those that are not psychostimulants, such as opioids, and alcohol. Also, the effect on behaviors associated with SUD, such as craving and withdrawal, needs to be explored. Further mechanistic studies such as manipulation of dopamine transporter availability and other biochemical essays are also warranted.

Previous literature also suggested there are persistent exposure of drugs does not necessarily lead to addictive behavior and dopamine is likely to be only one contributing factor to the behavioral changes observed. Therefore, one must consider the impact of other biological processes, such as changes in synaptic plasticity and other neurochemicals (e.g., serotonin) (Pascoli et al., 2011; Li et al., 2021; Yuen et al., 2022a).

4. Conclusion

In summary, this study elucidated the tonic dopaminergic dynamics with NAc and VTA HFS with high spatiotemporal resolution. HFS appeared to have an alleviating effect on the elevations in tonic dopamine levels associated with cocaine administration. This may explain how NAc DBS was found to be therapeutic in both preclinical models and patients suffering from SUD. Dopamine, measured by M-CSWV, may provide a useful closed-loop biomarker for DBS, given the pivotal role of dopamine in many neuropsychiatric pathologies.

Data availability statement

The raw data supporting the conclusions of this article will be made available by the authors, without undue reservation.

Ethics statement

This animal study was reviewed and approved by the Mayo Clinic IACUC.

Author contributions

KL, YO, and JY conceptualized the study. JY conducted experiments, collected the data, and drafted the first manuscript. AR manufactured the 3D-printed electrode holder. JY, YO, and HS designed the analyses. JY and HS conducted the analyses. KL, HS, and YO supervised all aspects of the work. JY and YO drafted the figures. All authors critically reviewed and revised the manuscript and accepted the final version of the manuscript.

Funding

This research was supported by the National Institutes of Health, NIH R01NS112176, R42NS125895, NS129549, and 1F30MH131254 awards. Training grant funding for AR was supported by the NIH F31NS115202-01A1, NIH R25GM055252-23, NIH TL1TR002380-03, and NIH T32GM065841-17. MB was supported by a NHMRC Senior Principal Research Fellowship (1156072).

Conflict of interest

The authors and Mayo Clinic have a Financial Conflict of Interest in technology used in the research and that the authors and Mayo Clinic may stand to gain financially from the successful outcome of the research.

Publisher's note

All claims expressed in this article are solely those of the authors and do not necessarily represent those of their affiliated organizations, or those of the publisher, the editors and the reviewers. Any product that may be evaluated in this article, or claim that may be made by its manufacturer, is not guaranteed or endorsed by the publisher.

Supplementary material

The Supplementary Material for this article can be found online at: https://www.frontiersin.org/articles/10.3389/fnins.2023.1061578/full#supplementary-material

References

Akram, H., Miller, S., Lagrata, S., Hyam, J., Jahanshahi, M., Hariz, M., et al. (2016). Ventral tegmental area deep brain stimulation for refractory chronic cluster headache. *Neurology* 86, 1676–1682.

Ashok, A. H., Marques, T. R., Jauhar, S., Nour, M. M., Goodwin, G. M., Young, A. H., et al. (2017). The dopamine hypothesis of bipolar affective disorder: The state of the art and implications for treatment. *Mol. Psychiatry* 22, 666–679. doi: 10.1038/mp.2017.16

Baldermann, J. C., Schuller, T., Huys, D., Becker, I., Timmermann, L., Jessen, F., et al. (2016). Deep brain stimulation for tourette-syndrome: A systematic review and meta-analysis. *Brain Stimul.* 9, 296–304.

Bass, C. E., Grinevich, V. P., Gioia, D., Day-Brown, J. D., Bonin, K. D., Stuber, G. D., et al. (2013). Optogenetic stimulation of VTA dopamine neurons reveals that tonic but not phasic patterns of dopamine transmission reduce ethanol self-administration. *Front. Behav. Neurosci.* 7:173. doi: 10.3389/fnbeh.2013.00173

Batra, V., Tran, T. L. N., Caputo, J., Guerin, G. F., Goeders, N. E., and Wilden, J. (2017). Intermittent bilateral deep brain stimulation of the nucleus accumbens shell reduces intravenous methamphetamine intake and seeking in Wistar rats. *J. Neurosurg.* 126, 1339–1350. doi: 10.3171/2016.4.JNS152524

Benoit-Marand, M., Borrelli, E., and Gonon, F. (2001). Inhibition of dopamine release via presynaptic D2 receptors: Time course and functional characteristics in vivo. *J. Neurosci.* 21, 9134–9141. doi: 10.1523/JNEUROSCI.21-23-09134.2001

Berk, M., Dodd, S., Kauer-Sant'anna, M., Malhi, G. S., Bourin, M., Kapczinski, F., et al. (2007). Dopamine dysregulation syndrome: Implications for a dopamine hypothesis of bipolar disorder. *Acta Psychiatr. Scand. Suppl.* 434, 41–49. doi: 10.1111/j.1600-0447.2007.01058.x

Bjorklund, A., and Dunnett, S. B. (2007). Dopamine neuron systems in the brain: An update. *Trends Neurosci.* 30, 194–202. doi: 10.1016/j.tins.2007.03.006

Blaha, C. D., Coury, A., and Phillips, A. G. (1996). Does monoamine oxidase inhibition by pargyline increase extracellular dopamine concentrations in the striatum? *Neuroscience* 75, 543–550.

Blaha, C. D., and Phillips, A. G. (1996). A critical assessment of electrochemical procedures applied to the measurement of dopamine and its metabolites during drug-induced and species-typical behaviours. *Behav. Pharmacol.* 7, 675–708.

Borland, L. M., Shi, G., Yang, H., and Michael, A. C. (2005). Voltammetric study of extracellular dopamine near microdialysis probes acutely implanted in the striatum of the anesthetized rat. *J. Neurosci. Methods* 146, 149–158. doi: 10.1016/j.jneumeth.2005.02.002

Brandon, T. H., Vidrine, J. I., and Litvin, E. B. (2007). Relapse and relapse prevention. *Annu. Rev. Clin. Psychol.* 3, 257–284.

Bregman, T., Reznikov, R., Diwan, M., Raymond, R., Butson, C. R., Nobrega, J. N., et al. (2015). Antidepressant-like effects of medial forebrain bundle deep brain stimulation in rats are not associated with accumbens dopamine release. *Brain Stimul.* 8, 708–713. doi: 10.1016/j.brs.2015.02.007

Bungay, P. M., Newton-Vinson, P., Isele, W., Garris, P. A., and Justice, J. B. (2003). Microdialysis of dopamine interpreted with quantitative model incorporating probe implantation trauma. *J. Neurochem.* 86, 932–946. doi: 10.1046/j.1471-4159.2003.01904.x

Buse, J., Schoenefeld, K., Munchau, A., and Roessner, V. (2013). Neuromodulation in Tourette syndrome: Dopamine and beyond. *Neurosci. Biobehav. Rev.* 37, 1069–1084.

Chang, S. Y., Kimble, C. J., Kim, I., Paek, S. B., Kressin, K. R., Boesche, J. B., et al. (2013). Development of the mayo investigational neuromodulation control system: Toward a closed-loop electrochemical feedback system for deep brain stimulation. *J. Neurosurg.* 119, 1556–1565. doi: 10.3171/2013.8.JNS122142

Chefer, V. I., Thompson, A. C., Zapata, A., and Shippenberg, T. S. (2009). Overview of brain microdialysis. *Curr. Protoc. Neurosci.* Chapter 7:Unit7.1.

Chen, L., Li, N., Ge, S., Lozano, A. M., Lee, D. J., Yang, C., et al. (2019). Long-term results after deep brain stimulation of nucleus accumbens and the anterior limb of the internal capsule for preventing heroin relapse: An open-label pilot study. *Brain Stimul.* 12, 175–183. doi: 10.1016/j.brs.2018.09.006

Clark, J. J., Sandberg, S. G., Wanat, M. J., Gan, J. O., Horne, E. A., Hart, A. S., et al. (2010). Chronic microsensors for longitudinal, subsecond dopamine detection in behaving animals. *Nat. Methods* 7, 126–129. doi: 10.1038/nmeth.1412

D'Andrea, G., Granella, F., Perini, F., Farruggio, A., Leone, M., and Bussone, G. (2006). Platelet levels of dopamine are increased in migraine and cluster headache. *Headache* 46, 585–591. doi: 10.1111/j.1526-4610.2006.00407.x

D'Andrea, G., Gucciardi, A., Perini, F., and Leon, A. (2019). Pathogenesis of cluster headache: From episodic to chronic form, the role of neurotransmitters and neuromodulators. *Headache* 59, 1665–1670. doi: 10.1111/head.13673

De Jong, J. W., Roelofs, T. J., Mol, F. M., Hillen, A. E., Meijboom, K. E., Luijendijk, M. C., et al. (2015). Reducing ventral tegmental dopamine D2 receptor expression selectively boosts incentive motivation. *Neuropsychopharmacology* 40, 2085–2095. doi: 10.1038/npp.2015.60

Denys, D., Mantione, M., Figee, M., Van Den Munckhof, P., Koerselman, F., Westenberg, H., et al. (2010). Deep brain stimulation of the nucleus accumbens for treatment-refractory obsessive-compulsive disorder. *Arch. Gen. Psychiatry* 67, 1061–1068. doi: 10.1001/archgenpsychiatry.2010.122

Denys, D., Zohar, J., and Westenberg, H. G. (2004). The role of dopamine in obsessive-compulsive disorder: Preclinical and clinical evidence. *J. Clin. Psychiatry* 65(Suppl. 14), 11–17. doi: 10.4088/JCP.v65n0106

Di Chiara, G. (2002). Nucleus accumbens shell and core dopamine: Differential role in behavior and addiction. *Behav. Brain Res.* 137, 75–114. doi: 10.1016/S0166-4328(02)00286-3

Di Chiara, G., Carboni, E., Morelli, M., Cozzolino, A., Tanda, G. L., Pinna, A., et al. (1993). Stimulation of dopamine transmission in the dorsal caudate nucleus by pargyline as demonstrated by dopamine and acetylcholine microdialysis and Fos immunohistochemistry. *Neuroscience* 55, 451–456. doi: 10.1016/0306-4522(93)90514-g

Fielding, J. R., Rogers, T. D., Meyer, A. E., Miller, M. M., Nelms, J. L., Mittleman, G., et al. (2013). Stimulation-evoked dopamine release in the nucleus accumbens following cocaine administration in rats perinatally exposed to polychlorinated biphenyls. *Toxicol. Sci.* 136, 144–153. doi: 10.1093/toxsci/kft171

Ford, C. P. (2014). The role of D2-autoreceptors in regulating dopamine neuron activity and transmission. *Neuroscience* 282, 13–22. doi: 10.1016/j.neuroscience.2014.01.025

Grace, A. A. (2016). Dysregulation of the dopamine system in the pathophysiology of schizophrenia and depression. *Nat. Rev. Neurosci.* 17, 524–532. doi: 10.1038/nrn.2016.57

Gu, H., Varner, E. L., Groskreutz, S. R., Michael, A. C., and Weber, S. G. (2015). In vivo monitoring of dopamine by microdialysis with 1 min temporal resolution using online capillary liquid chromatography with electrochemical detection. *Anal. Chem.* 87, 6088–6094. doi: 10.1021/acs.analchem.5b00633

Guo, L., Zhou, H., Wang, R., Xu, J., Zhou, W., Zhang, F., et al. (2013). DBS of nucleus accumbens on heroin seeking behaviors in self-administering rats. *Drug Alcohol. Depend.* 129, 70–81. doi: 10.1016/j.drugalcdep.2012.09.012

Hamilton, J., Lee, J., and Canales, J. J. (2015). Chronic unilateral stimulation of the nucleus accumbens at high or low frequencies attenuates relapse to cocaine seeking in an animal model. *Brain Stimul.* 8, 57–63. doi: 10.1016/j.brs.2014.09.018

Helbing, C., Brocka, M., Scherf, T., Lippert, M. T., and Angenstein, F. (2016). The role of the mesolimbic dopamine system in the formation of blood-oxygen-level dependent responses in the medial prefrontal/anterior cingulate cortex during high-frequency stimulation of the rat perforant pathway. *J. Cereb. Blood Flow Metab.* 36, 2177–2193. doi: 10.1177/0271678X15615535

Henderson, M. B., Green, A. I., Bradford, P. S., Chau, D. T., Roberts, D. W., and Leiter, J. C. (2010). Deep brain stimulation of the nucleus accumbens reduces alcohol intake in alcohol-preferring rats. *Neurosurg. Focus* 29:E12. doi: 10.3171/2010.4.FOCUS10105

Holtzheimer, P. E., and Mayberg, H. S. (2011). Deep brain stimulation for psychiatric disorders. *Annu. Rev. Neurosci.* 34, 289–307. doi: 10.1146/annurev-neuro-061010-113638

Horvitz, J. C. (2000). Mesolimbocortical and nigrostriatal dopamine responses to salient non-reward events. *Neuroscience* 96, 651–656. doi: 10.1016/S0306-4522(00)00019-1

Kallupi, M., Kononoff, J., Melas, P. A., Qvist, J. S., De Guglielmo, G., Kandel, E. R., et al. (2021). Deep brain stimulation of the nucleus accumbens shell attenuates cocaine withdrawal but increases cocaine self-administration, cocaine-induced locomotor activity, and GluR1/GluA1 in the central nucleus of the amygdala in male cocaine-dependent rats. *Brain Stimul.* 15, 13–22. doi: 10.1016/j.brs.2021.11.003

Kennedy, R. T., Jones, S. R., and Wightman, R. M. (1992). Dynamic observation of dopamine autoreceptor effects in rat striatal slices. *J. Neurochem.* 59, 449–455. doi: 10.1111/j.1471-4159.1992.tb09391.x

Knapp, C. M., Tozier, L., Pak, A., Ciraulo, D. A., and Kornetsky, C. (2009). Deep brain stimulation of the nucleus accumbens reduces ethanol consumption in rats. *Pharmacol. Biochem. Behav.* 92, 474–479. doi: 10.1016/j.pbb.2009.01.017

Lee, K. H., Lujan, J. L., Trevathan, J. K., Ross, E. K., Bartoletta, J. J., Park, H. O., et al. (2017). WINCS Harmoni: Closed-loop dynamic neurochemical control of therapeutic interventions. *Sci. Rep.* 7:46675. doi: 10.1038/srep46675

Lepper, A., Frese, A., Summ, O., Nofer, J. R., and Evers, S. (2013). Hypothalamic dopaminergic stimulation in cluster headache. *Cephalalgia* 33, 1155–1159. doi: 10.1177/0333102413487445

Lester, D. B., Rogers, T. D., and Blaha, C. D. (2010). Acetylcholine-dopamine interactions in the pathophysiology and treatment of CNS disorders. *CNS Neurosci. Ther.* 16, 137–162. doi: 10.1111/j.1755-5949.2010.00142.x

Li, Y., Simmler, L. D., Van Zessen, R., Flakowski, J., Wan, J. X., Deng, F., et al. (2021). Synaptic mechanism underlying serotonin modulation of transition to cocaine addiction. *Science* 373, 1252–1256. doi: 10.1126/science.abi9086

Liu, H.-Y., Jin, J., Tang, J.-S., Sun, W.-X., Jia, H., Yang, X.-P., et al. (2008). Chronic deep brain stimulation in the rat nucleus accumbens and its effect on morphine reinforcement. *Addict. Biol.* 13, 40–46. doi: 10.1111/j.1369-1600.2007.00088.x

Lokkegaard, A., Werdelin, L. M., Regeur, L., Karlsborg, M., Jensen, S. R., Brodsgaard, E., et al. (2007). Dopamine transporter imaging and the effects of deep brain stimulation in patients with Parkinson's disease. *Eur. J. Nucl. Med. Mol. Imaging* 34, 508–516.

Loser, J., Luthardt, J., Rullmann, M., Weise, D., Sabri, O., Meixensberger, J., et al. (2021). Striatal dopamine transporter availability and individual clinical course within the 1-year follow-up of deep brain stimulation of the subthalamic nucleus in patients with Parkinson's disease. *J. Neurosurg.* 1–7. doi: 10.3171/2020.8.JNS192740 [Epub ahead of print].

Ma, Y., Chen, N., Wang, H. M., Meng, F. G., and Zhang, J. G. (2013). Inhibition of the reinstatement of morphine-induced place preference in rats by high-frequency stimulation of the bilateral nucleus accumbens. *Chin. Med. J. (Engl.)* 126, 1939–1943.

Maia, T. V., and Conceicao, V. A. (2018). Dopaminergic disturbances in Tourette syndrome: An integrative account. *Biol. Psychiatry* 84, 332–344. doi: 10.1016/j.biopsych.2018.02.1172

McKittrick, C. R., and Abercrombie, E. D. (2007). Catecholamine mapping within nucleus accumbens: Differences in basal and amphetamine-stimulated efflux of norepinephrine and dopamine in shell and core. *J. Neurochem.* 100, 1247–1256. doi: 10.1111/j.1471-4159.2006.04300.x

Melchior, J. R., Ferris, M. J., Stuber, G. D., Riddle, D. R., and Jones, S. R. (2015). Optogenetic versus electrical stimulation of dopamine terminals in the nucleus accumbens reveals local modulation of presynaptic release. *J. Neurochem.* 134, 833–844. doi: 10.1111/jnc.13177

Morelli, M., Carboni, E., Cozzolino, A., Tanda, G. L., Pinna, A., and Di Chiara, G. (1992). Combined microdialysis and Fos immunohistochemistry for the estimation of dopamine neurotransmission in the rat caudate-putamen. *J. Neurochem.* 59, 1158–1160.

Müller, U. J., Sturm, V., Voges, J., Heinze, H. J., Galazky, I., Büntjen, L., et al. (2016). Nucleus accumbens deep brain stimulation for alcohol addiction - safety and clinical long-term results of a pilot trial. *Pharmacopsychiatry* 49, 170–173. doi: 10.1055/s-0042-104507

Oh, Y., Heien, M. L., Park, C., Kang, Y. M., Kim, J., Boschen, S. L., et al. (2018). Tracking tonic dopamine levels in vivo using multiple cyclic square wave voltammetry. *Biosens. Bioelectron.* 121, 174–182. doi: 10.1016/j.bios.2018.08.034

Oh, Y., Park, C., Kim, D. H., Shin, H., Kang, Y. M., Dewaele, M., et al. (2016). Monitoring in vivo changes in tonic extracellular dopamine level by charge-balancing multiple waveform fast-scan cyclic voltammetry. *Anal. Chem.* 88, 10962–10970. doi: 10.1021/acs.analchem.6b02605

Oliva, I., and Wanat, M. J. (2016). Ventral tegmental area afferents and drug-dependent behaviors. *Front. Psychiatry* 7:30. doi: 10.3389/fpsyt.2016.00030

Pascoli, V., Turiault, M., and Lüscher, C. (2011). Reversal of cocaine-evoked synaptic potentiation resets drug-induced adaptive behaviour. *Nature* 481, 71–75. doi: 10.1038/nature10709

Paxinos, G., and Watson, C. (2007). *The rat brain in stereotaxic coordinates*. Amsterdam: Elsevier.

Peacock, A., Leung, J., Larney, S., Colledge, S., Hickman, M., Rehm, J., et al. (2018). Global statistics on alcohol, tobacco and illicit drug use: 2017 status report. *Addiction* 113, 1905–1926. doi: 10.1111/add.14234

Rusheen, A. E., Gee, T. A., Jang, D. P., Blaha, C. D., Bennet, K. E., Lee, K. H., et al. (2020). Evaluation of electrochemical methods for tonic dopamine detection in vivo. *Trends Analyt. Chem.* 132(Suppl. 2):116049. doi: 10.1016/j.trac.2020.116049

Salgado, S., and Kaplitt, M. G. (2015). The nucleus accumbens: A comprehensive review. *Stereotact. Funct. Neurosurg.* 93, 75–93.

Saloner, B., and Karthikeyan, S. (2015). Changes in substance abuse treatment use among individuals with opioid use disorders in the United States, 2004-2013. *JAMA* 314, 1515–1517.

Schippers, M. C., Gaastra, M., Mesman, T., Schetters, D., Van Mourik, Y., Denys, D., et al. (2017). Deep brain stimulation of the nucleus accumbens core but not shell reduces motivational components of heroin taking and seeking in rats. *Brain Neurosci. Adv.* 1:2398212817711083.

Schultz, W. (2016). Dopamine reward prediction error coding. *Dialogues Clin. Neurosci.* 18, 23–32.

Schultz, W., Dayan, P., and Montague, P. R. (1997). A neural substrate of prediction and reward. *Science* 275, 1593–1599.

Schumacher, A., Haegele, M., Spyth, J., and Moser, A. (2020). Electrical high frequency stimulation of the nucleus accumbens shell does not modulate depressive-like behavior in rats. *Behav. Brain Res.* 378:112277.

Settell, M. L., Testini, P., Cho, S., Lee, J. H., Blaha, C. D., Jo, H. J., et al. (2017). Functional circuitry effect of ventral tegmental area deep brain stimulation: Imaging and neurochemical evidence of mesocortical and mesolimbic pathway modulation. *Front. Neurosci.* 11:104. doi: 10.3389/fnins.2017.00104

Sildatke, E., Schuller, T., Huys, D., Grundler, T. O. J., Ullsperger, M., Visser-Vandewalle, V., et al. (2020). Error-related activity in striatal local field potentials and medial frontal cortex: Evidence from patients with severe opioid abuse disorder. *Front. Hum. Neurosci.* 14:627564. doi: 10.3389/fnhum.2020.627564

Sora, I., Hall, F. S., Andrews, A. M., Itokawa, M., Li, X. F., Wei, H. B., et al. (2001). Molecular mechanisms of cocaine reward: Combined dopamine and serotonin transporter knockouts eliminate cocaine place preference. *Proc. Natl. Acad. Sci. U.S.A.* 98, 5300–5305.

Substance Abuse and Mental Health Services Administration [SAMHSA] (2020). *Key substance use and mental health indicators in the United States: Results from the 2019 national survey on drug use and health*. Rockville, MD: Substance Abuse and Mental Health Services Administration.

Tye, K. M., Mirzabekov, J. J., Warden, M. R., Ferenczi, E. A., Tsai, H. C., Finkelstein, J., et al. (2013). Dopamine neurons modulate neural encoding and expression of depression-related behaviour. *Nature* 493, 537–541. doi: 10.1038/nature11740

United States Department of Health and Human Services [USDHHS] (2016). *Facing addiction in America: The surgeon general's report on alcohol, drugs, and health*. Washington, DC: USDHHS.

Van Dijk, A., Mason, O., Klompmakers, A. A., Feenstra, M. G., and Denys, D. (2011). Unilateral deep brain stimulation in the nucleus accumbens core does not affect local monoamine release. *J. Neurosci. Methods* 202, 113–118.

Varatharajan, R., Joseph, K., Neto, S. C., Hofmann, U. G., Moser, A., and Tronnier, V. (2015). Electrical high frequency stimulation modulates GABAergic activity in the nucleus accumbens of freely moving rats. *Neurochem. Int.* 90, 255–260.

Vassoler, F. M., White, S. L., Hopkins, T. J., Guercio, L. A., Espallergues, J., Berton, O., et al. (2013). Deep brain stimulation of the nucleus accumbens shell attenuates cocaine reinstatement through local and antidromic activation. *J. Neurosci.* 33, 14446–14454. doi: 10.1523/JNEUROSCI.4804-12.2013

Vreeland, R. F., Atcherley, C. W., Russell, W. S., Xie, J. Y., Lu, D., Laude, N. D., et al. (2015). Biocompatible PEDOT:Nafion composite electrode coatings for selective detection of neurotransmitters in vivo. *Anal. Chem.* 87, 2600–2607. doi: 10.1021/ac502165f

Watson, C. J., Venton, B. J., and Kennedy, R. T. (2006). In vivo measurements of neurotransmitters by microdialysis sampling. *Anal. Chem.* 78, 1391–1399.

Weidner, T. C., Vincenz, D., Brocka, M., Tegtmeier, J., Oelschlegel, A. M., Ohl, F. W., et al. (2020). Matching stimulation paradigms resolve apparent differences between optogenetic and electrical VTA stimulation. *Brain Stimul.* 13, 363–371. doi: 10.1016/j.brs.2019.11.005

Westerink, B. H., Kwint, H. F., and Devries, J. B. (1996). The pharmacology of mesolimbic dopamine neurons: A dual-probe microdialysis study in the ventral tegmental area and nucleus accumbens of the rat brain. *J. Neurosci.* 16, 2605–2611.

Wieczorek, W., and Kruk, Z. L. (1995). Influences of neuronal uptake and D2 autoreceptors on regulation of extracellular dopamine in the core, shell and rostral pole of the rat nucleus accumbens. *Brain Res.* 699, 171–182. doi: 10.1016/0006-8993(95)00894-v

Yan, N., Chen, N., Zhu, H., Zhang, J., Sim, M., Ma, Y., et al. (2013). High-frequency stimulation of nucleus accumbens changes in dopaminergic reward circuit. *PLoS One* 8:e79318. doi: 10.1371/journal.pone.0079318

Yuen, J., Goyal, A., Rusheen, A. E., Kouzani, A. Z., Berk, M., Kim, J. H., et al. (2021a). Cocaine-induced changes in tonic dopamine concentrations measured using multiple-cyclic square wave voltammetry in vivo. *Front. Pharmacol.* 12:705254. doi: 10.3389/fphar.2021.705254

Yuen, J., Rusheen, A. E., Price, J. B., Barath, A. S., Shin, H., Kouzani, A. Z., et al. (2021b). Biomarkers for deep brain stimulation in animal models of depression. *Neuromodulation.* 25, 161–170. doi: 10.1111/ner.13483

Yuen, J., Kouzani, A. Z., Berk, M., Tye, S. J., Rusheen, A. E., Blaha, C. D., et al. (2022b). Deep brain stimulation for addictive disorders-where are we now? *Neurotherapeutics* 19, 1193–1215. doi: 10.1007/s13311-022-01229-4

Yuen, J., Goyal, A., Rusheen, A. E., Kouzani, A. Z., Berk, M., Kim, J. H., et al. (2022a). Cocaine increases stimulation-evoked serotonin efflux in the nucleus accumbens. *J. Neurophysiol.* 127, 714–724. doi: 10.1152/jn.00420.2021

frontiers | Frontiers in Neuroscience

TYPE Original Research
PUBLISHED 08 February 2023
DOI 10.3389/fnins.2023.1088666

OPEN ACCESS

EDITED BY
Jing Teng,
North China Electric Power University, China

REVIEWED BY
Guoyi Gao,
Shanghai General Hospital, China
Junfeng Feng,
Shanghai Jiao Tong University, China
Lei Wu,
Second Affiliated Hospital of Nanchang University, China

*CORRESPONDENCE
Jian Wang
✉ 1172268798@qq.com
Xin Chen
✉ chenxin1983@csu.edu.cn

†These authors share first authorship

SPECIALTY SECTION
This article was submitted to Translational Neuroscience, a section of the journal Frontiers in Neuroscience

RECEIVED 03 November 2022
ACCEPTED 23 January 2023
PUBLISHED 08 February 2023

CITATION
Zhou L, Chen Y, Liu Z, You J, Chen S, Liu G, Yu Y, Wang J and Chen X (2023) A predictive model for consciousness recovery of comatose patients after acute brain injury. *Front. Neurosci.* 17:1088666. doi: 10.3389/fnins.2023.1088666

A predictive model for consciousness recovery of comatose patients after acute brain injury

Liang Zhou[1,2†], Yuanyi Chen[3†], Ziyuan Liu[1,2], Jia You[1,2], Siming Chen[1,2], Ganzhi Liu[1,2], Yang Yu[4], Jian Wang[1,2*] and Xin Chen[1,2*]

[1]Department of Neurosurgery, Xiangya Hospital of Central South University, Changsha, Hunan, China, [2]National Clinical Research Center for Geriatric Disorders, Xiangya Hospital, Changsha, Hunan, China, [3]Central of Stomatology, Xiangya Hospital of Central South University, Changsha, Hunan, China, [4]College of Intelligence Science and Technology, National University of Defense Technology, Changsha, Hunan, China

Background: Predicting the consciousness recovery for comatose patients with acute brain injury is an important issue. Although some efforts have been made in the study of prognostic assessment methods, it is still unclear which factors can be used to establish model to directly predict the probability of consciousness recovery.

Objectives: We aimed to establish a model using clinical and neuroelectrophysiological indicators to predict consciousness recovery of comatose patients after acute brain injury.

Methods: The clinical data of patients with acute brain injury admitted to the neurosurgical intensive care unit of Xiangya Hospital of Central South University from May 2019 to May 2022, who underwent electroencephalogram (EEG) and auditory mismatch negativity (MMN) examinations within 28 days after coma onset, were collected. The prognosis was assessed by Glasgow Outcome Scale (GOS) at 3 months after coma onset. The least absolute shrinkage and selection operator (LASSO) regression analysis was applied to select the most relevant predictors. We combined Glasgow coma scale (GCS), EEG, and absolute amplitude of MMN at Fz to develop a predictive model using binary logistic regression and then presented by a nomogram. The predictive efficiency of the model was evaluated with AUC and verified by calibration curve. The decision curve analysis (DCA) was used to evaluate the clinical utility of the prediction model.

Results: A total of 116 patients were enrolled for analysis, of which 60 had favorable prognosis (GOS $\geq$ 3). Five predictors, including GCS (OR = 13.400, $P < 0.001$), absolute amplitude of MMN at Fz site (FzMMNA, OR = 1.855, $P = 0.038$), EEG background activity (OR = 4.309, $P = 0.023$), EEG reactivity (OR = 4.154, $P = 0.030$), and sleep spindles (OR = 4.316, $P = 0.031$), were selected in the model by LASSO and binary logistic regression analysis. This model showed favorable predictive power, with an AUC of 0.939 (95% CI: 0.899–0.979), and calibration. The threshold probability of net benefit was between 5% and 92% in the DCA.

Conclusion: This predictive model for consciousness recovery in patients with acute brain injury is based on a nomogram incorporating GCS, EEG background activity, EEG reactivity, sleep spindles, and FzMMNA, which can be conveniently obtained during hospitalization. It provides a basis for care givers to make subsequent medical decisions.

KEYWORDS

acute brain injury, coma, electroencephalogram (EEG), mismatch negativity (MMN), prognosis, prediction model

Introduction

Acute brain injury, such as, severe traumatic brain injury and intracerebral hemorrhage, results in a heavy burden in low- and middle- income countries for its high mortality and disability rates (Injury, 2019; Krishnamurthi et al., 2020). With the advances of medical care, an increasing number of comatose patients survive. The issue of whether these comatose patients can regain consciousness is significant for doctors and families, especially with regard to the follow-up medical decisions. As we all know, the early intervention is critical for the patients with promising prognosis to regain consciousness. Up to now, there are many methods to assess the prognosis of comatose patients after acute brain injury according to the previous studies (Logi et al., 2011; Ballesteros et al., 2018; Claassen et al., 2019; Monteiro et al., 2021; Romagnosi et al., 2022).

The Glasgow Coma Scale (GCS) score, a reflection of the severity of patients' condition is currently the most widely used in clinic for its simplicity (Teasdale and Jennett, 1974). Besides, neuroelectrophysiological examinations, including Electroencephalogram (EEG) and event related potentials (ERPs) get more and more attention in clinical practice (Monteiro et al., 2021; Zhou et al., 2021). Among them, EEG plays an important role for outcome prediction in comatose patients (Synek, 1988; Sandroni et al., 2021). EEG background activity, to a large extent, reflects the functional state of the cerebral cortex and subcortex (Estraneo et al., 2020) and EEG reactivity and sleep spindles can provide the additional information about the sensory conduction pathway and thalamic-cortex circuit (Kang et al., 2015; Wang et al., 2022b).

Auditory mismatch negativity (MMN), one of the event-related potentials (ERPs) components, which can be obtained by subtracting the waveform evoked by standard stimuli from the waveform evoked by deviant stimuli, has been increasingly used in comatose patients or prolonged disorders of consciousness in recent years. The presence of MMN indicates that the patient has the ability to voluntarily distinguish and to induce attention orientation to two stimuli, which called pre-attention processing (Alho, 1995). The appearance of MMN suggests a favorable neurological outcome in patients with low responsiveness (Daltrozzo et al., 2007). In addition, the increase of absolute amplitude of MMN was correlated with recovery of consciousness (Wijnen et al., 2007; Zhou et al., 2021).

However, it is an important but still unclear clinical issue which assessment indicators to choose to achieve the best predictive performance. In this study, we used least absolute shrinkage and selection operator (LASSO) and binary logistic regression analysis methods to establish a prediction model, which made the probability of the consciousness recovery for comatose patients visualized by nomogram. In this way, it can provide a better basis for clinical practice.

Materials and methods

Patients

We retrospectively reviewed the records of patients with severe brain injury who were admitted to the Neurosurgical Intensive Care Unit of Central South University Xiangya Hospital from May 2019 to May 2022. The inclusion criteria were as follows: (1) craniocerebral injury caused by traumatic brain injury and intracerebral hemorrhage and confirmed by computed tomography or magnetic resonance imaging; (2) GCS $\leq$ 8 at the time of electrophysiological assessment; (3) age $\geq$ 18 years old; and (4) EEG and auditory MMN examinations performed within 28 days from coma onset. The exclusion criteria were: (1) pre-existing neurological diseases; (2) known hearing impairment; (3) received sedatives and/or muscle relaxants, except for dexmedetomidine or low dose of midazolam ($\leq$ 0.02 mg/kg/h) (Riker et al., 2009), during the course of EEG and MMN examinations; and (4) incomplete clinical data. The charts of patients enrollment process of this study was in **Figure 1**.

MMN paradigm

We used a classical oddball auditory paradigm to elicit auditory MMN. It comprised two types of pure sound with different frequencies: 800 Hz and 1,500 Hz for the standard and deviant stimuli, respectively. In this paradigm, 700 pure sound stimuli (comprising 90% standard stimuli and 10% deviant stimuli, 80 dB sound pressure level, lasting for 75 ms) with a stimulus onset asynchrony of 800 ms were presented to every patient to elicit the MMN response. The sound stimuli were continuously and pseudorandomly presented, although there were at least three standard stimuli between two consecutive deviants. The sound was delivered through headphones. The whole examination lasted about 11 min. Schematic diagram of MMN paradigm was presented in **Figure 2**.

MMN data acquisition and analysis

Scalp MMN examinations were performed at the patients' besides, while they were free from visible body shaking. Data were

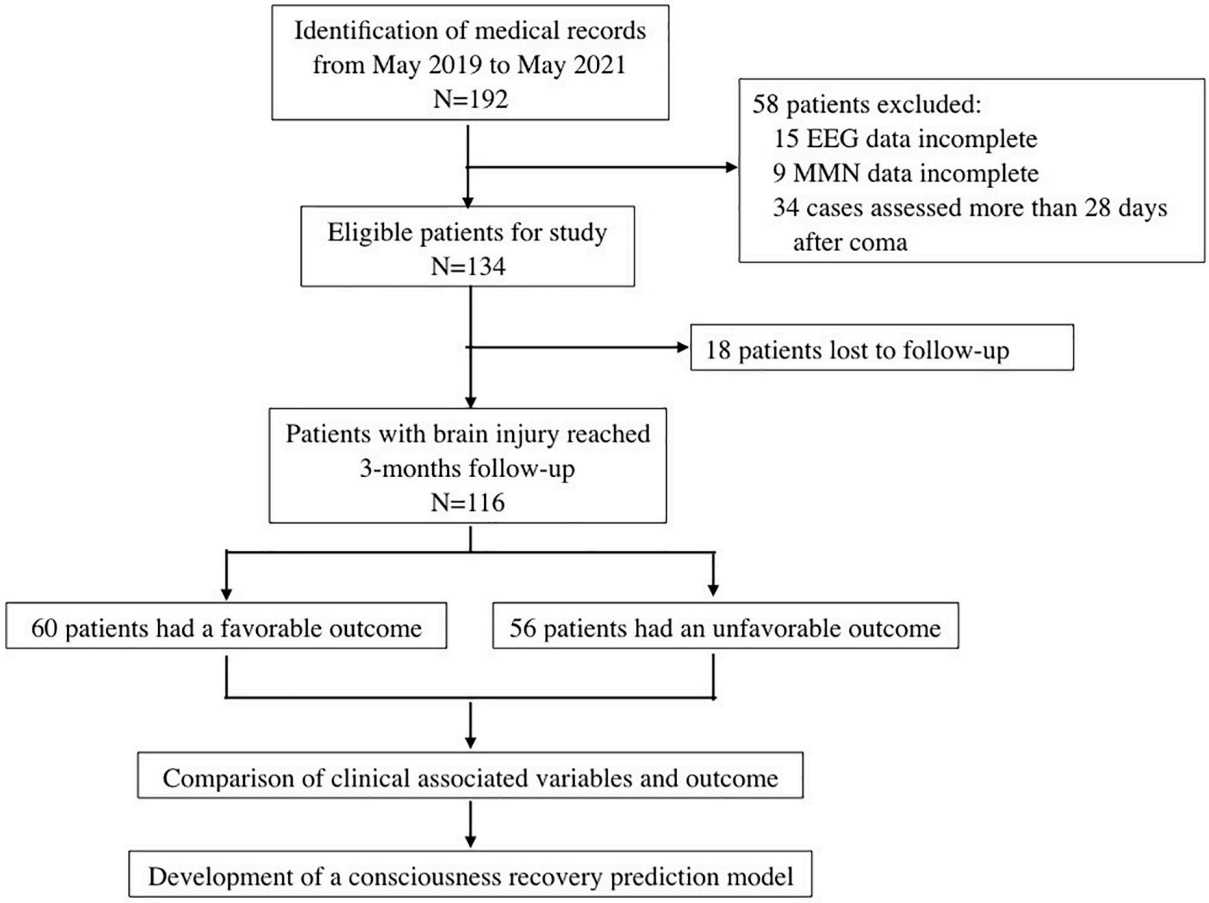

FIGURE 1
Flow chart of this study.

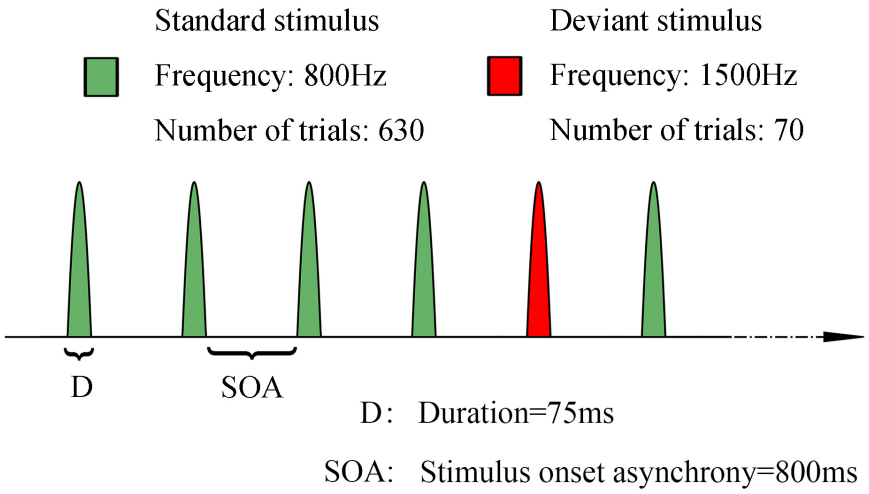

FIGURE 2
Schematic representation of the stimulus paradigm of mismatch negativity. Green: standard stimuli, 800 Hz, 630 trials. Red: deviant stimuli, 1500 Hz, 70 trials. Duration of each sound stimuli is 75 ms. SOA: 800 ms. The sound stimuli were continuously and pseudorandomly presented, although there were at least three standard stimuli between two consecutive deviants.

recorded at four electrodes (F3, F4, Fz, and Cz) according to the 10–20 international system using a Rinjie medical event-related potentiometer (WJ-IA, Guangzhou, China). The impedance of all electrodes was kept below 5 KΩ, and the sampling rate was 1,024 Hz with an online 1–100 Hz bandpass filter. Data were referenced with the mean potential at electrodes A1 and A2.

Raw ERP data with amplitudes exceeding 100 μV were automatically rejected, thus eliminating eye movements and other

artifacts. Subsequently, the standard and deviant responses were averaged by extracting the data of 100 ms before each stimulus onset and 500 ms after the stimulus; the former was primarily used for baseline correction. After that, a 3–30 Hz bandpass filter is applied and the MMN can be obtained by subtracting the waveform evoked by standard stimuli from the waveform evoked by deviant stimuli. Finally, ERP components such as N1 and MMN were presented and calculated by an automatic algorithm.

The criteria for identifying MMN components were: (1) Considering that N1 is one of the representative indicators of the auditory gating system and the information stream among the auditory cortex areas is directed from the core area to the band area and then to the sub-band area. Meanwhile, the core area and band area are the main generators of the standard N1 and deviation N1 components, respectively (Jones, 2002). We considered that MMN was not present only if the standard and deviation N1 were both evoked (Rosburg, 2019); (2) The largest negative waves of averaged difference waveforms in the latency interval between 100 and 300 ms were considered to represent the presence of MMN components (Grimm et al., 2011; Wang et al., 2018); (3) Considering that some of the patients underwent unilateral or bilateral decompressive craniectomy and MMN had maximal amplitude at Fz (Wang et al., 2018), we mainly investigated the absolute amplitude of MMN at the Fz site in this study.

EEG data acquisition and analysis

Continuous digital EEG monitoring (SOLAR electroencephalogram acquisition system, Beijing, China) was routinely performed and lasted for over 24 h in the study, with 16 electrodes (FP1, FP2, F3, F4, C3, C4, P3, P4, 01, 02, F7, F8, T3, T4, T5, and T6) placed according to the 10–20 international system. Video was simultaneously recorded to identify clinical events and artifacts. All EEG data were analyzed by two certified neurophysiologists.

Electroencephalogram background activity was classified into spindle coma, alpha coma, and five other categories as follows (Synek, 1988; Estraneo et al., 2020): (1) normal EEG activity, with a predominant posterior alpha rhythm and anterior-posterior gradient (APG), without focal or hemispheric slowing or epileptiform abnormalities; (2) mildly abnormal (MiA) EEG, characterized by predominant posterior theta activity ($> 20\ \mu V$), symmetric or not, with frequent (10–49% of recording) posterior alpha rhythms; (3) moderately abnormal (MoA) EEG, characterized by predominant posterior theta activity ($> 20\ \mu V$), symmetric or not, poorly organized APG, with rare ($< 1\%$ of recording) or occasional (1–9% of recording) posterior alpha rhythms; (4) diffuse slowing (DS), defined as EEG background activity with predominant diffuse theta or theta/delta rhythms with an amplitude $> 20\ \mu V$, without APG; (5) low voltage (LV) EEG, defined as predominant EEG activity (theta or delta) $< 20\ \mu V$ over most brain regions.

Sleep spindles were defined as 10–15 Hz bursts, lasting 0.5–2 s, that were best seen in the central channel (Rasch and Born, 2013). Sleep spindles that were not clearly detectable were considered as absent.

EEG-R was performed as follows (Admiraal et al., 2018): (1) pain stimulus: the patient's nail bed was pressed using a pen for at least 5 s. There were three repeats at each side with each pressing separated by a 5-min interval. (2) Sound stimulus: loud claps were performed for at least 5 s near the patient's ear on one side. There were three repeats at each side with each clapping separated by a 5-min interval. The presence of EEG-R was defined as stable and repeatable (at least twice) changes in amplitude or frequency in the EEG, which were visible with the naked eye, except for muscle and eye blink artifacts within at least one stimulus type.

The percent of alpha variability (PAV) was determined by visual inspection of three points on the PA histogram: the PA baseline, the PA peak value, and the PA trough value that most directly follows the peak. The PA baseline was deemed to the mean PA occurring during the 4 h prior to a peak in PA. The PAV was calculated using the following formula: (Peak PA–Trough PA)/(Peak PA + Trough PA). Then, the PAV were divided into four levels, which were poor (level 1, $< 2\%$), fair (level 2, 2–10%), good (level 3, 10–15%), and excellent (level 4, $> 15\%$), respectively (Vespa et al., 1997). PAV of two bipolar channels of each patients were calculated using bilateral frontoparietal, which were (F3–P3) and (F4–P4) (Friberg et al., 2013). Besides, the global PAV scores were evaluated as the mean of the two hemispheric PAV values (Hebb et al., 2007).

Prognosis assessment

The prognosis of patients was determined by telephone follow-up 3 months after coma onset. The Glasgow Outcome Scale (GOS) ranging from 1 to 5 (1, dead; 2, vegetative state or minimally conscious state; 3, able to follow commands but unable to live independently; 4, able to live independently but unable to return to work or school; or 5, able to return to work or school) (Jennett et al., 1981), was used to evaluate prognosis. GOS scores 1–2 were defined as unfavorable prognosis (no recovery of consciousness), and GOS scores 3–5 were defined as favorable prognosis (recovery of consciousness).

Predictive variables

The variables including sex, age, etiology, pupillary light reflex, GCS, absolute amplitude of N1 at electrode Fz (FzN1A), absolute amplitude of MMN at electrode Fz (FzMMNA), EEG background activity, sleep spindles, EEG-R, and PAV, which were generally considered to be associated with the prognosis of comatose patients. These 11 factors were preliminary screened, using the least absolute shrinkage and selection operator (LASSO) analysis. LASSO analysis was conducted with R software (version 4.2.1).

Statistical analysis

In this study, continuous and categorical variables were expressed by the mean value ± standard deviation or median (interquartile range, IQR) and the frequency (percentage), respectively.

The binary logistic regression model was used for multivariate analysis of wakefulness in comatose patients. A nomogram for the predictive model was developed based on the results of the binary logistic analysis. The calibration of the nomogram was used for internal validation by the 100 bootstrap resampling procedure. In addition, the predictive efficiency of the nomogram was quantified with area under the curve (AUC) of receiver operating characteristic curve (ROC). Furthermore, the clinical utility of the nomogram was

assessed by the decision curve analysis (DCA). Statistical analysis was conducted with R software (version 4.2.1). For all tests, statistically significance was set at $P < 0.05$.

Results

Patients

A total of 116 patients, including 29 females and 87 males, were enrolled in our study. There were 73 cases of traumatic brain injury and 43 cases of intracerebral hemorrhage. The mean age was 51.8 ± 16.4 years old, and the EEG and MMN recordings took place on average 14 (10.0, 21.3) days after coma onset. The most frequent pattern of predominant EEG activity was diffuse slowing (DS), followed by moderately abnormal (MoA); 4 patients showed a spindle coma pattern and 2 showed an alpha coma pattern. Of 116 patients, 60 had favorable outcomes and 56 had unfavorable outcomes. Additionally, components N1 and MMN were absent in 19 patients. And in our study, there were no patients with normal or alpha coma EEG background activity. Compared with the unfavorable prognosis group, the percentage of the GCS 6–8 scores, presence of EEG-R and sleep spindles, and better EEG background activity in favorable prognosis group were significantly higher. Furthermore, the mean amplitude of FzMMNA in favorable prognosis group was higher than the other group. These baseline characteristics were shown in Table 1.

TABLE 1 Demographic and clinical characteristics of the patients in favorable and unfavorable prognosis groups.

Factors	Favorable prognosis (n = 60)	Unfavorable prognosis (n = 56)
Sex [n (%)]		
Male	49 (56.3)	38 (43.7)
Female	11 (37.9)	18 (62.1)
Etiology [n (%)]		
Traumatic brain injury	37 (50.7)	36 (49.3)
Intracerebral hemorrhage	23 (53.5)	20 (46.5)
Pupillary light reflex* [n (%)]		
Presence	58 (56.3)	45 (43.7)
Absence	2 (15.4)	11 (84.6)
GCS [n (%)]		
3–5	15 (23.8)	48 (76.2)
6–8	45 (84.9)	8 (15.1)
EEG background activity [n (%)]		
Normal/MiA/MoA/Spindle coma	48 (71.6)	19 (28.4)
DS/LV/Alpha coma	12 (24.5)	37 (75.5)
EEG-R [n (%)]		
Presence	32 (78.0)	9 (22.0)
Absence	28 (37.3)	47 (62.7)
Sleep spindles [n (%)]		
Presence	39 (86.7)	6 (13.3)
Absence	21 (29.6)	50 (70.4)
PAV [n (%)]		
Level 1	13 (40.6)	19 (59.4)
Level 2	25 (46.3)	29 (53.7)
Level 3	22 (73.3)	8 (26.7)
Age (years, $\bar{x} \pm s$)	50.4 ± 17.1	53.4 ± 15.6
FzN1A (μV, $\bar{x} \pm s$)	1.4 ± 1.1	0.9 ± 1.1
FzMMNA (μV, $\bar{x} \pm s$)	2.1 ± 1.2	1.2 ± 0.8

*Only if pupillary light reflex disappeared bilaterally was considered as absent. FzN1L, the peak latency of N1 at electrode Fz; FzN1A, the absolute amplitude of N1 at electrode Fz; FzMMNL, the peak latency of MMN at electrode Fz; FzMMNA, the absolute amplitude of MMN at electrode Fz; EEG-R, electroencephalogramactivity; MiA, mildly abnormal; MoA, moderately abnormal; DS, diffuse slowing; LV, low voltage; PAV, percent alpha variability.

Predictors selection

Eleven factors, sex, age, etiology, pupillary light reflex, GCS, FzN1A, FzMMNA, EEG background activity, EEG-R, sleep spindles, and PAV, were extracted from demographic characteristics, clinical features, and EEG and MMN examination related indictors. Of these, 5 factors, GCS, FzMMNA, EEG background activity, EEG-R, and sleep spindles, were selected as potential predictors by LASSO analysis (Figure 3). It should be mentioned that Lasso analysis did not provide p-value in R language. Furthermore, these 5 predictors have been shown to be significantly associated with wakefulness of comatose patients after acute brain injury by binary logistic regression analysis ($P < 0.05$). Additionally, the results were expressed as odd ratio (95% confidence interval) for GCS [13.400 (3.976, 54.478)], FzMMNA (μV) [1.855 (1.085, 3.510)], EEG background activity [4.309 (1.262, 16.251)], EEG-R [4.154 (1.177, 15.965)], and sleep spindles [4.316 (1.169, 17.253)]. The Positive Predictive Value (PPV) and Negative Predictive Value (NPV) of EEG-R were 78.0 and 62.7%, respectively. The results of binary logistic regression was shown in Table 2.

Development of a prediction nomogram

After the binary logistic regression analysis, the independent predictors including GCS, FzMMNA, EEG background activity, EEG-R, and sleep spindles were used for developing a prediction nomogram. Nomogram, like a scoring system, was established based on the odd ratio values. The score of each predictor can be clearly seen in this system. In addition, the sum of scores and corresponding probabilities for the consciousness recovery of each comatose patient after acute brain injury can be effectively estimated and visualized in the nomogram (Figure 4).

Validation of the nomogram

The performance of nomogram was internally validated by using the 100 bootstrap resampling method, in which the model development cohort (original sample) served as the validation set, and each resampled sample cohort served as the training set. The calibration curve (Figure 5) showed a high consistency between the observed and predicted values in the probability of the consciousness recovery of comatose patients after acute brain injury. Besides, the

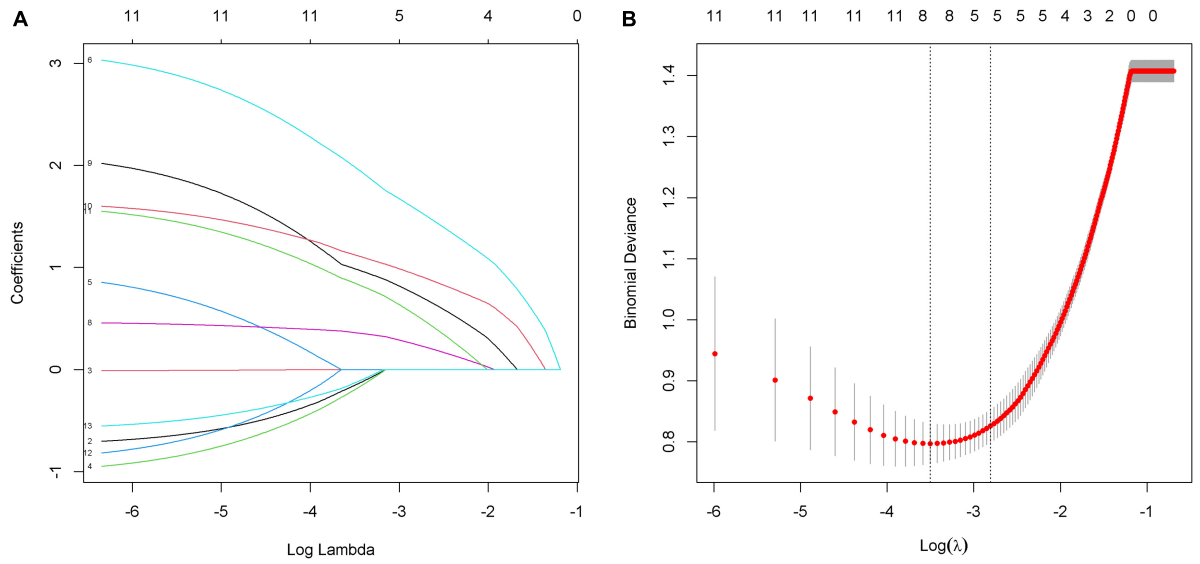

FIGURE 3
Predictors selection by using the least absolute shrinkage and selection operator (LASSO) model. **(A)** LASSO coefficient profiles of 11 alternative factors. Each curve represents a factor. Since PAV is a triadic variable, it was divided into three variables when analyzed in R language software. As a result, there are thirteen curves shown in the figure. **(B)** Tuning parameter (λ) selection in the LASSO model using 10-fold cross-validation *via* minimum criteria. The red dots in the figure indicate the binomial deviance corresponding to each lambda. The two dashed lines represent two special lambda values, min and 1 s, respectively. The 1 s corresponds to the optimal lambda value of a model with excellent performance and the smallest number of independent variables. Finally, combined with figure **(A)**, five factors (GCS, FzMMNA, EEG background activity, EEG-R, and sleep spindles) were selected into the following binary logistic regression analysis.

TABLE 2 Binary logistic regression analysis of the predictors of consciousness recovery in comatose patients.

Predictors	OR (95% CI)	*P*-values
GCS	13.400 (3.976, 54.478)	<0.001
FzMMNA	1.855 (1.085, 3.510)	0.038
EEG background activity	4.309 (1.262, 16.251)	0.023
EEG-R	5.154 (1.177, 15.965)	0.030
Sleep spindles	4.316 (1.169, 17.253)	0.031

OR, odd ratio; CI, confidence interval; FzMMNA, the absolute amplitude of MMN at electrode Fz; EEG-R, electroencephalogram activity.

AUC [0.939 (95% CI: 0.899–0.979)] was obtained for evaluating the accuracy of this predictive model by ROC (Figure 6).

Clinical utility of the nomogram

In the DCA shown in Figure 7, the threshold probability of the nomogram ranged from 5 to 92%, which indicated a wide range of clinical utility. In other words, the nomogram will achieve the net benefit in varying degrees when the threshold probability value of the predictive model is between 0.05 and 0.92. Moreover, the reason for the fluctuation at the end of the prediction model curve is mainly considered as the sample size is not large enough.

Discussion

Multimodal monitoring can be applied in the assessment of consciousness recovery of comatose patients after acute brain injury. Although some efforts have been made in resolving this issue, it is still unclear which factors can be used to establish model to directly predict the probability of patients' consciousness recovery. In fact, the results of the comprehensive assessment will affect doctors' medical decisions determining final outcome of patients to a great extent. In this study, clinical characteristics and parameters derived from electrophysiological examinations, including GCS, FzMMNA and EEG background activity, EEG-R, and sleep spindles have been selected in the predictive model by LASSO and binary logistic regression analysis. By intuitively predicting the consciousness recovery of comatose patients after acute brain injury, this predictive model can identify patients with relatively favorable prognosis at early stages and allows active clinical intervention.

Glasgow coma scale, a clinical behavioral scale, is easy to perform and widely used in the intensive care unit and often included in prognostic models. Our study found that GCS correlated with the outcomes of comatose patients ($P < 0.001$); the findings are in accordance with those in previous studies (Emami et al., 2016; Nik et al., 2018).

Electroencephalogram is the result of recording the spontaneous electrophysiological activity emitted by cortical vertebral cells of the human brain. Three EEG related indicators in the predictive model can be applied to assess the brain injury condition of comatose patients from different layers. The EEG background activity reflects the electrical activity of the patient's brain and it's a clue to how active the brain is. EEG background activity was classified into two categories based on predominant frequency and amplitude (Wang et al., 2022a), and proved to be associated with the prognosis of comatose patients. At baseline, the two prognostic groups differed significantly for predominant EEG background activity, since poor EEG patterns was more frequently observed in patients in unfavorable group, whereas mildly and moderate

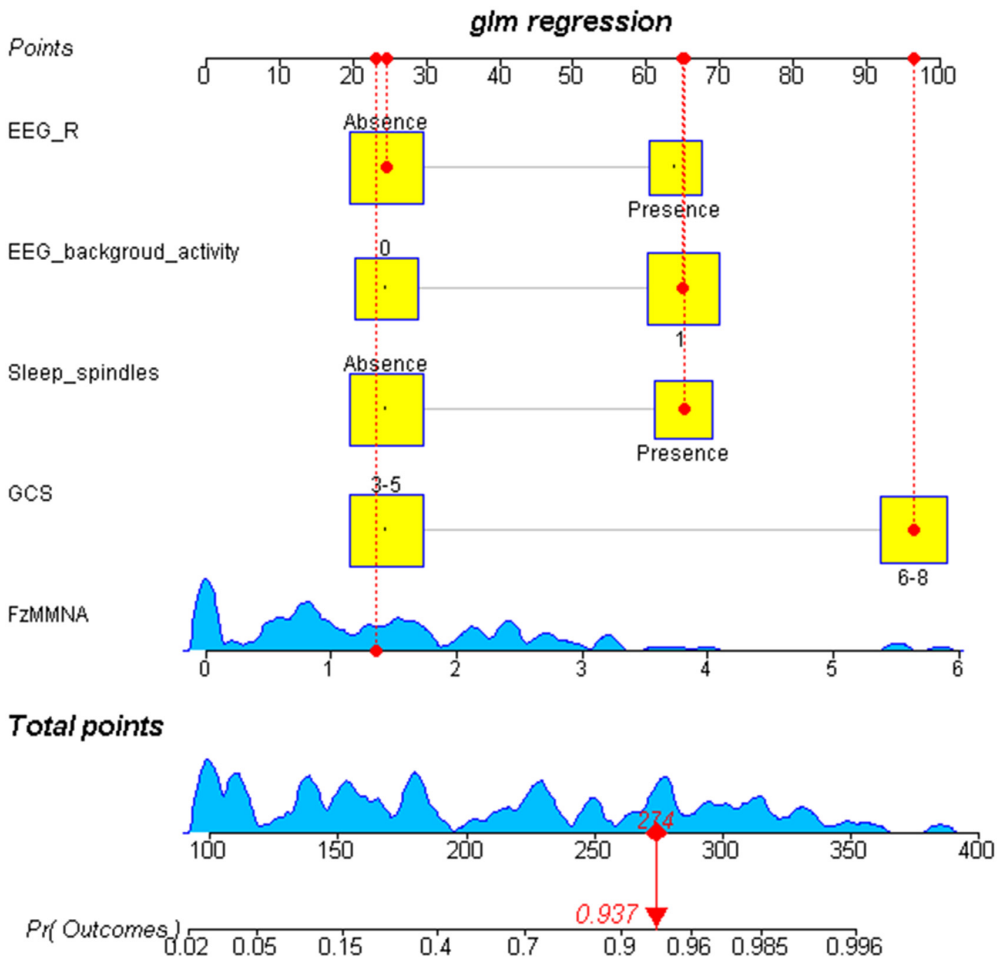

FIGURE 4
Visualization nomogram to predict the consciousness recovery of comatose patients after acute brain injury. The total score of each variable and the corresponding probability of consciousness recovery of comatose patients can be visualized in the nomogram. For example, a case is shown in the nomogram (red). This case represents a comatose patient with GCS scores of 8, the EEG-R is absent, the sleep spindles is present, the EEG background activity at level 3, and the FzMMNA is 1.42 μV. In consideration of these five variables, the total score for this patient was 274, corresponding to a probability of regaining consciousness of 0.937. Number 0 in EEG background activity refers to diffuse slowing (DS), low voltage (LV), and Alpha coma. Number 1 in EEG background activity refers to normal, mildly abnormal (MiA), moderately abnormal (MoA), and spindle coma.

abnormal EEG activities in another group. Besides, two special EEG coma patterns, alpha and spindle coma were also included. When a prominent generalized, often frontally predominant, non-reactive alpha frequency activity constitute the principal EEG features in comatose patients, the patterns are referred to as alpha coma (Nuwer, 2021). And this kind of pattern often imply a poor prognosis, because its appearance suggests either the inputs from the thalamus or the neural filtering networks of the cortex are disturbed, or both are damaged. Spindle coma is an electroclinical entity that has been used to describe an EEG pattern of "sleep-like" activity in comatose patients (Emidio et al., 2019). Although, the spindle coma is usually resulted from a pontomesencephalic junction lesion (Husain, 2006), it is associated with favorable outcome in most situations, according to previous studies (Cologan et al., 2013; Rasch and Born, 2013). For the reason that existence of spindles often indicates the residual function of thalamus and thalamic-cortex circuit. On the contrary, the absence of spindles in comatose patients with acute brain injury results from the interruption of either the ascending reticular thalamocortical pathway or of the thalamocortical loops, which may result in difficulty in regaining consciousness.

EEG-R is defined as the diffuse, transient, and repeatable changes in electroencephalogram activity (amplitude and/or frequency) following environmental stimuli, such as pain or sound (Azabou et al., 2018a). The presence of EEG-R suggests the integrity of the peripheral sensory pathways, brainstem, subcortical structure, and cerebral cortex, and lack of EEG-R may indicate severe dysfunction in any of the aforementioned structures, tampering the cortical activity secondary to external stimuli (Altwegg-Boussac et al., 2017). Our study found that EEG-R was an independent predictive factor for outcome in comatose patients with acute brain injury. In addition, we noticed that EEG-R had a PPV of 78.0% and a relatively low NPV of 62.7%. We propose that this finding might be attributed to the fact that the results were evaluated with the naked eye because the stimulation protocol in EEG-R has not been uniformly standardized. Accordingly, subjectivity cannot be ruled out when assessing the presence of EEG-R. In other words, the absence of EEG-R, as judged by the examiner, does not necessarily reflect the real brain functional status of the patients. Thus, further studies are warranted to better standardize and clarify the EEG-R protocol.

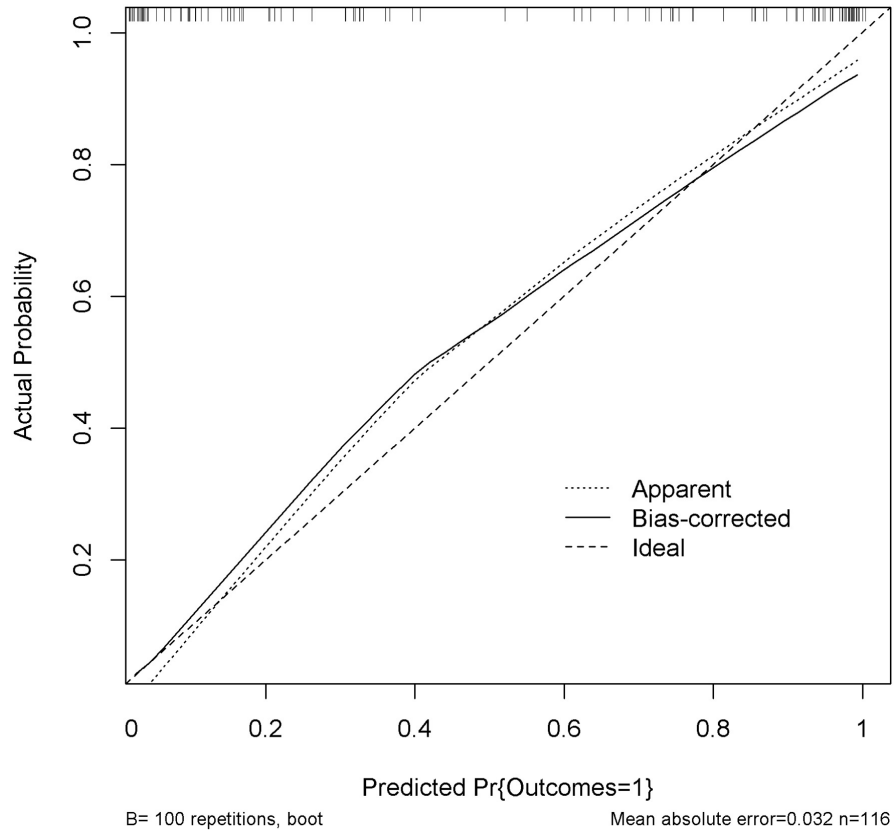

FIGURE 5
Calibration curve of the nomogram. Internal validation was performed using the 100 bootstrap resampling method. The predicted probability and the actual probability are presented by the *X* and *Y* axes, respectively.

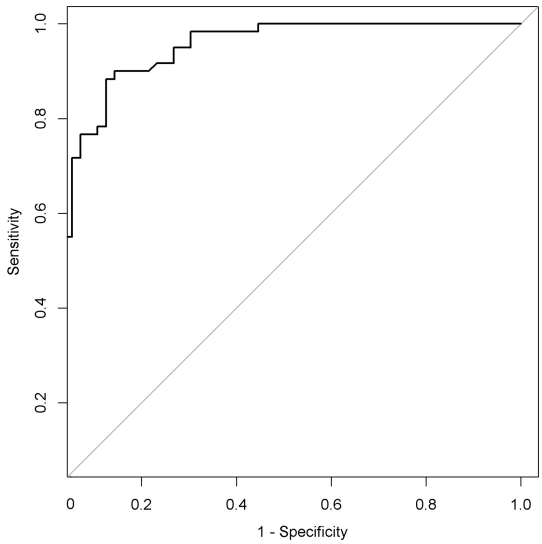

FIGURE 6
Receiver operating characteristic curve (ROC) of the nomogram. The AUC of the nomogram was 0.939 (95% CI: 0.899–0.979). AUC, area under the curve.

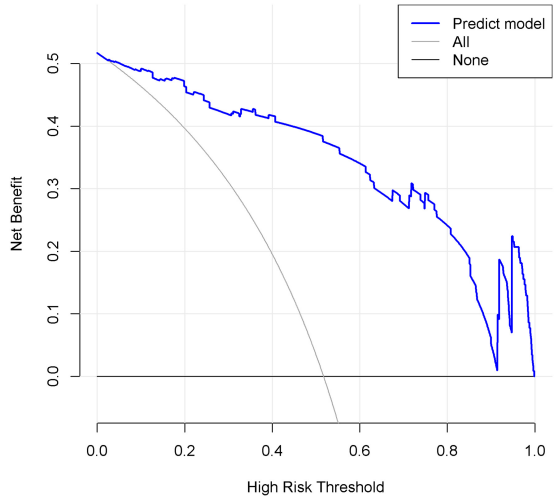

FIGURE 7
Decision curve analysis (DCA) of the nomogram. *X*-axis and *y*-axis represent threshold probability and net benefit, respectively. When the threshold probability value of the predictive model is between 0.05 and 0.92, the patients will obtain the corresponding net benefit.

Mismatch negativity is the maximal negative wave presented after standard and deviant stimuli during the latency of 100–250 ms. In patients with disorders of consciousness, the latency can be up to 300 ms (Wang et al., 2018). MMN indicates the cortical function of differentiation and orientation to different sound stimuli, or so-called pre-attention processing. MMN originates from the auditory cortex in the Heschl's gyri and fronto-central area, and

generally has a maximal amplitude at the Fz site (Pakarinen et al., 2007; Wang et al., 2020). Besides, MMN can also be evoked in patients under sedation (Azabou et al., 2018b), anesthesia (Kenemans and Kahkonen, 2011), sleep (Chennu and Bekinschtein, 2012), and disorders of consciousness (Morlet and Fischer, 2014; Wang et al., 2020). Previous studies have demonstrated a correlation between MMN and favorable outcomes, yet few studies have incorporated the MMN amplitude into quantitative analysis. Subjective factors can easily be mixed into the interpretation of MMN, and it is difficult to apply in clinical practice (Morlet and Fischer, 2014; Schall, 2016). Therefore, we investigated the relationship between FzMMNA and patient's outcomes and found that FzMMNA could be a valuable indicator to predict consciousness recovery of comatose patients. It is worth mentioning that patients who regained consciousness had higher MMN amplitudes than patients who did not. A higher MMN amplitude suggests an increase in alertness levels, which is crucial for detecting changes in the environment and adapting behavior. Indeed, the MMN amplitude is also possibly associated with the binding of the glutamic acid and the N-methyl-D-aspartate receptors, which play an important role in modulating MMN-indexed auditory discrimination (Impey et al., 2016); this may be the reason why MMN amplitude increased in DoC patients who regained consciousness after tDCS treatment (Wang et al., 2020).

In this study, age, coma etiology, pupillary light reflex as well as PAV were not associated significantly with prognosis in our study. This result may be attributed to the selection bias and limited sample size. Certainly, further studies with a larger sample size are needed for verification.

In deed, 5 indicators in our predictive model evaluated the brain function of the comatose patients after acute brain injury from different dimensions and achieved a high accuracy (AUC = 0.939). As long as conditions permit, we should use as many tools as possible to predict the prognosis of patients synthetically in clinical practice.

Limitations

There are three major limitations in our study. Firstly, the sample size of this study was not large enough to support the selection of more factors into the model. As we all know, the prognosis assessment of comatose patients after brain injury requires as many monitoring methods as possible to achieve a more accurate and stable prediction. Secondly, taking into account the medical safety and clinical needs of patients, it was impossible to eliminate prognosis in clinical work without using any sedative drugs when EEG and MMN examinations were performed; thus, we included patients treated with dexmedetomidine, which is commonly used in our ward for sedation. Thirdly, most of the patients in our study underwent neurosurgery, while a small number did not. This difference may affect the outcome of patients. These three limitations may affect the results of this study.

Conclusion

In summary, our study develops a promising prediction model with a wide range of clinical utility for the consciousness recovery of comatose patients after acute brain injury. Besides, considering the spread of clinical practice, it is critical that, as a clinical tool, the predictors in the model can be conveniently obtained at the patients' bedsides, which will provide important reference value for clinicians. Certainly, further prospective multimodal monitoring to predict the consciousness recovery of comatose patients after brain injury study is needed for the establishment of prediction model.

Data availability statement

The raw data supporting the conclusions of this article will be made available by the authors, without undue reservation.

Ethics statement

The studies involving human participants were reviewed and approved by the Medical Ethics Committee of Xiangya Hospital of Central South University ethical approval number (202210230). Written informed consent for participation was not required for this study in accordance with the national legislation and the institutional requirements.

Author contributions

LZ, JW, YC, and XC contributed to the consult literature materials and design the study. LZ and JW acquired the data. LZ, YY, and XC analyze the data. LZ, SC, and GL prepared the tables and figures. LZ, JW, and ZL were major contributors in writing the manuscript. JY, YC, and XC revised the manuscript and made the final version of the manuscript. All authors read and approved the final manuscript.

Funding

This work was supported by grants from the Research and Development Plan of Key Areas of Hunan Province, China (2020SK2070) and the China Foundation for International Medical Exchange for Young and Middle-aged Medical Research Special Fund (Z-2018-35-2004).

Conflict of interest

The authors declare that the research was conducted in the absence of any commercial or financial relationships that could be construed as a potential conflict of interest.

Publisher's note

All claims expressed in this article are solely those of the authors and do not necessarily represent those of their affiliated organizations, or those of the publisher, the editors and the reviewers. Any product that may be evaluated in this article, or claim that may be made by its manufacturer, is not guaranteed or endorsed by the publisher.

References

Admiraal, M. M., van Rootselaar, A. F., and Horn, J. (2018). International consensus on EEG reactivity testing after cardiac arrest: Towards standardization. *Resuscitation* 131, 36–41. doi: 10.1016/j.resuscitation.2018.07.025

Alho, K. (1995). Cerebral generators of mismatch negativity (MMN) and its magnetic counterpart (MMNm) elicited by sound changes. *Ear Hear* 16, 38–51. doi: 10.1097/00003446-199502000-00004

Altwegg-Boussac, T., Schramm, A. E., Ballestero, J., Grosselin, F., Chavez, M., and Lecas, S. (2017). Cortical neurons and networks are dormant but fully responsive during isoelectric brain state. *Brain* 140, 2381–2398. doi: 10.1093/brain/awx175

Azabou, E., Navarro, V., Kubis, N., Gavaret, M., Heming, N., and Cariou, A. (2018a). Value and mechanisms of EEG reactivity in the prognosis of patients with impaired consciousness: A systematic review. *Crit. Care* 22:184. doi: 10.1186/s13054-018-2104-z

Azabou, E., Rohaut, B., Porcher, R., Heming, N., Kandelman, S., and Allary, J. (2018b). Mismatch negativity to predict subsequent awakening in deeply sedated critically ill patients. *Br. J. Anaesth.* 121, 1290–1297. doi: 10.1016/j.bja.2018.06.029

Ballesteros, M. A., Rubio-Lopez, M., San Martín, M., Padilla, A., López-Hoyos, M., Llorca, J., et al. (2018). Serum levels of S100B from jugular bulb as a biomarker of poor prognosis in patients with severe acute brain injury. *J. Neurol. Sci.* 385:109. doi: 10.1016/j.jns.2017.12.017

Chennu, S., and Bekinschtein, T. A. (2012). Arousal modulates auditory attention and awareness: Insights from sleep, sedation, and disorders of consciousness. *Front. Psychol.* 3:65. doi: 10.3389/fpsyg.2012.00065

Claassen, J., Doyle, K., Matory, A., Couch, C., and Rohaut, B. (2019). Detection of Brain Activation in Unresponsive Patients with Acute Brain Injury. *J. N. England J. Med.* 380, 2497–2505.

Cologan, V., Drouot, X., Parapatics, S., Delorme, A., Gruber, G., Moonen, G., et al. (2013). Sleep in the unresponsive wakefulness syndrome and minimally conscious state. *J. Neurotrauma.* 30, 339–346. doi: 10.1089/neu.2012.2654

Daltrozzo, J., Wioland, N., Mutschler, V., and Kotchoubey, B. (2007). Predicting coma and other low responsive patients outcome using event-related brain potentials: A meta-analysis. *Clin. Neurophysiol.* 118, 606–614. doi: 10.1016/j.clinph.2006.11.019

Emami, P., Czorlich, P., Fritzsche, F., Westphal, M., Rueger, J., Lefering, R., et al. (2016). Impact of Glasgow Coma Scale score and pupil parameters on mortality rate and outcome in pediatric and adult severe traumatic brain injury: A retrospective, multicenter cohort study. *J. Neurosurg.* 126, 760–767. doi: 10.3171/2016.1.JNS152385

Emidio, A. C., Faria, R., Patricio, P., Canas, N., Messias, A., and Meneses-Oliveira, C. (2019). Spindle coma in the intensive care unit: Different aetiologies - different outcomes. *Eur. J. Case Rep. Intern. Med.* 6:001316. doi: 10.12890/2019_001316

Estraneo, A., Fiorenza, S., Magliacano, A., Formisano, R., Mattia, D., and Grippo, A. (2020). Multicenter prospective study on predictors of short-term outcome in disorders of consciousness. *Neurology* 95, e1488–e1499. doi: 10.1212/wnl.0000000000010254

Friberg, H., Westhall, E., Rosén, I., Rundgren, M., Nielsen, N., and Cronberg, T. (2013). Clinical review: Continuous and simplified electroencephalography to monitor brain recovery after cardiac arrest. *Crit Care* 17:233. doi: 10.1186/cc12699

Grimm, S., Escera, C., Slabu, L., and Costa-Faidella, J. (2011). Electrophysiological evidence for the hierarchical organization of auditory change detection in the human brain. *Psychophysiology* 48, 377–384. doi: 10.1111/j.1469-8986.2010.01073.x

Hebb, M. O., McArthur, D. L., Alger, J., Etchepare, M., Glenn, T. C., and Bergsneider, M. (2007). Impaired percent alpha variability on continuous electroencephalography is associated with thalamic injury and predicts poor long-term outcome after human traumatic brain injury. *J. Neurotrauma.* 24, 579–590. doi: 10.1089/neu.2006.0146

Husain, A. M. (2006). Electroencephalographic assessment of coma. *J. Clin. Neurophysiol.* 23, 208–220. doi: 10.1097/01.wnp.0000220094.60482.b5

Impey, D., de la Salle, S., Baddeley, A., and Knott, V. (2016). Effects of an NMDA antagonist on the auditory mismatch negativity response to transcranial direct current stimulation. *J. Psychopharmacol.* 31, 614–624. doi: 10.1177/0269881116665336

Injury (2019). Global, regional, and national burden of traumatic brain injury and spinal cord injury, 1990-2016: A systematic analysis for the Global Burden of Disease Study 2016. *Lancet Neurol.* 18, 56–87. doi: 10.1016/s1474-4422(18)30415-0

Jennett, B., Snoek, J., Bond, M. R., and Brooks, N. (1981). Disability after severe head injury: Observations on the use of the Glasgow Outcome Scale. *J. Neurol. Neurosurg. Psychiatry* 44, 285–293. doi: 10.1136/jnnp.44.4.285

Jones, S. J. (2002). The internal auditory clock: What can evoked potentials reveal about the analysis of temporal sound patterns, and abnormal states of consciousness? *Neurophysiol. Clin.* 32, 241–253. doi: 10.1016/s0987-7053(02)00309-x

Kang, X. G., Yang, F., Li, W., Ma, C., Li, L., and Jiang, W. (2015). Predictive value of EEG-awakening for behavioral awakening from coma. *Ann. Intensive. Care* 5:52. doi: 10.1186/s13613-015-0094-4

Kenemans, J. L., and Kahkonen, S. (2011). How human electrophysiology informs psychopharmacology: From bottom-up driven processing to top-down control. *Neuropsychopharmacology* 36, 26–51. doi: 10.1038/npp.2010.157

Krishnamurthi, R. V., Ikeda, T., and Feigin, V. L. (2020). Global, regional and country-specific burden of ischaemic stroke, intracerebral haemorrhage and subarachnoid haemorrhage: A systematic analysis of the global burden of disease study 2017. *Neuroepidemiology* 54, 171–179. doi: 10.1159/000506396

Logi, F., Pasqualetti, P., and Tomaiuolo, F. (2011). Predict recovery of consciousness in post-acute severe brain injury: The role of EEG reactivity. *Brain Inj.* 25, 972–979. doi: 10.3109/02699052.2011.589795

Monteiro, E., Ferreira, A., Mendes, E., Dias, C., Czosnyka, M., Paiva, J., et al. (2021). Brain multimodal monitoring in severe acute brain injury: Is it relevant to patient outcome and mortality? *Acta Neurochir. Suppl.* 131, 83–86.

Morlet, D., and Fischer, C. (2014). MMN and Novelty P3 in coma and other altered states of consciousness: A review. *Brain Topogr.* 27, 467–479. doi: 10.1007/s10548-013-0335-5

Nik, A., Sheikh Andalibi, M. S., Ehsaei, M. R., Zarifian, A., Ghayoor Karimiani, E., and Bahadoorkhan, G. (2018). The efficacy of glasgow coma scale (GCS) score and acute physiology and chronic health evaluation (APACHE) II for predicting hospital mortality of icu patients with acute traumatic brain injury. *Bull. Emerg. Trauma.* 6, 141–145. doi: 10.29252/beat-060208

Nuwer, M. R. (2021). Alpha coma in COVID encephalopathy. *Clin. Neurophysiol.* 132, 202–203. doi: 10.1016/j.clinph.2020.10.005

Pakarinen, S., Takegata, R., Rinne, T., Huotilainen, M., and Näätänen, R. (2007). Measurement of extensive auditory discrimination profiles using the mismatch negativity (MMN) of the auditory event-related potential (ERP). *J. Clinical.* 118, 177–185.

Rasch, B., and Born, J. (2013). About sleep's role in memory. *Physiol. Rev.* 93, 681–766. doi: 10.1152/physrev.00032.2012

Riker, R. R., Shehabi, Y., Bokesch, P. M., Ceraso, D., Wisemandle, W., Koura, F., et al. (2009). Dexmedetomidine vs midazolam for sedation of critically ill patients: A randomized trial. *JAMA* 301, 489–499. doi: 10.1001/jama.2009.56

Romagnosi, F., Bernini, A., Bongiovanni, F., Iaquaniello, C., Miroz, J. P., Citerio, G., et al. (2022). Neurological pupil index for the early prediction of outcome in severe acute brain injury patients. *Brain Sci.* 12:609. doi: 10.3390/brainsci12050609

Rosburg, T. (2019). Filtering and other methodological issues of auditory N100 gating studies. *Clin. Neurophysiol.* 130, 197–198. doi: 10.1016/j.clinph.2018.11.004

Sandroni, C., Cronberg, T., and Sekhon, M. (2021). Brain injury after cardiac arrest: Pathophysiology, treatment, and prognosis. *Intensive Care Med.* 47, 1393–1414. doi: 10.1007/s00134-021-06548-2

Schall, U. (2016). Is it time to move mismatch negativity into the clinic? *Biol. Psychol.* 116, 41–46. doi: 10.1016/j.biopsycho.2015.09.001

Synek, V. M. (1988). Prognostically important EEG coma patterns in diffuse anoxic and traumatic encephalopathies in adults. *J. Clin. Neurophysiol.* 5, 161–174. doi: 10.1097/00004691-198804000-00003

Teasdale, G., and Jennett, B. (1974). Assessment of coma and impaired consciousness. A practical scale. *Lancet* 2, 81–84. doi: 10.1016/s0140-6736(74)91639-0

Vespa, P. M., Nuwer, M. R., Juhász, C., Alexander, M., Nenov, V., Martin, N., et al. (1997). Early detection of vasospasm after acute subarachnoid hemorrhage using continuous EEG ICU monitoring. *Electroencephalogr. Clin. Neurophysiol.* 103, 607–615. doi: 10.1016/s0013-4694(97)00071-0

Wang, J., Huang, L., Ma, X., Zhao, C., Liu, J., and Xu, D. (2022b). Role of quantitative EEG and EEG reactivity in traumatic brain injury. *Clin. EEG Neurosci.* 53, 452–459. doi: 10.1177/1550059420984934

Wang, J., Chen, X., Zhou, L., Liu, Z. Y., Xia, Y. G., and You, J. (2022a). Assessment of electroencephalography and event-related potentials in unresponsive patients with brain injury. *Neurophysiol. Clin.* 52, 384–393. doi: 10.1016/j.neucli.2022.07.007

Wang, X. Y., Guo, Y. K., Zhang, Y. G., and Li, J. J. (2020). Combined Behavioral and mismatch negativity evidence for the effects of long-lasting high-definition tDCS in disorders of consciousness: A pilot study. *Front. Neurosci.* 14:381. doi: 10.3389/fnins.2020.00381

Wang, X., Fu, R., Xia, X., Chen, X., Wu, H., and Landi, N. (2018). Spatial properties of mismatch negativity in patients with disorders of consciousness. *Neurosci. Bull.* 34, 700–708. doi: 10.1007/s12264-018-0260-4

Wijnen, V. J., van Boxtel, G. J., Eilander, H. J., and de Gelder, B. (2007). Mismatch negativity predicts recovery from the vegetative state. *Clin. Neurophysiol.* 118, 597–605. doi: 10.1016/j.clinph.2006.11.020

Zhou, L., Wang, J., Wu, Y., Liu, Z. Y., Yu, Y., Liu, J. F., et al. (2021). Clinical significance of mismatch negativity in predicting the awakening of comatose patients after severe brain injury. *J. Neurophysiol.* 126, 140–147. doi: 10.1152/jn.00658.2020

frontiers | Frontiers in Neuroscience

TYPE Original Research
PUBLISHED 03 March 2023
DOI 10.3389/fnins.2023.1105816

OPEN ACCESS

EDITED BY
Jing Teng,
North China Electric Power University, China

REVIEWED BY
Yuzhe Liu,
Stanford University, United States
Min Zhang,
Changzhou Second People's Hospital Affiliated to Nanjing Medical University, China

*CORRESPONDENCE
Liangfu Zhu
✉ sumslfzhu@163.com

†These authors have contributed equally to this work

SPECIALTY SECTION
This article was submitted to Translational Neuroscience, a section of the journal Frontiers in Neuroscience

RECEIVED 23 November 2022
ACCEPTED 13 February 2023
PUBLISHED 03 March 2023

CITATION
Wu L, Liu Y, Zhu L, Li T, Wang L, Zhang Y, Zhou Z, Xing Y, Wang M and Gao B (2023) MRI arterial spin labeling in evaluating hemorrhagic transformation following endovascular recanalization of subacute ischemic stroke. *Front. Neurosci.* 17:1105816. doi: 10.3389/fnins.2023.1105816

MRI arterial spin labeling in evaluating hemorrhagic transformation following endovascular recanalization of subacute ischemic stroke

Liheng Wu[1†], Yanghui Liu[1†], Liangfu Zhu[1*], Tianxiao Li[1], Li'na Wang[1], Yang Zhang[1], Zhilong Zhou[1], Ying Xing[1], Meiyun Wang[2] and Bulang Gao[1]

[1]Department of Cerebrovascular Diseases, National Advanced Stroke Center, Henan Provincial People's Hospital, People's Hospital of Henan University, Zhengzhou, China, [2]Department of Imaging, Henan Provincial People's Hospital, People's Hospital of Henan University, Zhengzhou, China

Objective: To investigate the value of the MRI arterial spin labeling (ASL) in evaluating the blood-brain barrier permeability of anterior circulation ischemic lesions in subacute ischemic stroke (SIS) and the risk of hemorrhage transformation (HT) after endovascular recanalization.

Materials and methods: Patients with anterior circulation SIS treated with endovascular recanalization were prospectively enrolled. The imaging presentations in the MRI ASL sequences, dynamic contrast-enhanced (DCE) sequence, and Xper CT were studied. The relative cerebral blood flow (rCBF), volume transfer constant (Ktrans), and the weighted Kappa coefficient (rKtrans) were analyzed.

Results: Among 27 eligible patients, HT occurred in 7 patients (25.92%). Patients with HT had significantly higher rCBF value (1.56 ± 0.16 vs. 1.16 ± 0.16), Ktrans, (0.08 ± 0.03 min vs. 0.03 ± 0.01 min) and rKtrans (3.02 ± 0.89 vs. 1.89 ± 0.56). The ASL imaging sequence had a high consistency with the DCE sequence and Xper CT with a high weighted Kappa coefficient of 0.91 for the DCE sequence and 0.70 for the Xper CT imaging. The DCE sequence was also highly consistent with the Xper CT in imaging classification with a high weighted Kappa coefficient of 0.78. The rCBF value in the 21 patients with the subcortical and basal ganglia infarction was significantly lower than that in the other 6 patients with the cortical infarction (1.222 ± 0.221 vs. 1.413 ± 0.259, t = 1.795, P = 0.004).

Conclusion: The MRI ASL sequence has an important role in evaluating the blood-brain barrier permeability and the risk of hemorrhagic transformation of anterior circulation SIS following endovascular recanalization.

KEYWORDS

ischemic stroke, arterial spin labeling, blood-brain barrier permeability, hemorrhagic transformation, arterial recanalization

Introduction

For patients with subacute ischemic stroke caused by symptomatic intracranial atherosclerotic stenosis or occlusion, endovascular recanalization can be safely performed with good effects after strict selection of appropriate indications, especially within two weeks after symptom onset (Topakian et al., 2007). Nonetheless, some patients may still have hemorrhagic transformation after endovascular recanalization (Arba et al., 2021). Hemorrhagic transformation is one of the main complications after endovascular treatment of ischemic stroke and may seriously affect the prognosis of these patients. How to effectively predict the hemorrhagic transformation is of great significance for guiding the endovascular treatment of ischemic stroke.

Destruction of the blood-brain barrier is one of the major pathological mechanisms of hemorrhagic transformation after ischemic stroke. To some extent, detection of the blood-brain barrier permeability can predict occurrence of hemorrhage transformation after endovascular recanalization of occluded arteries. However, because the damage and dynamic repair of the blood-brain barrier are highly individualized, how to accurately detect the permeability of the blood-brain barrier becomes the key. It has been reported that dynamic contrast-enhanced (DCE) sequence magnetic resonance imaging (MRI) can be applied to quantitatively assess the permeability of the blood-brain barrier according to its sequence parameter, the volume transfer constant (Ktrans) across the blood-brain barrier [3–4]. The Ktrans is proportional to the barrier permeability, but evaluation of the blood-brain barrier with the Ktrans requires injection of contrast agents, which may lead to some adverse reactions (Raja et al., 2018; Varatharaj et al., 2019). Arterial spin labeling (ASL) MRI examination only marks the patient's own water proton imaging without contrast agent injection. In the study of acute ischemic stroke, it was found that local measurement of the ASL's sequence parameters relative to the cerebral blood flow (rCBF) could also be used to evaluate the permeability of the blood-brain barrier, and the rCBF value $>$ 1.3 could effectively predict the presence of hemorrhagic transformation after endovascular treatment (Nogueira et al., 2015; Niibo et al., 2017). It was hypothesized that ASL could be used to efficiently evaluate the permeability of blood-brain barrier in patients with cerebral infarction and predict hemorrhagic transformation after endovascular recanalization of stenotic or occluded arteries. This study was thus performed to investigate the value of ASL in assessing the permeability of blood-brain barrier and predicting hemorrhagic transformation after the endovascular treatment in patients with subacute anterior circulation ischemic stroke caused by severe intracranial atherosclerotic stenosis or occlusion. This may provide more technical support for evaluation of the brain tissue status during the perioperative period, facilitate targeted classification and staging treatment of patients, and prevent hemorrhagic transformation.

Materials and methods

Subjects

This prospective one-center study was carried out after approval by the ethics committee of our hospital (2020108), and all patients or their family members had signed the informed consent to participate. Between January 2021 and September 2021, consecutive patients with subacute ischemic stroke of the anterior circulation who received endovascular recanalization were prospectively enrolled. The inclusion criteria were age $\geq$ 18 years, the modified Rankin scale (mRS) score before stroke onset $<$ 3, anterior circulation ischemic stroke confirmed by clinical and imaging examinations and managed with medication for 2–3 weeks after stroke onset, responsible arteries being the middle cerebral artery and the intra- or extracranial segments of the internal carotid artery with the stenosis $\geq$ 70% or complete occlusion, examination of the MRI ASL sequence and DCE sequence 24 h before and immediately after endovascular balloon angioplasty alone or stent angioplasty, and Xper CT being performed immediately after the endovascular treatment. The exclusion criteria were non-intracranial atherosclerotic stenosis caused by Moyamoya disease, Moyamoya syndrome or vasculitis, a previous ischemic lesion $\geq$ 1.5 cm in diameter in the responsible vascular basin of this ischemic stroke lesion, presence of hemorrhagic transformation before endovascular treatment confirmed by imaging examination, suffering from malignant tumors, and complicated with renal insufficiency or allergy to gadolinium contrast agent.

Imaging examination

All the MRI ASL sequence, DCE sequence and Xper CT examinations were completed on the "one-stop multimodal image fusion stroke treatment platform." The platform was composed of a 3.0T MR scanner (MAGNETOM Skyra), a 64 row multi-slice CT scanner (SOMATOM Definition AS), and a dual C-arm DSA system (Artis Q biplane) (Siemens, Germany). In MRI, images were collected with a 8-channel head coil. The repeatition time of axial T1WI fast echo sequence was 4.1 ms, an echo time 120 ms, and a visual field 24 cm $\times$ 24 cm. The DWI sequence had a repetition time 4200 ms, an echo time 100 ms, a b value 1000 s/mm^2, and a field of view 24 cm $\times$ 24 cm. The repeat time of 3D-ASL sequence was 4564 ms, an echo time 10.5 ms, a matrix 128 $\times$ 128, a field of view 24 cm $\times$ 24 cm, layer thickness 3 mm, excitation times 2 times, delay time after labeling 1550 ms, 2550 ms (multi-delay technique), and scanning time 447 s. The repetition time of DCE sequence was 5.3 ms, an echo time 1.9 ms, layer thickness 5 mm, no spacing, a matrix 256 $\times$ 256, a field of view 24 cm $\times$ 24 cm, a reverse angle 15°, time resolution 380/35 s, tracer kinetic model of the Tofts model, and same scanning and positioning parameters as the above sequence. The number of layers was 40, including 35 times of acquisition. After the third image acquisition, the contrast agent (Gdap injection, 20 mL/tube, Guangzhou Kangchen Pharmaceutical Co., Ltd.) was injected through the elbow vein at a rate 4 mL/s and a dose 0.1 mmol/kg, and the scanning time was 380 s with a temporal resolution of 380/35 s.

Imaging post-processing

The imSTROKE software (Nanjing Yuexi Medical Technology Co., Ltd., Nanjing, China) was used for the ASL image *post*-processing. Firstly, ASL, DWI and apparent dispersion coefficient (ADC) data were input before rigid registration of the ASL data with the DWI and ADC data. After the DWI and ADC sequences were classified with the artificial intelligence, the infarct core region was automatically calculated, and the final region of interest (ROI) was obtained through morphological processing. The contralateral healthy region corresponding to the infarcted ROI was selected to obtain the median value of the pixel in the region as the reference value before calculating the rCBF and converting it into pseudo-color display in the ROI. The Siemens Syngo workstation software was used to select the corresponding ROI on the DCE sequence according to the ROI on the ASL sequence before automatically measuring and recording the Ktrans value and rKtrans value (the ratio of the ROI Ktrans value on the infarcted side to that on the healthy side). The rCBF parameters in the MRI ASL sequence and the Ktrans parameters in the DCE sequence were used, respectively, to reflect the permeability of blood-brain barrier and local hyperperfusion state. The Ktrans is a parameter of the MRI DCE sequence and calculated as the mean value in a certain ROI region, and it is a volume transfer constant across the blood-brain barrier (Raja et al., 2018; Varatharaj et al., 2019) and can be applied to quantitatively assess the permeability of the blood-brain barrier because it is proportional to the barrier permeability (Raja et al., 2018; Varatharaj et al., 2019).

Imaging classification of hemorrhagic transformation

On the ASL and DCE sequences, hemorrhagic transformation was presented as areas of high signals (high signals on the ASL sequence represented an increase of local rCBF, and high signals on the DCE sequence represented an increase of contrast agent exudation, which reflected the increase of blood-brain barrier permeability) (Nogueira et al., 2015; Niibo et al., 2017; Raja et al., 2018; Varatharaj et al., 2019). According to the high-signal distribution range of hemorrhagic transformation, the imaging presentations of hemorrhagic transformation were classified as follows: Type I: the high signal areas were distributed in dots or stripes around the edge of the cerebral infarction focus; Type II: The high signal areas in the cerebral infarction focus were distributed in patches, with the volume less than 30% of the cerebral infarction focus; Type III: The high signal areas in the cerebral infarction focus were distributed in sheets, with the volume $\geq$ 30% of the cerebral infarction focus (**Figure 1**). On Xper CT imaging, high-density lesions in low-density background infarction area immediately after endovascular treatment were hemorrhagic transformation. According to the range of high-density lesions shown on the Xper CT imaging immediately after endovascular treatment (Sandoval and Witt, 2008), the imaging classification was as follows: Type I: the contrast agent exuded around the edge of the cerebral infarction, and high-density lesions were distributed in spots or strips; Type II: the contrast agent exuded in the cerebral infarction focus, and high-density lesions were distributed in patches, with the volume less than 30% of the cerebral infarction focus; Type III: the contrast agent exuded in the cerebral infarction focus, and high-density lesions were distributed in sheets, with the volume $\geq$ 30% of the cerebral infarction focus (**Figure 1**). The ASL, DCE and Xper CT imaging classifications were independently assessed by two imaging experts with senior professional titles who were not aware of the diagnosis, treatment and prognosis of the disease. If disagreements arose, consultation to a third senior physician was performed to reach a consensus.

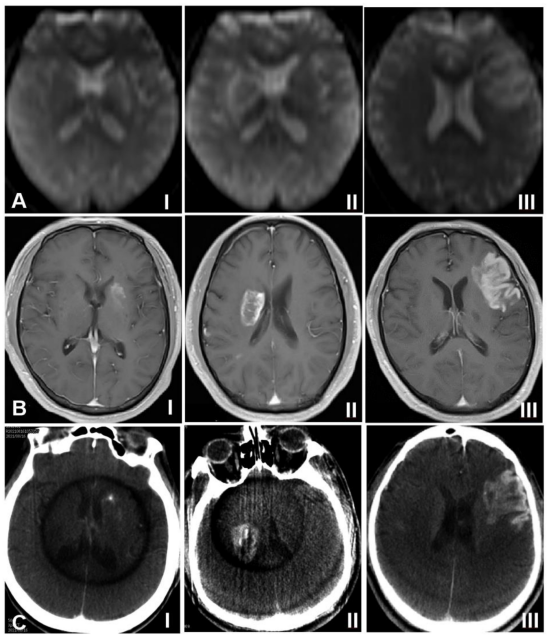

FIGURE 1
Classification of hemorrhagic transformation on arterial spin labeling imaging (ASL), dynamic contrast-enhanced (DCE) sequence of magnetic resonance imaging, and Xper CT. **(A)** ASL sequence imaging, **(B)** DCE sequence imaging, and **(C)** Xpert CT imaging. I indicates type I, II indicates type II, and III indicates type III.

In addition, all patients were reexamined with plain CT scan 24–48 h after endovascular treatment. Presence of high-density lesions on the low-density background layer of cerebral infarction was defined as the occurrence of hemorrhagic transformation, and the Heidelberg classification standard was used for the classification of three entities (von Kummer et al., 2015): HI type 1 (scattered small petechiae with no mass effect), HI type 2 (confluent petechiae with no mass effect), and PH 1 Hematoma within the infarcted tissue occupying < 30% with no substantive mass effect.

Treatment plan

Before endovascular recanalization, all patients were treated with dual antiplatelet therapy. After successful arterial puncture during the endovascular procedure, intravenous bolus loading of unfractionated heparin (70 IU/kg) was administered. During the procedure, 1000 IU of unfractionated heparin was added every hour. Glycoprotein II b/III α receptor antagonists such as tirofiban were not used during the perioperative period.

TABLE 1 Clinical and imaging data in the HT and non-HT groups.

Variables		Total	HT	Non-HT	Z/t/χ 2	*P*
Gender (M/F)		17/10	6/1	11/9	–	0.204
Age [M (Q1, Q3)]		63.5 (63, 67)	63 (50.25, 65)	64 (63, 67.50)	−1.518	0.129
Risk factors (n)	Hypertension	19	4	15	–	0.633
	Diabetes mellitus	9	3	6	–	0.653
	Hyperlipidemia	21	6	15	–	1
	History of stroke	14	4	10	–	1
Responsible arteries (n)	MCA	13	4	9	0.678	0.712
	Intracranial ICA	7	6	1		
	Extracranial ICA	7	5	2		
Cerebral infarction (n)	Cortex	6	2	2	–	0.633
	Subcortical and basal ganglia	21	5	16		
Degree of vascular disease (n)	Severe stenosis	14	2	9	–	0.678
	Occlusion	13	3	8		
Endovascular treatment (n)	Balloon angioplasty	4	0	3	–	1
	Stent angioplasty	23	5	14		
Time from onset to imaging (d)		18.96 ± 1.81 (14–21)	18.29 ± 1.25 (16–20)	19.2 ± 1.94 (14–21)	−2.410	0.26
rCBF (x ± s)		1.26 ± 0.234 (0.8–1.9)	1.56 ± 0.16 (1.4–1.9)	1.16 ± 0.16 (0.8–1.42)	5.943	<0.001
rKtrans (x ± s)		2.18 ± 0.82 (1–4.3)	3.02 ± 0.89 (2.01–4.3)	1.89 ± 0.56 (1–2.86)	3.371	<0.001
Ktrans [/min, M(Q1, Q3)]		0.04 ± 0.02 (0.01–0.16)	0.08 ± 0.03 (0.04–0.16)	0.03 ± 0.01 (0.01–0.06)	5.291	<0.001
ASL (n)	Type I	8	0	8	15.20	0.26
	Type II	11	1	10		
	Type III	8	6	2		
DCE (n)	Type I	9	0	9	12.10	0.21
	Type II	11	2	9		
	Type III	7	5	2		
Xper CT (n)	Type I	12	0	12	13.6	0.24
	Type II	11	4	7		
	Type III	4	3	1		

HT, hemorrhagic transformation; MCA, middle cerebral artery; ICA, internal carotid artery; ASL, arterial spin labeling; DCE, dynamic contrast-enhanced magnetic resonance sequence; rCBF, relative cerebral blood flow; Ktrans, volume transfer constant; rKtrans, relative volume transfer constant.

Statistical analysis

The SPSS 25.0 software (IBM, Chicago, IL, USA) was used for data analysis. Measurement data were expressed as the mean ± standard deviation if in the normal distribution and tested with the *t*-test but as the median (interquartile range) if in the skew distribution and tested with the Mann–Whitney U test. Categorical variables were presented in frequency and percentages and tested with the Chi square test or Fisher's exact probability test. The weighted Kappa coefficients were used to check the consistency among ASL, DCE and Xper CT imaging classifications. The difference was statistically significant if $P < 0.05$.

Results

General information

Twenty-seven patients were enrolled, including 17 males and 10 females, with a mean age of 62.37 ± 7.76 (61–76) years (Table 1). Hypertension was present in 19 cases, diabetes mellitus in 9, hyperlipidemia in 21, and stroke history in 14. The responsible vessels were the middle cerebral artery in 13 cases, the internal carotid artery intracranial segment in 7 cases, and the extracranial segment of the internal carotid artery in 7 cases. The cerebral infarction site was in the cortex in 6 cases and in the subcortical and basal ganglia in 21 cases (Figures 2, 3). Severe arterial stenosis was presented in 14 cases, and occlusion in 13 cases. In endovascular treatment, balloon angioplasty alone was performed in 4 cases, and stent angioplasty in 23 cases.

The time from onset to imaging examination was 18.96 ± 1.81 (14–21) days. On the ASL imaging, type I was in 8 cases, type II in 11, and type III in 8, with an average rCBF of 1.32 (1.120, 1.510). On the DCE imaging, type I was in 9 cases, type II in 11, and type III in 7. The Ktrans was 0.04 ± 0.02 (0.01–0.16), and the rKtrans was 2.18 ± 0.82 (1–4.3). On the Xper CT imaging, type I was in 12 cases, type II in 11, and type III in 4.

Clinical and imaging presentations

Among 27 patients, 7 (25.92%) patients had hemorrhagic transformation after endovascular recanalization, all of whom were

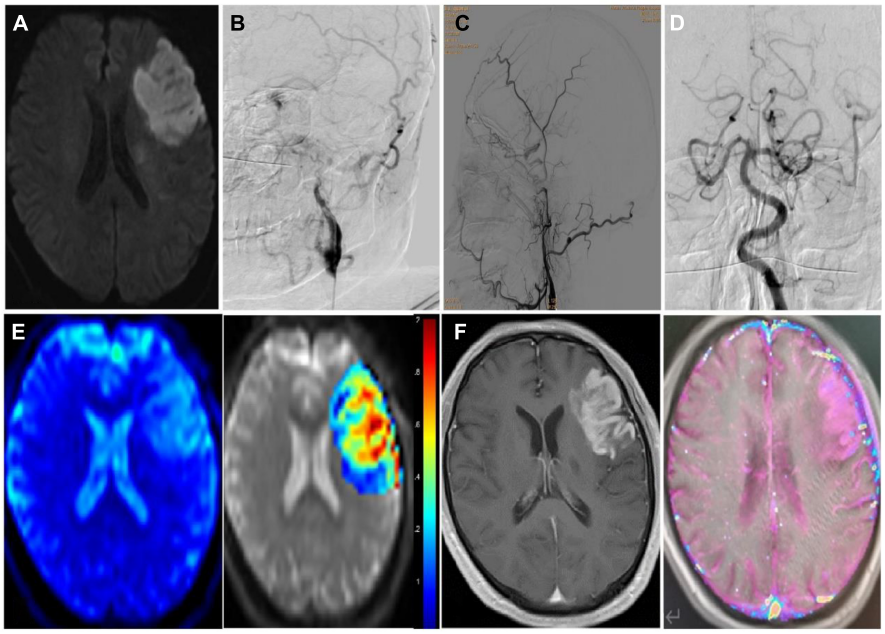

FIGURE 2
Imaging data of a patient with subacute ischemic stroke with hemorrhagic transformation after endovascular therapy. **(A)** Seven days after stroke onset, diffusion weighted imaging sequence of MRI shows subacute cerebral infarction in left frontal temporal lobe. **(B–D)** Cerebral angiography revealed long-segment occlusion of the left internal carotid artery, but the left middle cerebral artery and its branches remain patent. **(E)** The pseudo color image (left) and *post*-processing image (right) of the ASL (arterial spin labeling) sequence are shown with the cerebral blood flow of 1.9. **(F)** The original image (left) and the *post*-processing image (right) of the DCE (dynamic contrast enhanced) MRI sequence are shown with the Ktrans of 0.16/min).

of Heidelberg type II (Figures 2, 3 and Table 1). There were no significant ($P > 0.05$) differences in the gender, age, high risk factors, location of cerebral infarction, distribution of responsible vessels, extent of disease, modes of endovascular treatment, time from onset to imaging examination, and imaging types on ASL sequence, XperCT and DCE MRI between patients with and those without hemorrhagic transformation. However, the rCBF value (1.56 ± 0.16 vs. 1.16 ± 0.16), Ktrans, (0.08 ± 0.03 vs. 0.03 ± 0.01) and rKtrans (3.02 ± 0.89 vs. 1.89 ± 0.56) were all significantly ($P < 0.05$) higher in patients with than those without hemorrhagic transformation.

Consistency between the ASL, DCE, and Xper CT imaging classifications

The imaging classification was consistent on the ASL sequence with that on the DCE sequence in 25 patients, but inconsistent in only 2 patients, with a weighted Kappa coefficient of 0.91 (95% CI: 0.79–1.03, $P < 0.001$), indicating strong consistency (Table 2). The imaging classification was consistent on the ASL sequence with that on the Xper CT imaging in 19 patients, but not in the other 8 patients, resulting in a weighted Kappa coefficient of 0.70 (95% CI: 0.50–0. 89, $P < 0.001$), with strong consistency (Table 2). The imaging classification was consistent on the DCE sequence with that on the Xper CT imaging in 19 patients, but not in the other 8 patients, leading to a weighted Kappa coefficient of 0.78 (95% CI: 0.60–0.96, $P < 0.001$), with strong consistency (Table 3).

rCBF and Ktrans values in different cerebral infarction sites

The rCBF value in the 21 patients with the subcortical and basal ganglia infarction was significantly lower than that in the other 6 patients with the cortical infarction (1.222 ± 0.221 vs. 1.413 ± 0.259, $t = 1.795$, $P = 0.004$), however, no significant difference was found in the Ktrans (0.04 ± 0.02 vs. 0.06 ± 0.03, $P = 0.13$) or rKtrans (2.08 ± 0.79 vs. 2.54 ± 0.89, $P = 0.23$) between the two groups.

Discussion

In this study investigating the value of the ASL imaging sequence in evaluating the blood-brain barrier permeability of anterior circulation ischemic lesions in subacute ischemic stroke and in assessing the risk of hemorrhage transformation after endovascular recanalization, it was found that the ASL sequence had a strong role in evaluating the blood-brain barrier permeability in patients with anterior circulation subacute ischemic stroke and that Type III ASL imaging presentation may have a high prediction effect on the risk of hemorrhagic transformation.

For patients with subacute ischemic stroke caused by severe stenosis or occlusion of large intracranial vessels, endovascular recanalization at an appropriate time can benefit most patients and effectively reduce the poor prognosis. However, some complications after endovascular arterial recanalization cannot be ignored. Among them, hemorrhage transformation is one

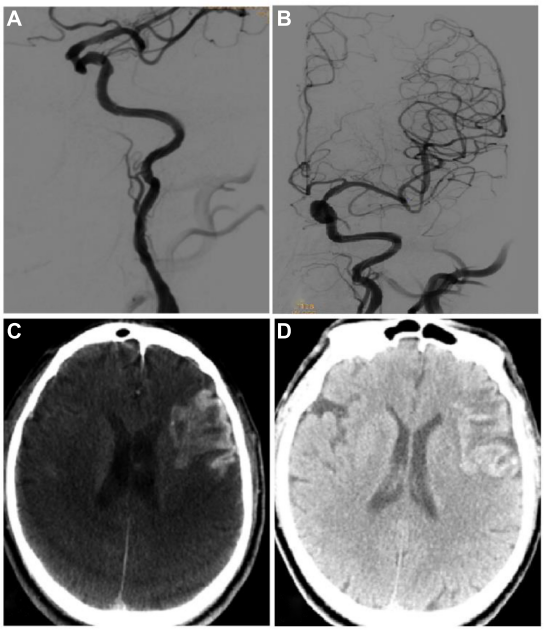

FIGURE 3
Imaging data of the same patient as in Figure 2. **(A,B)** On the 20th day after symptom onset, endovascular recanalization was performed to recanalize the long-segment occlusion of the left internal carotid artery, and two resolute stents (4.0 mm × 33 mm and 4.0 mm × 36 mm) were deployed in sequence. After recanalization, the occluded internal carotid artery was successfully recanalized. **(C)** Xper CT immediately after the surgery showed that the imaging classification of hemorrhagic transformation was type III. **(D)** Hemorrhage transformation was detected by CT plain scan on the next day after surgery.

of the serious and even fatal complications after endovascular treatment of ischemic stroke, and its occurrence is closely related to the increase of blood-brain barrier permeability (Sandoval and Witt, 2008). Damage of the blood-brain barrier will cause large-molecular neurotoxic proteins in the blood to leak out into the brain tissue gap, mediating inflammatory reaction to cause perivascular interstitial edema, neuronal and nerve fiber damage and subsequent blood leakage out of the cerebral arteries (or bleeding), which is the hemorrhagic transformation from ischemic stroke after endovascular treatment. This hemorrhagic transformation cannot be directly measured, but can be indirectly reflected by measurement of the blood-brain barrier permeability. In addition, increased permeability in the blood-brain barrier caused by cerebral ischemic injury appears not only in the acute phase, but also in the subacute phase and the early stage of angiogenesis associated with the recovery of ischemic stroke (Jiang et al., 2012). Therefore, quantitative analysis of the blood-brain barrier permeability is a promising approach to predict the risk of hemorrhagic transformation in patients with subacute ischemic stroke.

The blood-brain barrier is crucial for maintaining a stable cellular environment in the central nervous system for regulation of cellular and solute traffic between the blood and the brain. Permeability of the blood-brain barrier is a physiological phenomenenon in the healthy state but increases with aging and in the disease status (Elwood et al., 2017). The first blood-brain interface is formed by the endothelial cells that have tight junction proteins, and the next layer is formed by the basal lamina which is composed of extracellular matrix proteins and surrounded by the astrocytic foot processes with embedded pericytes. Under normal conditions, the interface between brain tissues and blood is a relatively limited "barrier" to non-lipid molecules and has low permeability. Besides the tight junction proteins, there are also transport or carrying molecules to facilitate transport into the brain, and enzymes may exist to degrade substances and prevent transport into the brain (Raja et al., 2018). When the blood-brain barrier is damaged in brain tumors, stroke or multiple sclerosis, large proteins may leak into the brain tissue and cerebrospinal fluid, which can be detected with CT or MRI. Disruption of the blood-brain barrier in chronic vascular disease is associated with hypoxia-induced inflammation (Raja et al., 2018). One potential condition to involve chronic vascular changes is secondary to long-standing elevated blood pressure, which may lead to stenosis of the vascular lumen, limiting blood flow and producing hypoxia. This finding has been proved by animal studies of hypertensive rats (Weaver et al., 2014) and human studies (Fernando et al., 2006) with hypoxia-induced factors being found in the brains of patients with vascular dementia. Nonetheless, measurement of the blood-brain barrier permeability is not straightforward. The ratio between the cerebrospinal fluid and the serum albumin is a well-established approach to evaluate the barrier permeability, but is invasive and may not reliably reflect the real permeability, with a great influence from the cerebrospinal fluid flow (Varatharaj et al., 2019). Neuro-imaging with use of an intravenous injection of tracer is an approach to measure the blood-brain barrier permeability, and positron emission tomography has also been used in this aspect (Varatharaj et al., 2019). Nonetheless, some disadvantages in these approaches have precluded the widespread application, including the suboptimal resolution and radioactivity.

Currently, a variety of neuroimaging techniques can be used to obtain the volume of cerebral infarction, the perfusion status of infarction focus, the degree of vascular disease, and the permeability

TABLE 2 Consistency of imaging types between ASL and DCE MRI.

ASL imaging	DCE imaging				Xper CT imaging			
	Type I	Type II	Type III	Total	Type I	Type II	Type III	Total
Type I	8	0	0	8	8	0	0	8
Type II	1	11	0	11	4	7	0	11
Type III	0	0	7	8	0	4	4	8
Total	9	11	7	27	12	11	4	27

ASL, arterial spin labeling; MRI, magnetic resonance imaging; DCE, dynamic contract enhanced; CT, computed tomography.

TABLE 3 Consistency of imaging types between Xper CT and DCE MRI.

DCE imaging	Xper CT imaging			Total
	Type I	Type II	Type III	
Type I	8	1	0	9
Type II	4	7	0	11
Type III	0	3	4	7
Total	12	11	4	27

CT, computed tomography; MRI, magnetic resonance imaging; DCE, dynamic contract enhanced.

of diseased vascular wall to predict the risk of hemorrhagic transformation in patients with ischemic stroke. The use of DCE sequence MRI is a commonly used imaging method to detect the permeability of the blood-brain barrier before endovascular treatment. Its parameter Ktrans represents the speed of contrast agent penetrating from the cerebral vessels into the interstitium and is calculated by measuring the mean Ktrans in a certain ROI region. It can reflect the concentration and flow of contrast agent in the blood of cerebral tissue. Thus, it can be used as an indicator of the blood-brain barrier permeability, and has been shown to be able to sensitively detect the changes of the blood-brain barrier permeability at the early stage of cerebral ischemia (2 to 3 h) (Jiang et al., 2005). However, it is undeniable that the sensitivity of MRI based on the gadolinium chelate contrast agent for ischemic stroke is relatively low, and adverse reactions such as nephrogenic systemic fibrosis and intracranial gadolinium deposition may occur. Immediate plain CT scanning after endovascular treatment can also detect contrast agent extravasation in the local cerebral infarction, so as to judge the permeability of the diseased vascular wall, extent of blood-brain barrier damage and risk of hemorrhagic transformation. Nonetheless, these findings are after rather than before endovascular recanalization, which is not conducive to early intervention. In addition, although the exudation of contrast agent on Xper CT after surgery had been demonstrated to be associated with the risk of hemorrhagic transformation (Seevinck et al., 2010; Chen et al., 2020), only qualitative analysis had been performed without classifying the exudation characteristics or quantity.

ASL is the only non-invasive technique using endogenous tracers in perfusion imaging. In a study investigating the MRI ASL sequence imaging in 27 patients with acute ischemic stroke after endovascular treatment (Shimonaga et al., 2019), it was found that among 13 patients with local hyperperfusion areas, 8 patients had hemorrhagic transformation after endovascular recanalization, and the prognosis of these patients was poor, suggesting that the increase of local cerebral blood flow in cerebral infarction can be used to predict the occurrence of hemorrhagic transformation. In our study, the image scanning of the ASL sequence, DCE sequence and Xper CT was completed on the "one-stop multimodal image fusion and stroke treatment platform" dedicated to stroke diagnosis and treatment, which not only helped to achieve unification of relevant parameters, but also reduced the time interval of image inspection, ensuring the accuracy and repeatability of image data to the maximal extent. In our study, the DCE sequence and Xper CT were used to cross verify the evaluation effect of the ASL sequence on the blood-brain barrier permeability of cerebral infarction focus in patients with subacute ischemic stroke and the predictive value of hemorrhage transformation. The results showed that in the same ROI, the rCBF and Ktrans values in patients with hemorrhagic transformation were significantly higher than those without hemorrhagic transformation.

After further classification of the high signal distribution on the ASL and DCE sequence and the high-density image characteristics on the Xper CT, it was found that the ASL imaging sequence had a high consistency with the DCE imaging sequence and the Xper CT with a Kappa coefficient of 0.91 and 0.70, respectively. Consequently, the ASL sequence may be just like the DCE sequence and the Xper CT, playing a strong role in assessing the blood-brain barrier permeability in the cerebral infarction area of subacute ischemic stroke. The risk of hemorrhagic transformation in patients with ASL type III was relatively high. The synergy of the three imaging tools may be able to make a more accurate prediction of postoperative hemorrhagic transformation, thus providing more objective evidence for guiding the classification, staging and individualized treatment of stroke patients.

The location of contrast agent extravasation is more valuable than the extravasation itself in predicting the hemorrhagic transformation. Because contrast agent is mostly injected near the opening of the lenticular artery in the middle cerebral artery trunk, contrast agent extravasation limited to the basal ganglia is common, but its value in predicting the hemorrhagic transformation is low. Extravasation of contrast agent in the cortex may indicate extensive damage of the blood-brain barrier, serious reperfusion injury, and increased risk of symptomatic hemorrhagic transformation (Kim et al., 2015). However, further analysis in our study found no significant difference in the Ktrans value between patients with subcortical and basal ganglia infarction and those with cortical infarction ($P > 0.05$), even though the rCBF value of the former was significantly lower than that of the latter. This may indicate differences in the blood-brain barrier permeability between infarcted tissues in different parts of subacute ischemic stroke, which may be associated with different ischemic tolerance of the blood-brain barrier in different parts of brain tissue with subacute ischemic stroke as well as different repair efficiency of the blood-brain barrier permeability. It has been found that the ischemic focus of subacute ischemic stroke will have functional neurovascular remodeling, which is accompanied by neovascularization, and establishment of collateral circulation will accordingly increase blood perfusion in the area with neovascularization (Bokkers et al., 2009; Yang and Torbey, 2020). In patients with subacute ischemic stroke, the leptomeningeal collateral branch is easier to be established in patients with cortical infarction than in patients with subcortical and basal ganglia infarction, which may lead to the earlier and more perfect repair of the blood-brain barrier in patients with cortical infarction.

Our study also suggested that the ASL and DCE sequences have different abilities in detecting the blood-brain barrier permeability in different parts of subacute ischemic stroke, which may be related to the difference in imaging characteristics between the two sequences. The ASL sequence is marked by water protons which are more sensitive to changes in the blood-brain barrier permeability than gadolinium ions (Lin et al., 2018; Mahroo et al., 2021). Therefore, the ASL sequence is more sensitive to changes in the blood-brain barrier permeability than the DCE sequence. Moreover, in our study, the ASL sequence imaging used the "multiple delay labeling" technology, which is easy to capture long

delayed signals in different parts of tissues (Mato Abad et al., 2016), resulting in more sensitivity of the ASL sequence to changes in the blood-brain barrier permeability in different parts than that of the DCE sequence. Based on the results of our study and the above analysis, the ASL sequence imaging using the "multiple delay labeling" technology in clinical work may be more suitable to detecting the nervous system diseases with slight changes in the blood-brain barrier permeability.

Some limitations existed in our study, including enrollment of Chinese patients only, one-center study design and a small cohort of patients due to the strict inclusion and exclusion criteria, which may all affect the bias of the outcome. Further prospective, randomized, controlled clinical trials with multicenters involved and a large sample size are needed to verify the outcomes of this study.

To sum up, application of the ASL sequence and its advanced *post*-processing technology can effectively assess the blood-brain barrier permeability in patients with subacute ischemic stroke in the anterior circulation and predict the risk of hemorrhagic transformation following endovascular recanalization, thus conducive to selection of surgical timing for different patients, reduction of perioperative complications, and achievement of real staging and individualized treatment for the patients.

Data availability statement

The original contributions presented in this study are included in this article/supplementary material, further inquiries can be directed to the corresponding author.

Ethics statement

The studies involving human participants were reviewed and approved by the Ethics Committee of Henan Provincial People's Hospital. The patients/participants provided their written informed consent to participate in this study.

Author contributions

LZ and BG: study design. LHW, YL, LNW, YZ, ZZ, YX, and MW: data collection. LHW, LNW, YL, LZ, and TL: data analysis. YL: writing of the original version. BG: revision. TL: supervision. All authors contributed to the validation article and approved the submitted version.

Funding

This study was supported by the Stroke Prevention and Treatment Project of National Health Commission–Research and Popularization of Appropriate Intervention Technology for the Stroke High Risk Group in China (GN-2018R0007).

Conflict of interest

The authors declare that the research was conducted in the absence of any commercial or financial relationships that could be construed as a potential conflict of interest.

Publisher's note

All claims expressed in this article are solely those of the authors and do not necessarily represent those of their affiliated organizations, or those of the publisher, the editors and the reviewers. Any product that may be evaluated in this article, or claim that may be made by its manufacturer, is not guaranteed or endorsed by the publisher.

References

Arba, F., Piccardi, B., Palumbo, V., Biagini, S., Galmozzi, F., Iovene, V., et al. (2021). Blood-brain barrier leakage and hemorrhagic transformation: the Reperfusion Injury in Ischemic StroKe (RISK) study. *Eur. J. Neurol.* 28, 3147–3154. doi: 10.1111/ene.14985

Bokkers, R. P., van der Worp, H. B., Mali, W. P., and Hendrikse, J. (2009). Noninvasive MR imaging of cerebral perfusion in patients with a carotid artery stenosis. *Neurology* 73, 869–875. doi: 10.1212/WNL.0b013e3181b7840c

Chen, Z., Zhang, Y., Su, Y., Sun, Y., He, Y., and Chen, H. (2020). Contrast extravasation is predictive of poor clinical outcomes in patients undergoing endovascular therapy for acute ischemic stroke in the anterior circulation. *J. Stroke Cerebrovasc. Dis.* 29:104494. doi: 10.1016/j.jstrokecerebrovasdis.2019.104494

Elwood, E., Lim, Z., Naveed, H., and Galea, I. (2017). The effect of systemic inflammation on human brain barrier function. *Brain Behav. Immun.* 62, 35–40. doi: 10.1016/j.bbi.2016.10.020

Fernando, M. S., Simpson, J. E., Matthews, F., Brayne, C., Lewis, C. E., Barber, R., et al. (2006). White matter lesions in an unselected cohort of the elderly: molecular pathology suggests origin from chronic hypoperfusion injury. *Stroke* 37, 1391–1398. doi: 10.1161/01.STR.0000221308.94473.14

Jiang, Q., Ewing, J. R., and Chopp, M. (2012). MRI of blood-brain barrier permeability in cerebral ischemia. *Transl. Stroke Res.* 3, 56–64. doi: 10.1007/s12975-011-0133-x

Jiang, Q., Ewing, J. R., Ding, G. L., Zhang, L., Zhang, Z. G., Li, L., et al. (2005). Quantitative evaluation of BBB permeability after embolic stroke in rat using MRI. *J. Cereb. Blood Flow Metab.* 25, 583–592. doi: 10.1038/sj.jcbfm.9600053

Kim, J. M., Park, K. Y., Lee, W. J., Byun, J. S., Kim, J. K., Park, M. S., et al. (2015). The cortical contrast accumulation from brain computed tomography after endovascular treatment predicts symptomatic hemorrhage. *Eur. J. Neurol.* 22, 1453–1458. doi: 10.1111/ene.12764

Lin, Z., Li, Y., Su, P., Mao, D., Wei, Z., Pillai, J. J., et al. (2018). Non-contrast MR imaging of blood-brain barrier permeability to water. *Magn. Reson. Med.* 80, 1507–1520. doi: 10.1002/mrm.27141

Mahroo, A., Buck, M. A., Huber, J., Breutigam, N. J., Mutsaerts, H., Craig, M., et al. (2021). Robust multi-TE ASL-based blood-brain barrier integrity measurements. *Front. Neurosci.* 15:719676. doi: 10.3389/fnins.2021.719676

Mato Abad, V., Garcia-Polo, P., O'Daly, O., Hernandez-Tamames, J. A., and Zelaya, F. (2016). ASAP (Automatic Software for ASL Processing): a toolbox for processing Arterial Spin Labeling images. *Magn. Reson. Imaging* 34, 334–344. doi: 10.1016/j.mri.2015.11.002

Niibo, T., Ohta, H., Miyata, S., Ikushima, I., Yonenaga, K., and Takeshima, H. (2017). Prediction of blood-brain barrier disruption and intracerebral hemorrhagic infarction

using arterial spin-labeling magnetic resonance imaging. *Stroke* 48, 117–122. doi: 10.1161/STROKEAHA.116.013923

Nogueira, R. G., Gupta, R., Jovin, T. G., Levy, E. I., Liebeskind, D. S., Zaidat, O. O., et al. (2015). Predictors and clinical relevance of hemorrhagic transformation after endovascular therapy for anterior circulation large vessel occlusion strokes: a multicenter retrospective analysis of 1122 patients. *J. Neurointerv. Surg.* 7, 16–21. doi: 10.1136/neurintsurg-2013-010743

Raja, R., Rosenberg, G. A., and Caprihan, A. (2018). MRI measurements of blood-brain barrier function in dementia: a review of recent studies. *Neuropharmacology* 134(Pt B), 259–271. doi: 10.1016/j.neuropharm.2017.10.034

Sandoval, K. E., and Witt, K. A. (2008). Blood-brain barrier tight junction permeability and ischemic stroke. *Neurobiol. Dis.* 32, 200–219.

Seevinck, P. R., Deddens, L. H., and Dijkhuizen, R. M. (2010). Magnetic resonance imaging of brain angiogenesis after stroke. *Angiogenesis* 13, 101–111. doi: 10.1007/s10456-010-9174-0

Shimonaga, K., Matsushige, T., Hosogai, M., Hashimoto, Y., Mizoue, T., Ono, C., et al. (2019). Hyperperfusion after endovascular reperfusion therapy for acute ischemic stroke. *J. Stroke Cerebrovasc. Dis.* 28, 1212–1218. doi: 10.1016/j.jstrokecerebrovasdis.2019.01.007

Topakian, R., Strasak, A. M., Sonnberger, M., Haring, H. P., Nussbaumer, K., Trenkler, J., et al. (2007). Timing of stenting of symptomatic carotid stenosis is predictive of 30-day outcome. *Eur. J. Neurol.* 14, 672–678. doi: 10.1111/j.1468-1331.2007.01815.x

Varatharaj, A., Liljeroth, M., Darekar, A., Larsson, H. B. W., Galea, I., and Cramer, S. P. (2019). Blood-brain barrier permeability measured using dynamic contrast-enhanced magnetic resonance imaging: a validation study. *J. Physiol.* 597, 699–709. doi: 10.1113/JP276887

von Kummer, R., Broderick, J. P., Campbell, B. C., Demchuk, A., Goyal, M., Hill, M. D., et al. (2015). The heidelberg bleeding classification: classification of bleeding events after ischemic stroke and reperfusion therapy. *Stroke* 46, 2981–2986. doi: 10.1161/STROKEAHA.115.010049

Weaver, J., Jalal, F. Y., Yang, Y., Thompson, J., Rosenberg, G. A., and Liu, K. J. (2014). Tissue oxygen is reduced in white matter of spontaneously hypertensive-stroke prone rats: a longitudinal study with electron paramagnetic resonance. *J. Cereb. Blood Flow Metab.* 34, 890–896. doi: 10.1038/jcbfm.2014.35

Yang, Y., and Torbey, M. T. (2020). Angiogenesis and blood-brain barrier permeability in vascular remodeling after stroke. *Curr. Neuropharmacol.* 18, 1250–1265. doi: 10.2174/1570159X18666200720173316

frontiers | Frontiers in Neuroscience

TYPE Original Research
PUBLISHED 06 March 2023
DOI 10.3389/fnins.2023.1118650

OPEN ACCESS

EDITED BY
Na Li,
Central South University, China

REVIEWED BY
Tzu-Yu Hsu,
Taipei Medical University, Taiwan
Si-Ping Zhang,
Xi'an Jiaotong University, China
Guozhen Zhao,
Institute of Psychology (CAS), China

*CORRESPONDENCE
Danmin Miao
✉ miaodanmin@126.com
Peng Fang
✉ fangpeng@fmmu.edu.cn

†These authors have contributed equally to this work

SPECIALTY SECTION
This article was submitted to Translational Neuroscience, a section of the journal Frontiers in Neuroscience

RECEIVED 07 December 2022
ACCEPTED 06 February 2023
PUBLISHED 06 March 2023

CITATION
Li Y, Li C, Zhang T, Wu L, Lin X, Li Y, Wang L, Yang H, Lu D, Miao D and Fang P (2023) Questionnaires based on natural language processing elicit immersive ruminative thinking in ruminators: Evidence from behavioral responses and EEG data.
Front. Neurosci. 17:1118650.
doi: 10.3389/fnins.2023.1118650

Questionnaires based on natural language processing elicit immersive ruminative thinking in ruminators: Evidence from behavioral responses and EEG data

Yulong Li[1†], Chenxi Li[1†], Tian Zhang[1], Lin Wu[1], Xinxin Lin[1], Yijun Li[1], Lingling Wang[1], Huilin Yang[1], Diyan Lu[1], Danmin Miao[1,2*] and Peng Fang[1,2,3,4*]

[1]Department of Military Medical Psychology, Air Force Medical University, Xi'an, China, [2]Key Laboratory of Military Medical Psychology and Stress Support of PLA, Xi'an, China, [3]Shaanxi Provincial Key Laboratory of Bioelectromagnetic Detection and Intelligent Perception, Xi'an, China, [4]School of Biomedical Engineering, Air Force Medical University, Xi'an, China

Rumination is closely related to mental disorders and can thus be used as a marker of their presence or a predictor of their development. The presence of masking and fabrication in psychological selection can lead to inaccurate detection of psychological disorders. Human language is considered crucial in eliciting specific conscious activities, and the use of natural language processing (NLP) in the development of questionnaires for psychological tests has the potential to elicit immersive ruminative thinking, leading to changes in neural activity. Electroencephalography (EEG) is commonly used to detect and record neural activity in the human brain and is sensitive to changes in brain activity. In this study, we used NLP to develop a questionnaire to induce ruminative thinking and then recorded the EEG signals in response to the questionnaire. The behavioral results revealed that ruminators exhibited higher arousal rates and longer reaction times, specifically in response to the ruminative items of the questionnaire. The EEG results showed no significant difference between the ruminators and the control group during the resting state; however, a significant alteration in the coherence of the entire brain of the ruminators existed while they were answering the ruminative items. No differences were found in the control participants while answering the two items. These behavioral and EEG results indicate that the questionnaire elicited immersive ruminative thinking, specifically in the ruminators. Therefore, the questionnaire designed using NLP is capable of eliciting ruminative thinking in ruminators, offering a promising approach for the early detection of mental disorders in psychological selection.

KEYWORDS

natural language analysis, immersive questionnaire, EEG coherence, psychological selection, rumination

Introduction

Rumination is defined as continuous attention to negative stimuli, including the causes and consequences of negative events and the resulting negative emotions, which may lead to depression, anxiety, and other mental disorders. This phenomenon is considered a non-adaptive way of regulating emotions (Nolen-Hoeksema, 1991; Nolen-Hoeksema and Morrow, 1991; Nolen-Hoeksema et al., 1995). In the Self-Regulatory Executive Function (S-REF) model of emotional disorders, Wells and Matthews identified a persistent thinking mode that included worry and rumination and further defined it as an ineffective coping strategy. Rumination involves persistently focusing on negative thinking and feelings rather than problem solving, which is counterproductive by way of amplifying and prolonging the experience of suffering (Wells and Matthews, 1996). The relationship between rumination and depression has been widely studied (Castanheira et al., 2019; Li et al., 2020; Van Doorn et al., 2021). According to response styles theory, rumination can prolong and intensify the pain of negative or stressful events, increase despair, and aggravate depressive symptoms (Nolen-Hoeksema et al., 2008). Rumination is also associated with alcohol abuse, anxiety symptoms, generalized anxiety disorder, social anxiety disorder, obsessive-compulsive disorder, PTSD, schizophrenia, borderline personality disorder, and bulimia nervosa, among others, and other mental disorders (Watkins and Roberts, 2020).

Although there are numerous scales available for assessing rumination, the most widely used remains the Ruminative Response Scale (RRS), developed by Nolen-Hoeksema in 1991 (Nolen-Hoeksema and Morrow, 1991) and compiled by Nolen Hoeksema in 1991. While RRS has been widely employed in ruminative research, the limitations of this scale are also significant, especially regarding the presence of psychological selection (Wang et al., 2020; Miao et al., 2021). Camouflage, falsification, social approval, and other issues (Dunning et al., 2005; Schwarz, 2012; Wang et al., 2020, 2021) have greatly affected the acceptance and validity of rumination-related psychological testing. Therefore, further advancements are necessary in inducing ruminative conscious activity accurately, measuring the associated brain activity objectively, and exploring the neural biomarkers of rumination to identify ruminators and predict future rumination for precise psychological selection.

Previous studies have found that rumination arises as a result of negative situational memories (Sutherland and Bryant, 2007). Hence, the resurfacing of specific situational memories is considered one of the most effective and rapid means to induce rumination. In episodic memory-related studies, Wilson Mendenhall proposed "scenario immersion" and defined it as precise language that could facilitate immersive psychological imagination and enable subjects to place themselves into various imagined situations and memories (Wilson-Mendenhall et al., 2019). After experiencing different emotions, subjects form an episodic memory in their long-term memory, thus affecting the emotions they will experience in similar situations in the future. For example, when someone perceives that a car is approaching them quickly in a given scenario, their episodic memory from a previous similar scenario is activated in response. This implicitly, rapidly, and synergistically generates fearful cognitive, interoceptive, and behavioral processes in relation to the current situation (Lebois et al., 2020). Research has shown that rumination can be activated quickly when encountering situations that are similar to a past fearful event or when encountering only a small component of the original event (Wilson-Mendenhall et al., 2015). In 2022, Priyamvada Rajasethupathy confirmed the core idea of the "scenario immersion" theory with the finding that a holistic episodic memory composed of multiple sensory experiences can indeed be evoked by a single sensory cue (Yadav et al., 2022). Therefore, eliciting a specific episodic memory can be the most effective and efficient means to initiate ruminative thinking (Sutherland and Bryant, 2007).

Natural language (i.e., the language used in daily life) is an important means of human communication and an essential feature that distinguishes human beings from other animals (Assale et al., 2019). A specific questionnaire based on natural language can be used to comprehensively induce the recall of the complete episodic memory (Wilson-Mendenhall et al., 2019; Ancin-Murguzur and Hausner, 2021). At present, natural language processing (NLP) technology has accomplished a series of complex functions, such as machine translation, automatic summarization, emotion analysis, and text classification (Castanheira et al., 2019). Compiling questionnaires based on natural language corpuses and NLP of rumination are the two methods that are considered effective in inducing and analyzing rumination accurately (Ferrario et al., 2020). The theory of "scenario immersion" is a useful tool for inducing rumination; therefore, we drew upon this theory and further incorporated NLP to develop a questionnaire that could elicit ruminative thinking both efficiently and effectively.

Compared to cognitive neural technologies, such as functional magnetic resonance imaging (fMRI), magnetoencephalography (MEG), and functional near-infrared spectroscopy (fNIRS), wireless EEG technology is cheap, easy to transport, convenient for recording brain activity during experiments, sensitive to the alternation of brain activity, flexible across various experimental paradigms, and provides high temporal resolution signals, thereby rendering it suitable for language evaluation and the detection of brain activity during psychological selection (Deshpande et al., 2017).

EEG coherence, first proposed by Robinson (Robinson, 2003), is an index of brain connectivity that is calculated by the covariance of the power spectral density at two electrodes. Coherence shows the synchronicity of neural activity and reflects brain dynamics (Markovska-Simoska et al., 2018). Neuroimaging studies have provided a great deal of data on the dysfunction and dysregulation that occurs in the brains of clinically and nonclinically depressed ruminators, including hypofunctional and hyperfunctional connectivity (Ferdek et al., 2016; Li et al., 2018; Benschop et al., 2020). Such studies were designed to examine network characteristics while ruminators were at rest or engaged in a task, thereby exposing the synchronicity of neural activity either between the brain areas (Ferdek et al., 2016) or between the brain networks (Zhang et al., 2020). Both EEG and fMRI studies have shown that altered functional connectivity in the brain networks of subjects with depression was positively related to ruminative thoughts (Benschop et al., 2020). These results indicated that the altered synchronicity within the brain might be an indicator of altered brain activity. EEG coherence may be a suitable indicator to depict the change of the brain activities in subjects with mental disorders.

TABLE 1 Demographic information of 4,591 participants (n = 4,591).

	Frequency/mean	Percentage/standard deviation
Gender (n, %)		
Women	65	1.42
Men	4,526	98.58
Age (mean ± SD)	21.29	2.59
Home location (n, %)		
Urban	1,191	25.94
Village	3,400	74.06
Ethnicity (n, %)		
Han	4,109	89.50
Others	482	10.50

TABLE 2 Demographic information of individuals who participated in the semi-structured interviews (n = 607).

	Frequency/mean	Percentage/standard deviation
Gender (n, %)		
Women	30	4.94
Men	577	95.06
Age (mean ± SD)	21.80	3.03
Home location (n, %)		
Urban	196	32.29
Village	411	67.71
Ethnicity (n, %)		
Han	525	86.49
Others	82	13.51

In this study, we developed a situational ruminative questionnaire using the natural language characteristics of ruminators to demonstrate the ability of the questionnaire to elicit immersive ruminative thinking in ruminators, as determined by their behavioral responses and characteristics of EEG signals.

Methods

The ruminative response scale

The Ruminative Response Scale (RRS) is a questionnaire composed of 22 items that is used to measure the ruminative tendency of an individual. Each item uses a 4-point Likert scale (1 = rarely, 2 = sometimes, 3 = often, 4 = almost always). The Chinese version used in this study was translated by Han Xiu and has been verified to have good reliability and validity among Chinese senior high school and college students (Han and Yang, 2009). The higher the total score, the higher the rumination level, and the highest score is 88. The demographic information of the participants is shown in Table 1.

Natural language processing and questionnaire development

We selected 607 subjects with a high tendency for rumination (577 men and 30 women) for semi-structured interviews that were conducted on an individual basis. The interviews were recorded and saved, and an intelligent conference system (version 5.0) was used to transcript the interview information for each interviewee. The demographic information of the participants is shown in Table 2. The obtained transcripts were analyzed, and the elicited material was compiled using the following six steps. (1) Proofreading and denoising: The text was thoroughly analyzed to check for errors and delete any extraneous characters, spaces, and so on. (2) Chinese participle: Chinese word segmentation was performed using Chinese LIWC software. (3) Stop word filtering: More uniform word segmentation text was created using the HIT edition of the "Stop Word Dictionary" to filter stop words. (4) Feature word extraction and coding: The TF-IDF approach was used to determine the frequency of feature words in the text (Reviewer-Lee, 2000; Jurafsky, 2009). The feature words were specifically selected by using the TF-IDF algorithm to calculate the frequency of all the words in the interview transcript of the extreme ruminators to obtain the high-frequency feature words first and then by referring to the 66 "scenario materials" words in Mendenhall's article (Wilson-Mendenhall et al., 2019). Only the content words (to construct the scenario) and the depictive words (to express the emotional experience) of the feature words were retained, and function words with no real meaning were removed. The bag-of-words model used a real-valued vector to label each transcribed word and encoded it using feature words (Ferrario et al., 2020). (5) Based on the semantic characteristics of the feature words, the LDA (latent Dirichlet allocation) topic model was used to extract text topics (Ghosh and Guha, 2013; Min et al., 2019, 2020), which were then used to group words under the topics. The detailed analysis pipeline of the LDA model and the document generation process are shown in Supplementary Figure 1 (Blei et al., 2003; Hao et al., 2017). Quantitative analysis was then used to identify the overarching topic of the interview material, while artificial naming was used to identify the situational topics. An example of extracting text topics is shown in Supplementary Table 1. (6) Creation of situational inducing materials: We recreated real-life scenarios that the interviewees had described, merged them with the six syntaxes of Mendenhall's "scenario immersion" theory, and then generated materials that elicited rumination. The neutral items were derived from paragraphs that were cut from the third edition of the Encyclopedia of China, whereby the number of words was kept similar to that of the rumination items and the chosen content was relatively boring and meaningless.

Questionnaire evaluation

The ruminative questionnaire was revised by three linguistics professors. The revisions made included connotation logic,

TABLE 3 Demographic information of the 1,685 participants ($n = 1,685$).

	Frequency/mean	Percentage/standard deviation
Gender (*n*, %)		
Women	0	0
Men	1,685	100
Age (mean ± SD)	21.19	1.60
Home location (*n*, %)		
Urban	308	18.28
Village	1,377	81.72
Ethnicity (*n*, %)		
Han	1,489	88.37
Others	196	11.63

TABLE 4 Demographic information of the 78 participants who participated in the evaluation of the questionnaire ($n = 78$).

	Frequency/mean	Percentage/standard deviation
Gender (*n*, %)		
Women	0	0
Men	78	100
Age (mean ± SD)	22.10	2.92
Home location (*n*, %)		
Urban	33	42.31
Village	45	57.69
Ethnicity (*n*, %)		
Han	71	91.03
Others	7	8.97

grammar application, and character norms, among others. To verify the validity of the questionnaire regarding its ability to induce rumination, it was evaluated again by high- and low-degree ruminators. We then recruited another 1,685 subjects (all males) to complete the RRS. Of these, 78 participants were randomly selected for the final evaluation of the developed questionnaire. These participants comprised 40 high-degree ruminators (ruminators, mean age = 23.30 years, SD = 3.40 years; RRS score: 53.65 ± 8.89) and 38 low-degree ruminators (controls, mean age = 20.84 years, SD = 1.55 years; RRS score: 22.13 ± 0.34). We based the degree of rumination on the cutoff values specified in the Rosenbaum et al. (2018b) article: high-degree ruminators were defined as having a mean RRS score higher than 2.36 (PR > 65), while low-degree ruminators were defined as having an RRS score lower than 1.9 (PR < 27) (Rosenbaum et al., 2018b). Neutral items were also evaluated in comparison with the rumination items. The evaluation included seven dimensions: (1) repetition; (2) persistence; (3) associativity; (4) vividness; (5) uncontrolled nature; (6) assumption; (7) representativeness. The first six dimensions represent ruminative characteristics summarized from both our literature review and from interviews conducted with a large number of highly ruminative individuals. The last dimension, representativeness, reflects the extent to which an entry matched the subject's recall. These seven dimensions combine to represent the level of "scenario immersion" experienced by subjects while they were filling out the questionnaire. The demographic information of the 1,685 and 78 participants is shown in Tables 3, 4, respectively.

EEG experimental procedures

EEG experiment participants

We recruited subjects from the 1,685 freshmen enrolled in the 2022 cohort of Shaanxi Police College to participate in the EEG experiment. Finally, 56 voluntary participants (mean age = 22.48 years, SD = 7.73 years) selected from the high-degree ruminators (PR > 65, RRS score: 63.79 ± 6.38) were recruited as the rumination group, while 29 voluntary participants (mean age = 20.59 years, SD = 1.64 years) (PR < 27, RRS score: 22.14 ± 0.44) were recruited as the control group. The exclusion criteria were as follows: (1) patients with a history of psychiatry; (2) patients who had been hospitalized in the psychiatric department; (3) patients with current or past use of antipsychotic drugs; (4) patients with a history of neurological disorders; (5) patients who were left-handed. The study was approved by the Ethics Committee of the Air Force Medical University and was conducted in accordance with the approved guidelines (Ethics Approval Number KY20193304-1). All participants provided their informed consent prior to undergoing the formal experiment and received a small amount of compensation.

Resting-state EEG data acquisition

Resting-state EEG data were collected for all subjects before the test. First, the subjects were instructed to sit down in front of a screen in a comfortable position, with their eyes distanced ~70 cm from the stimulating screen. When the subjects were ready, the experimenter instructed them to close their eyes for more than 1 min and then to open them for more than 1 min.

Task EEG data acquisition under material stimulation

After recording resting-state EEG data, the subjects were instructed to complete the exam using the 53-item questionnaire (containing 37 rumination items and 16 neutral items). Items were displayed on the screen randomly, with a fixed 500-ms plus sign separating each stimulus from the next. All items presented the same following question: "Does the above description induce you to have repeated/continuous recall?". The subjects selected "yes" or "no" as their response to this question using the mouse or keyboard. There were no time constraint for how long subjects were allowed to respond to each question. The item inquiry was completed as soon as the subject clicked the mouse to answer the questions.

EEG recording and data preprocessing

A 32-channel semi-dry electrode cap was used to record EEG data using a wireless multi-channel EEG acquisition device (ZhenTec NT1, ZhenTec Intelligence, China) (Yuan et al., 2021; Han et al., 2022). The sampling rate was 500 Hz. Data were referenced to CPz with a ground at FPz, and electrode placement followed the International 10-10 system. Impedance levels were set at <20 kΩ. The common mode rejection ratio was 120 dB, the input impedance was 1 G, and the input noise was <0.4 uVrms for all EEG channels.

For each subject, more than 2 min of resting-state EEG signals were recorded under two conditions: with eyes closed and with eyes open, with each condition lasting more than 1 min. Additionally, while participants completed the test items, EEG signals were acquired. All of the EEGs were pre-processed prior to the commencement of further research using the FildTrip (Version 20221122) (Oostenveld et al., 2011) toolbox implemented in MATLAB 2018b. We first checked the quality of the data and processed the band channel using the interpolation method. Both the resting state and task signals were notched by 50 Hz to remove power-line interference. Then, the EEGs were band filtered with a 1–100 Hz zero-phase band filter. Subsequently, the signals were divided into two 1-min epochs for the eyes-closed and eyes-open conditions for resting-state EEGs. We segmented the task EEGs into each item-related signal epoch based on the time markers of eye movements where signals were acquired simultaneously (53 items and 53 task signals for each participant in each channel). We manually checked and removed any data with large interference. The data were considered invalid if the faulty segments totaled more than five. The task EEG analysis was performed on 75 subjects—the average EEG length of the ruminator.

The remaining EEG data were then subjected to independent component analysis (ICA) to determine brain signals. Based on the spatial distribution and spectral power, FildTrip was used to find the independent components (ICs), including motor activity, eyeblinks, and ECG, which were then eliminated prior to further analysis.

EEG power analysis

After preprocessing, both the eyes-closed and eyes-open resting state signals were filtered into theta, delta, alpha, and beta bands. Then, we employed the "pwelch" function in MATLAB to calculate the spectral power during the resting state for all 30 channels in each of the four frequency bands: delta (0.5–4 Hz), theta (4–8 Hz), alpha (8–13 Hz), and beta (13–30 Hz).

Coherence analysis

Referring to the analysis method of a previous study by Bakker, we also adopted the coherence method to reflect the alternation in brain activity (den Bakker et al., 2018). The task EEG signals were then filtered into theta and gamma frequency bands (4–80 Hz). The bands were theta (4–8 Hz), alpha (8–13 Hz), beta (13–30 Hz), gamma1 (30–60 Hz), and gamma2 (60–80 Hz). Subsequently, we employed the "mscohere" function in MATLAB to calculate magnitude-squared coherence, which reflects how well signal x corresponds to signal y at each frequency band. The "mscohere" function estimates the magnitude-squared coherence function using Welch's overlapped averaged periodogram method (we used 512 points per window with 90% overlap). The coherence value of signals x and y $C_{xy}(f)$ was calculated as a function of the following: the spectral densities of signal x, which was denoted *as* $P_{xx}(f)$; the spectral densities of y, which was denoted as $P_{yy}(f)$; and the cross spectral density of x and y, which was denoted as $P_{xy}(f)$:

$$C_{xy}(f) = \frac{|P_{xy}(f)|^2}{P_{xx}(f)P_{yy}(f)}$$

Then, the coherence values were averaged across all pairs of electrodes over the brain for further analysis. We also calculated the average coherence in each band. To minimize the effects of volume conduction, we set the coherence of neighboring electrodes to zero before calculating the average coherence in each band (Peters et al., 2013; den Bakker et al., 2018).

Correlation between the coherence of EEGs and the arousal rate

The arousal rate of each participant induced by the rumination items was calculated as the proportion of "yes" responses given to the total number of rumination items. Finally, we adopted the Pearson correlation method to investigate the relationship between brain EEG coherence in different frequency bands and the arousal rate induced by the rumination items.

Statistical analysis

Both the behavior results and EEG characteristics were analyzed statistically using SPSS 26 (IBM). To examine the behavioral difference between the two groups across the two item types in each of the seven dimensions, a two-sample t-test was utilized. To determine the power differential of the resting-state EEGs in each frequency band, we utilized a two-way repeated ANOVA using the group and channel as factors. Mauchly's test was applied to test for sphericity, while the Greenhouse–Geisser correction was used to correct the sphericity. The coherence in the five bands was then compared, both in-group and item-wise. The statistical method was also referred to in the previous study (den Bakker et al., 2018). For group-wise comparison, we first employed a two-way repeated ANOVA with the item type and band as factors to compare the averaged coherence across the brain. The difference between the rumination items and the neutral items was determined using the two-sample t-test, and Bonferroni's correction was used for multiple comparisons ($p < 0.01$). We then adopted a two-way ANOVA using item type and frequency as factors to assess their differences in each frequency band (theta, alpha, beta, gamma1, and gamma2). For item-wise comparison, we set the group and band as factors and performed the same statistical procedure.

Results

Demographic information of the participants

Table 1 shows the demographic information of the 4,591 subjects who used the RRS. In this study, the total average score of the RRS was 31.57 ± 8.33 ($n = 4,591$), and Cronbach's α coefficient for this scale was 0.925 ($n = 4,591$).

Table 2 shows the demographic information of the 607 high-degree ruminators (577 men and 30 women) who participated in the semi-structured interviews.

Table 3 shows the demographic information of the 1,685 subjects. In this part, the total average score of the RRS was 28.64 ± 6.97 ($n = 1,685$), and Cronbach's α coefficient for this scale was 0.925 ($n = 1,685$).

Table 4 shows the demographic information of the 78 chosen subjects from the 1,685 pool of subjects who completed the questionnaire.

Table 5 shows the demographic information of the 75 participants who were recruited for the following EEG experiment.

Natural language feature adaptation paradigm

Using NLP techniques, we identified 17 ruminative scenario themes and constructed 37 ruminative arousal-inducing items (including 28 social dilemmas and 9 personal injuries). The validation results for the rumination questionnaire showed that the main effects of the item types were significant in all dimensions ($p < 0.001$). Further simple effect analysis showed that the ruminators' scores on rumination items were higher than those of the control group ($p < 0.05$), while the rumination group scores of the neutral items were no different from those of the control group (Figure 1). This result confirmed the effectiveness and reliability of the rumination items.

TABLE 5 Demographic information of the 75 participants who participated in the EEG study ($n = 75$).

	Frequency/mean	Percentage/standard deviation
Gender (*n*, %)		
Women	0	0
Men	75	100
Age (mean ± SD)	21.75	6.18
Home location (*n*, %)		
Urban	23	30.67
Village	52	69.33
Ethnicity (*n*, %)		
Han	66	88.00
Others	9	12.00

The reaction time was longer in ruminators for rumination items

The ANOVA of the two groups and item type revealed that the main effect of the two groups was not significant [$F_{(1,73)} = 0.792$, $p = 0.377$, $\eta p^2 = 0.11$], while the main effect of the item type was significant [$F_{(1,73)} = 107.968$, $p < 0.001$, $\eta p^2 = 0.597$], reflecting that the reaction time of rumination items was longer than that of the neutral items. Additionally, a significant interaction between item type and person category was found [$F_{(1,73)} = 31.901$, $p < 0.001$, $\eta p^2 = 0.304$]. Therefore, further simple effects analysis was conducted, and the results are as follows (Table 6).

The results of the simple effects analysis showed that the response time of the ruminators while engaging with rumination items was longer than that of the control group ($df = 73$, $p < 0.01$), while the response time of the ruminators while engaging with neutral items did not differ from that of the control group. This result further verified the effectiveness of the ruminative questionnaire in inducing the ruminators to immerse themselves in and resonate with the different scenarios established by the questionnaires.

The arousal rate was significantly higher in ruminators for rumination items

In the questionnaire response task, whether for the rumination items or the neutral items, we set the same following question: "Does the above description induce you to have repeated/continuous recall?". This question reflects the core definition of the concept of rumination. Therefore, we interpreted the choice of "yes" to mean that the participants were aroused by the scenario. Conversely, participants who chose "no" were not considered to be aroused.

Arousal rate: the arousal rates elicited by the two item types were calculated as the proportion of the given response "yes" to the total for each kind of item (i.e., the number of "yes" responses given in rumination items/the total number of rumination items).

The main effect of the two groups was found to be significant, $F_{(1,73)} = 32.554$, $p < 0.001$, $\eta p^2 = 0.308$, and the arousal rate of the ruminators was higher than that of the control group. The main

TABLE 6 Response times ($\bar{x}$ ± SD) of the ruminators and the controls (NC) on both item types.

Type of item	Ruminators ($n = 46$)	Controls ($n = 29$)	*t*	*P*
Rumination	15.731 ± 4.624	12.823 ± 3.143	−3.240	<0.01
Neutral	9.663 ± 4.045	11.028 ± 3.524	1.494	0.139

TABLE 7 Arousal rates ($\bar{x}$ ± SD) of the ruminators and controls on both item types.

Type of item	Ruminators ($n = 46$)	Controls ($n = 29$)	*t*	*P*
Rumination	0.616 ± 0.324	0.158 ± 0.187	−7.746	<0.001
Neutral	0.079 ± 0.146	0.082 ± 0.123	0.095	0.925

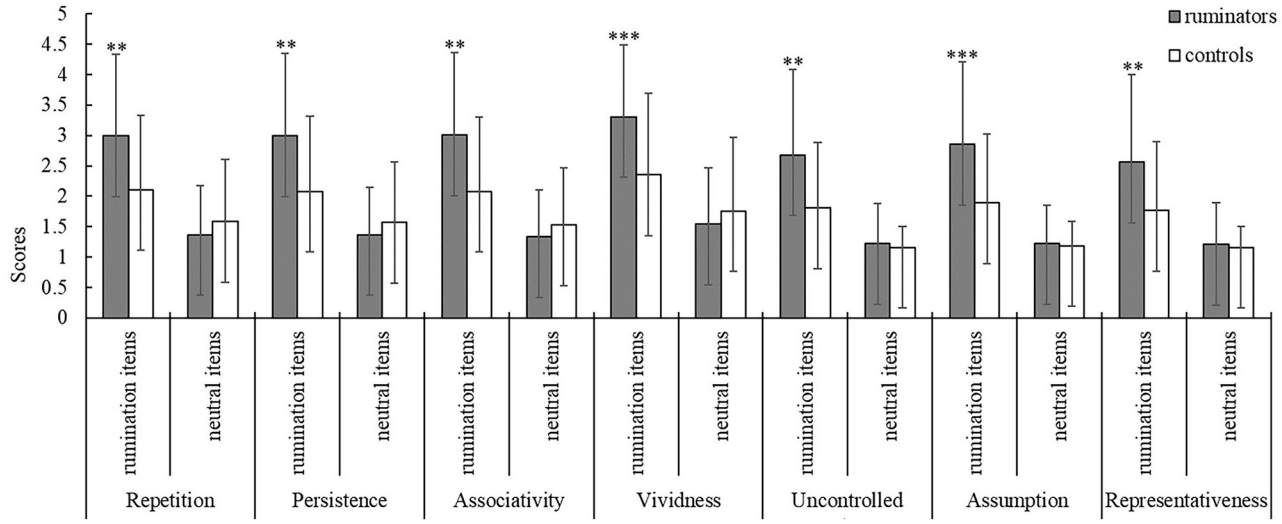

FIGURE 1
Comparison of ruminator and control subject scores on the rumination and neutral items under the seven dimensions. $^{**}p < 0.05$, $^{***}p < 0.001$, error line represents the standard deviation.

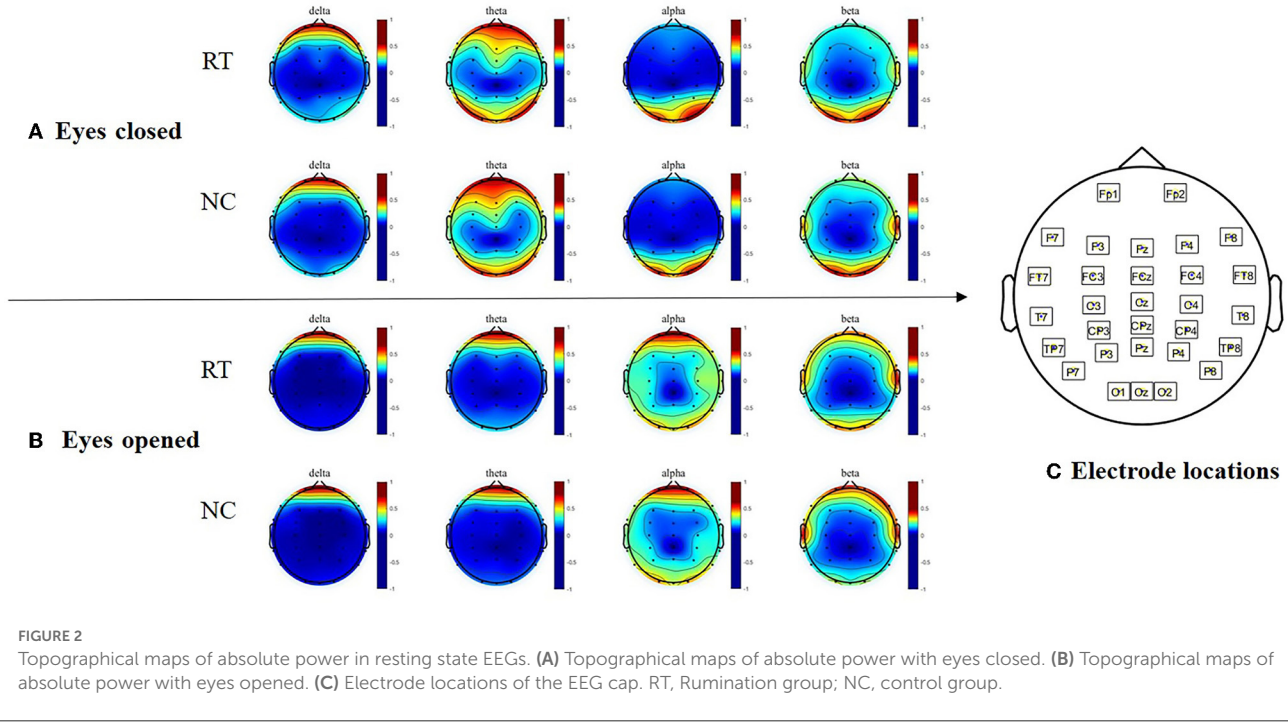

FIGURE 2
Topographical maps of absolute power in resting state EEGs. **(A)** Topographical maps of absolute power with eyes closed. **(B)** Topographical maps of absolute power with eyes opened. **(C)** Electrode locations of the EEG cap. RT, Rumination group; NC, control group.

effect of the item type was also significant, $F_{(1,73)} = 82.300$, $p < 0.001$, $\eta p^2 = 0.530$, and the arousal rate for the rumination items was higher than that for the neutral items. The main effect of the item type and group was found to be significant, $F_{(1,73)} = 82.300$, $p < 0.001$, $\eta p^2 = 0.530$, and was higher than that of the neutral items. A significant interaction of the item type with the two groups was found [$F_{(1,73)} = 46.382$, $p < 0.001$, $\eta p^2 = 0.389$]. Therefore, further simple effects analysis was conducted, and the results are as follows (Table 7).

The results of the simple effects analysis showed that, for the rumination items, the arousal of the ruminators was significantly higher than that of the control group ($df = 73$, $p < 0.001$), while for the neutral items, the arousal of the ruminators did not differ from that of the control group. This finding indicates that the rumination items constructed in this study targeted the recall of the rumination group and thus triggered continuous and repeated recall.

TABLE 8 Average EEG length (time points) of the two types of items in different groups ($\bar{x} \pm SD$).

Type of item	Ruminators ($n = 46$)	Controls ($n = 29$)
Rumination	6,750 ± 1,993	7,124 ± 2,146
Neutral	6,695 ± 2,274	6,709 ± 1,963

The brain power of normal subjects and high-degree rumination subjects were highly similar

The topography of the two groups in terms of the absolute power of each frequency band is depicted in Figure 2. In both the eyes-closed and eyes-open conditions, the two-way ANOVA did not reveal any group differences.

The coherence of the whole brain was decreased while engaging with the rumination items

Table 8 shows the average EEG length of each group in different kinds of items. No significant differences were found in the length of EEG data either in groups or items.

As shown in Figure 3, the coherence of the whole brain was decreased in both groups while engaging with the rumination items compared to the neutral items in the test. In the rumination group, the two-way repeated ANOVA revealed a significant main effect on the item type [$F_{(1,90)} = 9.445$, $p = 0.003$]. Additionally, a no item × frequency band interaction effect was found [Greenhouse–Geisser corrected, $F_{(1.452,130.724)} = 0.271$, $p = 0.691$]. All the two-sample *t*-tests for *post hoc* analysis satisfied the test of homogeneity of variance ($p > 0.05$) and revealed that the coherence decreased significantly in the theta (two-tail, $t = -3.373$, $df = 90$, $p = 0.001$), alpha ($t = -2.827$, $df = 90$, $p = 0.006$), beta ($t = -3.287$, $df = 90$, $p = 0.001$), and gamma1 ($t = -2.649$, $df = 90$, $p = 0.01$) bands. In the subjects from the control group, there was no significant effect of the item type [$F_{(1,56)} = 1.724$, $p = 0.195$] and no item type × frequency band interaction effect [Greenhouse–Geisser correction, $F_{(1.583,88.654)} = 0.015$, $p = 0.967$]. The two-sample *t*-test showed no significant change in the coherence in the five bands while engaging with the two kinds of items in the normal subject group.

The coherence of the whole brain increased in the rumination group

Next, we assessed the difference in coherence between the subjects from both groups while they were engaged with the two kinds of items. As shown in Figure 4, the coherence of all frequency bands increased [main effect of group $F_{(1,73)} = 4.916$, $p = 0.030$, no group × frequency band interaction effect, $F_{(1.496,109.172)} = 0.834$, $p = 0.407$, Greehouse-Geisser corrected], especially for the beta (two-tail, $t = 2.301$, $df = 71.088$ $p = 0.017$) and gamma2 (two-tail, $t = 2.411$, $df = 72.953$, $p = 0.018$) bands while the subjects were engaged with the rumination test. It is worth noting that the two groups showed a significant difference while interacting with the neutral items [main effect of group $F_{(1,73)} = 16.844$, $p < 0.000$, no group × frequency band interaction effect, $F_{(1.538,112.238)} = 1.467$, $p = 0.235$, Greehouse-Geisser corrected]. As Figure 4D shows, significantly increased coherence emerged in all frequency bands (two-tail: theta, $t = 4.698$, $df = 72.949$, $p < 0.000$; alpha, $t = 4.160$, $df = 72.224$, $p < 0.000$; beta, $t = 4.684$, $df = 72.210$, $p < 0.000$; gamma1, $t = 3.446$, $df = 71.754$, $p = 0.001$, and gamma2, $t = 4.057$, $df = 72.662$, $p < 0.000$) in ruminators engaging with the neutral items compared to the normal subjects. This phenomenon may have been due to the decreasing speed of the ruminative mood. This will be discussed later.

The arousal rate was only significantly correlated with the coherence of the gamma2 frequency band

We conducted a Pearson correlation analysis to identify the relationship between the arousal rate induced by the rumination items and the EEG coherence of different frequency bands. We only found a significant correlation for the gamma2 band ($r = 0.231$, $p = 0.046$).

Discussion

In this study, we first developed an immersive rumination-inducing questionnaire that could elicit situational recall in ruminators using NLP combined with scales, interviews, and "scenario immersion" theory. The results of behavioral indicators revealed that, for the rumination items of the questionnaire, the average reaction time was longer for the ruminators, and their arousal rate was significantly higher than that of the subjects in the control group. Then, we used EEG techniques to investigate whether the immersive ruminative questionnaire could induce certain neural activities, specifically in the ruminators. The resting-state EEG results showed that there was no difference in the power of the brain between the ruminators and the control group. However, the EEG coherence analysis showed that the brain activity of the ruminators was significantly higher than that of the control group for the rumination items. Combined with the behavior result and EEG evidence, the immersive ruminative questionnaire developed with natural language features and the scenario immersion theory was successful in eliciting more immersive ruminative thinking, specifically in the ruminators. In conclusion, the questionnaire based on NLP appears to be suitable as a novel paradigm for psychological selection in the early detection of mental disorders.

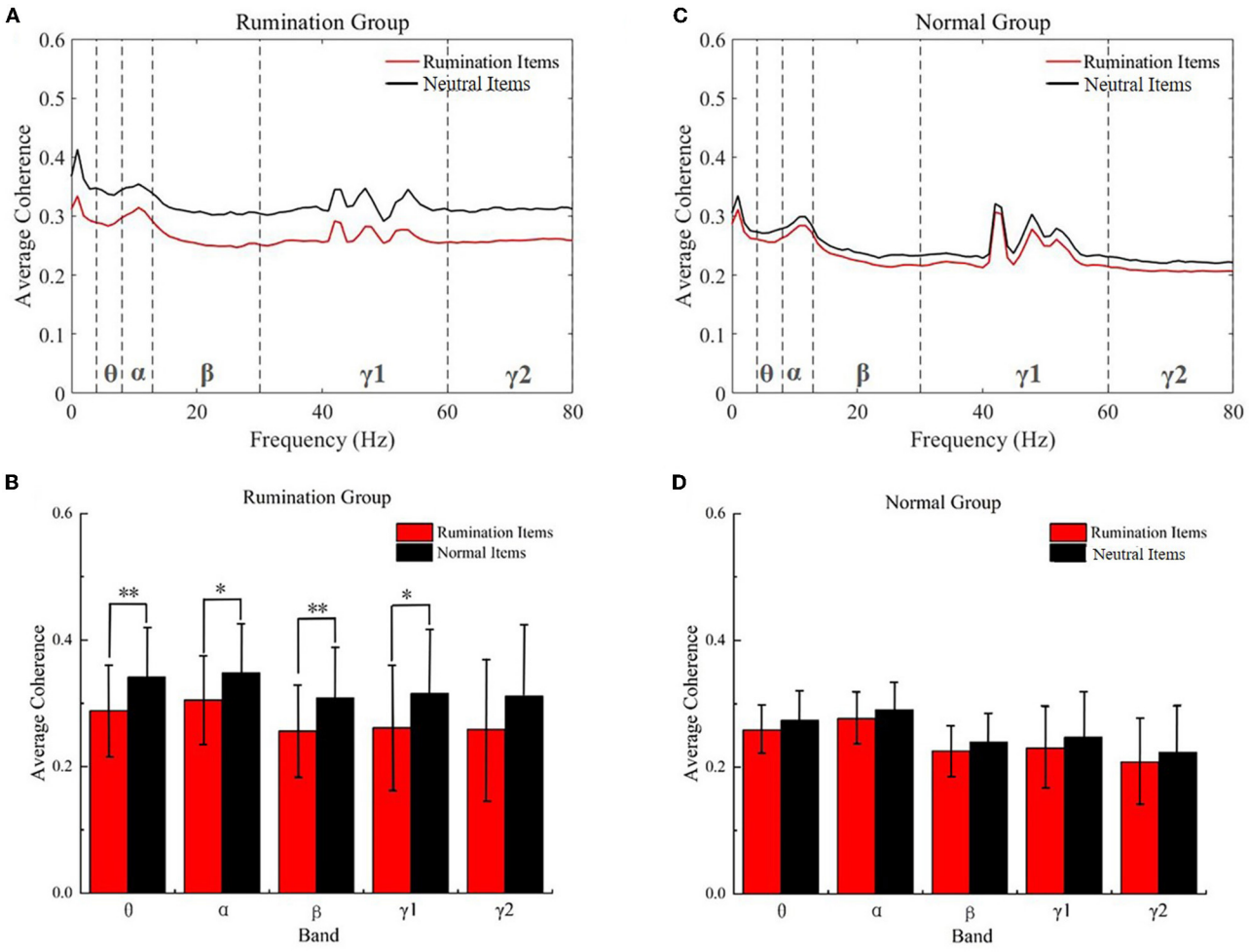

FIGURE 3
Within the group coherence analysis, the subjects completed the rumination items and neutral items. **(A)** Average coherence of all frequency bands in the rumination group. **(B)** Average coherence for the five frequency bands in the rumination group. **(C)** Average coherence of all frequency bands in the controls. **(D)** Average coherence in the five frequency bands in the controls. *$p < 0.01$, **$p < 0.001$. Red, rumination items; black, neutral items; Normal Groups means control groups.

The immersive ruminative questionnaire elicited immersive ruminative thinking, specifically in the ruminators

Previous studies have used various methods to induce rumination, including short statement prompts (Cooney et al., 2010; Berman et al., 2014; Milazzo et al., 2016), texts extracted from Wikipedia (Curci et al., 2015), characteristic words (Yoshimura et al., 2009; Moran et al., 2014; Apazoglou et al., 2019), music clips (Figueroa et al., 2017), self-reports (Rosenbaum et al., 2018a), emotive facial expressions (Aker et al., 2014), goal prompting tasks (Zhan et al., 2017; Mollaahmetoglu et al., 2021), videos (Bostanov et al., 2018), and other materials. However, it remains unclear whether these methods successfully induce subjects' rumination. Natural language is the first means by which humans express their thoughts and rapidly communicate accurately (Sun et al., 2013; Lee et al., 2014). Written materials pertaining to specific episodic memories represent one of the most effective forms of content to induce rumination (Haque et al., 2014; Wilson-Mendenhall et al., 2019). Rapidly developing NLP technology and "scenario immersion" theory provide us with technical support and a theoretical basis for constructing state-inducing questionnaires.

In this study, we used the natural language corpus of 607 ruminators and NLP to develop a mental state-eliciting questionnaire that could elicit situational memories according to "scenario immersion" theory to activate the unique ruminative state of rumination-prone individuals both effectively and accurately. The evaluation results showed that the scores of ruminators were significantly higher than those of the control group only on the rumination items in all dimensions. On the contrary, there was no significant difference between the neutral items. Therefore, the results indicate that the ruminators agreed with the scenario description constructed by the rumination items, which could not only trigger repeated, vivid, and continuous negative immersive memories but was also highly representative of ruminative elicitation. In other words, the questionnaire we developed could elicit immersive ruminative thinking in ruminators.

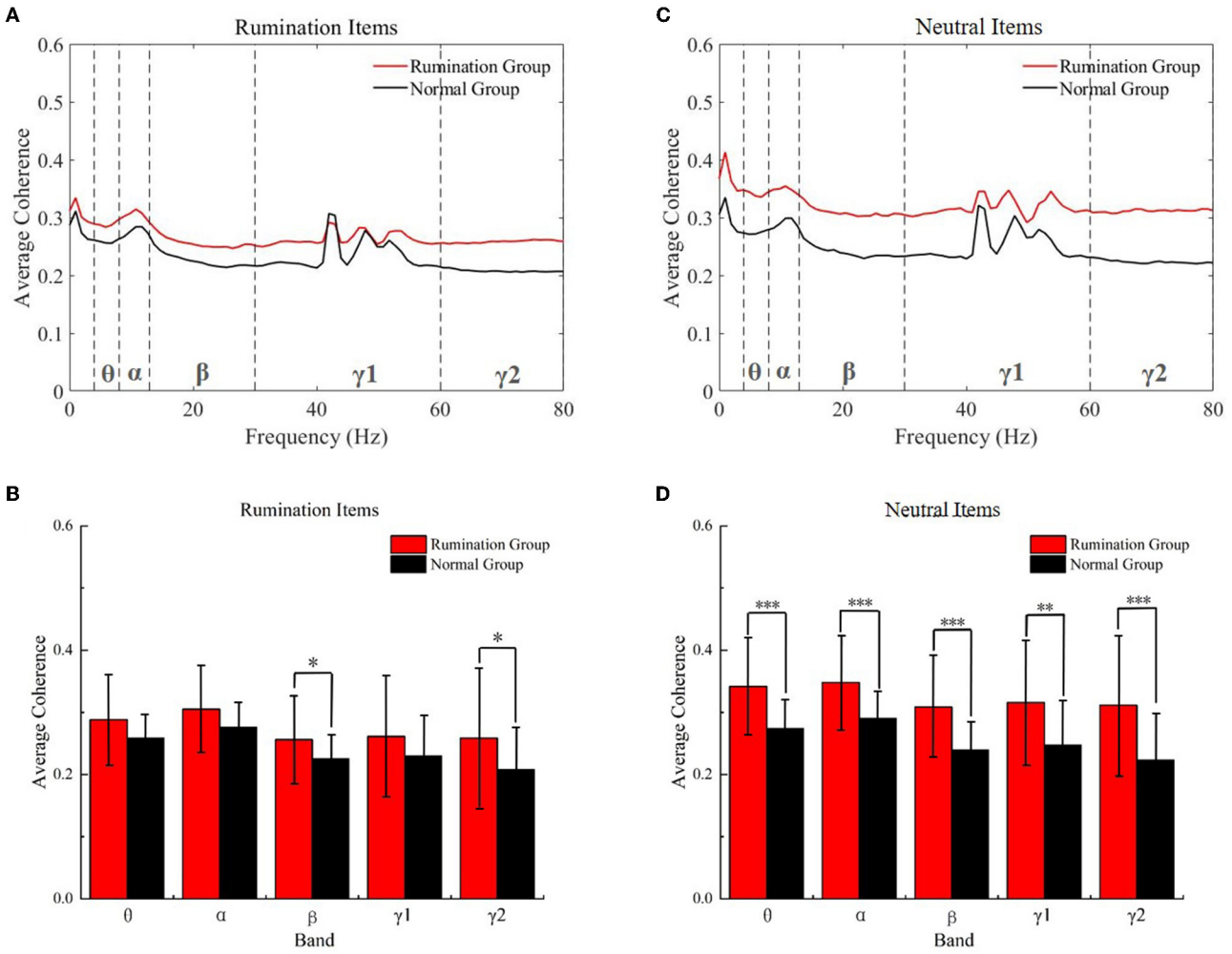

FIGURE 4
Within-item coherence analysis of the two groups while they engaged with the rumination items and neutral items. **(A)** Average coherence of all frequency bands in the rumination items. **(B)** Average coherence of the five frequency bands in the rumination items. **(C)** Average coherence of all frequency bands in the neutral items. **(D)** Average coherence of the five frequency bands in the neutral items. *$p < 0.01$, **$p < 0.001$, ***$p < 0.001$. Red, rumination items; black, neutral items; Normal Groups means control groups.

The rumination items were capable of inducing brain activity in ruminators

The analysis of EEG power in the four frequency bands revealed no significant difference between the ruminators and the control group while they were at rest, indicating that there was no difference in brain activity between the ruminators and the control group in this state, which might be a contributing factor to the difficulty of diagnosing depression during its nonclinical state.

EEG coherence is a measure of synchronization of the two recorded EEG signals and has been widely used to indict the dysregulation of the human brain (den Bakker et al., 2018; Minami et al., 2022; Wang et al., 2022). We examined the task EEG data from both the item type aspect and group aspect to study if the different items could elicit different brain activities in the two groups. First, we discovered that EEG coherence decreased in both groups while subjects engaged with the rumination items. The ruminators presented a significantly greater decrease in the theta, alpha, beta, and gamma frequency bands. Although a slight decrease was also observed in the control group, no statistically significant differences were identified for any of the frequency bands. EEG coherence reflects the synchronization between brain cortical regions (Markovska-Simoska et al., 2018), whereby the observed significant decrease in the coherence of the whole brain indicates that the rumination items caused more dyssynchronization of the whole brain in the ruminators, thereby demonstrating that the questionnaire was capable of inducing ruminative thinking in these subjects. We also discovered that the EEG coherence of the ruminators dramatically increased both in the beta and gamma2 bands compared to the control group while engaging with the rumination items. In the ruminators, this aberrantly elevated coherence may indicate a decreased inhibitory ability of the brain, which might be caused by a depressed state of mind (Cheng et al., 2016), excessive self-focus, and the recall of unpleasant memories that the rumination items elicited (Berman et al., 2011; Zamoscik et al., 2014). The hyper-synchronization in the beta band combined with the longer reaction time suggests

that the attention ability was damaged in the ruminators (Li et al., 2017). As the EEG gamma band has been shown to be related to emotions (Li et al., 2015), the increased coherence observed in the gamma2 band provides evidence that the rumination items induced an unpleasant mood in the ruminators. Finally, we found that the coherence of the whole brain in the five frequency bands increased significantly, which can be explained by the phenomenon where the influence of the rumination items did not subside immediately in the ruminators but instead was prolonged to influence the brain activity of these subjects while they were engaged with the neutral items. This also indicates a decline in their ability to control the brain after engaging with the rumination items.

The above findings showed that ruminators are more susceptible to negative scenarios, such as poor memories, bad moods, and inaccurate self-referential thinking. Over the past several years, studies have been conducted to identify the neurological bases of rumination in both clinical and nonclinical psychological diseases with the goal of developing potential biomarkers for the diagnosis and therapy of rumination-related mood disorders such as depression (Zhang et al., 2020), euthymic bipolar disease (Apazoglou et al., 2019), posttraumatic stress disorder (Philippi et al., 2020), and so on. Prior fMRI and EEG studies revealed that rumination is associated with altered brain functional connectivity, both increased (Benschop et al., 2020) and decreased (Tozzi et al., 2021). According to some studies, ruminators process self-related information excessively when exposed to external, which may be related to the overactive core subsystem in the default mode network (Lin et al., 2022), particularly the functional connectivity to the prefrontal cortex, which can be a useful neural marker to identify an individual at risk for depression (Benschop et al., 2020). Consistent with the findings of previous studies, we found that the EEG coherence of the whole brain increased significantly in the ruminators, suggesting that, through situational immersion, the questionnaire we developed can elicit excessive processing of self-related information in the high ruminators. This result indicates the validity of the questionnaire we developed. However, more research is required to determine the neurological mechanisms underlying the brain alteration that the questionnaire elicited, i.e., the prefrontal cortex activity and the relationship between different brain networks, which might be used as a neural marker of ruminative thinking.

Limitations

There are some limitations to this study. First, all the participants were men due to the nature of the police academy. Although it is widely acknowledged that women tend to ruminate more than men do, one review reported that both men and women showed strong and significant statistical correlations between depressive symptoms and ruminative thoughts (rho $>$ 0.50; $p < 0.05$), suggesting that the relationship between depressive symptoms and rumination does not necessarily explain the sex differences observed in depression (Shors et al., 2017). Hence, further study is required to explore the responses of women. Moreover, since all the subjects were enrolled in the Shaanxi Police College, more subjects will be needed from the general population in the following experiment. Second, the EEG evidence of ruminative thoughts from the perspective of the entire brain was the focus of this study, while specific brain regions or brain networks should be considered to identify the neuromechanism underlying rumination. Finally, neural biomarkers of rumination may be used to predict ruminators, which would be of great significance in psychological selection. In the future, we will explore the predictive power of the rumination items and EEG data.

Data availability statement

The original contributions presented in the study are included in the article/Supplementary material, further inquiries can be directed to the corresponding authors.

Ethics statement

The studies involving human participants were reviewed and approved by Ethics Committee of the Air Force Medical University. The patients/participants provided their written informed consent to participate in this study.

Author contributions

YuL contributed to the development of the questionnaire and completed the whole experiment. CL analysis the EEG data and wrote the manuscript. TZ and LWu contributed to revision of the manuscript. XL, YiL, and LWa helped to analyze the questionnaire behavior data. DL and HY contribute big work to the experiment. DM and PF organized and managed the whole experiment and manuscript. All authors contributed to the article and approved the submitted version.

Funding

This study was financially supported by the Science and Technology Innovation Special Zone Project (18-163-15-ZT-001-007-37), China Postdoctoral Science Foundation (2019M653963), Scientific and Technological Research Projects for Major Problems in Aviation Medicine (2020ZTD01), Air Force Medical University Everest project (2020cyjhfp), and Medical Science and Technology Youth Cultivation Plan (20QNPY049).

Conflict of interest

The authors declare that the research was conducted in the absence of any commercial or financial relationships that could be construed as a potential conflict of interest.

Publisher's note

All claims expressed in this article are solely those of the authors and do not necessarily represent those of

their affiliated organizations, or those of the publisher, the editors and the reviewers. Any product that may be evaluated in this article, or claim that may be made by its manufacturer, is not guaranteed or endorsed by the publisher.

Supplementary material

The Supplementary Material for this article can be found online at: https://www.frontiersin.org/articles/10.3389/fnins.2023.1118650/full#supplementary-material

References

Aker, M., Harmer, C., and Landrø, N. I. (2014). More rumination and less effective emotion regulation in previously depressed women with preserved executive functions. *BMC Psychiatry* 14, 334. doi: 10.1186/s12888-014-0334-4

Ancin-Murguzur, F. J., and Hausner, V. H. (2021). CausalizeR: a text mining algorithm to identify causal relationships in scientific literature. *PeerJ* 9, e11850. doi: 10.7717/peerj.11850

Apazoglou, K., Küng, A., Cordera, P., Aubry, J., Dayer, A., Vuilleumier, P., et al. (2019). Rumination related activity in brain networks mediating attentional switching in euthymic bipolar patients. *Int. J. Bipolar Disord.* 7, 3. doi: 10.1186/s40345-018-0137-5

Assale, M., Dui, L. G., Cina, A., Seveso, A., and Cabitza, F. (2019). The revival of the notes field: leveraging the unstructured content in electronic health records. *Front. Med.* 6, e00066. doi: 10.3389/fmed.2019.00066

Benschop, L., Poppa, T., Medani, T., Shahabi, H., Baeken, C., Leahy, R. M., et al. (2020). Electrophysiological scarring in remitted depressed patients: elevated EEG functional connectivity between the posterior cingulate cortex and the subgenual prefrontal cortex as a neural marker for rumination. *J. Affect. Disord.* 281, 493–501. doi: 10.1016/j.jad.2020.12.081

Berman, M., Peltier, G., Scott, N., Evan, D., and Patricia, J. (2011). Depression, rumination and the default network. *Soc. Cogn. Affect. Neurosci.* 6, 548–555. doi: 10.1093/scan/nsq080

Berman, M. G., Misic, B., Buschkuehl, M., Kross, E., Deldin, P. J., Peltier, S., et al. (2014). Does resting-state connectivity reflect depressive rumination? A tale of two analyses. *NeuroImage* 103, 267–279. doi: 10.1016/j.neuroimage.2014.09.027

Blei, D. M., Ng, A., and Jordan, M. I. (2003). Latent dirichlet allocation. *J. Mach. Learn. Res.* 3, 993–1022. doi: 10.1162/jmlr.2003.3.4-5.993

Bostanov, V., Ohlrogge, L., Britz, R., Hautzinger, M., and Kotchoubey, B. (2018). Measuring mindfulness: a psychophysiological approach. *Front. Hum. Neurosci.* 12, e00249. doi: 10.3389/fnhum.2018.00249

Castanheira, L., Silva, C., Cheniaux, E., and Telles-Correia, D. (2019). Neuroimaging correlates of depression-implications to clinical practice. *Front Psychiatry* 10, 703. doi: 10.3389/fpsyt.2019.00703

Cheng, W., Rolls, E. T., Qiu, J., Liu, W., Tang, Y., Huang, C., et al. (2016). Medial reward and lateral non-reward orbitofrontal cortex circuits change in opposite directions in depression. *Brain.* 139, 3296–3309. doi: 10.1093/brain/aww255

Cooney, R. E., Joormann, J., F., Eugène, Dennis, E. L., and Gotlib, I. H. (2010). Neural correlates of rumination in depression. *Cogn. Affect. Behav. Neurosci.* 10, 470–478. doi: 10.3758/CABN.10.4.470

Curci, A., Soleti, E., Lanciano, T., Doria, V., and Rimé, B. (2015). Balancing emotional processing with ongoing cognitive activity: the effects of task modality on intrusions and rumination. *Front. Psychol.* 6, e01275. doi: 10.3389/fpsyg.2015.01275

den Bakker, H., Sidorov, M. S., Fan, Z., Lee, D. J., Bird, L. M., Chu, C. J., et al. (2018). Abnormal coherence and sleep composition in children with Angelman syndrome: a retrospective EEG study. *Mol. Autism* 9, 32. doi: 10.1186/s13229-018-0214-8

Deshpande, G., Rangaprakash, D., Oeding, L., Cichocki, A., and Hu, X. P. (2017). A new generation of brain-computer interfaces driven by discovery of latent EEG-fMRI linkages using tensor decomposition. *Front. Neurosci.* 11, e00246. doi: 10.3389/fnins.2017.00246

Dunning, D., Heath, C., and Suls, J. M. (2005). *Picture Imperfect*. Scientific American Mind.

Ferdek, M. A., van Rijn, C. M., and Wyczesany, M. (2016). Depressive rumination and the emotional control circuit: an EEG localization and effective connectivity study. *Cogn. Affect. Behav. Neurosci.* 16, 1099–1113. doi: 10.3758/s13415-016-0456-x

Ferrario, A., Demiray, B., Yordanova, K., Luo, M., and Martin, M. (2020). Social reminiscence in older adults' everyday conversations: automated detection using natural language processing and machine learning. *J. Med. Internet Res.* 22, e19133. doi: 10.2196/19133

Figueroa, C. A., Mocking, R. J. T., van Wingen, G., Martens, S., Ruhé, H. G., and Schene, A. H. (2017). Aberrant default-mode network-hippocampus connectivity after sad memory-recall in remitted-depression. *Social Cogn. Affect. Neurosci.* 12, 1803–1813. doi: 10.1093/scan/nsx108

Ghosh, D. D., and Guha, R. (2013). What are we 'tweeting' about obesity? Mapping tweets with topic modeling and Geographic Information System. *Cartogr. Geogr. Inform. Sci.* 40, 90–102. doi: 10.1080/15230406.2013.776210

Han, C., Xu, G., Zheng, X., Tian, P., Zhang, K., Yan, W., et al. (2022). Assessing the effect of the refresh rate of a device on various motion stimulation frequencies based on steady-state motion visual evoked potentials. *Front. Neurosci.* 15, e757679. doi: 10.3389/fnins.2021.757679

Han, X., and Yang, H. (2009). Chinese version of Nolen-Hoeksema ruminative responses scale (RRS) used in 912 college students: reliability and validity. *Chin. J. Clin. Psychol.* 5, 550–551

Hao, H., Zhang, K., Wang, W., and Gao, G. (2017). A tale of two countries: international comparison of online doctor reviews between China and the United States. *Int. J. Med. Inform.* 99, 37–44. doi: 10.1016/j.ijmedinf.2016.12.007

Haque, S., Juliana, E., Khan, R., and Hasking, P. (2014). Autobiographical memory and hierarchical search strategies in depressed and non-depressed participants. *BMC Psychiatry* 14, 310. doi: 10.1186/s12888-014-0310-z

Jurafsky, D. M. J. H. (2009). *Speech and Language Processing, 2nd Edn*. Prentice Hall Series in Artificial Intelligence.

Lebois, L. A. M., Wilson-Mendenhall, C. D., Simmons, W. K., Barrett, L. F., and Barsalou, L. W. (2020). Learning situated emotions. *Neuropsychologia* 145, 106637. doi: 10.1016/j.neuropsychologia.2018.01.008

Lee, M. C., Chang, J. W., and Hsieh, T. C. (2014). A grammar-based semantic similarity algorithm for natural language sentences. *Sci. World J.* 2014, 1–17. doi: 10.1155/2014/437162

Li, B. J., Karl, F., Maria, M., Wang, H. N., Lu, H. B., and Hu, D. W. (2018). A brain network model for depression: from symptom understanding to disease intervention. *CNS Neurosci. Therap.* 24, 1004–1019. doi: 10.1111/cns.12998

Li, E. T., Luyten, P., and Midgley, N. (2020). Psychological mediators of the association between childhood emotional abuse and depression: a systematic review. *Front. Psychiatry* 11, 559213. doi: 10.3389/fpsyt.2020.559213

Li, H., Zhao, Q., Huang, F., Cao, Q., Qian, Q., Johnstone, S. J., et al. (2017). Increased beta activity links to impaired emotional control in ADHD adults with high IQ. *J. Atten. Disord.* 23, 754–764. doi: 10.1177/1087054717739120

Li, Y., Cao, D., Wei, L., Tang, Y., and Wang, J. (2015). Abnormal functional connectivity of EEG gamma band in patients with depression during emotional face processing. *Clin. Neurophysiol.* 126, 2078–2089. doi: 10.1016/j.clinph.2014.12.026

Lin, W., He, H., and Guan, Q. (2022). Functional brain networks underlying rumination. *Adv. Psychol. Sci.* 30, 1262–1269. doi: 10.3724/SP.J.1042.2022.01262

Markovska-Simoska, S., Pop-Jordanova, N., and Pop-Jordanov, J. (2018). Inter- and intra-hemispheric EEG coherence study in adults with neuropsychiatric disorders. *Prilozi* 39, 5–19. doi: 10.2478/prilozi-2018-0037

Miao, B., Liu, X., and Zhu, T. (2021). Automatic mental health identification method based on natural gait pattern. *PsyCh J.* 8, 434. doi: 10.1002/pchj.434

Milazzo, A., Ng, B., Jiang, H., Shirer, W., Varoquaux, G., Poline, J. B., et al. (2016). Identification of mood-relevant brain connections using a continuous, subject-driven rumination paradigm. *Cerebral. Cortex* 26, 933–942. doi: 10.1093/cercor/bhu255

Min, J. Y., Song, S. H., Kim, H. J., and Min, K. B. (2019). Mining hidden knowledge about illegal compensation for occupational injury: topic model approach. *JMIR Med. Inform.* 7, e14763. doi: 10.2196/14763

Min, K., Song, S., and Min, J. (2020). Topic modeling of social networking service data on occupational accidents in Korea: latent dirichlet allocation analysis. *J. Med. Internet Res.* 22, e19222. doi: 10.2196/19222

Minami, S., Kato, M., Ikeda, S., Yoshimura, M., Ueda, S., Koshikawa, Y., et al. (2022). Association between the rostral anterior cingulate cortex and anterior insula in the salience network on response to antidepressants in major depressive

disorder as revealed by isolated effective coherence. *Neuropsychobiology* 81, 475–483. doi: 10.1159/000525338

Mollaahmetoglu, O. M., Palmer, E., Maschauer, E., Nolan, M. C., Stevens, T., Carlyle, M., et al. (2021). The acute effects of alcohol on state rumination in the laboratory. *Psychopharmacology* 238, 1671–1686. doi: 10.1007/s00213-021-05802-1

Moran, J. M., Macrae, C. N., Heatherton, T. F., Wyland, C. L., and Kelley, W. M. (2014). Neuroanatomical evidence for distinct cognitive and affective components of self. *J. Cogn. Neurosci.* 18, 1586–1594. doi: 10.1162/jocn.2006.18.9.1586

Nolen-Hoeksema, S. (1991). Responses to depression and their effects on the duration of depressive episodes. *J. Abnormal Psychol. (1965)* 100, 569–582. doi: 10.1037/0021-843X.100.4.569

Nolen-Hoeksema, S., and Morrow, J. (1991). A prospective study of depression and posttraumatic stress symptoms after a natural disaster: the 1989 Loma Prieta Earthquake. *J. Pers. Soc. Psychol.* 61, 115–121. doi: 10.1037/0022-3514.61.1.115

Nolen-Hoeksema, S., Wisco, B. E., and Lyubomirsky, S. (2008). Rethinking rumination. *Perspect. Psychol. Sci.* 3, 400–424. doi: 10.1111/j.1745-6924.2008.00088.x

Nolen-Hoeksema, S., Wolfson, A., Mumme, D., and Guskin, K. (1995). Helplessness in children of depressed and nondepressed mothers. *Develop. Psychol.* 31, 377–387 doi: 10.1037/0012-1649.31.3.377

Oostenveld, R., Fries, P., Maris, E., and Schoffelen, J. M. (2011). FieldTrip: open source software for advanced analysis of MEG, EEG, and invasive electrophysiological data. *Comput. Intellig. Neurosci.* 2011, 156869. doi: 10.1155/2011/156869

Peters, J. M., Taquet, M., Vega, C., Jeste, S. S., Fernandez, I. S., Tan, J., et al. (2013). Brain functional networks in syndromic and non-syndromic autism: a graph theoretical study of EEG connectivity. *BMC Med.* 11, 54. doi: 10.1186/1741-7015-11-54

Philippi, C. L., Pessin, S., Reyna, L., Floyd, T., and Bruce, S. E. (2020). Cortical midline structures associated with rumination in women with PTSD. *J. Psychiatric Res.* 131, 69–76. doi: 10.1016/j.jpsychires.2020.09.001

Reviewer-Lee, L. (2000). *Review of "Foundations of Statistical Natural Language Processing"*, eds C. D. Manning and H. Schütze. The MIT Press.

Robinson, P. A. (2003). Neurophysical theory of coherence and correlations of electroencephalographic and electrocorticographic signals. *J. Theor. Biol.* 222, 163–175. doi: 10.1016/S0022-5193(03)00023-7

Rosenbaum, D., Hilsendegen, P., Thomas, M., Haeussinger, F. B., Nuerk, H., Fallgatter, A. J., et al. (2018a). Disrupted prefrontal functional connectivity during post-stress adaption in high ruminators. *Sci. Rep.* 8, 15588. doi: 10.1038/s41598-018-33777-1

Rosenbaum, D., Thomas, M., Hilsendegen, P., Metzger, F. G., Haeussinger, F. B., Nuerk, H., et al. (2018b). Stress-related dysfunction of the right inferior frontal cortex in high ruminators: an fNIRS study. *NeuroImage: Clin.* 18, 510–517. doi: 10.1016/j.nicl.2018.02.022

Schwarz, N. (2012). *Why Researchers Should Think "Real-Time": A Cognitive Rationale: Handbook of Research Methods for Studying Daily Life.*

Shors, T. J., Millon, E. M., Chang, H. Y. M., Olson, R. L., and Alderman, B. L. (2017). Do sex differences in rumination explain sex differences in depression? *J. Neurosci. Res.* 95, 711–718. doi: 10.1002/jnr.23976

Sun, W., Rumshisky, A., and Uzuner, O. (2013). Temporal reasoning over clinical text: the state of the art. *J. Am. Med. Inform. Assoc.* 20, 814–819. doi: 10.1136/amiajnl-2013-001760

Sutherland, K., and Bryant, R. A. (2007). Rumination and overgeneral autobiographical memory. *Behav. Res. Ther.* 45, 2407–2416. doi: 10.1016/j.brat.2007.03.018

Tozzi, L., Zhang, X., Chesnut, M., Holt-Gosselin, B., Ramirez, C. A., and Williams, L. M. (2021). Reduced functional connectivity of default mode network subsystems in depression: Meta-analytic evidence and relationship with trait rumination. *NeuroImage: Clin.* 30, 102570. doi: 10.1016/j.nicl.2021.102570

Van Doorn, M., Nijhuis, L. A., Egeler, M. D., Daams, J. G., Popma, A., van Amelsvoort, T., et al. (2021). Online indicated preventive mental health interventions for youth: a scoping review. *Front. Psychiatry* 12, 580843. doi: 10.3389/fpsyt.2021.580843

Wang, X., Liu, X., Wang, Y., and Zhu, T. (2021). How can people express their trait self-esteem through their faces in 3D space? *Front. Psychol.* 12, e591682. doi: 10.3389/fpsyg.2021.591682

Wang, X., Wang, Y., Zhou, M., Li, B., and Zhu, T. (2020). Identifying psychological symptoms based on facial movements. *Front. Psychiatry* 168, S58. doi: 10.3389/fpsyt.2020.607890

Wang, Z., Dong, F., Sun, Y., Wang, J., Zhang, M., Xue, T., et al. (2022). Increased resting-state alpha coherence and impaired inhibition control in young smokers. *Front. Neurosci.* 16, e1026835. doi: 10.3389/fnins.2022.1026835

Watkins, E. R., and Roberts, H. (2020). Reflecting on rumination: consequences, causes, mechanisms and treatment of rumination. *Behav. Res. Ther.* 127, 103573. doi: 10.1016/j.brat.2020.103573

Wells, A., and Matthews, G. (1996). Modelling cognition in emotional disorder: the S-REF model. *Behav. Res. Ther.* 34, 881–888. doi: 10.1016/S0005-7967(96)00050-2

Wilson-Mendenhall, C. D., Barrett, L. F., and Barsalou, L. W. (2015). Variety in emotional life: within-category typicality of emotional experiences is associated with neural activity in large-scale brain networks. *Soc. Cogn. Affect. Neurosci.* 10, 62–71. doi: 10.1093/scan/nsu037

Wilson-Mendenhall, C. D., Henriques, A., Barsalou, L. W., and Barrett, L. F. (2019). Primary interoceptive cortex activity during simulated experiences of the body. *J. Cogn. Neurosci.* 31, 221–235. doi: 10.1162/jocn_a_01346

Yadav, N., Noble, C., Niemeyer, J. E., Terceros, A., Victor, J., Liston, C., et al. (2022). Prefrontal feature representations drive memory recall. *Nature* 608, 153–160. doi: 10.1038/s41586-022-04936-2

Yoshimura, S., Ueda, K., Suzuki, S., Onoda, K., Okamoto, Y., and Yamawaki, S. (2009). Self-referential processing of negative stimuli within the ventral anterior cingulate gyrus and right amygdala. *Brain Cogn.* 69, 218–225. doi: 10.1016/j.bandc.2008.07.010

Yuan, Z., Peng, Y., Wang, L., Song, S., Chen, S., Yang, L., et al. (2021). Effect of BCI-controlled pedaling training system with multiple modalities of feedback on motor and cognitive function rehabilitation of early subacute stroke patients. *IEEE Trans. Neural Syst. Rehabil. Eng.* 29, 2569–2577. doi: 10.1109/TNSRE.2021.3132944

Zamoscik, V., Huffziger, S., Ebner-Priemer, U., Kuehner, C., and Kirsch, P. (2014). Increased involvement of the parahippocampal gyri in a sad mood predicts future depressive symptoms. *Soc. Cogn. Affect. Neurosci.* 12, 2034–2040. doi: 10.1093/scan/nsu006

Zhan, J., Tang, F., He, M., Fan, J., Xiao, J., Liu, C., et al. (2017). Regulating rumination by anger: evidence for the mutual promotion and counteraction (MPMC) theory of emotionality. *Front. Psychol.* 8, e01871. doi: 10.3389/fpsyg.2017.01871

Zhang, R., Kranz, G., Zou, W., Deng, Y., Huang, X., Lin, K., et al. (2020). Rumination network dysfunction in major depression: a brain connectome study. *Prog. Neuro-Psychopharmacol. Biol. Psychiatry* 98, 109819. doi: 10.1016/j.pnpbp.2019.109819

frontiers | Frontiers in Neuroscience

TYPE Review
PUBLISHED 14 March 2023
DOI 10.3389/fnins.2023.1136143

OPEN ACCESS

EDITED BY
Jing Teng,
North China Electric Power University, China

REVIEWED BY
Songlin Zhou,
Nantong University, China
Luiz Royes,
Federal University of Santa Maria, Brazil

*CORRESPONDENCE
Yan-Ling Yang
✉ yangyanling8889@163.com

†These authors share first authorship

SPECIALTY SECTION
This article was submitted to Translational Neuroscience, a section of the journal Frontiers in Neuroscience

RECEIVED 02 January 2023
ACCEPTED 27 February 2023
PUBLISHED 14 March 2023

CITATION
Bai X-Y, Liu X-L, Deng Z-Z, Wei D-M, Zhang D, Xi H-L, Wang Q-Y, He M-Z and Yang Y-L (2023) Ferroptosis is a new therapeutic target for spinal cord injury.
Front. Neurosci. 17:1136143.
doi: 10.3389/fnins.2023.1136143

Ferroptosis is a new therapeutic target for spinal cord injury

Xin-Yue Bai†, Xiao-Long Liu†, Zhi-Zhong Deng†, Dong-Min Wei, Die Zhang, Hui-Lin Xi, Qing-Yan Wang, Meng-Ze He and Yan-Ling Yang*

School of Medicine, Yan'an University, Yan'an, China

Spinal cord injury is a serious traumatic disease. As Ferroptosis has been increasingly studied in recent years, it has been found to be closely related to the pathophysiological processes of spinal cord injury. Iron overload, reactive oxygen species accumulation, lipid peroxidation and glutamate accumulation associated with Ferroptosis are all present in spinal cord injury, and thus Ferroptosis is thought to be involved in the pathological processes secondary to spinal cord injury. This article highlights the relationship between Ferroptosis and spinal cord injury, lists substances that improve spinal cord injury by inhibiting Ferroptosis, and concludes with a discussion of the problems that may be encountered in the clinical translation of Ferroptosis inhibitors as a means of enabling their faster use in clinical treatment.

KEYWORDS

spinal cord injury, Ferroptosis, Ferroptosis inhibitors, clinical translation, animal models

1. Introduction

Spinal cord injury (SCI) is a serious traumatic condition (Quadri et al., 2020) that is most commonly caused by car accidents and falls (Zipser et al., 2022). The global incidence rate is 10.4–83 cases per million per year (Karsy and Hawryluk, 2019), and SCI is associated with a high rate of disability and mortality (Chen C. et al., 2022), placing a severe physical burden on the patient. In addition, SCI is associated with a higher incidence of psychological disorders such as depression and anxiety than the general population (Hearn and Cross, 2020). The annual cost of treatment and care for each SCI patient has been reported to be as high as US$77,334 (Lo et al., 2021). However, in current clinical management, the treatment of SCI mainly includes surgery and related anti-inflammatory and anti-swelling medication (Liu X. et al., 2021). However, due to the complex pathophysiological process of SCI, the current treatment outcome is not satisfactory. Therefore, it is particularly important to explore the pathological process of SCI and new treatment methods.

Ferroptosis is a type of programmed cell death (PCD) (Shi et al., 2021). Its main mechanism is to catalyze the lipid peroxidation of polyunsaturated fatty acids (PUFA) highly expressed on cell membranes in the presence of divalent iron (Fe^{2+}) or lipoxygenase (LOX), thereby inducing cell death (Ursini and Maiorino, 2020). It is mainly characterized by a decrease in the core enzyme glutathione peroxidase 4 (GPX4), the regulatory core of the antioxidant system glutathione (GSH) system (Wu et al., 2021). In recent years, Ferroptosis has been extensively studied in a number of conditions including cardiovascular disease (Wu et al., 2021), renal disease (Ni et al., 2022), and neurological disorders (Song and Long, 2020).

The pathological process of SCI is divided into primary and secondary injury (Shen and Cai, 2023), with primary injury being irreversible and secondary injury being reversible (Liu X. et al., 2021). Secondary injury is a cascade amplification response triggered by primary injury, which is divided into three stages: acute, subacute, and chronic injury, manifested as post-traumatic inflammatory response, free radical formation, and PCD of cells (Alcántar-Garibay et al., 2022). While PCD includes autophagy, necroptosis, cell scorching, and Ferroptosis, among others (Li et al., 2022), and it has been recently demonstrated that iron overload (Gong et al., 2022), ROS accumulation (Feng et al., 2021), lipid peroxidation (Baazm et al., 2021), and glutamate accumulation (Zhao et al., 2022) associated with Ferroptosis are all present in SCI, it is therefore suggested that Ferroptosis may be involved in the pathological process of secondary injury associated with SCI.

There is a large body of literature that demonstrates the close association of Ferroptosis with SCI, but very little literature that specifies the involvement of Ferroptosis in the pathological process of SCI. There is also little literature summarizing the substances that repair SCI by inhibiting Ferroptosis. And there is no literature that identifies the problems that may arise in the clinical translation of Ferroptosis inhibitors associated with SCI. This review therefore first describes the basic process of Ferroptosis and its close relationship with SCI, then briefly outlines the substances currently available to ameliorate SCI by inhibiting Ferroptosis, thus demonstrating that Ferroptosis is involved in the pathophysiology of SCI and that we can repair SCI by inhibiting Ferroptosis. Finally, this review discusses the problems that may be encountered in the clinical translation of Ferroptosis inhibitors associated with SCI and looks at the future direction of Ferroptosis research in SCI. It opens up a new way of thinking for the treatment of SCI.

2. The basic process of Ferroptosis and its relation to SCI

2.1. Iron metabolism

Iron is one of the important trace elements essential to the human body (Das et al., 2020). Abnormal iron metabolism is an important cause of Ferroptosis. When intracellular iron is overloaded, on the one hand, large amounts of Fe^{2+}undergo Fenton reaction with hydrogen peroxide (H_2O_2), generating hydroxyl radicals with stronger oxidative capacity, thus increasing intracellular levels of reactive oxygen species (ROS) and promoting lipid peroxidation and ultimately Ferroptosis (Liu J. et al., 2022). On the other hand, Fe is a cofactor that enhances the activity of various metabolic enzymes such as LOX, which directly catalyze lipid peroxidation and induce Ferroptosis (Tang D. et al., 2021; **Figure 1**).

Basic experiments have found that in animal models of SCI, there is massive erythrocyte rupture at the site of injury, which can be observed as early as 1 h after injury and more commonly at 24 h (Wang Z. et al., 2022). In contrast, massive bleeding leads to increased iron concentrations at the site of injury (Gong et al., 2022), followed by Ferroptosis from ROS accumulation (Feng et al., 2021). Other researchers conducted *in vivo* and *in vitro* experiments with SCI rats and primary cortical neurons and found that there was significant microglia activation in the motor cortex after SCI resulting in the release of excess nitric oxide (NO), and that the large amount of NO interfered with the expression of proteins related to iron metabolism, ultimately leading to iron overload in the motor cortex of SCI rats at 4 weeks, resulting in ROS accumulation leading to neuronal Ferroptosis (Feng et al., 2021). Furthermore, the researchers found that iron deposition in the motor cortex was significantly increased in SCI patients compared to healthy controls. This triggered the accumulation of ROS, lipid peroxidation, mitochondrial atrophy and dysregulation of genes related to Ferroptosis, which ultimately led to Ferroptosis in motor neurons (Feng et al., 2021). And there are also many neurological disorders such as stroke (Cao et al., 2018), traumatic brain injury and neurodegenerative diseases (Daglas and Adlard, 2018) whose pathogenesis is linked to iron overload in the brain.

2.2. Lipid metabolism

Studies have shown that the polyunsaturated fatty acid (PUFA) family of arachidonic acid (AA)/adrenaline (AdA) undergoes acylation and lipidation to phosphatidylethanolamine-polyunsaturated fatty acids [Phosphatidyl Ethanolamine (PE-PUFA)] (Kagan et al., 2017). Ultimately PE-PUFA is involved in the downstream process of Ferroptosis, which can be divided into two pathways: (i) non-enzymatic oxidation (Conrad and Pratt, 2019) and (ii) enzymatic oxidation. Non-enzymatic reactions involve the Fenton reaction involving Fe^{2+} to produce hydroxyl radicals (HO-) that deprive lipids of H- to form lipid radicals, which then form lipid peroxides, leading to lipid peroxidation leading to Ferroptosis (Conrad and Pratt, 2019). In contrast, two pathways have been identified for enzymatic oxidation reactions. One is the formation of oxides PE-PUFA-OOH and related derivatives such as malondialdehyde (MDA) and 4-hydroxynonenal (4-HNE), which in turn react with DNA bases, proteins and other nucleophilic molecules, catalyzed by LOX leading to severe cytotoxicity (Kagan et al., 2020). Another pathway is the promotion of lipid peroxidation by cytochrome P450 oxidoreductase (POR), which leads to Ferroptosis (Zou et al., 2020; **Figure 1**).

It has been shown that the spinal cord contains high levels of polyunsaturated fatty acids, which have been shown to be involved in the oxidative stress response following SCI (Baazm et al., 2021). Studies on the regulation of SCI by unsaturated fatty acids such as short-chain fatty acids (SCFA) have been widely reported in recent years (Filippone et al., 2020). Thus suggesting that lipid metabolism in Ferroptosis may be involved in the pathological process of SCI. And SCFAs are also major metabolites produced by fermentation of dietary fiber bacteria in the gastrointestinal tract. It has been shown that SCFAs can directly or indirectly affect the brain-gut axis and have a mediating role in the microbiota-gut-brain axis (Dalile et al., 2019). Moreover, SCFAS is also a metabolite of intestinal bacteria and its concentration depends on the composition of the intestinal microbial population (Markowiak-Kopeć and Śliżewska, 2020). In contrast, Ferroptosis is an emerging mode of cell death in which lipid metabolism plays a crucial role (Conrad and Pratt, 2019). We therefore speculate that Ferroptosis, intestinal flora and the brain-gut axis may be linked around lipid metabolism as a regulatory factor, which may also provide some ideas and directions for future studies.

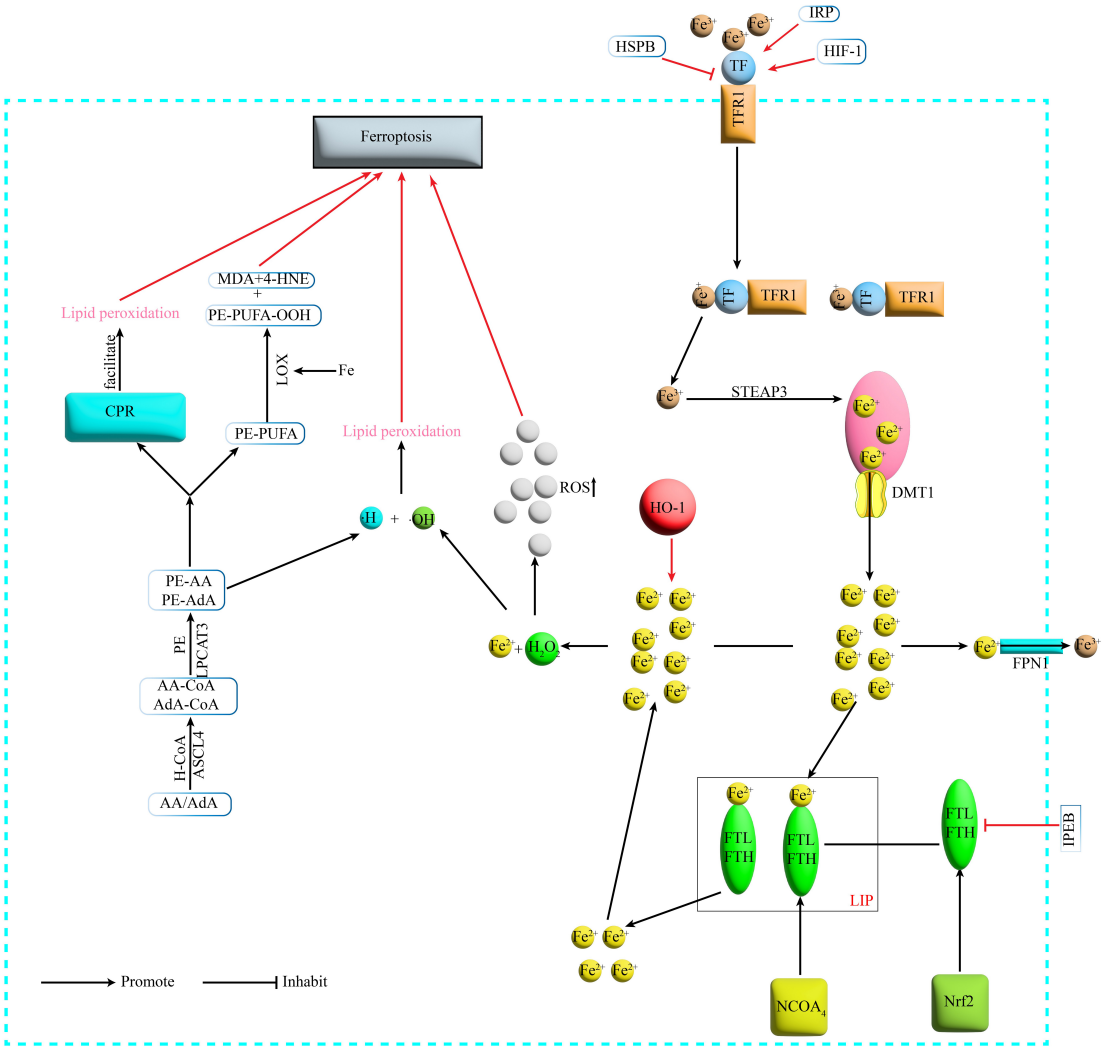

FIGURE 1
Mechanism of Ferroptosis. Fe^{3+} binds to TF on the cell membrane and is transported via TFR1 on the cell membrane surface, and the TFR1-TF-Fe^{3+} complex enters the cell by endocytosis. Under acidic conditions, Fe^{3+} is released from the binding and reduced by STEAP3 to Fe^{2+}, which then enters the cytoplasm via DMT1 from the endosome. In the cytoplasm Fe^{2+} is partly transported outside the cell and converted to Fe^{3+} by FPN1, partly bound to ferritin to form LIP, and NCOA4 can recognize and rely on the autophagic pathway to degrade ferritin in the iron pool, releasing large amounts of Fe^{2+}. TF, transferrin; TFR1, transferrin receptor1; STEAP3, six-transmembrane epithelial antigen of prostate 3; DMT1, divalent metal transporter 1; FPN1, membrane iron transporter 1; FPN1, ferroportin1; FTL, ferritin light chain; FTH, ferritin heavy chain; LIP, labile iron pool; NCOA4, nuclear receptor coactivator 4; H_2O_2, hydrogen peroxide; ACSL4, acyl-CoA synthetase long-chain family member 4; LPCAT3, lyso-phosphatidylcholine acyltransferase-3; LOX, lipoxygenase; MDA, malondialdehyde; 4-HNE, 4-hydroxynonenal; POR, cytochrome P450 oxidoreductase; IREB2, iron-responsive element-binding protein 2; HSPB1, heat shock protein beta-1; IRP, iron- regulatory protein; HIF-1, hypoxia-inducible factor-1; HO-1, heme oxygenase-1.

2.3. System Xc-GSH-GPX4 axis

The cystine/glutamate antiporter (System Xc-) transports glutamate out of the cell and transports cystine into the cell, where the transported cystine is reduced to cysteine (Parker et al., 2021) and then combined with glutamate and glycine in the presence of glutathione synthetase (Wu et al., 2022) (GPX4 is a selenocysteine-containing and GSH-dependent enzyme that is a key regulator of Ferroptosis (Seibt et al., 2019). It converts GSH to oxidized glutathione (GSSG) and reduces lipid peroxidation, thereby reducing lipid peroxide formation and oxidative stress damage and ultimately inhibiting Ferroptosis (Forcina and Dixon, 2019; **Figure 2**). Currently modulating cystine uptake, interfering with GSH and the expression of GPX4 remain the most common means of Ferroptosis in basic research.

One study found that GPX4 knockout-induced degeneration of spinal motor neurons exhibits Ferroptosis, and when supplemented with the Ferroptosis inhibitor vitamin E delayed the onset of paralysis and death in GPX4 knockout-induced mice (Chen et al., 2015). And some researchers have observed downregulation of GPX4 and upregulation of acyl-CoA synthetase long-chain family member 4 (ACSL4) in the acute phase of an animal model of SCI (Zhou et al., 2020). It can therefore be hypothesized that the pathological process of SCI is closely related to the Xc-GAH-GPX4 axis, a protective mechanism system for Ferroptosis.

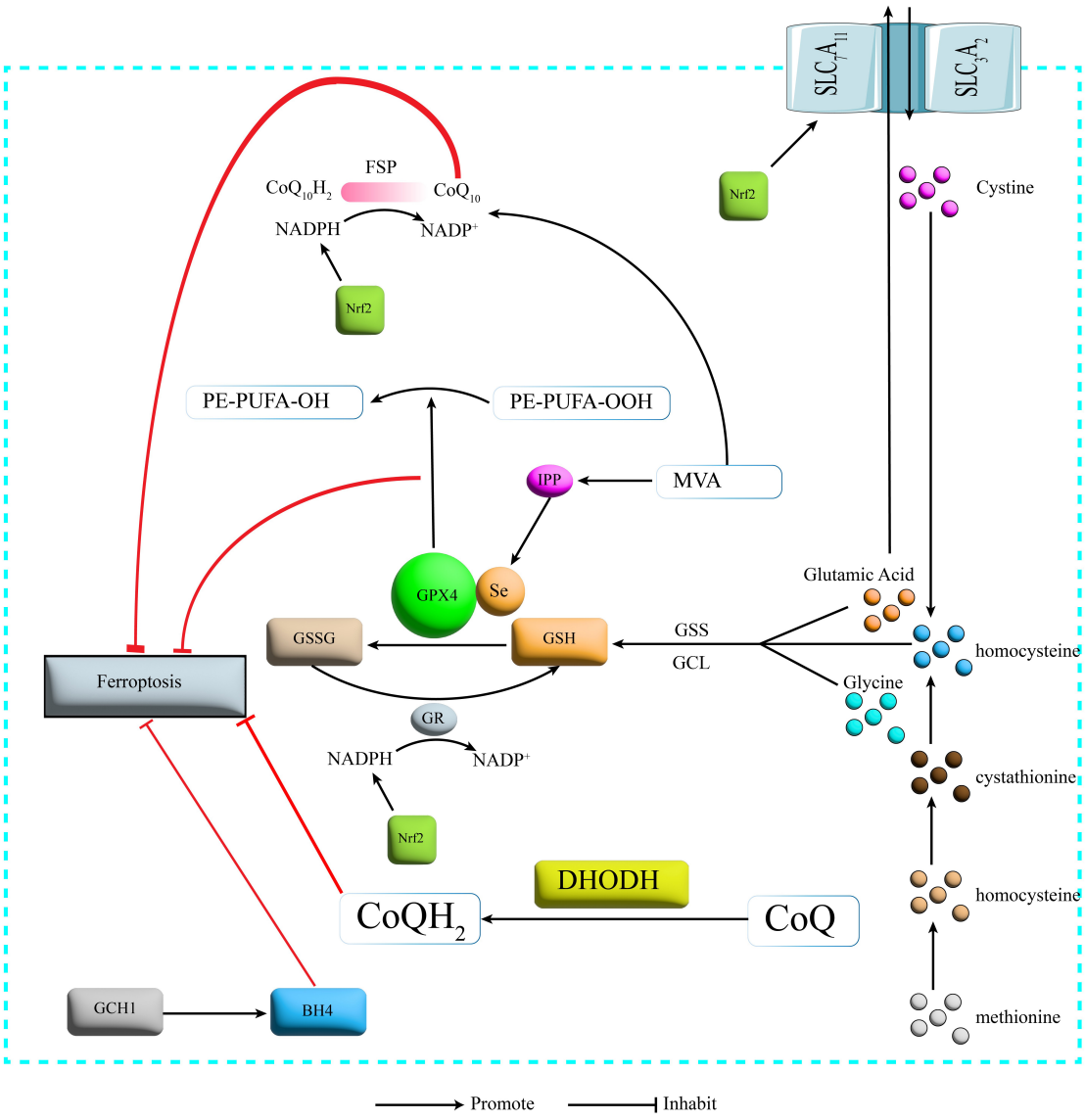

FIGURE 2
Protection mechanism for Ferroptosis. SLC7A11, recombinant solute carrier family 7, member 11; SLC3A2, recombinant solute carrier family 3, member 2; GSS, glutathione synthetase; GCL, glutamate cysteine ligase; GSH, glutathione; GPX4, glutathione peroxidase 4; GR, glutathione reductase; GSSG, glutathione oxidized; NADPH: nicotinamide adenine dinucleotide phosphate; NADP, nicotinamide adenine dinucleotide phosphate; FSP1, Ferroptosis inhibitory protein 1; CoQ10, Coenzyme Q10; DHODH, dihydroorotate dehydrogenase; CoQ Coenzyme Q; GCH1, GTP cyclohydrolase-1; BH4, tetrahydrobiopterin; IPP, isopentenyl pyrophosphate; MVA, mevalonate; Nrf2, nuclear factor erythroid 2-related factor 2.

2.4. NADPH-FSP1-CoQ10 pathway

CoQ10 is a lipophilic free radical trapping antioxidant that blocks the delivery of lipid peroxides and thus inhibits Ferroptosis (Liu J. et al., 2021). The glutathione non-dependent Ferroptosis inhibitory protein (Ferroptosis inhibitory protein 1, FSP1) is one of the redox enzymes of coenzyme Q10 (CoQ10), and FSP1 can, in the presence of reduced coenzyme II (nicotinamide adenine dinucleotide phosphate, NADPH) to reduce CoQ10 to reduced coenzyme Q10 (CoQ10H2) and also catalyze the regeneration of CoQ10 via NAD(P)H (Santoro, 2020; **Figure 2**).

It has been found that in animal models of SCI, the IncGm36569/miRNA-5627-5p/FSP1 axis was inhibited by molecular sponge action and thus targeting of the IncGm36569/miRNA-5627-5p/FSP1 axis to inhibit neuronal Ferroptosis (Shao et al., 2022). In the NADPH-FSP1-CoQ10 pathway, FSP1 has already been reported in basic studies at the molecular level as another target protein for Ferroptosis. Future studies on FSP1 may not only target the molecular level, but also natural and synthetic drugs that interfere with FSP1 expression may be one of the hot spots for future Ferroptosis studies.

2.5. DHODH-CoQH2 pathway

The dihydroorotate dehydrogenase-dihydroubiquione (DHODH-CoQH2) pathway is the third major Ferroptosis protection system on mitochondria in addition to the GPX4

pathway on the cytoplasm and mitochondria and the FSP1 pathway on the plasma membrane (Mao et al., 2021). CoQH2 acts as an antioxidant to eliminate lipid peroxyl radicals and thus inhibit Ferroptosis (Mao et al., 2021; **Figure 2**). Little linkage of SCI to this pathway has been reported and future studies could focus on this pathway.

2.6. GCH1-BH4 pathway

The GTP cyclohydrolase-1-tetrahydrobiopterin (GCH1-BH4) pathway is a lipid antioxidant pathway independent of the Xc-GSH-GPX4 axis and the NADPH-FSP1-CoQ10 pathway (Liu M. et al., 2022). GTP cyclohydrolase-1 (GTP Cyclohydrolase-1, GCH1) is a rate-limiting enzyme of BH4 (Larbalestier et al., 2022). overexpression of GCH1 enhances the production of BH4 (Kraft et al., 2020), a potent free radical-trapping antioxidant that protects cells from Ferroptosis by reducing lipid peroxidation (Vasquez-Vivar et al., 2022; **Figure 2**).

It has been shown that the GCH1-BH4 metabolic pathway is a protective mechanism for cellular Ferroptosis and that GCH1 inhibitors are a novel therapeutic measure for the treatment of colorectal cancer (Hu et al., 2022). However, this pathway has been largely unreported in SCI, and the development of related studies will certainly enhance the emerging field of Ferroptosis.

2.7. The MVA pathway

The mevalonate (MVA) pathway plays a key role in the regulation of Ferroptosis (Yao et al., 2021). the MVA pathway can influence GPX4 synthesis by regulating the maturation of selenocysteine tRNA (Warner et al., 2000), while CoQ10 can be synthesized using acetyl-coenzyme A (Acetyl-CoA) via the MVA pathway (Ball et al., 2021). The MVA pathway therefore links the Xc-GSH-GPX4 axis and the NADPH-FSP1-CoQ10 pathway (**Figure 2**). However, little research has been reported on the inhibition of Ferroptosis and thus repair of SCI through modulation of the MVA pathway. In contrast, MVA, as a synthetic precursor of cholesterol (Guerra et al., 2021), also has a considerable role in lipid metabolism. The MVA pathway therefore re-emphasizes the role of lipid metabolism in Ferroptosis. Aerobic oxidation, glucose metabolism and lipid metabolism play a crucial role in life activities, all three being interconnected and independent of each other. The role of lipid metabolism in Ferroptosis has been widely reported (Baazm et al., 2021). In contrast, the role of aerobic oxidation and sugar metabolism in Ferroptosis has hardly been reported. Some researchers have found that the role of both the mitochondrial tricarboxylic acid cycle (TCA cycle) and the electron transport chain (ETC) is required for Ferroptosis, and that the mitochondrial ETC can regulate Ferroptosis induced by cysteine deprivation In contrast, the mitochondrial TCA cycle can be involved in cysteine deprivation-induced Ferroptosis (Gao et al., 2019). In turn, the tricarboxylic acid cycle is the ultimate metabolic pathway for the three major nutrients (sugars, lipids, and amino acids) and is the hub for the metabolic linkage of sugars, lipids, and amino acids (Martínez-Reyes and Chandel, 2020). We therefore hypothesize that aerobic oxidation as well as sugar metabolism may also have an integral role in Ferroptosis. Future studies that focus on this will be of great significance for Ferroptosis and related areas of research.

2.8. Nrf2

Nuclear factor erythroid 2-related factor 2 (Nrf2) is an important anti-oxidative stress transcription factor that improves cellular tolerance to oxidative stress (He et al., 2020). It has been shown that its downstream target proteins and enzymes include (i) proteins related to iron metabolism: ferritin light chain (FTL), ferritin heavy chain (FTH), and ferroportin1 (FPN1), which is responsible for iron transport (Chen et al., 2021). (ii) Enzymes related to NADPH regeneration: glucose-6-phosphate dehydrogenase (G-6-PD), phosphogluconate dehydrogenase (PGD), and malic enzyme (ME) (Zhang H. S. et al., 2019). ME) (Zhang H. S. et al., 2019), and NADPH regeneration is essential for GPX4 activity. (iii) Proteins and enzymes related to GSH metabolism: Solute Carrier Family 7 Member 11 (SLC7A11), a subunit of the cystine/glutamate transporter protein xCT (Dong et al., 2020) and GSS (Zheng et al., 2014). All these proteins and enzymes are involved in the regulation of Ferroptosis and therefore Nrf2 is considered a key regulator of Ferroptosis (Dodson et al., 2019) and has been a star target in Ferroptosis studies in recent years (**Figure 2**).

In summary, the two most critical targets for the inhibition of Ferroptosis initiation, xCT and GPX4, have been modulated by NRF2. It has also been shown that Nrf2 can be used to regulate Ferroptosis to treat neurodegenerative diseases (Song and Long, 2020), delay the progression of diabetic nephropathy (DN) (Li S. et al., 2021) and prevent acute lung injury due to intestinal ischemia/reperfusion (Dong et al., 2020), and it has been found that proanthocyanidins (Zhou et al., 2020), alginose (Gong et al., 2022), metformin (Wang H. et al., 2020), and growth differentiation factor-15 (Xia et al., 2022) are all inhibited by NRF2. These materials have been found to inhibit Ferroptosis through the Nrf2 pathway to treat SCI, but the specific downstream target proteins and enzymes that these substances affect through the Nrf2 pathway to inhibit Ferroptosis to treat SCI have not been clearly investigated. The above-mentioned roles of Nrf2 in various diseases demonstrate the importance of the Nrf2 pathway in Ferroptosis, which suggests that we need to focus more on the star targets such as Nrf2 in future Ferroptosis research, especially in the study of novel drugs, which may play an indispensable role in the application of Ferroptosis-related drugs and the treatment of related diseases.

3. Related substances that improve SCI by inhibiting Ferroptosis

3.1. Natural materials

3.1.1. Proanthocyanidins

Proanthocyanidins (PACs), often extracted from grape seeds, are potent free radical scavengers (Wang C. et al., 2022). PACs have been shown to promote recovery of motor function in rats with SCI (Liu W. Z. et al., 2022). And in 2020 an investigator

found that proanthocyanidins promote recovery of motor function in SCI mice by inhibiting Ferroptosis (Zhou et al., 2020). PACs inhibit the recovery of motor function in SCI mice by upregulating the expression of GSH, GPX4, Nrf2, and HO-1 and downregulating the expression of iron, ACSL4 and thiobarbituric acid reactive substances (TBARS). TBARS expression to suppress Ferroptosis in the microenvironment at the site of injury (Zhou et al., 2020). However, PACs treatment had no significant effect on the expression of Recombinant Lysophosphatidylcholine Acyltransferase 3 (LPCAT3) levels in SCI, so it is uncertain whether PACs inhibit Ferroptosis by affecting AA/AdA levels and further studies are needed. further study.

3.1.2. Epigallocatechin gallate

Epigallocatechin gallate (EGCG) is a catechin isolated from green tea. It has very strong antioxidant activity, at least 100 times more active than vitamin C (Tang G. et al., 2020). EGCG has been shown to have neuroprotective effects in SCI (Wang F. et al., 2022). Zhang H. S. et al. (2019) researchers found that EGCG can upregulate the expression of GPX4 and FTH1 and downregulate the expression of ACSL4, thereby inhibiting Ferroptosis to promote recovery of motor function in rats after spinal cord transection (ST). Thus, EGCG may have a very good future as a promising novel natural substance in the clinical treatment of SCI.

3.1.3. Carnosic

Carnosic acid is a natural phenolic diterpene that can be extracted from rosemary (Satoh et al., 2022). Cheng et al. (2021) showed that Carnosic acid could down-regulate the expression of iron, ROS and MDA and up-regulate the expression of GSH in Erastin-treated PC12 cells. It was further demonstrated that syringic acid inhibited Erastin-induced Ferroptosis in PC12 cells by activating the Nrf2 pathway (Cheng et al., 2021), further demonstrating that the Nrf2 pathway is closely related to Ferroptosis.

3.1.4. Trehalose

Trehalose, a non-reducing disaccharide composed of two glucose molecules, is a typical stress metabolite (Zhang and DeBosch, 2019). Gong et al. (2022) first demonstrated that trehalose inhibited Ferroptosis of neurons after SCI in mice by activating the Nrf2/HO-1 pathway, thereby promoting neuronal survival and improving recovery of motor function. In addition, alglucan also inhibited the expansion of neural tissue cavities and suppressed neuronal loss and inflammatory responses in SCI mice (Gong et al., 2022).

3.2. Metabolites

3.2.1. Lipoxin A4

Lipoxin A4 (LXA4) is a metabolite of arachidonate lipoxygenase (ALOXE). LXA4 has been previously shown to repair SCI by activating the Nrf2/HO-1 signaling pathway (Lu et al., 2018). Wei et al. (2021) used Erastin to induce Ferroptosis in neuronal cells, and LXA4 effectively alleviated the downregulation of GPX4, GSH, and cysteine, and prevented the downregulation of Prostaglandin Endoperoxide Synthase 2 (PTGS2), ACSL4, and ROS upregulation. This study provides strong evidence that LXA4 improves SCI even more.

3.2.2. Colony-stimulating factor

Erythropoietin (EPO), also known as erythropoietin-stimulating factor, is a human endogenous protein hormone that stimulates erythropoiesis. EPO has been reported to improve recovery of motor function in rats with SCI (Zhong et al., 2020). However, whether its mechanism is related to Ferroptosis has not been clarified. Recently, some investigators found that EPO has similar effects to Ferrostatin-1, an Ferroptosis inhibitor, on inhibiting the expression of Ferroptosis-related proteins and restoring mitochondrial morphology. EPO was also found to increase the expression of xCT and GPX4. Thus suggesting a potential anti-Ferroptosis effect of EPO (Kang et al., 2023), further improving the rationale for the use of EPO in the clinic.

3.3. Drug

3.3.1. Edaravone

Edaravone is a free radical scavenger (Dang et al., 2022). Pang et al. (2022) found that edaravone upregulated GPX4/xCT and downregulated ACSL4/5-LOX to inhibit Ferroptosis during the acute phase of SCI in rats, thereby improving recovery of motor function in SCI.

3.3.2. Metformin

Metformin (Met) is an organic compound that is a first-line drug for the treatment of type 2 diabetes (Flory and Lipska, 2019). One study found that Met promotes axonal regeneration after SCI via the Nrf2 pathway (Wang H. et al., 2020). And Met has also been found to upregulate GPX4 expression (Ma et al., 2021) and reduce MDA levels (Zeng et al., 2019), thereby improving recovery of motor function in rats with SCI (Wang Z. et al., 2022).

Taken together, these substances can improve motor recovery after SCI by inhibiting Ferroptosis, providing further evidence for their clinical application and also suggesting that SCI is closely related to Ferroptosis and that Ferroptosis will be a new target for the treatment of SCI in the future.

3.4. Trace elements

3.4.1. Zinc

Zinc is an essential trace element in the human body (Kim and Lee, 2021). Researchers found that zinc increased the expression of Nrf2/HO-1 and thus upregulated GPX4 and GSH in a mouse model of SCI, and that zinc also effectively prevented oxidative stress in mitochondria and effectively reduced inflammation (Ge et al., 2021).

3.4.2. Selenium

Selenium can replace sulfur in cysteine and is incorporated into selenoproteins as a selenosubstituted cysteine. GPX4 is the most important of the selenoproteins in human 25 (Zhang and Song, 2021). Therefore selenium is essential for GPX4. One researcher injected sodium selenite in a rat model of SCI and found that sodium selenite treatment downregulated iron levels and the expression of lipid peroxidation products MDA and 4-HNE, in addition to finding that sodium selenite inhibited Ferroptosis via

the FSP1/GPX4 pathway thereby improving recovery of motor function in SCI rats (Chen Y. X. et al., 2022).

The role played by zinc and selenium in SCI provides a solid theoretical basis and dosing recommendations for the clinical use of micronutrients that can protect against neurological injury.

3.5. miRNAs

miRNA is a non-coding RNA of 21-25 amino acids in length, which can inhibit translation or induce target mRNA degradation at the post-transcriptional level by binding to the 3′-untranslated region (UTR) in messenger RNA (mRNA) (Saliminejad et al., 2019). One study found that miRNA-672-3p could inhibit Ferroptosis via the FSP1 pathway, thereby improving motor function in rats (Wang F. et al., 2022). Since miRNA is an RNA that does not encode a protein, one target protein may be regulated by multiple miRNAs, and one miRNA may also regulate multiple target proteins, so it may also be involved in the regulatory mechanisms related to Ferroptosis. However, little research has been reported on Ferroptosis and miRNAs. More importantly, miRNAs are only one type of non-coding RNAs, and studies on non-coding RNAs such as IncRNAs, CirRNAs, and co-regulatory networks between non-coding RNAs and Ferroptosis have also been rarely reported. Therefore, future studies on Ferroptosis could focus more on the molecular level, especially in non-coding RNAs, to provide more targets for Ferroptosis studies at the molecular level.

3.6. Mesenchymal stem cell transplantation

Mesenchymal stem cells (MSCs) and long non-coding RNA (lncRNA) are an important class of exosome contents. It has been found that exosomes from MSCs are dependent on a novel lncRNA, Gm36569, which inhibits Ferroptosis in neuronal cells by competing for the expression of miR-5627-5p and thereby enhancing the expression of FSP1 (Shao et al., 2022). This study links MSC transplantation, exosomes, Ferroptosis and SCI closely together, further promoting the development of MSC transplantation in SCI and providing theoretical support for the clinical application of MSC transplantation.

3.7. Cytokines

Growth-differentiation-factor-15 (GDF-15) is a cytokine that is a member of the transforming growth factorβ (TGF-β) superfamily, which is a stress response protein (Wang D. et al., 2021). One researcher examined the level of GDF-15 in SCI and found that the expression level of GDF-15 was significantly elevated in SCI and in neuronal Ferroptosis *in vitro*. And the knockdown of GDF-15 significantly exacerbated Ferroptosis. Subsequent researchers have found that GDF-15 inhibits Ferroptosis by activating the p62-Keap1-Nrf2 signaling pathway, thereby improving motor recovery in SCI (Xia et al., 2022). However, other modulatory effects of GDF-15 on Ferroptosis and neuroinflammation in the neurocloud after SCI remain uncertain, and therefore further studies on the modulatory effects of GDF-15 are needed in the future.

3.8. Newly synthesized substances

3.8.1. SRS16-86

SRS16-86 is a newly synthesized small molecule inhibitor of Ferroptosis (Linkermann et al., 2014). One study found that SRS16-86 upregulated the levels of XCT, GSH and GPX4 in rat SCI and downregulated the lipid peroxidation product 4-hydroxynonenalal (4-HNE) thereby inhibiting Ferroptosis. In addition, SRS16-85 inhibited the inflammatory response and astrocyte proliferation after SCI. SRS16-85 increased neuronal survival and improved motor recovery from SCI in rats by inhibiting Ferroptosis (Zhang Y. et al., 2019).

3.8.2. DFO

Deferoxamine (DFO) is an effective iron chelator that has been approved by the Food and Drug Administration (FDA) for the treatment of iron overload disorders (Li et al., 2019). It has been found that DFO promotes the repair of rat SCI by upregulating the levels of XCT, GSH, and GPX4 and inhibiting lipid reactive oxygen species in rat SCI, which in turn upregulates Ferroptosis related genes Acyl-CoA synthase family member 2 (ACSF2) and iron response element binding protein 2 (IREB2) ultimately inhibiting the Ferroptosis pathway (Yao et al., 2019). The application of DFO directly indicates its great promise in Ferroptosis. This may accelerate the clinical application of DFO in SCI.

3.8.3. Liproxstatin-1

In 2021 a study found that Liproxstatin-1 was more effective than edaravone and DFO in rescuing oligodendrocytes. And Liproxstatin-1 was found to not only inhibit mitochondrial lipid peroxidation but also restore the expression of GSH, GPX4, and FSP1 (Fan et al., 2021).

3.8.4. Ferrostatin-1

Ferrostatin-1 was shown to inhibit Ferroptosis in neurons, thereby improving functional recovery after TBI and SCI (Xie et al., 2019). Ge et al. (2022) found that Ferrostatin-1 could inhibit Ferroptosis in oligodendrocytes by reducing the accumulation of iron and ROS and downregulating the Ferroptosis-related genes IREB2 and PTGS2 (Ge et al., 2022).

The above studies provide a theoretical basis for the clinical use of these substances in the treatment of SCI. In particular, studies of natural compounds and related molecules have confirmed the potential of these substances in Ferroptosis and clinical treatment. It is also clear from the above table that both natural and newly synthesized substances inhibit Ferroptosis and thus repair SCI mainly by affecting xCT, GSH, GPX4, FSP1, and Nrf2 factors (**Table 1**). However, this does not mean that substances that inhibit Ferroptosis and thus repair SCI only do so by affecting the above pathways, but may also inhibit Ferroptosis and thus repair SCI by affecting the DHODH-CoQH2 pathway, the GCH1-BH4 pathway and the MVA pathway, etc. However, there is little research on these pathways, so the targets of future Ferroptosis inhibitors for repairing SCI and Therefore, future studies on the targets of Ferroptosis inhibitors for SCI repair and the mechanisms of action of natural products that can inhibit Ferroptosis and thereby repair SCI could focus on these pathways.

TABLE 1 Improvement of SCI-related substances through Ferroptosis.

Classification	Substance	Type	Mechanism
Natural products	PACs	Free radical scavengers Antioxidants	Upregulation of GSH, GPX4, Nrf2 (Zhou et al., 2020) Downregulation of ACSL4, Fe, TBARS (Zhou et al., 2020)
	EGCG	Antioxidants	Upgraded GPX4, FTH (Wang J. et al., 2020) Downward revision of ACSL4 (Wang J. et al., 2020)
	Carnosic	Anti-inflammatory Neuroprotective	Upregulation of GSH, Nrf2 (Cheng et al., 2021) Downregulation of iron content, ROS, MDA (Cheng et al., 2021)
	Trehalose	Prevents lipid peroxidation Inhibits inflammation	Upregulates Nrf2 (Gong et al., 2022)
Metabolic products	LXA4	Anti-inflammatory	Upregulation of GSH, GPX4, Nrf2 (Wei et al., 2021) Downregulation of ACSL4, PTGS2, ROS (Wei et al., 2021)
	EPO	Colony-stimulating factor	Up-regulation of xCT GPX4 (Kang et al., 2023)
Drugs	Edaravone	Free radical scavenger	Upregulated xCT GPX4 (Pang et al., 2022) Downregulation of ACSL4, 5-LOX (Pang et al., 2022)
	Met	Glucose-lowering drugs	Upregulated GPX4, Nrf2 (Ma et al., 2021) Downregulation of MDA (Zeng et al., 2019)
Trace elements	Zinc	Trace elements	Upregulation of GSH, GPX4, Nrf2 (Ge et al., 2021) Downregulation of ROS (Ge et al., 2021)
	Selenium	Trace elements	Upregulation of GPX4 FSP1 (Chen Y. X. et al., 2022) Downregulation of MDA 4-HNE (Ge et al., 2021)
miRNA	miRNA-672-3p	RNA	Upregulates FSP1 (Wang F. et al., 2022)
Stem cell transplantation	lncRNA-Gm36569	RNA	Upregulates FSP1 (Shao et al., 2022)
Cytokines	GDF-15	Neuroprotective factor	Upregulated Nrf2 (Xia et al., 2022)
New synthetic substances	SRS16-86	Small molecule Ferroptosis inhibitors	Upregulates xCT, GSH, GPX4 (Zhang Y. et al., 2019)
	DFO	Iron chelator	Upregulates xCT, GSH, GPX4 (Yao et al., 2019)
	Liproxstatin-1	Ferroptosis Inhibitors	Upregulates xCT, GPX4, FSP1 (Fan et al., 2021)
	Ferrostatin-1	Ferroptosis Inhibitors	Downregulation of Iron, ROS, IPEB2, PTGS2 (Ge et al., 2022)

4. Possible problems in the clinical translation of Ferroptosis inhibitors for the treatment of spinal cord injury

Recently, DFO has been approved by the US Food and Drug Administration (FDA) for the treatment of iron overload disorders (Li et al., 2019), for example to reduce systemic iron load in patients with thalassemia major and sickle cell (Farr and Xiong, 2021). However, DFO currently has some limitations for clinical translation in other diseases. For example, in Intracerebral Hemorrhage (ICH), studies have shown that high doses of DFO are dangerous in treating patients with ICH (Farr and Xiong, 2021). In SCI, it has been shown that DFO can improve SCI by promoting neovascularization in rats, but there are limitations to this study such as the uncertainty of the therapeutic effect of DFO in the chronic phase of SCI and the need to verify the therapeutic effect of DFO in SCI in high quality clinical studies, of which there are few (Tang G. et al., 2020). Most other Ferroptosis inhibitors have not yet been translated for clinical use and face many challenges.

4.1. Mode of administration

4.1.1. Injection localized at the traumatized spinal cord

In basic research, some investigators microinjected Ferrostatin-1, an Ferroptosis inhibitor, into the dorsal 2 mm cephalad and 2 mm caudal aspects of the spinal cord in a rat model of SCI and inhibited the accumulation of iron and ROS, resulting in improved functional recovery after SCI (Ge et al., 2022). Other studies have injected sodium selenite spinal cord into a rat model of SCI and found downregulation of iron levels, MDA and 4-HNE expression levels and functional recovery after SCI (Chen Y. X. et al., 2022). Although this method is accurate in its localization (Falsafi et al., 2021), this localization of drug delivery at the traumatized spinal cord may be difficult to manipulate when applied clinically and may predispose patients to secondary injury (**Table 2**).

4.1.2. Intraperitoneal injection

Some researchers injected DFO (Yao et al., 2019) and SRS16-86 (Zhang Y. et al., 2019) intraperitoneally into a rat model of SCI and found that the Xc-GSH-GPX4 axis was upregulated to inhibit Ferroptosis, thereby improving the functional recovery of SCI in rats. However, whether the drug crosses the blood–brain barrier

(BBB) or blood–spinal cord barrier (BSCB) during intraperitoneal injection for clinical application still deserves further study (Table 2).

4.1.3. Intranasal administration

Intranasal administration has been shown to bypass the BBB or BSCB and allow access to the central nervous system in animal models (Long et al., 2020), and it has been shown that intranasal administration of Liproxstatin-1 and Ferrostatin-1 treatment significantly improved infarct size in a mouse stroke model (MCAO ischemic stroke model) (Tuo et al., 2017), so the mode of administration may be clinically applicable in the treatment of spinal cord injury (Table 2).

4.1.4. Intravenous injection

Intravenous injection is probably the most suitable mode of administration for emergency treatment in clinical practice because of its ease of handling, high volume of administration and low risk. However, the ability of this mode of administration to cross the blood-brain barrier during clinical application is still debatable (Table 2). One investigator injected the third generation Ferroptosis inhibitor SRS16-86 (Zhang Y. et al., 2019) intravenously into mice and collected cerebrospinal fluid, brain tissue fluid and serum samples. Both cerebrospinal fluid and brain tissue fluid were found to be below detection levels, indicating that intravenous SRS16-86 did not cross the BBB.

In the treatment of central nervous system diseases, the BBB limits the ability of 98% of small molecules and almost all large molecules to reach the lesion effectively. Therefore, it is extremely important that the mode of administration of Ferroptosis inhibitors crosses the BBB when used in clinical practice. There are several ways to increase the BBB, for example (i) carotid artery injection of high concentrations of mannitol can deliver drugs to the brain that are not permeable to the BBB. However, this method is not clinically applicable as it is complex and has a high risk of causing seizures, cerebral artery embolism, cerebral hemorrhage and cerebral edema (Wang W. et al., 2021). (ii) Use of vasoactive agents to increase BBB permeability throughout the brain (Gao et al., 2014). (iii) Use of cell-penetrating peptides, adenovirus-associated virus (AAV) that penetrates the BBB (Yao et al., 2022) and receptor-mediated transcytosis to increase brain transport (Terstappen et al., 2021). (iv) Localized increase in brain penetration by ultrasound stimulation of microvesicles (Rezai et al., 2020). (v) Molecularly targeted nanoparticles irradiated by picosecond pulsed laser to reversibly open the BBB and deliver drugs to brain tissue, specifically by synthesizing a gold nanoparticles (AuNPs) that are specifically targeted intravenously to tight junctions (TJs) on the BBB, followed by cranial picosecond laser stimulation to increase BBB permeability, a strategy that allows immunoglobulin and viral gene therapy vectors and drug-laden liposomes to enter the brain, and a process that is reversible and does not result in spontaneous vascular diastole or significant disruption of the structure of the neurovascular unit (Li X. et al., 2021). Although the above possible solutions for BBB have not been studied in BMSC, they may also provide relevant ideas and inspiration for the clinical use of Ferroptosis inhibitors in SCI.

TABLE 2 Advantages and disadvantages of drug delivery methods.

Method of administration	Advantages	Disadvantages
SCI site injection	Accurate positioning (Falsafi et al., 2021)	May be difficult to use in clinical practice and may cause secondary harm to patients
Intraperitoneal injection	Easy to absorb (Dou et al., 2013)	Improper handling can easily cause damage to organs
Intranasal drug delivery	Easy to pass BBB or BSCB (Long et al., 2020)	Improper handling can easily lead to upper respiratory tract infections
Intravenous injection	Easy handling, high dosingand, low risk	Difficult to pass BBB or BSCB (Zhang Y. et al., 2019)

4.2. Dosing

4.2.1. Selection based on preliminary experiments

For example, when the researchers selected the dose to be administered for SRS16-86, five groups were modeled as sham group, SCI group, SCI + 5 mg/kg SRS16-86 group, SCI + 10 mg/kg SRS16-86 group and SCI + 15 mg/kg SRS16-86 group, and then tested motor recovery 2 weeks after SCI to select a dose of 15 mg/kg SRS16-86 (Zhang Y. et al., 2019).

4.2.2. Selection based on experience

For example the dose of 100 mg/kg administered for DFO was selected by the investigators with slight modifications based on previous studies.

The dose administered in the basic study was determined in both of these ways, but in the clinical setting the dose needs to be studied further, taking into account the patient's age, weight and dosing pattern. If too small a dose is administered, it may not be effective, and if too large a dose is administered, adverse effects and side effects may occur.

4.3. Time window for dosing

Some of the Ferroptosis inhibitors in basic studies were administered before SCI, for example DFO was administered to rats 30 min before injury and then injected once a day for 7 days after injury. However, this dosing time window is not achievable in clinical applications and therefore needs to be further explored.

5. Conclusion and outlook

In summary: (1) The existing studies suggest that Ferroptosis is closely related to SCI and that Ferroptosis may be a new target for SCI treatment. (2) Most of the current studies on Ferroptosis in SCI are at the animal stage, and future studies could be conducted on human cell lines or non-human primates to lay the foundation for

clinical development of Ferroptosis inhibitors. (3) Although there is increasing evidence that Ferroptosis inhibitors can be used as a new generation of targets for the treatment of SCI, future clinical translation may face a number of problems such as poor *in vivo* solubility, short half-life, dose and mode of administration. (4) In addition to Ferroptosis, studies on the characteristics of different death modes, such as cuproptosis (Tsvetkov et al., 2022) and parthanatos (Wang and Ge, 2020), as well as studies on the linkage between these death modes, are still a hot topic for future research.

Author contributions

X-YB, X-LL, and Z-ZD were responsible for writing and revising the text. X-YB played a major role in writing this article. X-LL was responsible for the preparation of figures and revisions of this article. Z-ZD was responsible for the post-writing and revisions of this article. D-MW and DZ were responsible for data collection. H-LX, Q-YW, and M-ZH were responsible for revising the article. Y-LY was responsible for conceptualizing, funding, and guiding the article. All authors contributed to the article and approved the submitted version.

Funding

This work was supported by the grants (YDBK2020-28,2022E010 and 2023-JC-QN-0125 to X-LL) from the Natural Science Foundation of Yan'an University, Shaanxi Provincial Health Research, and Natural Science Foundation of Shaanxi Province.

Conflict of interest

The authors declare that the research was conducted in the absence of any commercial or financial relationships that could be construed as a potential conflict of interest.

Publisher's note

All claims expressed in this article are solely those of the authors and do not necessarily represent those of their affiliated organizations, or those of the publisher, the editors and the reviewers. Any product that may be evaluated in this article, or claim that may be made by its manufacturer, is not guaranteed or endorsed by the publisher.

References

Alcántar-Garibay, O. V., Incontri-Abraham, D., and Ibarra, A. (2022). Spinal cord injury-induced cognitive impairment: a narrative review. *Neural. Regen. Res.* 17, 2649–2654. doi: 10.4103/1673-5374.339475

Baazm, M., Behrens, V., Beyer, C., Nikoubashman, O., and Zendedel, A. (2021). Regulation of inflammasomes by application of Omega-3 polyunsaturated fatty acids in a spinal cord injury model. *Cells* 10:3147. doi: 10.3390/cells10113147

Ball, H. S., Girma, M. B., Zainab, M., Soojhawon, I., Couch, R. D., Noble, S. M., et al. (2021). Characterization and inhibition of 1-Deoxy-d-Xylulose 5-phosphate reductoisomerase: a promising drug target in *Acinetobacter baumannii* and *Klebsiella pneumoniae*. *ACS Infect. Dis.* 7, 2987–2998. doi: 10.1021/acsinfecdis.1c00132

Cao, S., Hua, Y., Keep, R. F., Chaudhary, N., and Xi, G. (2018). Minocycline effects on intracerebral hemorrhage-induced iron overload in aged rats: brain iron quantification with magnetic resonance imaging. *Stroke* 49, 995–1002. doi: 10.1161/STROKEAHA.117.019860

Chen, C., Qiao, X., Liu, W., Fekete, C., and Reinhardt, J. D. (2022). Epidemiology of spinal cord injury in China: a systematic review of the chinese and english literature. *Spinal Cord* 60, 1050–1061. doi: 10.1038/s41393-022-00826-6

Chen, L., Hambright, W. S., Na, R., and Ran, Q. (2015). Ablation of the ferroptosis inhibitor glutathione peroxidase 4 in neurons results in rapid motor neuron degeneration and paralysis. *J. Biol. Chem.* 290, 28097–28106. doi: 10.1074/jbc.M115.680090

Chen, Y., Wang, J., Li, J., Zhu, J., Wang, R., Xi, Q., et al. (2021). Astragalus polysaccharide prevents ferroptosis in a murine model of experimental colitis and human Caco-2 cells via inhibiting NRF2/HO-1 pathway. *Eur. J. Pharmacol.* 911:174518. doi: 10.1016/j.ejphar.2021.174518

Chen, Y. X., Zuliyaer, T., Liu, B., Guo, S., Yang, D. G., Gao, F., et al. (2022). Sodium selenite promotes neurological function recovery after spinal cord injury by inhibiting ferroptosis. *Neural Regen. Res.* 17, 2702–2709. doi: 10.4103/1673-5374.339491

Cheng, J., Xu, T., Xun, C., Guo, H., Cao, R., Gao, S., et al. (2021). Carnosic acid protects against ferroptosis in PC12 cells exposed to erastin through activation of Nrf2 pathway. *Life Sci.* 266:118905. doi: 10.1016/j.lfs.2020.118905

Conrad, M., and Pratt, D. A. (2019). The chemical basis of ferroptosis. *Nat. Chem. Biol.* 15, 1137–1147. doi: 10.1038/s41589-019-0408-1

Daglas, M., and Adlard, P. A. (2018). The involvement of iron in traumatic brain injury and neurodegenerative disease. *Front. Neurosci.* 12:981. doi: 10.3389/fnins.2018.00981

Dalile, B., Van Oudenhove, L., Vervliet, B., and Verbeke, K. (2019). The role of short-chain fatty acids in microbiota-gut-brain communication. *Nat. Rev. Gastroenterol. Hepatol.* 16, 461–478. doi: 10.1038/s41575-019-0157-3

Dang, R., Wang, M., Li, X., Wang, H., Liu, L., Wu, Q., et al. (2022). Edaravone ameliorates depressive and anxiety-like behaviors via Sirt1/Nrf2/HO-1/Gpx4 pathway. *J. Neuroinflammation* 19, 41. doi: 10.1186/s12974-022-02400-6

Das, N. K., Schwartz, A. J., Barthel, G., Inohara, N., Liu, Q., Sankar, A., et al. (2020). Microbial metabolite signaling is required for systemic iron homeostasis. *Cell Metab.* 31, 115–130. doi: 10.1016/j.cmet.2019.10.005

Dodson, M., Castro-Portuguez, R., and Zhang, D. D. (2019). NRF2 plays a critical role in mitigating lipid peroxidation and ferroptosis. *Redox Biol.* 23:101107. doi: 10.1016/j.redox.2019.101107

Dong, H., Qiang, Z., Chai, D., Peng, J., Xia, Y., Hu, R., et al. (2020). Nrf2 inhibits ferroptosis and protects against acute lung injury due to intestinal ischemia reperfusion via regulating SLC7A11 and HO-1. *Aging* 12, 12943–12959. doi: 10.18632/aging.103378

Dou, S., Smith, M., Wang, Y., Rusckowski, M., and Liu, G. (2013). Intraperitoneal injection is not always a suitable alternative to intravenous injection for radiotherapy. *Cancer Biother Radiopharm.* 28, 335–342. doi: 10.1089/cbr.2012.1351

Falsafi, M., Baghianimoghadam, B., Bahrami-Freiduni, M., and Esmaeilnejad-Ganji, S. M. (2021). Examining the accuracy of ultrasound-guided lumbar transforaminal injection controlled by fluoroscopic imaging in patients with lumbar radiculopathy: a modified technique. *Turk Neurosurg.* 31, 582–586. doi: 10.5137/1019-5149.JTN.32660-20.1

Fan, B. Y., Pang, Y. L., Li, W. X., Zhao, C.-X., Zhang, Y., et al. (2021). Liproxstatin-1 is an effective inhibitor of oligodendrocyte ferroptosis induced by inhibition of glutathione peroxidase 4. *Neural Regen. Res.* 16, 561–566. doi: 10.4103/1673-5374.293157

Farr, A. C., and Xiong, M. P. (2021). Challenges and opportunities of deferoxamine delivery for treatment of Alzheimer's disease, parkinson's disease, and intracerebral hemorrhage. *Mol. Pharm.* 18, 593–609. doi: 10.1021/acs.molpharmaceut.0c00474

Feng, Z., Min, L., Chen, H., Deng, W., Tan, M., Liu, H., et al. (2021). Iron overload in the motor cortex induces neuronal ferroptosis following spinal cord injury. *Redox Biol.* 43:101984. doi: 10.1016/j.redox.2021.101984

Filippone, A., Lanza, M., Campolo, M., Casili, G., Paterniti, I., Cuzzocrea, S., et al. (2020). Protective effect of sodium propionate in Aβ(1-42) -induced neurotoxicity and spinal cord trauma. *Neuropharmacology* 166:107977.

Flory, J., and Lipska, K. (2019). Metformin in 2019. *JAMA* 321, 1926–1927.

Forcina, G. C., and Dixon, S. J. (2019). GPX4 at the crossroads of lipid homeostasis and ferroptosis. *Proteomics* 19:e1800311. doi: 10.1002/pmic.201800311

Gao, M., Yi, J., Zhu, J., Minikes, A. M., Monian, P., Thompson, C. B., et al. (2019). Role of mitochondria in ferroptosis. *Mol. Cell* 73, 354–363.

Gao, X., Qian, J., Zheng, S., Changyi, Y., Zhang, J., Ju, S., et al. (2014). Overcoming the blood-brain barrier for delivering drugs into the brain by using adenosine receptor nanoagonist. *ACS Nano* 8, 3678–3689. doi: 10.1021/nn5003375

Ge, H., Xue, X., Xian, J., Yuan, L., Wang, L., Zou, Y., et al. (2022). Ferrostatin-1 alleviates white matter injury via decreasing ferroptosis following spinal cord injury. *Mol. Neurobiol.* 59, 161–176. doi: 10.1007/s12035-021-02571-y

Ge, M. H., Tian, H., Mao, L., Li, D. Y., Lin, J. Q., Hu, H. S., et al. (2021). Zinc attenuates ferroptosis and promotes functional recovery in contusion spinal cord injury by activating Nrf2/GPX4 defense pathway. *CNS Neurosci. Ther.* 27, 1023–1040. doi: 10.1111/cns.13657

Gong, F., Ge, T., Liu, J., Xiao, J., Wu, X., Wang, H., et al. (2022). Trehalose inhibits ferroptosis via NRF2/HO-1 pathway and promotes functional recovery in mice with spinal cord injury. *Aging* 14, 3216–3232. doi: 10.18632/aging.204009

Guerra, B., Recio, C., Aranda-Tavío, H., Guerra-Rodríguez, M., García-Castellano, J. M., Fernández-Pérez, L., et al. (2021). The mevalonate pathway, a metabolic target in cancer therapy. *Front. Oncol.* 11:626971. doi: 10.3389/fonc.2021.626971

He, F., Antonucci, L., and Karin, M. (2020). NRF2 as a regulator of cell metabolism and inflammation in cancer. *Carcinogenesis* 41, 405–416.

Hearn, J. H., and Cross, A. (2020). Mindfulness for pain, depression, anxiety, and quality of life in people with spinal cord injury: a systematic review. *BMC Neurol.* 20:32. doi: 10.1186/s12883-020-1619-5

Hu, Q., Wei, W., Wu, D., Huang, F., Li, M., Li, W., et al. (2022). Blockade of GCH1/BH4 axis activates ferritinophagy to mitigate the resistance of colorectal cancer to erastin-induced ferroptosis. *Front. Cell Dev. Biol.* 10:810327. doi: 10.3389/fcell.2022.810327

Kagan, V. E., Mao, G., Qu, F., Angeli, J. P., Doll, S., Croix, C. S., et al. (2017). Oxidized arachidonic and adrenic PEs navigate cells to ferroptosis. *Nat. Chem. Biol.* 13, 81–90. doi: 10.1038/nchembio.2238

Kagan, V. E., Tyurina, Y. Y., Vlasova, I. I., Kapralov, A. A., Amoscato, A. A., Anthonymuthu, T. S., et al. (2020). Redox epiphospholipidome in programmed cell death signaling: catalytic mechanisms and regulation. *Front. Endocrinol.* 11:628079. doi: 10.3389/fendo.2020.628079

Kang, Y., Zhu, R., Li, S., Qin, K. P., Tang, H., Shan, W. S., et al. (2023). Erythropoietin inhibits ferroptosis and ameliorates neurological function after spinal cord injury. *Neural. Regen. Res.* 18, 881–888. doi: 10.4103/1673-5374.353496

Karsy, M., and Hawryluk, G. (2019). Modern medical management of spinal cord injury. *Curr. Neurol. Neurosci. Rep.* 19:65.

Kim, B., and Lee, W. W. (2021). Regulatory role of zinc in immune cell signaling. *Mol. Cells* 44, 335–341.

Kraft, V., Bezjian, C. T., Pfeiffer, S., Ringelstetter, L., Müller, C., Zandkarimi, F., et al. (2020). GTP cyclohydrolase 1/Tetrahydrobiopterin counteract ferroptosis through lipid remodeling. *ACS Cent Sci.* 6, 41–53. doi: 10.1021/acscentsci.9b01063

Larbalestier, H., Keatinge, M., Watson, L., White, E., Gowda, S., Wei, W., et al. (2022). GCH1 deficiency activates brain innate immune response and impairs tyrosine hydroxylase homeostasis. *J. Neurosci.* 42, 702–716. doi: 10.1523/JNEUROSCI.0653-21.2021

Li, B., Espósito, B. P., Wang, S., Zhang, J., Xu, M., Zhang, S., et al. (2019). Desferrioxamine-caffeine shows improved efficacy in chelating iron and depleting cancer stem cells. *J. Trace Elem Med. Biol.* 52, 232–238. doi: 10.1016/j.jtemb.2019.01.004

Li, M., Wang, Z. W., Fang, L. J., Cheng, S. Q., Wang, X., Liu, N. F., et al. (2022). Programmed cell death in atherosclerosis and vascular calcification. *Cell Death Dis.* 13:467.

Li, S., Zheng, L., Zhang, J., Liu, X., and Wu, Z. (2021). Inhibition of ferroptosis by up-regulating Nrf2 delayed the progression of diabetic nephropathy. *Free Radic. Biol. Med.* 162, 435–449. doi: 10.1016/j.freeradbiomed.2020.10.323

Li, X., Vemireddy, V., Cai, Q., Xiong, H., Kang, P., Li, X., et al. (2021). Reversibly modulating the blood-brain barrier by laser stimulation of molecular-targeted nanoparticles. *Nano Lett.* 21, 9805–9815. doi: 10.1021/acs.nanolett.1c02996

Linkermann, A., Skouta, R., Himmerkus, N., Mulay, S. R., Dewitz, C., De Zen, F., et al. (2014). Synchronized renal tubular cell death involves ferroptosis. *Proc. Natl. Acad. Sci. U S A.* 111, 16836–16841. doi: 10.1073/pnas.1415518111

Liu, J., Kang, R., and Tang, D. (2021). Signaling pathways and defense mechanisms of ferroptosis. *FEBS J.* 289, 7038–7050. doi: 10.1111/febs.16059

Liu, J., Kang, R., and Tang, D. (2022). Signaling pathways and defense mechanisms of ferroptosis. *FEBS J.* 289, 7038–7050.

Liu, M., Kong, X. Y., Yao, Y., Wang, X. A., Yang, W., Wu, H., et al. (2022). The critical role and molecular mechanisms of ferroptosis in antioxidant systems: a narrative review. *Ann. Transl. Med.* 10:368. doi: 10.21037/atm-21-6942

Liu, W. Z., Ma, Z. J., Kang, J. H., Lin, A. X., Wang, Z. H., Chen, H. W., et al. (2022). Grape seed proanthocyanidins exert a neuroprotective effect by regulating microglial M1/M2 polarisation in rats with spinal cord injury. *Mediators Inflamm* 2022:2579003. doi: 10.1155/2022/2579003

Liu, X., Zhang, Y., Wang, Y., and Qian, T. (2021). Inflammatory response to spinal cord injury and its treatment. *World Neurosurg.* 155, 19–31.

Lo, J., Chan, L., and Flynn, S. (2021). A systematic review of the incidence, prevalence, costs, and activity and work limitations of amputation, osteoarthritis, rheumatoid arthritis, back pain, multiple sclerosis, spinal cord injury, stroke, and traumatic brain injury in the united states: a 2019 update. *Arch. Phys. Med. Rehabil.* 102, 115–131. doi: 10.1016/j.apmr.2020.04.001

Long, Y., Yang, Q., Xiang, Y., Zhang, Y., Wan, J., Liu, S., et al. (2020). Nose to brain drug delivery - A promising strategy for active components from herbal medicine for treating cerebral ischemia reperfusion. *Pharmacol. Res.* 159:104795. doi: 10.1016/j.phrs.2020.104795

Lu, T., Wu, X., Wei, N., Liu, X., Zhou, Y., Shang, C., et al. (2018). Lipoxin A4 protects against spinal cord injury via regulating Akt/nuclear factor (erythroid-derived 2)-like 2/heme oxygenase-1 signaling. *Biomed. Pharmacother.* 97, 905–910. doi: 10.1016/j.biopha.2017.10.092

Ma, W. Q., Sun, X. J., Zhu, Y., and Liu, N. F. (2021). Metformin attenuates hyperlipidaemia-associated vascular calcification through anti-ferroptotic effects. *Free Radic. Biol. Med.* 165, 229–242. doi: 10.1016/j.freeradbiomed.2021.01.033

Mao, C., Liu, X., Zhang, Y., Lei, G., Yan, Y., Lee, H., et al. (2021). DHODH-mediated ferroptosis defence is a targetable vulnerability in cancer. *Nature* 593, 586–590.

Markowiak-Kopeć, P., and Śliżewska, K. (2020). The effect of probiotics on the production of short-chain fatty acids by human intestinal microbiome. *Nutrients* 12:1107.

Martínez-Reyes, I., and Chandel, N. S. (2020). Mitochondrial TCA cycle metabolites control physiology and disease. *Nat. Commun.* 11:102.

Ni, L., Yuan, C., and Wu, X. (2022). Targeting ferroptosis in acute kidney injury. *Cell Death Dis.* 13:182. doi: 10.1038/s41419-022-04628-9

Pang, Y., Liu, X., Wang, X., Shi, X., Ma, L., Zhang, Y., et al. (2022). Edaravone modulates neuronal gpx4/acsl4/5-lox to promote recovery after spinal cord injury. *Front. Cell Dev. Biol.* 10:849854. doi: 10.3389/fcell.2022.849854

Parker, J. L., Deme, J. C., Kolokouris, D., Kuteyi, G., Biggin, P. C., Lea, S. M., et al. (2021). Molecular basis for redox control by the human cystine/glutamate antiporter system xc. *Nat. Commun.* 12:7147. doi: 10.1038/s41467-021-27414-1

Quadri, S. A., Farooqui, M., Ikram, A., Zafar, A., Khan, M. A., Suriya, S. S., et al. (2020). Recent update on basic mechanisms of spinal cord injury. *Neurosurg. Rev.* 43, 425–441.

Rezai, A. R., Ranjan, M., D'Haese, P. F., Haut, M. W., Carpenter, J., Najib, U., et al. (2020). Noninvasive hippocampal blood-brain barrier opening in Alzheimer's disease with focused ultrasound. *Proc. Natl. Acad. Sci. U S A.* 117, 9180–9182. doi: 10.1073/pnas.2002571117

Saliminejad, K., Khorram, K. H., Soleymani, F. S., and Ghaffari, S. H. (2019). An overview of microRNAs: biology, functions, therapeutics, and analysis methods. *J. Cell Physiol.* 234, 5451–5465.

Santoro, M. M. (2020). The antioxidant role of non-mitochondrial CoQ10: mystery solved! *Cell Metab.* 31, 13–15. doi: 10.1016/j.cmet.2019.12.007

Satoh, T., Trudler, D., Oh, C. K., and Lipton, S. A. (2022). Potential therapeutic use of the rosemary diterpene carnosic acid for Alzheimer's disease, Parkinson's disease, and long-COVID through NRF2 activation to counteract the NLRP3 inflammasome. *Antioxidants* 11:124. doi: 10.3390/antiox11010124

Seibt, T. M., Proneth, B., and Conrad, M. (2019). Role of GPX4 in ferroptosis and its pharmacological implication. *Free Radic. Biol. Med.* 133, 144–152.

Shao, C., Chen, Y., Yang, T., Zhao, H., and Li, D. (2022). Mesenchymal stem cell derived exosomes suppress neuronal cell ferroptosis via lncGm36569/miR-5627-5p/FSP1 axis in acute spinal cord injury. *Stem Cell Rev. Rep.* 18, 1127–1142. doi: 10.1007/s12015-022-10327-x

Shen, Y., and Cai, J. (2023). The importance of using exosome-loaded miRNA for the treatment of spinal cord injury. *Mol. Neurobiol.* 60, 447–459. doi: 10.1007/s12035-022-03088-8

Shi, Z., Yuan, S., Shi, L., Li, J., Ning, G., Kong, X., et al. (2021). Programmed cell death in spinal cord injury pathogenesis and therapy. *Cell Prolif.* 54:e12992.

Song, X., and Long, D. (2020). Nrf2 and ferroptosis: a new research direction for neurodegenerative diseases. *Front. Neurosci.* 14:267. doi: 10.3389/fnins.2020.00267

Tang, D., Chen, X., Kang, R., and Kroemer, G. (2021). Ferroptosis: molecular mechanisms and health implications. *Cell Res.* 31, 107–125.

Tang, G., Chen, Y., Chen, J., Chen, Z., and Jiang, W. (2020). Deferoxamine ameliorates compressed spinal cord injury by promoting neovascularization in rats. *J. Mol. Neurosci.* 70, 1437–1444. doi: 10.1007/s12031-020-01564-1

Tang, G., Xu, Y., Zhang, C., Wang, N., Li, H., Feng, Y., et al. (2021). Green tea and epigallocatechin gallate (EGCG) for the management of nonalcoholic fatty liver diseases (NAFLD): insights into the role of oxidative stress and antioxidant mechanism. *Antioxidants* 10:1076. doi: 10.3390/antiox10071076

Terstappen, G. C., Meyer, A. H., Bell, R. D., and Zhang, W. (2021). Strategies for delivering therapeutics across the blood-brain barrier. *Nat. Rev. Drug Discov.* 20, 362–383.

Tsvetkov, P., Coy, S., Petrova, B., Dreishpoon, M., Verma, A., Abdusamad, M., et al. (2022). Copper induces cell death by targeting lipoylated TCA cycle proteins. *Science* 375, 1254–1261.

Tuo, Q. Z., Lei, P., Jackman, K. A., Li, X.-L., Xiong, H., Li, X.-L., et al. (2017). Tau-mediated iron export prevents ferroptotic damage after ischemic stroke. *Mol. Psychiatry* 22, 1520–1530. doi: 10.1038/mp.2017.171

Ursini, F., and Maiorino, M. (2020). Lipid peroxidation and ferroptosis: the role of GSH and GPx4. *Free Radic. Biol. Med.* 152, 175–185. doi: 10.1016/j.freeradbiomed.2020.02.027

Vasquez-Vivar, J., Shi, Z., and Tan, S. (2022). Tetrahydrobiopterin in cell function and death mechanisms. *Antioxid. Redox Signal.* 37, 171–183. doi: 10.1089/ars.2021.0136

Wang, C., Li, J., Han, X., Liu, S., Gao, X., Guo, C., et al. (2022). Silk sericin stabilized proanthocyanidins for synergetic alleviation of ulcerative colitis. *Int. J. Biol. Macromol.* 220, 1021–1030. doi: 10.1016/j.ijbiomac.2022.08.134

Wang, D., Day, E. A., Townsend, L. K., Djordjevic, D., Jørgensen, S. B., Steinberg, G. R., et al. (2021). GDF15: emerging biology and therapeutic applications for obesity and cardiometabolic disease. *Nat. Rev. Endocrinol.* 17, 592–607. doi: 10.1038/s41574-021-00529-7

Wang, F., Li, J., Zhao, Y., Guo, D., Liu, D., Chang, S., et al. (2022). miR-672-3p promotes functional recovery in rats with contusive spinal cord injury by inhibiting ferroptosis suppressor protein 1. *Oxid. Med. Cell Longev.* 2022:6041612. doi: 10.1155/2022/6041612

Wang, H., Zheng, Z., Han, W., Yuan, Y., Li, Y., Zhou, K., et al. (2020). Metformin promotes axon regeneration after spinal cord injury through inhibiting oxidative stress and stabilizing microtubule. *Oxid. Med. Cell Longev.* 2020:9741369. doi: 10.1155/2020/9741369

Wang, J., Chen, Y., Chen, L., Duan, Y., Kuang, X., Peng, Z., et al. (2020). EGCG modulates PKD1 and ferroptosis to promote recovery in ST rats. *Transl. Neurosci.* 11, 173–181. doi: 10.1515/tnsci-2020-0119

Wang, W., Marín-Ramos, N. I., He, H., Zeng, S., Cho, H. Y., Swenson, S. D., et al. (2021). NEO100 enables brain delivery of blood-brain barrier impermeable therapeutics. *Neuro Oncol.* 23, 63–75.

Wang, X., and Ge, P. (2020). Parthanatos in the pathogenesis of nervous system diseases. *Neuroscience* 449, 241–250.

Wang, Y., Luo, W., Lin, F., Liu, W., and Gu, R. (2022). Epigallocatechin-3-gallate selenium nanoparticles for neuroprotection by scavenging reactive oxygen species and reducing inflammation. *Front. Bioeng. Biotechnol.* 10:989602. doi: 10.3389/fbioe.2022.989602

Wang, Z., Wu, Z., Xie, Z., Zhou, W., and Li, M. (2022). Metformin attenuates ferroptosis and promotes functional recovery of spinal cord injury. *World Neurosurg.* 167, e929–e939. doi: 10.1016/j.wneu.2022.08.121

Warner, G. J., Berry, M. J., Moustafa, M. E., Carlson, B. A., Hatfield, D. L., Faust, J. R., et al. (2000). Inhibition of selenoprotein synthesis by selenocysteine tRNA[Ser]Sec lacking isopentenyladenosine. *J. Biol. Chem.* 275, 28110–28119. doi: 10.1074/jbc.M001280200

Wei, N., Lu, T., Yang, L., Dong, Y., and Liu, X. (2021). Lipoxin A4 protects primary spinal cord neurons from erastin-induced ferroptosis by activating the Akt/Nrf2/HO-1 signaling pathway. *FEBS Open Bio* 11, 2118–2126. doi: 10.1002/2211-5463.13203

Wu, X., Li, Y., Zhang, S., and Zhou, X. (2021). Ferroptosis as a novel therapeutic target for cardiovascular disease. *Theranostics* 11, 3052–3059.

Wu, Y., Wang, D., Lou, Y., Liu, X., Huang, P., Jin, M., et al. (2022). Regulatory mechanism of α-hederin upon cisplatin sensibility in NSCLC at safe dose by destroying GSS/GSH/GPX2 axis-mediated glutathione oxidation-reduction system. *Biomed. Pharmacother.* 150:112927. doi: 10.1016/j.biopha.2022.112927

Xia, M., Zhang, Q., Zhang, Y., Li, R., Zhao, T., Chen, L., et al. (2022). Growth differentiation factor 15 regulates oxidative stress-dependent ferroptosis post spinal cord injury by stabilizing the p62-Keap1-Nrf2 signaling pathway. *Front. Aging Neurosci.* 14:905115. doi: 10.3389/fnagi.2022.905115

Xie, B. S., Wang, Y. Q., Lin, Y., Mao, Q., Feng, J. F., Gao, G. Y., et al. (2019). Inhibition of ferroptosis attenuates tissue damage and improves long-term outcomes after traumatic brain injury in mice. *CNS Neurosci. Ther.* 25, 465–475. doi: 10.1111/cns.13069

Yao, X., Xie, R., Cao, Y., Tang, J., Men, Y., Peng, H., et al. (2021). Simvastatin induced ferroptosis for triple-negative breast cancer therapy. *J. Nanobiotechnol.* 19:311. doi: 10.1186/s12951-021-01058-1

Yao, X., Zhang, Y., Hao, J., Duan, H.-Q., Zhao, C.-X., Sun, C., et al. (2019). Deferoxamine promotes recovery of traumatic spinal cord injury by inhibiting ferroptosis. *Neural Regen. Res.* 14, 532–541.

Yao, Y., Wang, J., Liu, Y., Qu, Y., Wang, K., Zhang, Y., et al. (2022). Variants of the adeno-associated virus serotype 9 with enhanced penetration of the blood-brain barrier in rodents and primates. *Nat. Biomed. Eng.* 6, 1257–1271. doi: 10.1038/s41551-022-00938-7

Zeng, J., Zhu, L., Liu, J., Zhu, T., Xie, Z., Sun, X., et al. (2019). Metformin protects against oxidative stress injury induced by ischemia/reperfusion via regulation of the lncRNA-H19/miR-148a-3p/Rock2 axis. *Oxid. Med. Cell Longev.* 2019:8768327. doi: 10.1155/2019/8768327

Zhang, H. S., Zhang, Z. G., Du, G. Y., Sun, H. L., Liu, H. Y., Zhou, Z., et al. (2019). Nrf2 promotes breast cancer cell migration via up-regulation of G6PD/HIF-1α/Notch1 axis. *J. Cell Mol. Med.* 23, 3451–3463. doi: 10.1111/jcmm.14241

Zhang, Y., and DeBosch, B. J. (2019). Using trehalose to prevent and treat metabolic function: effectiveness and mechanisms. *Curr. Opin. Clin. Nutr. Metab. Care* 22, 303–310. doi: 10.1097/MCO.0000000000000568

Zhang, Y., et al. (2022). Edaravone modulates neuronal GPX4/ACSL4/5-LOX to promote recovery after spinal cord injury. *Front. Cell Dev. Biol.* 10:849854. doi: 10.3389/fcell.2022.849854

Zhang, Y., Sun, C., Zhao, C., Hao, J., Zhang, Y., Fan, B., et al. (2019). Ferroptosis inhibitor SRS 16-86 attenuates ferroptosis and promotes functional recovery in contusion spinal cord injury. *Brain Res.* 1706, 48–57. doi: 10.1016/j.brainres.2018.10.023

Zhang, Z. H., and Song, G. L. (2021). Roles of selenoproteins in brain function and the potential mechanism of selenium in Alzheimer's disease. *Front. Neurosci.* 15:646518. doi: 10.3389/fnins.2021.646518

Zhao, Q., Liu, F., Zhou, B., Liu, H., Wang, X., Li, S., et al. (2022). Ferroptosis: a novel therapeutic direction of spinal cord injury. *Comput. Math. Methods Med.* 2022:7906218. doi: 10.1155/2022/7906218

Zheng, J., Piao, M. J., Kim, K. C., Yao, C. W., Cha, J. W., Hyun, J. W., et al. (2014). Fucoxanthin enhances the level of reduced glutathione via the Nrf2-mediated pathway in human keratinocytes. *Mar. Drugs* 12, 4214–4230. doi: 10.3390/md12074214

Zhong, L., Zhang, H., Ding, Z. F., Li, J., Lv, J. W., Pan, Z. J., et al. (2020). Erythropoietin-Induced autophagy protects against spinal cord injury and improves neurological function via the extracellular-regulated protein kinase signaling pathway. *Mol. Neurobiol.* 57, 3993–4006. doi: 10.1007/s12035-020-01997-0

Zhou, H., Yin, C., Zhang, Z., Tang, H., Shen, W., and Zha, X. (2020). Proanthocyanidin promotes functional recovery of spinal cord injury via inhibiting ferroptosis. *J. Chem. Neuroanat.* 107:101807. doi: 10.1016/j.jchemneu.2020.101807

Zipser, C. M., Cragg, J. J., Guest, J. D., Fehlings, M. G., Jutzeler, C. R., Anderson, A. J., et al. (2022). Cell-based and stem-cell-based treatments for spinal cord injury: evidence from clinical trials. *Lancet Neurol.* 21, 659–670. doi: 10.1016/S1474-4422(21)00464-6

Zou, Y., Li, H., Graham, E. T., Deik, A. A., Eaton, J. K., Wang, W., et al. (2020). Cytochrome P450 oxidoreductase contributes to phospholipid peroxidation in ferroptosis. *Nat. Chem. Biol.* 16, 302–309. doi: 10.1038/s41589-020-0472-6

frontiers | Frontiers in Neuroscience

TYPE Original Research
PUBLISHED 05 May 2023
DOI 10.3389/fnins.2023.1136110

OPEN ACCESS

EDITED BY
Jing Teng,
North China Electric Power University, China

REVIEWED BY
Chenxi Li,
Air Force Medical University, China
Yu Luo,
Johns Hopkins University, United States

*CORRESPONDENCE
Lingling Deng
✉ 307027521@qq.com
Wei Wang
✉ cjr.wangwei@vip.163.com
Ding Liu
✉ liuding@csu.edu.cn

†These authors have contributed equally to this work

RECEIVED 02 January 2023
ACCEPTED 11 April 2023
PUBLISHED 05 May 2023

CITATION
Liu Y, Li Q, Yi D, Duan J, Zhang Q, Huang Y, He H, Liao Y, Song Z, Deng L, Wang W and Liu D (2023) Topological abnormality of structural covariance network in MRI-negative frontal lobe epilepsy.
Front. Neurosci. 17:1136110.
doi: 10.3389/fnins.2023.1136110

Topological abnormality of structural covariance network in MRI-negative frontal lobe epilepsy

Yin Liu[1†], Quanji Li[2†], Dali Yi[1†], Junhong Duan[1], Qingxia Zhang[2], Yunchen Huang[1], Haibo He[1], Yunjie Liao[1], Zhi Song[2], Lingling Deng[3*], Wei Wang[1*] and Ding Liu[2*]

[1]Department of Radiology, The Third Xiangya Hospital, Central South University, Changsha, China, [2]Department of Neurology, The Third Xiangya Hospital, Central South University, Changsha, China, [3]Department of Radiology, The Second Affiliated Hospital, University of South China, Hengyang, China

Background: Frontal lobe epilepsy (FLE) is the second most common type of focal epilepsy, however, imaging studies of FLE have been far less than Temporal lobe epilepsy (TLE) and the structural findings were not consistent in previous literature.

Object: Investigate the changes in cortical thickness in patients with FLE and the alteration of the structural covariance networks (SCNs) of cortical thickness with graph-theory.

Method: Thirty patients with FLE (18 males/12 females; 28.33±11.81years) and 27 demographically matched controls (15 males/12 females; 29.22±9.73years) were included in this study with high-resolution structural brain MRI scans. The cortical thickness was calculated, and structural covariance network (SCN) of cortical thickness were reconstructed using 68×68 matrix and analyzed with graph-theory approach.

Result: Cortical thickness was not significantly different between two groups, but path length and node betweenness were significantly increased in patients with FLE, and the regional network alterations were significantly changed in right precentral gyrus and right temporal pole (FDR corrected, $p<0.05$). Comparing to HC group, network hubs were decreased and shifted away from frontal lobe.

Conclusion: The topological properties of cortical thickness covariance network were significantly altered in patients with FLE, even without obvious surface-based morphological damage. Graph-theory based SCN analysis may provide sensitive neuroanatomical biomarkers for FLE.

KEYWORDS

graph theory, structural covariance network, cortical thickness, frontal lobe epilepsy, default mode network (DMN)

1. Introduction

Frontal lobe epilepsy (FLE) is the second common type of focal epilepsy behind temporal lobe epilepsy, accounting for ~20%–30% of sufferers (Manford et al., 1996). As the largest lobe of neocortex, the highly interconnected nature of the frontal lobe allows for a quick and widespread propagation of epileptic activity to the other brain regions, which may give rise to

the perplexing clinical and electrophysiological finding of FLE. A variety of semiologies are common for FLE patients, such unilateral clonic seizures, tonic asymmetric seizures with preserved consciousness, hypermotor seizures, and secondary generalized seizures. The ambiguity in localization and lateralization of deficits of EEG is well known, even false negative EEG is not uncommon (Beleza and Pinho, 2011). Seizures in FLE are mostly likely to be associated with multi-cognitive defects and motor-related abnormality networks (Kellinghaus and Lüders, 2004; Beleza and Pinho, 2011), and the treatment outcome is disappointing, as only 20%–30% of patients achieve seizure freedom with medication (Regesta and Tanganelli, 1999). Of all patients with refractory focal epilepsies referred to epilepsy surgery, 25% have FLE, and only 30%–50% achieve seizure freedom with surgery (Bagla and Skidmore, 2011). As epileptogenic zone may be subtle and not obvious in routine MRI examination (Bonini et al., 2014), it presents challenges in FLE patients with ambiguous EEG pattern, and calls for better clarification of the underlying neuroanatomic characteristic of FLE, especially for patients with normal routine MRI examination.

As a brain network disorder, epilepsy has been widely studied using quantitative neuroimaging data, which supported that epileptogenic network are involved in the generation and expression of seizures, and to the maintenance of the disorder (Spencer, 2002). In contrast to make low-level regional and connectional alterations with conventional approach, graph-theory analysis provides a correlational framework to reveal the persistent functional-trophic cross-talk, maturational inter-change, as well as common developmental and pathological influences (Bullmore and Sporns, 2012; Alexander-Bloch et al., 2013; Bernhardt et al., 2013), and can be used for various modalities of neuroimaging data. Normal topological network is characterized by high clustering coefficients and short average path lengths. According to previous graph-theory based fMRI and diffusional MRI (dMRI) studies (Vaessen et al., 2013, 2014; Gleichgerrcht et al., 2015; Zhou et al., 2019; Lin et al., 2020; Togo et al., 2022), rearrangement of global and local topological parameters has been found in patients of focal epilepsy (including FLE and TLE), such as diminished network strength, clustering coefficient, path length, and global efficiency, both within and beyond the epileptogenic zone.

Unlike fMRI and dMRI, structural T1-weighted images is a standard component of every clinical imaging protocol with short acquisition time. These images are generally unaffected by distortion and signal drop out artifacts in orbitofrontal and temporo-basal regions which often occur in echo-planar functional and diffusion MRI sequences (Bernhardt et al., 2013; Gleichgerrcht et al., 2015). Graph theory based structural covariance network (SCN) of cortical thickness directly seeds from cortical gray matter regions in a high-resolution space, which is not limited by the imaging voxels but by the sampling density of the points on the cortical mesh (Hosseini et al., 2012; Alexander-Bloch et al., 2013). SCN analysis has been applied to investigate in various central nervous system disorders (Hosseini et al., 2012; Singh et al., 2013), and considered a promising tool in investigating the brain network alterations in epilepsy (Li et al., 2020), but it was rarely used in FLE patients. In order to investigate the topological property alteration of cortical thickness in FLE, SCN analysis was performed between a group of clinically diagnosed FLE patients with negative MRI and a age-, gender-, education-matched healthy control (HC) group in the present study.

2. Patients and methods

2.1. Patients

Thirty FLE patients (18 males, age range = 16–62 years; average age ± standard deviation = 28.33 years; standard deviation = 11.81 years) were recruited from Department of Neurology, the Third Xiangya Hospital, Central South University. All patients were diagnosed by senior neurologists based on comprehensive evaluation of clinical history, 24-h video-EEG recording, ictal semiology, routine MRI examination according to the International League Against Epilepsy (ILAE) guidelines (Engel, 2001). No structural abnormalities can be identified responsible for these FLE patients through the routine MRI examination, such as malformation, tumor, reactive gliosis, and other epileptogenic lesions. All patients underwent 24-h (overnight including the sleep period) scalp video-EEG recordings (EEG-1200C, Nihon Kohden, Tokyo, Japan). For EEG, 16 electrodes were distributed according to 10–20 international standard system, and the sampling rate was set at 256 Hz. All patients received antiepileptic drug (AED) treatments with regular out-patient follow-up. The detailed demographic information and the clinical characteristics of FLE patients can be seen in Table 1. A total of 27 age-, gender- and education-matched healthy volunteers were also recruited as controls (15 males, age range = 18–60 years, average age ± standard deviation = 29.22 years; standard deviation = 9.73 years). Written consent forms of all FLE patients and controls were obtained. The study protocol was approved by the Ethics Committee of the Third Xiangya Hospital, Central South University.

Duration of illness, epileptic seizure types, initial and follow-up EEGs, medication protocol, the follow-up seizure attacks after treatment were also collected for all patients. The National Hospital Seizure Severity Scale (NHS3) which contains seven seizure-related factors on a score of 1 to 27 was used to assess the severity of epilepsy (O'Donoghue et al., 1996). The seizure attack frequency after treatment for each patient was evaluated according to International League Against Epilepsy (ILAE) scale (Wieser et al., 2001).

TABLE 1 Demographic, clinical, and neuropsychological test difference between FLE and HC group.

Clinical characteristic	FLE patients (n=30)	HC (n=27)	p value
Age at examination/year[a]	28.33 (11.81)	29.22 (9.73)	0.76
Gender/male[b]	18 (60%)	15 (56%)	0.73
Eduacation/year[a]	12.47 (2.73)	13.04 (3.31)	0.48
Disease duration/year[a]	8.50 (9.64)		
Localization (left/right/bilateral/unknown)	3/5/21/1		
Seizure frequency (grade 0/1/2/3)	9/13/1/7		
Medication (mono/multi medication)	24/6		

[a]Data in average (standard deviation).
[b]Data in number (percent).

2.2. Image acquisition

MRI data were acquired using a 3.0 T MRI scanner (Ingenia, Philips Medical Systems, Netherlands) with a 15-channel receiver array head coil at the Department of Radiology, Third Xiangya Hospital, Central South University. The participants were instructed to lie quietly with their eyes closed but remain awake, and to avoid specific thoughts during scanning. To improve image quality, earplugs were used to attenuate scanner noise, and foam pads were applied to minimize head movements.

Structural images were acquired with a three-dimensional turbo fast echo (3D-TFE) T1WI sequence with high resolution as follows: repetition time (TR)/echo time (TE) = 9.1/4.5 ms; slices = 170; thickness = 1 mm; gap = 0 mm; flip angle (FA) = 8°; acquisition matrix = 256 × 256; field of view (FOV) = 240 mm × 240 mm.

2.3. Data preprocessing

The cortical thickness (CT) was determined using CAT12[1] and SPM12[2] based on the MATLAB 2014a operating environment (MathWorks, Natick, MA, USA). Briefly, the T1-weighted images underwent tissue segmentation to estimate white matter distance. Local maxima were then projected to other grey matter voxels by using a neighbor relationship described by the white matter distance. These values equal cortical thickness. Topological correction was performed through an approach based on spherical harmonics (Fischl and Dale, 2000). After preprocessing and visual checks for artefacts, all scans passed through the automated quality check promoted in the manual of CAT12. No participant was excluded by the automated quality check protocol. The brain was parcellated into 68 cortical regions using the Desikan-Killiany atlas (Desikan et al., 2006) and the mean cortical thickness was calculated for each region. The individual map of CT was smoothed with a Gaussian filter with a full-width at half-maximum of 15 mm to statistical analysis.

2.4. Cortical thickness structural covariance networks construction

Graph Analysis Toolbox (GAT) was used to construct the SCNs based on CT (Hosseini et al., 2012). A linear regression analysis was conducted for each cortical region to adjust the effect of age and gender, so that the corrected cortical thickness was obtained to construct SCN. According to the Desikan–Killiany Atlas (Desikan et al., 2006), a 68 × 68 correlation matrix was established for each group by calculating Pearson correlation coefficients between interregional corrected CT values. Thereafter, the correlation matrix was converted into a binary adjacency matrix by thresholding correlation coefficients into values of 1 or 0 (Figure 1). Here, these thresholds were defined as a range of network densities varying from 0.38 to 0.5 (increments of 0.02), which ensured that FLE and HC SCNs had the same number of nodes and edges at each density. The minimum density (0.38) was determined to ensure that the networks were not fragmented for both groups. For density above 0.5 the networks approached random configuration (Humphries et al., 2006; Singh et al., 2013). Inter-group differences of network topologies were compared across the range.

2.5. Global and regional network analyses

According to the definitions of these parameters in previous studies (He et al., 2008; Rubinov and Sporns, 2010), a series of global and regional network parameters was calculated to characterize the topological properties of the SCNs. Global network parameters included normalized clustering coefficient, normalized path length, and small-world index. Briefly, the human brain can be regarded as a small-world network that has the highest clustering coefficient (Cp) and shortest path length (Lp). Cp of a node pertains the number of existing connections linking the adjacent nodes divided by all their possible connections. The Cp of a network is the average of clustering coefficients across all nodes in a network, which represents network segregation. The shortest path length (Lp) is equal to the minimum number of edges that connect two nodes. The Lp of a network pertains to the average shortest path length involving all node pairs in the network, which represents network integration. The normalized clustering coefficient (gamma) and normalized path length (lamda) were calculated, respectively, by comparing the CP and Lp to the mean Cp and mean Lp of 1,000 random network (Maslov and Sneppen, 2002).

The nodal characteristics of the CT structural covariance network were examined and the alteration of regional network between groups were analyzed. Which included that the nodal local efficiency, nodal clustering coefficient and nodal betweenness centrality. The node local efficiency reflects the connection degree between a node and other nodes, representing the communication efficiency of the node. Nodal betweenness centrality is an important index which is defined as the number of shortest paths between any two nodes in the network that pass through a given node (Rubinov and Sporns, 2010). The graph index is used to detect important functional or anatomical connections. The quantified nodal local efficiency, clustering coefficient, and betweenness centrality were, respectively, normalized by the average network local efficiency, clustering coefficient, and betweenness centrality. Inter-group differences of these normalized region network parameters were compared.

2.6. Network hubs

Hubs are the most globally connected regions in the brain and are essential for coordinating brain function through the connectivity with numerous brain regions. Hubs play a central role in integrating diverse information sources and supporting fast information communication with minimal energy cost. In our study, the criteria for defining hub is that the node's betweenness was at least 2 standard deviation higher than the mean network betweenness centrality (Hosseini et al., 2012).

1 http://dbm.neuro.uni-jena.de/cat/

2 http://www.fil.ion.ucl.ac.uk/spm

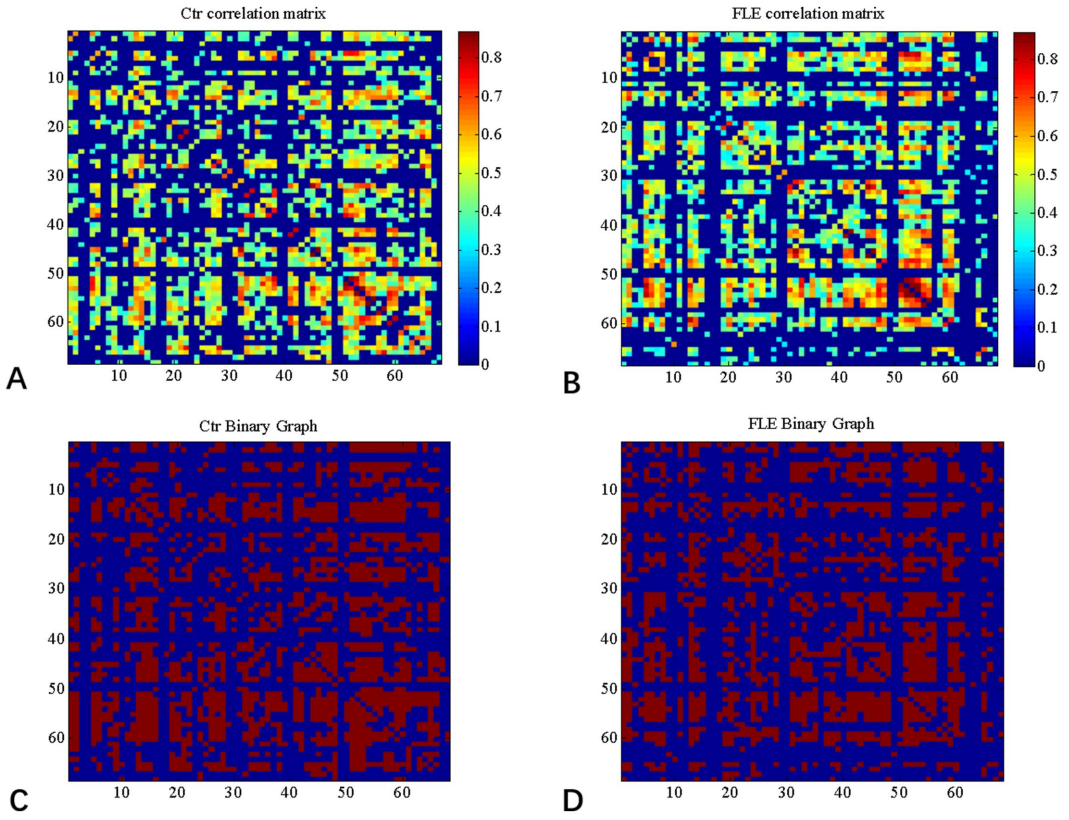

FIGURE 1
Correlation matrices and adjacency matrices with 68×68 for healthy controls (Ctrl) and frontal lobe epilepsy (FLE) patients. Correlation matrices for HC **(A)** and FLE patients **(B)** and binary adjacency matrices at the minimum density (0.38) for HC **(C)** and FLE patients **(D)**. Correlation matrices show the Pearson correlation coefficient between any two regions of the network and the color bar denotes the absolute value of the Pearson correlation coefficient and represents the strength of the connections.

2.7. Statistical analysis

Clinical data analysis was completed using IBM SPSS 26.0. Chi-square tests were used to compare categorical variables. Student's *t*-test or the Mann–Whitney U-test were used to compare continuous variables between two groups.

For the CT maps, general linear modeling, installed in the CAT toolbox, was used to perform vertex-wise group inference on the smoothed cortical surfaces. To calculate significance of the differences in SCN parameters between groups, we analyzed the network parameters both at Dmin and across the density range (0.38–0.5 with an interval of 0.02) using area under the curve (AUC). A non-parametric permutation test (1,000 repetitions) was used to investigate the statistical significance of the difference in global and regional network parameters. The comparison of the global and regional parameters between groups was completed with the GAT toolbox with the result corrected by $p < 0.05$ with false discovery rate (FDR) considered to be statistically significant.

3. Results

3.1. Demographic and clinical characteristics

The demographic and clinical information of FLE and HC groups were listed in Table 1. All the patients were complex-partial seizure with secondary generalized tonic–clonic attack, with typical frontal lobe epilepsy characteristic such as hypermotion, dominance of attack during sleep. The average duration of disease was 8.50 (SD = 9.64). The NHS3 score for the patients ranged from 2 to 18, with the average ± SD of 9.67 ± 4.14.

3.2. Between-group comparison of CT

Comparing to HC group, only the cortical thickness of left postcentral gyrus was decreased in FLE group ($p < 0.001$,uncorrected), but the difference was not significant after FDR correction.

3.3. Inter-group differences in global network metrics

Changes and between-group differences in global network parameters were significant between two groups at densities ranging from 0.38 to 0.50, as shown in Figure 2. Compared to HC group, both the characteristic and normalized path length of FLE group were significantly longer, and the mean node betweenness was also significantly higher in FLE group. The global and local efficiency, clustering coefficient (Gamma), and small-world index (Sigma) were lower in FLE, but they did not reach statistical significance (data not shown).

3.4. Inter-group differences in regional network metrics

Inter-group differences in regional network metrics of normalized clustering and local efficiency were shown in Figure 3. Compared to HC group, both the normalized clustering and local efficiency of right precentral gyrus were significantly higher, and that of right temporal pole were significantly lower in FLE ($p < 0.05$ with FDR correction).

3.5. Network hubs

Figure 4 displayed group-specific hubs for HC and FLE groups. Hubs determined for HC group network included left inferior temporal gyrus, left medial orbito-frontal gyrus, bilateral precuneus gyri, and superior frontal gyrus. Hub number for FLE group was reduced, which included left inferior parietal gyrus, right inferior parietal gyrus, and left supramarginal gyrus.

4. Discussions

This study investigated the topological property alteration of cortical thickness based SCN in FLE patients without structural abnormality on conventional MR. Both the global and regional network parameters were significantly different between FLE and HC groups. The results revealed that the structural network properties were significantly changed in MRI-negative FLE patients, suggesting higher sensitivity of graph-theory based analysis in detecting the neurobiological injury in FLE patients. To the best of our knowledge, the present study reported for the first time the cortical-thickness related topological property alteration in MRI-negative FLE patients and it may be a valuable tool in future clinical practice.

The structural alterations of FLE were not consistent in previous studies. In the study of Widjaja et al. (2011), widespread cortical thinning was found, while in other studies, there was no significant difference in cortical /GM volume between FLE and HC (Lu et al., 2022). In the present study, cortical thickness was not significantly different between the two groups. However, our study demonstrated that FLE patients had significantly different topological change for both global and regional network parameters, though both groups showed a small-world topology. Consistent with previous functional graph-theory based neuroimaging studies of epilepsy (Vaessen et al., 2013), the path length and node betweenness were significantly increased in FLE, indicating the global network topology was altered toward a regularized pattern. However, variations in structural network were also found. In the study of Vaessen et al. (2013), the structural path length and clustering remained normal in children with FLE, structural modularity was different between two groups and it was increased with stronger cognitive impairment. Thus modularity may be associated with cognitive status, which was not included in present study and warrants further investigation. In addition to methodological approach difference (e.g., different atlases and morphometric features), patient selection variation may also contribute to the discrepancy. For the study of Vaessen et al. (2013, 2014) and Widjaja et al. (2011), the patients recruited were children, but the patients in the present study were adults older than 14 years old. As cortical structure should be closely associate with age, and the variation during development and maturation of frontal lobe may be huge even in normal population (Silver et al., 2021; Herring et al., 2022), future studies with larger sample size is warranted to clarify the influence of age.

In FLE, the clinical symptoms of these seizures are variable and dependent on the brain regions, which may include peri-rolandic, supplementary sensorimotor area, dorsolateral frontal, orbitofrontal, anterior frontopolar, opercular, and cingulate types (Bagla and

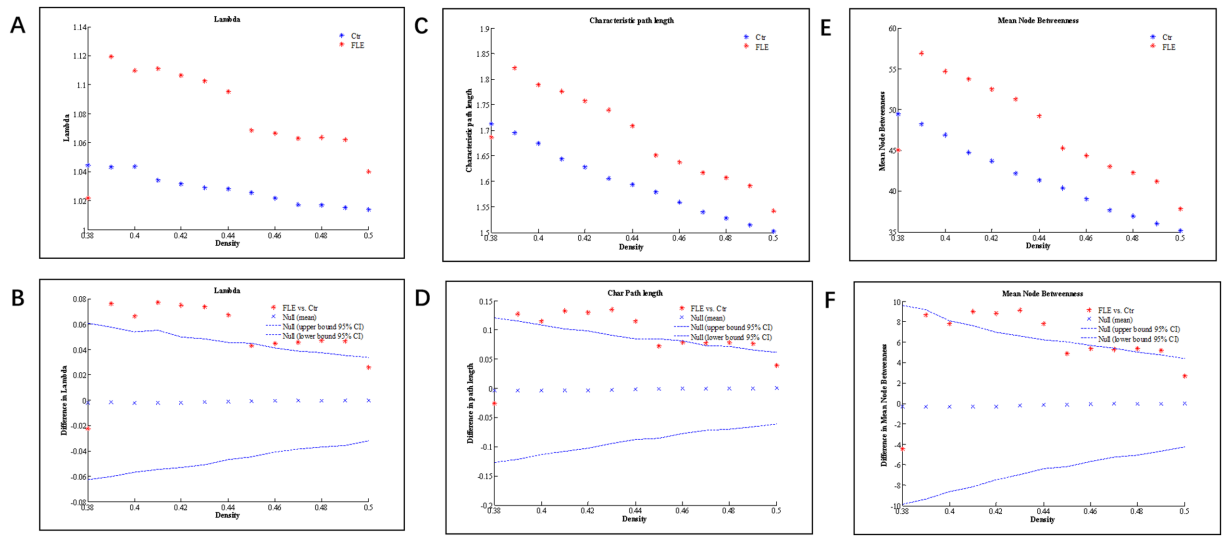

FIGURE 2
Changes and between-group differences of normalized path length (**A,B**; Lamda), characteristic path length **(C,D)**, and mean node betweenness **(E,F)** as a function of network density in healthy control (Ctrl) and frontal lobe epilepsy (FLE) groups. For between-group differences **(B,D,E)**, Except for a few densities, there are significant difference between two groups, as indicated by dots lying outside the 95% confidence intervals (dashed lines) (p<0.05 after FDR correction).

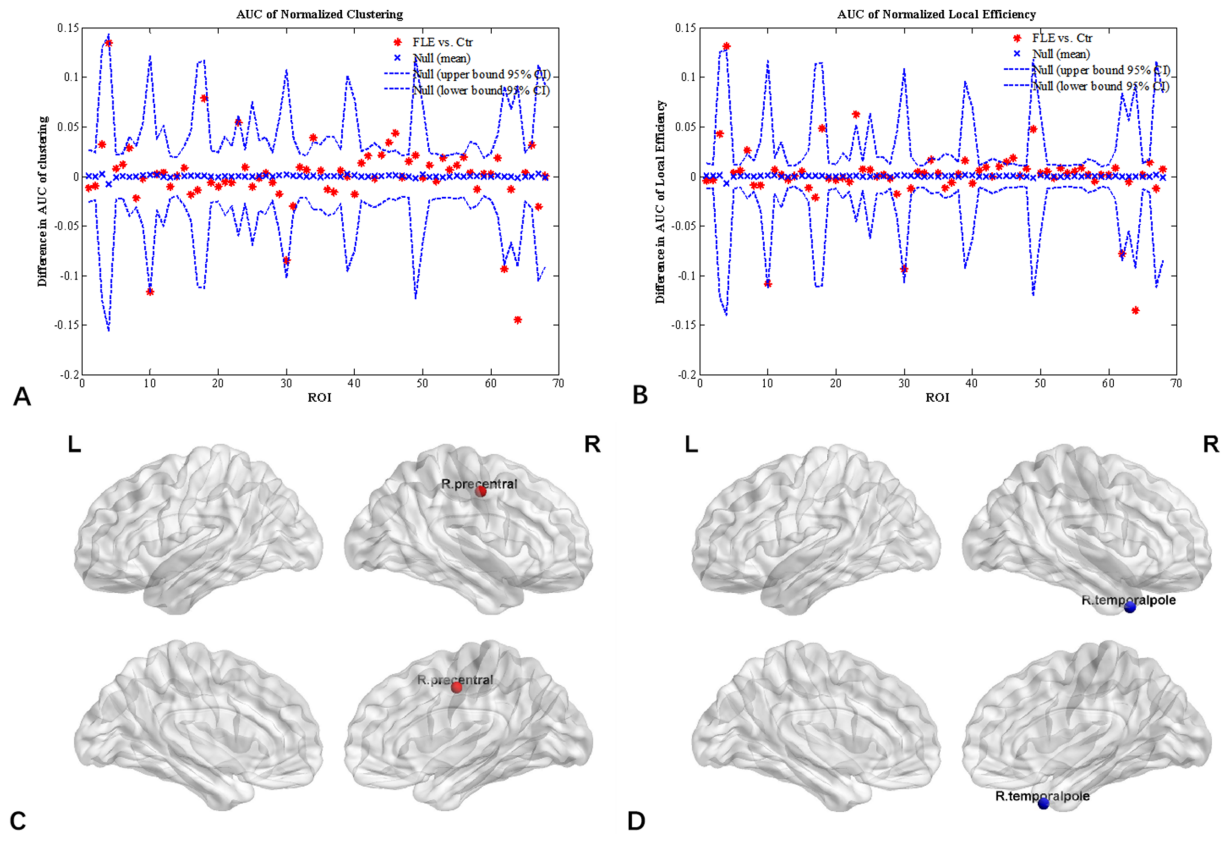

FIGURE 3
Regional network parameter difference between HC and FLE groups. Between-group differences of normalized clustering coefficient **(A)** and normalized local efficiency **(B)** across a range of network densities was shown. The red * lying outside of the confidence intervals indicates regions different between the two groups in this density, and cortical regions survived FDR correction ($p<0.05$) were right precentral gyrus **(C)** with a increased clustering coefficient and local efficiency, and right temporal pole **(D)** with decreased clustering coefficient and local efficiency in FLE patients compared with HCs.

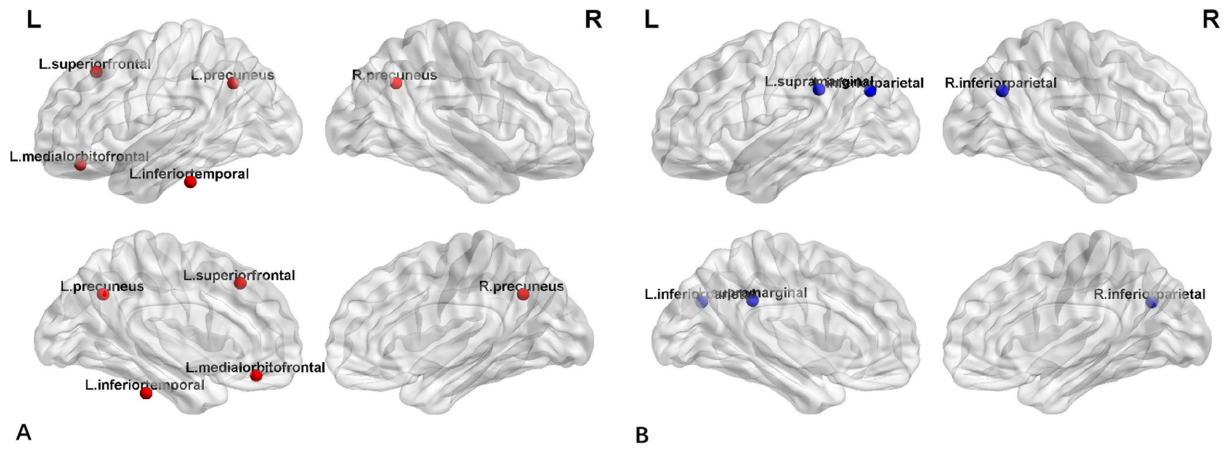

FIGURE 4
The distribution of network hubs in HCs **(A)** and FLE patients **(B)**.

Skidmore, 2011). But most FLE patients usually are recognized as multi-cognitive defects and motor-related networks defects (Kellinghaus and Lüders, 2004; Beleza and Pinho, 2011). In the present study, all the patients were clinically diagnosed FLE, with the prominent seizure characteristics of hypermotor attacks and secondary generalized clonic–tonic seizure. This is in agreement with previous report on FLE (Bagla and Skidmore, 2011; Bonini et al., 2014) and we speculated that motor-related network abnormality

should be found. In agreement with this speculation, both normalized clustering and local efficiency of right precentral gyrus were significantly increased, indicating an abnormal increase in network segregation in sensorimotor network. Similar findings were reported in previous study of FLE (Woodward et al., 2014).

Connections between temporal lobe and sensorimotor cortex have been repeatedly reported in previous neuroimaging studies of MRI-negative TLE patients, especially for right MTS to influence ipislateral thalamus and temporal pole (Coan et al., 2014; Roggenhofer et al., 2020). In addition to TLE, temporal pole and precentral gyrus involvement is also reported for patients with GTCS (Liu et al., 2017; Li et al., 2020). Thus, it is not surprising that regional topological parameters were also compromised for right temporal pole in the study. As a seizure is typically the result of the networks that are recruited or traveled by the epileptiform discharges, therefore seizure-onset localization can be misled by clinical manifestations that may arise from recruited networks that are remotely located from the ictal source. The decreased clustering and local efficiency of right temporal pole may reflect the intrinsic network pattern of fronto-limbic system.

Similarly, network hub analysis showed that there were significant difference between FLE and HC groups. In HC group, the hubs were evenly distributed around the neocortex, including bilateral precuneus, left inferior temporal gyrus and left medial orbitofrontal gyrus, which was consistent with DMN network hubs (Zhou et al., 2019). However, for FLE patients, the hubs were reduced and shifted posterior and none was found in frontal lobes. The hubs identified in FLE group, the inferior parietal lobule which is usually closely connected with precuneus (Togo et al., 2022). Together with supramarginal gyrus, IPL is a region implicated in a diverse range of higher cognitive functions and may be associated with multiple brain networks, including DMN, Frontoparietal control network, and cingulo-opercular network (Igelström and Graziano, 2017). This hub alteration pattern may reflect the DMN abnormality in FLE, which was also reported in previous fMRI studies of epilepsy (Lin et al., 2020; Togo et al., 2022). The mechanism was unknown, but it may result from the interrupted small-world properties within frontal lobe in FLE, as noted by the disappearance of network hub in frontal lobe in FLE.

In addition, the hubs found in FLE, were among regions of reduced cortical thickness reported by Widjaja et al. (2011), in a study of FLE children. Similarly, in the functional connectivity study of FLE patients by Wu et al. (2019), increased ALFF in the precuneus of FLE patient, despite their response to antiepileptic medication, and these were the hubs for HC group in the present study. Inferior parietal lobules were also found to be affected in patients with hyperkinetic seizures (Sasagawa et al., 2021). The clinical significance of the network hub alteration remains unknown and warrants further investigation.

The present study has several limitations. Firstly, the FLE patients were clinically diagnosed, which was based on seizure semiology and EEG; while magneto encephalography, FDG-PET, and invasive intracranial monitoring were unavailable for the patients. Thus the possibility of multiple origin other than frontal lobe could not be completely excluded. In addition, most of the patients could not be lateralized, thus it is not clear whether the laterality affected the cortical thickness and brain volume distribution. Also, the sample size was relatively small with various illness duration, and the medicine used was not the same among subjects. These would have potential effects on the topological results, and future studies with larger sample size and better homogeneity of FLE patients may provide further insights. Secondly, cross-sectional design was used in the present study which brings difficulty to get a causal conclusion. Longitudinal design may be needed in the future to further confirm our finding and assess whether the changes of network graph properties is the consequence of seizures.

In summary, the present study investigated topological properties of cortical thickness covariance network alteration in patients with FLE using the graph theory method. Both global and regional network parameters were significantly different between patients with FLE and normal controls, despite the surface-based cortical thickness was not significantly different between two groups. These results indicated that graph-theory based structural covariance network analysis may provide clues to reveal the structural alterations in MRI-negative FLE.

Data availability statement

The raw data supporting the conclusions of this article will be made available by the authors, without undue reservation.

Ethics statement

The studies involving human participants were reviewed and approved by the Ethics Committee of the Third Xiangya Hospital, Central South University. The patients/participants provided their written informed consent to participate in this study.

Author contributions

YiL, WW, DL, and ZS designed the study. QL, DY, QZ, JD, YH, and HH collected the clinical and imaging data. DY, QL, and LD analyzed the data. YiL, QL, DY, DL, LD, and WW co-wrote the manuscript. All authors contributed to the article and approved the submitted version.

Funding

This study was supported by Hunan Provincial Natural Science Foundation (2022JJ30890) and Natural Science Foundation of Changsha City (No. kq2208363).

Conflict of interest

The authors declare that the research was conducted in the absence of any commercial or financial relationships that could be construed as a potential conflict of interest.

Publisher's note

References

Alexander-Bloch, A., Giedd, J., and Bullmore, E. J. N. R. N. (2013). Imaging structural co-variance between human brain regions. *Nat. Rev. Neurosci.* 14, 322–336. doi: 10.1038/nrn3465

Bagla, R., and Skidmore, C. J. T. N. (2011). Frontal lobe seizures. *Neurologist* 17, 125–135. doi: 10.1097/NRL.0b013e31821733db

Beleza, P., and Pinho, J. J. J. O. C. N. O. J. O. T. N. S. O. A. (2011). Frontal lobe epilepsy. *J. Clin. Neurosci.* 18, 593–600. doi: 10.1016/j.jocn.2010.08.018

Bernhardt, B., Hong, S., Bernasconi, A., and Bernasconi, N. J. F. I. H. N. (2013). Imaging structural and functional brain networks in temporal lobe epilepsy. *Front. Hum. Neurosci.* 7:624. doi: 10.3389/fnhum.2013.00624

Bonini, F., McGonigal, A., Trébuchon, A., Gavaret, M., Bartolomei, F., Giusiano, B., et al. (2014). Frontal lobe seizures: from clinical semiology to localization. *Epilepsia* 55, 264–277. doi: 10.1111/epi.12490

Bullmore, E., and Sporns, O. J. N. R. N. (2012). The economy of brain network organization. *Nat. Rev. Neurosci.* 13, 336–349. doi: 10.1038/nrn3214

Coan, A., Campos, B., Beltramini, G., Yasuda, C., Covolan, R., and Cendes, F. J. E. (2014). Distinct functional and structural MRI abnormalities in mesial temporal lobe epilepsy with and without hippocampal sclerosis. *Epilepsia* 55, 1187–1196. doi: 10.1111/epi.12670

Desikan, R., Ségonne, F., Fischl, B., Quinn, B., Dickerson, B., Blacker, D., et al. (2006). An automated labeling system for subdividing the human cerebral cortex on MRI scans into gyral based regions of interest. *NeuroImage* 31, 968–980. doi: 10.1016/j.neuroimage.2006.01.021

Engel, J. (2001). A proposed diagnostic scheme for people with epileptic seizures and with epilepsy: Report of the ILAE task force on classification and terminology. *Epilepsia* 42, 796–803. doi: 10.1046/j.1528-1157.2001.10401.x

Fischl, B., and Dale, A. J. P. O. T. N. A. O. S. O. T. U. S. O. A. (2000). Measuring the thickness of the human cerebral cortex from magnetic resonance images. *Proc. Natl. Acad. Sci. U. S. A.* 97, 11050–11055. doi: 10.1073/pnas.200033797

Gleichgerrcht, E., Kocher, M., and Bonilha, L. J. E. (2015). Connectomics and graph theory analyses: Novel insights into network abnormalities in epilepsy. *Epilepsia* 56, 1660–1668. doi: 10.1111/epi.13133

He, Y., Chen, Z., and Evans, A. J. T. J. O. N. T. O. J. O. T. S. F. N. (2008). Structural insights into aberrant topological patterns of large-scale cortical networks in Alzheimer's disease. *J. Neurosci.* 28, 4756–4766. doi: 10.1523/jneurosci.0141-08.2008

Herring, C., Simmons, R., Freytag, S., Poppe, D., Moffet, J., Pflueger, J., et al. (2022). Human prefrontal cortex gene regulatory dynamics from gestation to adulthood at single-cell resolution. *Cell* 185, 4428–4447.e4428. doi: 10.1016/j.cell.2022.09.039

Hosseini, S., Hoeft, F., and Kesler, S. J. P. O. (2012). GAT: a graph-theoretical analysis toolbox for analyzing between-group differences in large-scale structural and functional brain networks. *PLoS One* 7:e40709. doi: 10.1371/journal.pone.0040709

Humphries, M., Gurney, K., and Prescott, T. J. P. B. S. (2006). The brainstem reticular formation is a small-world, not scale-free, network. *Proc. Biol. Sci.* 273, 503–511. doi: 10.1098/rspb.2005.3354

Igelström, K., and Graziano, M. J. N. (2017). The inferior parietal lobule and temporoparietal junction: a network perspective. *Neuropsychologia* 105, 70–83. doi: 10.1016/j.neuropsychologia.2017.01.001

Kellinghaus, C., and Lüders, H. J. E. D. I. E. J. W. V. (2004). Frontal lobe epilepsy. *Epileptic Disord.* 6, 223–239.

Li, Y., Wang, Y., Wang, Y., Wang, H., Li, D., Chen, Q., et al. (2020). Impaired topological properties of gray matter structural covariance network in epilepsy children with generalized tonic-Clonic seizures: a graph theoretical analysis. *Front. Neurol.* 11:253. doi: 10.3389/fneur.2020.00253

Lin, H., Leng, X., Qin, C., Wang, W., Zhang, C., and Qiu, S. J. F. I. N. (2020). Altered white matter structural network in frontal and temporal lobe epilepsy: a graph-theoretical study. *Front. Neurol.* 11:561. doi: 10.3389/fneur.2020.00561

Liu, F., Wang, Y., Li, M., Wang, W., Li, R., Zhang, Z., et al. (2017). Dynamic functional network connectivity in idiopathic generalized epilepsy with generalized tonic-clonic seizure. *Hum. Brain Mapp.* 38, 957–973. doi: 10.1002/hbm.23430

Lu, C., Gosden, G., Okromelidze, L., Jain, A., Gupta, V., Grewal, S., et al. (2022). Brain structural differences in temporal lobe and frontal lobe epilepsy patients: a voxel-based morphometry and vertex-based surface analysis. *Neuroradiol J.* 35, 193–202. doi: 10.1177/19714009211034839

Manford, M., Fish, D., and Shorvon, S. J. B. A. J. O. N. (1996). An analysis of clinical seizure patterns and their localizing value in frontal and temporal lobe epilepsies. *Brain* 119, 17–40. doi: 10.1093/brain/119.1.17

Maslov, S., and Sneppen, K. J. S. (2002). Specificity and stability in topology of protein networks. *Science* 296, 910–913. doi: 10.1126/science.1065103

O'Donoghue, M., Duncan, J., and Sander, J. J. E. (1996). The National Hospital Seizure Severity Scale: a further development of the Chalfont seizure severity scale. *Epilepsia* 37, 563–571. doi: 10.1111/j.1528-1157.1996.tb00610.x

Regesta, G., and Tanganelli, P. J. E. R. (1999). Clinical aspects and biological bases of drug-resistant epilepsies. *Epilepsy Res* 34, 109–122. doi: 10.1016/s0920-1211(98)00106-5

Roggenhofer, E., Muller, S., Santarnecchi, E., Melie-Garcia, L., Wiest, R., Kherif, F., et al. (2020). Remodeling of brain morphology in temporal lobe epilepsy. *Brain Behav.* 10:e01825. doi: 10.1002/brb3.1825

Rubinov, M., and Sporns, O. J. N. (2010). Complex network measures of brain connectivity: uses and interpretations. *Neuroimage* 52, 1059–1069. doi: 10.1016/j.neuroimage.2009.10.003

Sasagawa, A., Enatsu, R., Kuribara, T., Arihara, M., Hirano, T., Ochi, S., et al. (2021). Cortical regions and networks of hyperkinetic seizures: Electrocorticography and diffusion tensor imaging study. *Epilepsy Behav.* 125:108405. doi: 10.1016/j.yebeh.2021.108405

Silver, E., Korja, R., Mainela-Arnold, E., Pulli, E., Saukko, E., Nolvi, S., et al. (2021). A systematic review of MRI studies of language development from birth to 2 years of age. *Dev Neurobiol.* 81, 63–75. doi: 10.1002/dneu.22792

Singh, M., Kesler, S., Hadi Hosseini, S., Kelley, R., Amatya, D., Hamilton, J., et al. (2013). Anomalous gray matter structural networks in major depressive disorder. *Biol Psychiatry* 74, 777–785. doi: 10.1016/j.biopsych.2013.03.005

Spencer, S. J. E. (2002). Neural networks in human epilepsy: Evidence of and implications for treatment. *Epilepsia* 43, 219–227. doi: 10.1046/j.1528-1157.2002.26901.x

Togo, M., Matsumoto, R., Usami, K., Kobayashi, K., Takeyama, H., Nakae, T., et al. (2022). Distinct connectivity patterns in human medial parietal cortices: Evidence from standardized connectivity map using cortico-cortical evoked potential. *Neuroimage* 263:119639. doi: 10.1016/j.neuroimage.2022.119639

Vaessen, M., Braakman, H., Heerink, J., Jansen, J., Debeij-van Hall, M., Hofman, P., et al. (2013). Abnormal modular organization of functional networks in cognitively impaired children with frontal lobe epilepsy. *Cereb. Cortex* 23, 1997–2006. doi: 10.1093/cercor/bhs186

Vaessen, M., Jansen, J., Braakman, H., Hofman, P., De Louw, A., Aldenkamp, A., et al. (2014). Functional and structural network impairment in childhood frontal lobe epilepsy. *PLoS One* 9:e90068. doi: 10.1371/journal.pone.0090068

Widjaja, E., Mahmoodabadi, S., Snead, O., Almehdar, A., and Smith, M. J. E. (2011). Widespread cortical thinning in children with frontal lobe epilepsy. *Epilepsia* 52, 1685–1691. doi: 10.1111/j.1528-1167.2011.03085.x

Wieser, H., Blume, W., Fish, D., Goldensohn, E., Hufnagel, A., King, D., et al. (2001). Proposal for a new classification of outcome with respect to epileptic seizures following epilepsy surgery. *Epilepsia* 42, 282–286. doi: 10.1046/j.1528-1157.2001.35100.x

Woodward, K., Gaxiola-Valdez, I., Goodyear, B., and Federico, P. J. B. C. (2014). Frontal lobe epilepsy alters functional connections within the brain's motor network: a resting-state fMRI study. *Brain Connect* 4, 91–99. doi: 10.1089/brain.2013.0178

Wu, X., Liu, W., Wang, W., Gao, H., Hao, N., Yue, Q., et al. (2019). Altered intrinsic brain activity associated with outcome in frontal lobe epilepsy. *Sci. Rep.* 9:8989. doi: 10.1038/s41598-019-45413-7

Zhou, X., Zhang, Z., Liu, J., Qin, L., and Zheng, J. J. N. L. (2019). Aberrant topological organization of the default mode network in temporal lobe epilepsy revealed by graph-theoretical analysis. *Neurosci. Lett.* 708:134351. doi: 10.1016/j.neulet.2019.134351

frontiers | Frontiers in Neuroscience

TYPE Review
PUBLISHED 19 May 2023
DOI 10.3389/fnins.2023.1137096

OPEN ACCESS

EDITED BY
Na Li,
Central South University, China

REVIEWED BY
Santosh Bashyal,
The University of Texas at Austin, United States
Rupinder Kaur Sodhi,
Panjab University, India

*CORRESPONDENCE
Kyo-in Koo
✉ kikoo@ulsan.ac.kr
Chang Ho Hwang
✉ chhwang1220@cnu.ac.kr

†These authors have contributed equally to this work and share first authorship

RECEIVED 04 January 2023
ACCEPTED 19 April 2023
PUBLISHED 19 May 2023

CITATION
Won S, An J, Song H, Im S, You G, Lee S, Koo K-i and Hwang CH (2023) Transnasal targeted delivery of therapeutics in central nervous system diseases: a narrative review. *Front. Neurosci.* 17:1137096. doi: 10.3389/fnins.2023.1137096

Transnasal targeted delivery of therapeutics in central nervous system diseases: a narrative review

Seoyeon Won[1†], Jeongyeon An[1†], Hwayoung Song[1], Subin Im[1], Geunho You[1], Seungho Lee[1], Kyo-in Koo[2*] and Chang Ho Hwang[3*]

[1]College of Medicine, Chungnam National University, Daejeon, Republic of Korea, [2]Major of Biomedical Engineering, Department of Electrical, Electronic, and Computer Engineering, University of Ulsan, Ulsan, Republic of Korea, [3]Department of Physical and Rehabilitation Medicine, Chungnam National University Hospital, College of Medicine, Chungnam National University, Daejeon, Republic of Korea

Currently, neurointervention, surgery, medication, and central nervous system (CNS) stimulation are the main treatments used in CNS diseases. These approaches are used to overcome the blood brain barrier (BBB), but they have limitations that necessitate the development of targeted delivery methods. Thus, recent research has focused on spatiotemporally direct and indirect targeted delivery methods because they decrease the effect on nontarget cells, thus minimizing side effects and increasing the patient's quality of life. Methods that enable therapeutics to be directly passed through the BBB to facilitate delivery to target cells include the use of nanomedicine (nanoparticles and extracellular vesicles), and magnetic field-mediated delivery. Nanoparticles are divided into organic, inorganic types depending on their outer shell composition. Extracellular vesicles consist of apoptotic bodies, microvesicles, and exosomes. Magnetic field-mediated delivery methods include magnetic field-mediated passive/actively-assisted navigation, magnetotactic bacteria, magnetic resonance navigation, and magnetic nanobots—in developmental chronological order of when they were developed. Indirect methods increase the BBB permeability, allowing therapeutics to reach the CNS, and include chemical delivery and mechanical delivery (focused ultrasound and LASER therapy). Chemical methods (chemical permeation enhancers) include mannitol, a prevalent BBB permeabilizer, and other chemicals—bradykinin and 1-O-pentylglycerol—to resolve the limitations of mannitol. Focused ultrasound is in either high intensity or low intensity. LASER therapies includes three types: laser interstitial therapy, photodynamic therapy, and photobiomodulation therapy. The combination of direct and indirect methods is not as common as their individual use but represents an area for further research in the field. This review aims to analyze the advantages and disadvantages of these methods, describe the combined use of direct and indirect deliveries, and provide the future prospects of each targeted delivery method. We conclude that the most promising method is the nose-to-CNS delivery of hybrid nanomedicine, multiple combination of organic, inorganic nanoparticles and exosomes, via magnetic resonance navigation following preconditioning treatment with photobiomodulation therapy or focused ultrasound in low intensity as a strategy for differentiating this review from others on targeted CNS delivery; however, additional studies are needed to demonstrate the application of this approach in more complex *in vivo* pathways.

KEYWORDS

therapeutics, central nervous system, wounds and injuries, targeted delivery, nanoparticles, exosomes, magnetics

1. Introduction

The main central nervous system (CNS) treatments used today, including neurointervention, surgery, medication, and CNS stimulation (Daroff et al., 2016), are often invasive, extending the patient's recovery and rehabilitation time. While the injection of neurotropic drugs such as chondroitinase (Kasinathan et al., 2016), anti-nogo (Zörner and Schwab, 2010), and Rho antagonists (Bertrand et al., 2005) has been considered a replacement for these other treatments in *in vitro/in vivo* CNS injury models, this method affects not only diseased tissues but also nonrelated healthy tissues (Perez-Herrero and Fernandez-Medarde, 2015). Therefore, CNS therapeutics have recently focused on targeted spatiotemporal therapy to rapidly induce the accumulation of high-concentration therapeutics in damaged areas, thereby making the treatment more intelligent, safer, more effective, and more efficient than the aforementioned methods.

To achieve targeted delivery into the CNS, it is essential for therapeutic agents to pass directly through the blood brain barrier (BBB; Chacko et al., 2013). The BBB is a semipermeable layer of endothelial cells between the circulatory system and the CNS. While the BBB functions to protect the CNS from toxic substances and regulate ions, molecules, and cells for proper neuronal function (Daneman and Prat, 2015), its high selectivity, in which enzymatic and physical barriers are involved, also prevents therapeutics from reaching the CNS (Tewabe et al., 2021). Therefore, direct delivery methods such as nanoparticles (NPs; Dong, 2018; Tewabe et al., 2021), extracellular vesicles (EVs), and magnetic-field mediated delivery (Yu et al., 2018), and indirect delivery methods such as chemical and physical delivery methods are being developed to pass through the BBB and directly affect the CNS: direct delivery methods that allow therapeutics to pass through the BBB as a vehicle or a navigator versus indirect delivery methods that increase the permeability of the BBB as a permeabilizer (Figure 1).

While the direct and indirect methods have been mainly used separately, the authors of this review seek to shed light upon cases where the two methods are used together to create a synergistic effect and introduce the limitations and/or remaining unknowns in the field in regard to their combination. The direct and indirect CNS-targeted delivery strategies introduced in this article have demonstrated promise in *in vitro* and in animal studies as the next-generation platform for the treatment of CNS diseases ranging from Alzheimer's disease to brain tumors. Therefore, this review aims to describe various direct and indirect CNS-targeted delivery methods and how they relate to one another to stimulate more interest and research in CNS-targeted delivery by defining the mechanism of each delivery method, discussing their advantages and disadvantages, and analyzing future perspectives for neuroscientists who may aim to understand or even use some of the ideas discussed here in the context of their own work. In addition, although numerous types of therapeutic agent administration, such as subcutaneous, intramuscular, intravascular, transintestinal, transperitoneal, and intrathecal ones, have been tried, all of these routes are currently being evaluated in pioneering studies and thus demand further investigation prior to discussion about whether these approaches have any validity on the CNS-targeted delivery of therapeutics. Just one type of administration, nose-to-CNS route, has been discovered as a promising tool in animal and human models, especially for neurological disease treatment (Mittal et al., 2014). Hence, it should be in mind that the current review is full of examples depicting nose-to-CNS delivery, using viral vectors for delivery, etc.

2. Direct targeted delivery

In direct CNS-targeted delivery, therapeutics may be preserved by methods such as encapsulation to permeabilize through the BBB safely, arrive in the CNS, and take effect. Among variety of direct methods in progress, nanomedicine and magnetic field-mediated deliveries are the most commonly used methods in a field of CNS disease treatment. Nanomedicine allows sustainable selective delivery

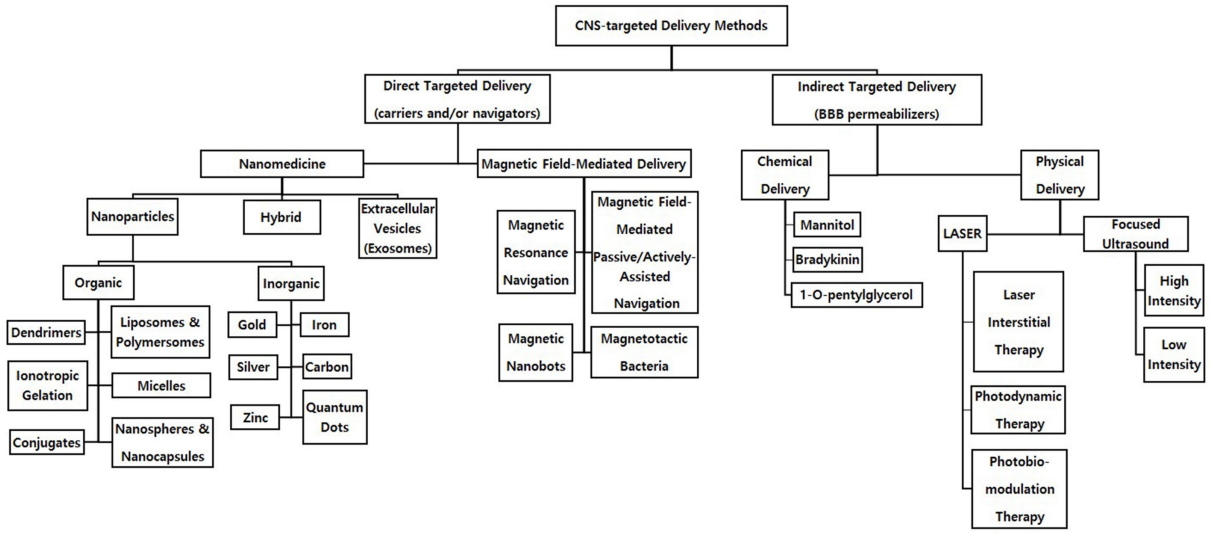

FIGURE 1
Direct and indirect targeted delivery methods to the central nervous system.

to the target tissue (Dong, 2018; Tewabe et al., 2021), and magnetic field-mediated deliveries incorporate an external or internal magnetic field to directly navigate and accumulate magnetic therapeutics to the targeted area, resulting in a higher controllability than nanomedicine (Yu et al., 2018). Both nanomedicine and magnetic field-mediated deliveries could be seen as effective, promising delivery platforms for CNS diseases ranging from acute stroke to neurodegenerative disease to brain tumors, which have been most affected by the advancements made in direct delivery methods (Tiebosch et al., 2012; Tietze et al., 2013; Tentillier et al., 2016).

2.1. Nanomedicine

There are three types of namomedicine: NPs, EVs, and hybrid. NP structures, including 1D nanowires, 2D nanosheets, and 3D structures (Huang et al., 2020), such as carbon nanotubes (CNTs), liposomes, micelles, dendrimers, nanocapsules/nanospheres, and polymeric NPs (Perez-Herrero and Fernandez-Medarde, 2015). This review focuses on 3D structures since they allow for easier encapsulation and additional protection of therapeutics. The current review divides NPs into organic and inorganic type. Such classification of NPs focuses on their biocompatibility and stability depending on the consistency of the drug-containing shell. Also, this review introduces EVs, especially exosomes, which are the most up-to-date nanomedicine. Recent studies have focused on hybrids, as they minimize the disadvantages and maximize the advantages of organic, inorganic NPs, and EVs by combining the two or more (Ferreira Soares et al., 2020). Additionally, nanomedicine may be magnetized and incorporated in magnetic field-mediated delivery.

2.2. Organic nanoparticles

Organic NPs consist of organic materials, including lipids and aqueous molecules (Xie et al., 2019), allowing for high biocompatibility. Usually, NPs (liposomes, dendrimers, etc.), are prepared with functional moieties such as polyethylene glycol (PEG). For example, organic NPs made of lipids break down into lactic and glycolic acids after the loaded therapeutics are released into the target area, which can then be used up in the metabolic cycle (Vanden-Hehir et al., 2019). Additionally, organic NPs such as dendrimers, which are polymeric molecules with numerous branch structures enabling their surface to be easily modified, exhibit high bioavailability (Palmerston Mendes et al., 2017). When combined with organic NPs, the unstable hydrophobic drugs showed improved dissolution and stability (Pentek et al., 2017). For instance, the 100% dissolution time of resveratrol, a compound often known as an antioxidant, was found to be approximately 4.5 h when tested alone, while it took approximately 0.5 h in dendrimer-drug complexes (Chauhan, 2018). Additionally, 90% of resveratrol remained in dendrimer-resveratrol complexes compared to 10% for pure resveratrol, which indicates that dendrimers can mitigate stability issues (Pentek et al., 2017). Furthermore, organic NPs have been designed to mitigate the issue of crossing the BBB so that such liposomes and micelles have been reported to protect their vehicles from degradation and transport their loaded therapeutics across the BBB (Spuch and Navarro, 2011; Zou et al., 2017). For another example, the CD163 receptor-targeted liposomes incorporating dexamethasone showed a 3-fold higher delivery rate in the brain than sham group in 6-hydroxydopamine Parkinson's disease rat models (Tentillier et al., 2016). The solid lipid NPs encapsulating acetylcholinesterase reactivators with the help of multiple emulsion technique presented a 9-fold higher delivery rate than acetylcholinesterase reactivator only group 45 min after injection in organophosphate-induced brain injury rat models (Pashirova et al., 2017).

Another notable advantage of organic NPs is their allowance for active cellular targeting; ligand tagging techniques allow the attachment of ligands, such as antibodies, peptides, aptamers, and folate molecules to the NP surface. The ligands make the organic NPs bind to target cell receptors, leading to efficiently selective delivery with high therapeutic efficacy (Mullen and Banaszak Holl, 2011); the L-carnitine-conjugated poly lactic-co-glycolic acid NPs containing paclitaxel showed a 10-fold higher accumulation in the brain than paclitaxel only injection 2 h after administration in brain tumor mouse models (Kou et al., 2018). In a review article in 2021, apolipoprotein E-conjugated polymeric NPs were emphasized regarding their merits such as the improved transport across the BBB, accumulation in the brain, and inhibition of the accumulation of neurodegenerative disease-related factors (Hartl et al., 2021). Similar to the protein derivative conjugation, glucose-coated micelles piled up in the mouse brains 56-fold higher than micelles without glucose conjugation (Anraku et al., 2017).

Despite exhibiting high biocompatibility, high bioavailability, high penetrability of the BBB, and high targetability, the use of organic NPs still faces several obstacles. One major problem is the difficulty of large-scale production. For example, liposome production currently involves numerous steps, increasing the complexity of the entire manufacturing process and making commercialization difficult (Roces et al., 2020). Moreover, light, temperature, and metal ions may trigger chemical changes in the NPs such as lipid oxidation, leading to permeability changes when these NPs could be exposed to such changes (e.g., during transportation, in storage, in the body after administration; Guimarães et al., 2021). Although promising results—the variety of polymer coatings has been developed to prevent the removal of NPs by mononuclear phagocyte systems, which almost recognize the administered NPs as a foreign body and make those defending systems activated, before they would arrive in the targeted CNS (Owens and Peppas, 2006) and coating NPs with PEG is the most effective manner to prohibit nonspecific protein adherence and subsequent phagocytosis—have been reported (Vonarbourg et al., 2006), potential problem with organic NPs such as liposomes is that they can still accumulate in the liver and spleen; this accumulation triggers phagocyte uptake by mononuclear phagocyte systems, dominantly by Kupffer cells in the liver, and 99% of the administered NPs can be eliminated (Campbell et al., 2018). Additionally, it is another issue that microglia facilitate NP clearance in the CNS, capturing even PEGylated NPs (Gu et al., 2020).

Many promising studies are in progress to overcome these limitations (Guimarães et al., 2021). For example, microfluidics used in liposome manufacturing can simplify and scale up production while enhancing drug encapsulation using "bottom-up" approaches, which have no needs of additional size reduction process (Forbes et al., 2019). Moreover, controlling cholesterol, phosphatidic acid, and PEG content in liposomes has been shown to improve stability (Szabová et al., 2021). However, studies on these areas are limited,

these may be described as possible future directions for the development of organic NPs. Despite the efforts to mitigate the limitations of organic NPs, recent studies have focused on hybrid NPs and indirect methods (Shah et al., 2020). But still, the biocompatible, bioavailable, BBB-penetrable characteristics of organic NPs are noteworthy (Table 1).

2.3. Inorganic nanoparticles

Inorganic NPs made of materials such as gold, iron oxide, and carbon have a high surface area to volume ratio (Yao et al., 2020), which enables a high drug-carrying capacity. For example, CNTs have a diameter of 0.4–3.0 nm and a length of 20.0–1000.0 nm, resulting in a high carrying capacity; when the antitumor agent 10-hydroxycamptothecin, which has been investigated for the treatment of brain glioma, was covalently attached to the surface of a multiwalled CNT, it showed a sufficient loading efficiency of approximately 16% (Kostarelos et al., 2005; Wu et al., 2009; Perez-Herrero and Fernandez-Medarde, 2015). Additionally, mesoporous silica NPs have a large inner pore amount, making them advantageous drug-carrying agents (Yao et al., 2020) with a carrying capacity of 100 wt% for anticancer drugs in mouse models (Cheng et al., 2019). The surface modifiability of inorganic NPs enables effective targeting; for example, attaching a folate-containing compound to CNTs enabled specific delivery of therapeutics to folate-receptor + cancer cells (Dhar et al., 2008; Perez-Herrero and Fernandez-Medarde, 2015). Gold NPs, Au-SMCC linker-doxorubicin nanoconjugates, also displayed surface modifiability made by connecting doxorubicin to the surface of gold NPs and showed effective drug accumulation in HepG2-R cancer cells (Cheng et al., 2013). Like aforementioned findings, modified gold NPs on strategies for CNS-targeted delivery have gained considerable attention as the relevance to the context of CNS disease treatment including brain tumors. In addition to the high drug-carrying capability, inorganic NPs such as silver, gold, or quantum dots can cross the BBB with their own mechanisms; gold NPs increased the BBB permeability by disrupting the endothelial tight junctions, in which Na, K, and/or Ca ion channels are be involved, and reached their the peak concentration in the cerebrospinal fluid (CSF) 3-fold higher than that in the blood 6 h after transperitoneal injection in rats, and quantum dots conjugated with fluorescein hydrochloride, which uses glucose transporters to penetrate the BBB, accumulated in the central canal and in the cervical spinal cord, especially in the gray matter, following transcardic and intravenous injection in zebrafishes and rats, respectively (Sela et al., 2015; Seven et al., 2021). Also, multi-walled CNTs, which use energy-dependent transcytosis, completely crossed the BBB and remained persistently in the brain even 24 h following intravascular injection in rats while notable decrement occurred in the peripheral capillaries (Kafa et al., 2015).

Despite the advantages of inorganic NPs, they exhibit immunotoxicity, genotoxicity, or specific tissue toxicities such as neurotoxicity, leading to inflammation, carcinogenesis, fibrosis, cardiovascular diseases, etc. (Mohammadpour et al., 2019). For example, after a month of accumulation in the spleen, gold NPs have been shown to downregulate the expression of genes relevant to wound healing, responses to external stimuli, and defense responses (Balasubramanian et al., 2010). In the liver, genes relevant to lipid metabolism or the cell cycle process were upregulated (e.g., squalene epoxidase expression showed a fold change of 2.9; Balasubramanian et al., 2010). Additionally, cells incubated with polymer-coated multiwalled nanotube F127 for 24 and 48 h showed 60 and 40% cell viability, respectively, indicating cytotoxicity (Ali-Boucetta et al., 2011).

However, inorganic NPs can be controlled by regulating size, morphology, dosage, and chemical factors to regulate their toxicity (Madani et al., 2011). During the generation of NPs, doping, a technique in which impurities are added to the NPs for chemical/physical improvements, may be used to reduce cytotoxicity (George et al., 2010). In doping methods, three types are commonly used; first, elemental doping is conducted at atomic level, and divided into metal doping using such as cerium, cobalt, copper, iron, lanthanum, manganese, potassium, silver, and zinc as dopants, among which manganese is widely used, and nonmetal doping using such as boron, carbon, fluorine, nitrogen, phosphorus and sulfur, among which nitrogen is the mostly applied dopant. Second, it can be performed at molecular level (molecular doping), in which active molecules are encapsulated into vehicles such as metal–organic frameworks, polymers, quantum dots, and silica, among which silica is the mostly used matrix. Third, codoping combines the benefits of codoped elements, through which metal combination, such as iron and sulfur, nitrogen and sulfur, copper and manganese, as well as combination of metal and nonmetal dopants have been achieved (Wang et al., 2022). However, such relationship between the matched dopants and NP matrix is not clearly known so that further studies will be required to establish a guideline for reliable manufacture of doped NPs.

Additionally, iron oxide NPs can be degraded into Fe ions in lysosomes of cells or under other acidic conditions, reducing the potential long-term toxicity (Yu et al., 2012; Mitchell et al., 2021). In a long-term (approximately 13 months) study regarding the safety of ferumoxytol, an FDA-approved iron oxide NP, in the treatment of iron-deficient anemia patients with chronic kidney disease on hemodialysis, no patients experienced intravenous ferumoxytol replacement treatment-related serious adverse events (Macdougall et al., 2019), indicating the relevance of the safety of iron NPs in the context of long-term administration. If toxicity issues can be resolved, inorganic NPs could have a high potential for use in effective direct delivery methods in the treatment of CNS disease due to their ability to easily cross the BBB and their efficient drug loading capacity (Table 1).

2.4. Extracellular vesicles/exosomes

While NPs are in common synthetic drug delivery vehicles (Sun et al., 2022), EVs are innate, nano-sized, phospholipid bilayer-enclosed vesicles (Elsharkasy et al., 2020) that can be, in theory, released by all kinds of cells (Rufino-Ramos et al., 2017) through exocytosis for intercellular communication. Recently, EVs have gained attention as a delivery tool of therapeutics owing to their groundbreaking preclinical success in brain-targeted delivery. Though the degree may vary depending on the type, EVs hold notable advantages for CNS-targeted delivery of therapeutics because of their noninvasiveness, high biocompatibility, permeability across the BBB, and high stability *in vivo* (Elsharkasy et al., 2020). Moreover, the surface of EVs can be engineered to increase brain targetability (Marie et al., 2021). Three main types of EVs include apoptotic bodies

TABLE 1 Types of nanoparticles.

Type	Advantage/Disadvantage		Authors	Subject	Result
Organic	Advantage	High biocompatibility/low immunogenicity	Vanden-Hehir et al. (2019)	Organic NPs made of lipids	Break down after delivering the drug to the target area, and are used up in the metabolism cycle
		Dissolution and stability improvements	Chauhan (2018)	Dendrimers combined with organic NPs	100% dissolution time took about 0.5 h but 4.5 h when tested alone
			Pentek et al. (2017)	Resveratrol in dendrimer-drug complexes	90% remained compared to 10% in pure resveratrol
	Disadvantage	Difficulty of large-scale production	Roces et al. (2020)	Producing organic NPs involves numerous steps	Increases the complexity of the entire manufacturing process and serves as an obstacle to commercialization
		Instability (chemical degradations by metal ions)	Guimarães et al. (2021)	Lipid oxidation	Lead to permeability changes
		Early elimination	Campbell et al. (2018)	Organic liposomes	The phagocyte system in the liver can take up to 99% of the administrated NPs
Inorganic	Advantages	High drug-carrying capacity	Kostarelos et al. (2005); Perez-Herrero and Fernandez-Medarde (2015); Wu et al. (2009)	HCPT covalently attached to the surface of a multi-walled carbon nanotube	Showed a sufficient loading efficiency of approximately 16%
			Cheng et al. (2019)	MSNs with a large internal pore volume	Resulting in a vast carrying capacity of 100 wt% for anticancer drugs
		Surface Modifiability/ Effective Targeting	Dhar et al. (2008)	CNTs with the folate compound	Allowed for specific delivery of the therapeutics to FR(+) cancer cells
			Cheng et al. (2013)	Au-SMCC-DOX nanoconjugates	Showed effective drug accumulation in hepG2-R cancer cells
	Disadvantages	Toxicity problem	Ali-Boucetta et al. (2011)	AuNPs accumulated for over 1 month in the spleen and liver of rats	Changed the expression of genes, squalene epoxidase showed fold change of 2.9 ± 0.7, $p < 0.05$
			Ali-Boucetta et al. (2011)	Cells incubated with polymer-coated multi-walled nanotube: F127	F127 (concentration of 125 μg/ml) for 24 h and 48 h showed 60 and 40% of cell viability
Hybrid	Advantages	Tunable size	Bose et al. (2020)	Antibiotic-loaded LPHNPs engineered with CA and ZA lipids	NA was shown to have a diameter of 226 ± 9.6 nm, CA LPHNPs were 203 ± 6.6 nm and ZA LPHNPs were 191 ± 5.4 nm in diameter,size of hybrid NPs are tunable
		Surface charge		CA or ZA LPHNPs introduced into the LPHNP formulation in the same study	Charge reduction of -29 ± 2.1 mV occured
		High drug loading yield	Bose et al. (2020)	Comparing the %EE and vancomycin %EE of BNPs and CA or ZA lipid layered LPHNPs	The %EE of both CA and ZA LPHNPs is greater than that of bare organic NPs
		Sustained drug release	Bose et al. (2020)	Cumulative antibiotic release from doxycycline-encapsulated BNPs and vancomycin-encapsulated BNPs	The antibiotic release rates of doxycycline BNPs at 12, 24, and 48 h were each 65, 69, and 75%
		High stability	Yang J. et al. (2021)	*In vivo* gene delivery study; bare pCas9/MGMT degraded within 3 min of incubation with DNase I, and the pCas9/MGMT plasmids in LPHNs-cRGD	Remained intact throughout varying incubation durations with DNAse I

(Continued)

TABLE 1 (Continued)

Type	Advantage/Disadvantage		Authors	Subject	Result
		Biocompatibility	Khan et al. (2020)	CCK-9 assay results of LPHN-cRGD	Demonstrated cell viability of >80% after exposure to varying concentrations of NPs
		Efficient selective delivery and higher therapeutic efficacy by tagging lignads	Anraku et al. (2017)	Glucose-administered micelles for the treatment of Alzheimer's	Showed a 56-times higher accumulation rate in the CNS than micelles without ligands
			Hartl et al. (2021)	Conjugation of apolipoprotein E(Apo E) with NPs	Improved transport across the BBB, accumulation in the brain, and inhibition of the accumulation of neurodegenerative disease-related factors
	Disadvantages	Unbalanced ratio of the components, less controlled antigen release, lipid layer not fully stabled, and unprotected hybrid structure integrity during long-term storage	Hu et al. (2010)		
		Harmful tissue deposition in the kidneys, reticuloendothelial system, and microvasculature, unintended activation of host immune response, and damage to target cells	Howard et al. (2014)	ALAs	

NPs, nanoparticles; HCPT, hydroxycamptothecin; MSNs, mesoporous silica nanoparticles; CNTs, carbon nanotubes; FR, folate-receptor; AuNPs, gold nanoparticles; LPHNPs, lipid-polymer hybrid nanoparticles; CA, cationic; ZA, zwitterionic; %EE, encapsulation efficiencies; BNPs, bare nanoparticles; CNS, central nerve system; and BBB, blood–brain barrier.

(ApoBDs), microvesicles (MVs), and exosomes. Major difference among the three types include their formation process, size, and origin (Shao et al., 2018; Nederveen et al., 2021). ApoBDs and most MVs have a large particle size (Elmore, 2007; Shao et al., 2018), making them not ideal candidates for targeted delivery to the CNS. Therefore, authors briefly introduce ApoBDs and MVs, and then concentrate on describing exosomes—the smallest EV type, which may easily pass through the BBB so that it holds a superior potential for CNS-targeted delivery than other EVs (Shao et al., 2018).

Apoptotic bodies are the largest of EVs (500–4,000 nm; Elmore, 2007) that are formed during apoptotic cell disassembly where fragmented cell contents such as organelles and nuclear content are enclosed in membrane-bound vesicles (Santavanond et al., 2021). ApoBDs successfully trigger clearance of damaged cells in tissue development and regeneration of the kidney and bone (Li et al., 2020). MVs are EV subtypes that are released directly from the cell surface of platelets, red blood cells, and endothelial cells (Yang J. et al., 2021) and range in size from 200 to 2,000 nm (Shao et al., 2018). MVs may transport proteins and miRNA between cells and have been used for the diagnosis of autoimmune diseases, treatment of acute kidney injury, etc. (Liu et al., 2016). While ApoBDs and MVs may be tried for CNS-targeted therapy with the help of indirect, BBB penetration-assisting methods, there is limited evidences on the two methods.

Exosomes are the smallest EVs (40–200 nm) that are formed in all types of cells when vesicles bud into endosomes inside cells (Shao et al., 2018). Exosomes may directly penetrate the BBB, are highly stable in peripheral circulation, and thus may protect disease-specific therapeutic molecules, unlike ApoBDs and MVs. At the beginning of researches, exosomes were studied as a biomarker to monitor disease development, allowing early diagnosis and treatment optimization in such stroke, glioma, Parkinson's diseases, Alzheimer's diseases, Huntington's diseases, and amyotrophic scleroses (Liu et al., 2019; Fan et al., 2022). After that period, exosome trials have been extended to therapeutic role for CNS disease as well (Fan et al., 2022). In a Martins et al.'s research, the ability of two Aβ-binding proteins—alpha-1-antichymotrypsin and C4b-binding protein alpha chains—was analyzed to validate exosome levels in patients by using antibody-based methods, indicating significant correlations between alpha-1-antichymotrypsin exosomal concentrations and mini-mental state examination scores and clinical dementia rating scores, indicators of cognitive alterations. Moreover, C4b-binding protein alpha chains was reported to limit the complement activation by Aβ and dead cells in Alzheimer's disease brains, potentially protecting the neurons from immune responses (Soares Martins et al., 2022). Recently, another notable advantage of exosomes was discovered; their inherited membrane proteins—such as CD9, CD63, prostaglandin F2 receptor negative regulator, and Lamp2b—can be genetically and/or chemically engineered to increase tissue-targetability, showing promising results in preclinical studies for CNS targeting (Sun et al., 2022). In a study by Alvarez-Erviti et al., Lamp2b-RVG plasmids were created to transfect autologous-derived dendritic cells, stimulating the secretion of engineered exosomes. Following that engineering, the exosomes were intravenously injected to mice, resulting in specific delivery of siRNA to neurons, oligodendrocytes, and microglia in the brain, ultimately leading to specific gene (BACE1) knockdown for Alzheimer's diseases (Alvarez-Erviti et al., 2011). As such, exosomes

may be used for targeted delivery of various therapeutics, such as proteins, siRNAs, miRNAs and even drug ingredients of low molecular weight, to injured CNS neurons with the help of genetically and/or chemically engineered surface modification (Sun et al., 2022; Zhou et al., 2022).

Despite such advantages, however, clinically approved CNS-targeted exosomes would require further investigation regarding detailed methods in pointed view of penetration efficiency of the BBB as well as the development of quantitative and qualitative monitoring and imaging tracking methods about targeted delivery to the CNS neurons (Hojun Choi et al., 2022). Moreover, in a research on wound healing promotion using adipose cell-derived exosomes, it was found that the metabolic condition of exosome donors affects the biogenesis, biological activity, and composition of the adipose stem cells (Cianfarani et al., 2013), thus affecting the adipose stem cell exosomes. Technically, isolation and purification methods should also be validated for reliable production in large scale (Rufino-Ramos et al., 2017).

2.5. Hybrid nanomedicine

Hybrid NPs are a combination of organic and inorganic NPs, which enable the combined advantages of both types of NPs to be leveraged for the treatment of CNS disease, and these NPs exhibit tunable size and surface charge based on the components included. The size and surface chemistry of NPs are critical since they affect the efficacy of NP delivery to diseased tissues, redistribution of NPs within the body, and potential toxicity (Walkey et al., 2012). One example of the tunability of the size of hybrid NPs is the use of different lipids; in a study comparing antibiotic-loaded lipid-polymer hybrid NPs (LPHNPs) engineered with cationic and zwitterionic lipids, the diameter of cationic LPHNPs was 203 ± 6.6 nm and that of zwitterionic LPHNPs was 191 ± 5.4 nm (Bose et al., 2020). Moreover, when cationic or zwitterionic LPHNPs were introduced into the LPHNP formulation, the charge was reduced by −29 ± 2.1 mV, indicating that LPHNPs are more advantageous in terms of their ability to interact with surrounding cells, their penetration of the BBB, and their colloidal stability (Bose et al., 2020).

High drug-loading yield and sustained drug release are other advantages of hybrid NPs; when the encapsulation efficiencies (%EE) of doxycycline-bare NPs and cationic or zwitterionic lipid layered LPHNPs loaded with doxycycline were compared, the results corresponded to a %EE of 63, 71, and 79%, respectively. Moreover, the antibiotic release rates of cationic LPHNPs at 12, 24, and 48 h were 38, 54, and 66% when zwitterionic LPHNPs were 32, 47, and 61% and doxycycline-bare NPs were 65, 69, and 75%, respectively (Bose et al., 2020).

Hybrid NPs also exhibit high stability and biocompatibility because their outer shells are combinations of the organic and inorganic shells. In an *in vivo* gene delivery study, bare pCas9/methylguanine methyltransferase degraded within 3 min of incubation with DNase I, and pCas9/MGMT plasmids loaded in LPHNPs remained intact throughout varying durations of incubation with DNAse I (Yang Q. et al., 2021). This result indicates that LPHNPs successfully protected pCas9/methylguanine methyltransferase from enzyme degradation and can be used as a stable delivery vehicle (Yang Q. et al., 2021). In addition, the application of LPHNPs after exposure to varying concentrations of cisplatin and curcumin demonstrated a cell viability of >80% based on CCK-9 assay results in A2780 tumor cells (Khan et al., 2020). Nevertheless, for the hybrid NPs, there were only *in vitro* performed studies that depicted *in vitro* or plainly brain cell update; for instance, Fe_3O_4 LPHNPs manufactured by self-assembly technique penetrated a BBB model composed of human brain microvascular endothelial cells (BMVECs) under magnetic field guidance (Qiao et al., 2020), and mesoporous silica liposome of poly(acryl acid)-hybrid NPs conjugated with angiopep-2 showed the enhanced penetration rate of the BBB model of BMVECs (Tao et al., 2019). Yet, without *in vivo* studies, it becomes difficult to explain the validity of the targeting experiment.

Despite such advantages, further studies are needed to determine the proper balance of the ratio of the components of the outer shell (i.e., cholesterol). This ratio is important in CNS targeting, as it affects the stability of antigen release, lipid layer stability, and the protection of the integrity of the hybrid structure during long-term storage (Hu et al., 2010). Therefore, recent studies have focused on manufacturing hybrid NPs in an appropriate ligand/receptor density ratio, as this ratio substantially affects their targeting abilities (Alkilany et al., 2019). For example, there was a study in which equimolar amounts of five different lipids—ethyl arachidate, myristic acid, stearic acid, ethyl myristate, and glycerol monostearate—were tested in the form of BBB-crossing terpolymer lipid-hybrid NP, in which polysorbate 80 was covalently attached to poly(methacrylic acid)-grafted-starch, for colloidal stability and *in vitro* application when delivering doxorubicin to glioblastoma multiform (GBM) brain tumor cells. Of the different lipids tested, the ethyl arachidate doxorubicin-hybrid NP showed the most ideal colloidal properties, stability, and highest cytotoxicity against GBM cells (Ahmed et al., 2021). To address the remaining challenges in identifying the ideal out shell composition of hybrid NPs for different CNS therapies, additional studies should focus on determining the proper ratio of the outer shell components in correspondence with degree of *in vivo* stability, targetability, and bioavailability, respectively, in individual types of CNS disease and therapeutics (Table 1).

Similar to the hybrid NPs, hybrid nanomedicine, a combination of NPs and exosomes, has been recently tried, especially in cancer researches; for example, a CD47-expressing exosome cRGD-modified liposome-hybrid nanomedicine inhibited activation of mTOR pathway in ovarian cancer cells indicating targeted codelivery of triptolide and miR_{497} (Li et al., 2022), and another hybrid nanomedicine combining granulocyte-macrophage colony-stimulating factor-overexpressing exosomes and docetaxel-loaded liposomes showed enhanced codelivery of granulocyte-macrophage colony-stimulating factor and docetaxel in metastatic peritoneal cancer rats (Lv et al., 2020). Meanwhile, reported are just few studies showing a potential of hybrid nanomedicine application to CNS-targeted delivery (Rufino-Ramos et al., 2017); for instance, enveloped protein nanocages precisely matching the targeted scaffold via viral glycoprotein were inserted into the EV (Votteler et al., 2016), and exosome-mimetic nanovesicle, in which therapeutic drugs were contained through repetitive macrophage and monocyte breakdown using sequential filtering of extrusion (Jang et al., 2013). However, application of hybrid nanomedicine to CNS-targeted delivery is at its initial stage of development so that it would require further approval in feasibility and validity as the limitations of hybrid NPs do.

In addition to researches on improving the hybrid.nanomedicine themselves, it is expected that future studies on hybrid nanomedicine will be focused on their combination with other indirect methods, such as focused ultrasound (FUS; Ahmed et al., 2021) and photodynamic therapy (PDT; Zhang et al., 2020), approaches of which will hold promise despite the need for additional studies.

3. Magnetic field-mediated delivery

This review introduces magnetic delivery in chronological order of their development: magnetic field-mediated passive navigation, magnetotactic bacteria (MTB), magnetic resonance navigation (MRN), and magnetic nanobots. It is important to note that due to preexisting categorical limitations of targeted delivery, this review classify magnetic field-mediated delivery as a direct method, although it actually has indirect characteristics in nature.

Magnetic navigation is a delivery method that accumulates magnetic micro/nanodrug carriers in the targeted area by controlling the direction and propulsion of the carriers with externally provided permanent magnets or electromagnets; this technique has the advantages of navigational delivery to an injury site and exclusive localization within the injury site, allowing therapeutics to escape from emulous binding with non-*in situ* receptors, specifically in the context of CNS-targeted delivery (Chorny et al., 2011). *In vitro* and *in vivo* studies involving centralizing scattered ferromagnetic rods/microcapsules have shown that magnetic forces may be used to successfully manipulate magnetic materials for directional navigation (Nacev et al., 2015; Voronin et al., 2017). Furthermore, magneto-nanobots can be utilized as magnetic field-mediated, actively assisted navigational vehicles that enable cell-specific targeting; in a study where an external magnetic field and magnetic nanobots consisting of magnetic NPs (Fe_3O_4NPs) were used to deliver anticancer drugs, the nanobots were shown to gain thrust from O_2 emissions produced from the decomposition of H_2O_2 released from tumor cells (Andhari et al., 2020). Attaching Fe_3O_4 to the NPs provides autonomous propulsion and superparamagnetic properties to the nanobot system (Andhari et al., 2020), suggesting a potential of the targeted delivery to deeply located lesions within the CNS. However, using an external magnetic field is difficult in tissues greater than 2 cm deep within the body, as the aforementioned advantages of magnetic field-mediated directional navigation sharply decrease with increasing distance between the magnets and the carriers (Hwang, 2020). Although internal methods such as the implantation of magnets within the body have been devised as an alternative (e.g., intrathecal implant; Lueshen et al., 2015), implants can trigger side effects such as infection and intolerance to them (Ganz, 2017). Thus, these disadvantages of external and internal methods should be augmented to promise better magnetic field-mediated delivery.

Magnetotactic bacteria are groups of bacteria that contain magnetosomes, which are intracellular structures that consist of biological materials such as magnetite (Fe_3O_4) and greigite (Fe_3S_4); MTB-derived magnetosomes thus have higher biocompatibility than artificial NPs due to their biological properties (Alphandery et al., 2017). Magnetosomes can be isolated from MTB and used as drug delivery carriers, and, as an alternative to paramagnetic/superparamagnetic NPs, MTB themselves can be loaded with drug-carrying vehicles for magnetic field-mediated navigation into target tissues. In one recent study, when magnetosome toxicity was evaluated in mice, complete blood counts and the results of a basic metabolic panel were within the normal range, and no change in the composition of urine or weight was found (Nan et al., 2021). Additionally, drug-carrying MTB with long actin-like filaments encoded by the mamK gene exhibit magneto-aerotaxis, which enables them to align with the direction of an applied magnetic field, move toward the hypoxic regions of targeted cells, and directly navigate the MTB-loaded vehicles to the CNS (Marcuello et al., 2018). In addition, magnetosomes have been shown to promote the axonal outgrowth of neurons through stretch growing when magnetic fields are applied (De Vincentiis et al., 2021). In one study, a total of 500–700 μg of magnetosomes coated with poly-L-lysine and magnetic fields of 202 kHz and 27 mT were used to treat GBM brain tumor cell models, and living GBM cells in all mice completely disappeared after 68 days (Alphandery et al., 2017). Although MTB have many advantages, they may adversely affect the human immune system by decreasing the level of lymphocyte proliferation (Nan et al., 2021). The composition of magnetosomes produced in MTB is often difficult to reproduce, leading to their low production yield (Alphandery et al., 2017). To overcome these limitations, MRN was developed.

Magnetic resonance navigation is a delivery method that uses a magnetic resonance imaging (MRI) scanner to provide propulsion to microcarriers (up to 400 mT/m) and to make them follow a preprogrammed route to the targeted area (Martel, 2010). Administrating MRN consists of three steps—steering, creating a magnetic gradient, and real-time tracking imaging—that are repeated until the carrier reaches the target (Pouponneau et al., 2014; Li et al., 2019). In a study testing MRN targeting in a two-level bifurcation, magnetic drug-eluting beads aggregated with targeting success rates of 84, 100, 84, and 92% for the four different ends of the branch routes (Li et al., 2019). In another study on rabbit hepatic arteries, the MRN successfully steered therapeutic magnetic microcarriers to the left lobes (Pouponneau et al., 2014). In these studies, MRN showed targeting effectivity both in the one-level bifurcation in an animal model and in the higher level of bifurcation of artificial pathways; these findings demonstrate its potential use in targeting more complex pathways in the human body (Pouponneau et al., 2014; Li et al., 2019). However, the references currently cited are based on the treatment of hepatocellular carcinoma by liver chemoembolization. Hence, it is unsure how will it perform well for the brain, which should be evaluated in future studies.

Furthermore, factors such as pulsatile flow can currently limit the use of MRN in *in vivo* studies to even simple pathways, such as one or two Y-bifurcations and 2D vascular phantoms (Folio and Ferreira, 2017). Moreover, some nonspherical microparticles navigated using MRN occasionally attach to the surface of nontarget tissues (Ghosh et al., 2021). However, this problem may be solved by increasing the magnetic gradient to overcome friction and by administering orthogonal pulses (Ghosh et al., 2021). While limitations exist, these studies demonstrate the targeting effectivity and potential of MRN for use in more complex pathways, making it one of the most promising tools for CNS-targeted therapy (Table 2). However, it should be in mind that it comes from the authors' personal extrapolation from the current information and their use in clinical paradigms cannot be justified yet due to such major limitations.

4. Indirect targeted delivery

The most considerable barrier to the use of direct targeted delivery has been their inability to allow therapeutics that exceed 400 Da to pass through the BBB (Pardridge, 2012; Cui and Cho, 2022). To overcome this disadvantage of the direct targeted delivery, development of indirect targeted methods has been demanded. In this section, the authors aim to introduce indirect chemical and physical methods that open the BBB, the mechanisms of each method, their advantages and disadvantages, and discussion of the recent findings with important implications. Chemical and physical methods can increase the permeability of the BBB using chemicals and physical energy, respectively. Mannitol has been widely used to decrease intracranial pressure (Chengyan Chu et al., 2018), but shown side effects such as edema and renal failure (Visweswaran et al., 1997) and a short efficacy time (Cosolo et al., 1989). Therefore, other chemicals, such as bradykinin and 1-O-pentylglycerol, have been studied. After briefly introducing chemical methods, this section mainly focuses on describing two main physical methods that are being developed: FUS and LASER therapy.

4.1. Chemical delivery

Indirect chemical targeted delivery is a method that chemically increases the permeability of the BBB, thereby allowing therapeutics to pass the BBB and take effect in the CNS (Pardridge, 2012; Dong, 2018; Cui and Cho, 2022). Hyperosmotic mannitol is the most widely used BBB permeabilizer (Chengyan Chu et al., 2018). It triggers dehydration of BBB endothelial tissues and deflates cell bodies, causing loosening of tight junctions, which enhances the permeability of drugs, stem cells, liposomal vehicles, and antibodies (Hendricks et al., 2015). However, when mannitol was injected into adult Sprague–Dawley rats at the optimum rate of 0.25 ml.s-1.kg-1 for 20 s, BBB disruption has been shown to last for approximately 5 min at maximum and then rapidly reverse (Cosolo et al., 1989), and administering 1,171 ± 376 g mannitol to a patient with normal baseline renal function resulted in acute renal failure (Dorman et al., 1990). Moreover, intracarotid arterial hyperosmolar mannitol increased the production of cytokines, chemokines, and trophic factors, leading to a neuroinflammatory response (Burks et al., 2021). Therefore, as mannitol has a short efficacy time and potential provocation of renal failure and systemic toxicity, and causes a neuroinflammatory response, other chemical methods are being developed to overcome such limitations.

Bradykinin is another agent used to permeabilize the BBB. Bradykinin is a vasoactive compound that selectively increases the permeability of abnormal brain capillaries (Black, 1995). A study using an RG2 rat glioma model demonstrated that stimulating the B2 bradykinin receptor rapidly increases the permeability of the BBB, especially in brain-tumor-associated tissue (Bartus et al., 1996). Moreover, treating female Wistar rats with bradykinin caused a 3.3-fold increase in the number of small arterioles, a 2.1-fold increase in the number of medium arterioles and a 1.5-fold increase in the number of large arterioles, alluding to an increase in pinocytotic vesicle density and BBB permeability (Raymond et al., 1986). However, it has a short half-life (27 ± 10 s; Cyr et al., 2001), may decrease the blood flow to the cerebrum, and causes extravasation, necrosis, edema, and BBB breakdown at high dosages or pathological conditions, since it is a potent vasoactive compound for arterial dilation (Wahl et al., 1999). To overcome such limitations, bradykinin receptor agonist NG291 is being developed to induce a rapid onset of transient BBB disruption without early brain injury. In a Sprague Dawley rat and CD-1 mouse model study, notable NG291-induced increase in BBB permeability was revealed in a localized, reversible, dose-dependent and P-gp efflux transport-mediated manner. Moreover, NG291 did not evoke short-term neurotoxicity, nor the increase of brain water content, the number of Fluoro-Jade C positive cells, and astrocyte activation (Rodríguez-Massó et al., 2021), indicating that biased agonism may play a role in enabling therapeutics to specifically target BBB opening without causing brain injury.

1-O-pentylglycerol is an alkylglycerol that has also been investigated for its ability to permeabilize the BBB. 1-O-pentylglycerol affects the endothelial cell morphology of the barrier and disrupts the BBB structure (Hülper et al., 2013). For example, an *in vivo* tumor-free and C6 glioma-bearing rat experiment indicated that intracarotid injection of 1-O-pentylglycerol caused a transfer of fluorescein and lissamine-rhodamine B200 across the BBB, as the mean ratio of ipsilateral to contralateral fluorescence intensity in the coronal sections for fluorescein was 6.45 ± 1.4, and the mean ratio of lissamine-rhodamine B200–albumin was 2.66 ± 1.0 (Erdlenbruch et al., 2003), which indicates applicability as one of brain tumor therapeutics. Additionally, no 1-O-pentylglycerol accumulation was found in the brain, and more than 70% of the administered dose was excreted within 270 min after administration, which suggests rapid renal elimination and the nontoxicity of 1-O-pentylglycerol (Erdlenbruch et al., 2005). While 1-O-pentylglycerol raised concerns regarding immunogenicity and thus adverse effects in nontarget cells, incubating bEnd3 mouse brain cells with poly(alkyl cyanoacrylate)-alkylglyceryl dextran did not show significant toxicity at concentrations <25 μg/mL (Ibegbu et al., 2017).

Although various indirect chemical targeted delivery methods exist and are under development, it is not easy to reach a consensus regarding a specific chemical to recommend. The most researched and used chemicals—mannitol, bradykinin, and 1-O-pentylglycerol—each has unignorable shortcomings, such as short efficacy time (Erdlenbruch et al., 2005), drug leakage (Rodríguez-Massó et al., 2021), and systemic toxicity (Dorman et al., 1990). Due to the aforementioned significant side effects, their use in clinical paradigms cannot be justified yet because of such major limitations. Therefore, indirect physical targeted delivery methods are being developed to remedy such limitations.

4.2. Physical delivery

4.2.1. Focused ultrasound

Focused ultrasound is a noninvasive augmentation method that opens the BBB through the application of high-intensity focused ultrasound (HIFU), which helps deliver therapeutics to the targeted brain region. When the FUS wave is applied in a pulsed manner, tissues experience a cycle of high and low pressure (Timbie et al., 2015). FUS is used to generate microbubbles, which act as contrast media, and these bubbles function as echo-enhancers that pass through the ultrasound field, resulting in stable cavitation (Lee et al.,

TABLE 2 Magnetic field-mediated delivery.

Type	Advantage/Disadvantage		Authors	Subject	Result
Magnetic field-mediated passive navigation using external magnetic field	Advantages	Magneto-nanobots allows cell-specific targeting	Andhari et al. (2020)	External magnetic field and magnetic nanobots consisting of Fe3O4 NPs	Provides autonomous propulsion ability and superparamagnetic property to the nanobot system
	Disadvantages	Sharply reduced effective delivery as the distance between the magnets and the carriers increases	Hwang (2020)		Unable to target tissues greater than 2 cm deep within the body
		Internal methods caused unexpected side effects to the body	Ganz (2017)	Magnetic implants around the gastroesophageal junction	Caused dysphagia, persistent nausea, and postoperative nausea
MTBs	Advantages	Higher biocompatibility than artificially synthesized NPs	Alphandery et al. (2017)	Magnetosomes consist of biological materials such as magnetite (Fe3O4) and greigite (Fe3S4) crystals	
		Less toxicity	Nan et al. (2021)	Tested its toxicity with mice	Complete blood count and basic metabolic panel showed normal range, and no change in the composition of urine and weight was found
		Exhibit magneto-aerotaxis which allows the drug to be directly navigated to the brain across the BBB when conjugated with NPs	Alphandery et al. (2017)	Magnetosome coated with poly-L-lysine (M-PLL) that contains 500–700 μg of iron was administered in a magnetic field of 202 kHz and 27 mT to treat GBM	Living GBM cells completely disappeared after 68 days for all treated mice
	Disadvantages	May adversely affect the human immune system	Nan et al. (2021)	Regarding the decreased level of lymphocyte proliferation	
		Difficulty in reproducing the composition of magnetosome and its low production yield	Alphandery et al. (2017)		
MRN	Advantages	Targeting effectivity both in the one-level bifurcation of an animal model and in the higher level of bifurcation of artificial pathways	Li et al. (2019)	Testing the MRN in a two-level bifurcation phantom with magnetic drug-eluting beads aggregates	Showed targeting success rates of 84, 100, 84, and 92%
			Pouponneau et al. (2014)	Rabbit's hepatic artery to the left/right liver lobes	Successfully steered therapeutic magnetic microcarriers to the left lobes
	Disadvantages	As pulsatile flow currently limits MRN to simple pathways *in vivo* studies	Folio and Ferreira (2017)	Applied to one or two simple Y-bifurcations or only 2D vascular phantoms	
		Some non-spherical microparticles occasionally attach to the surface of tissues and cannot travel to the target	Ghosh et al. (2021)		

CNS, central nerve system; BBB, blood–brain barrier; MTBs, magnetotactic bacteria; GBM, glioblastoma; and MRN, magnetic resonance navigation.

2017). Then, the blood vessels are mechanically stimulated by the microbubbles, which leads to opening of the BBB. Since the microbubbles can concentrate the ultrasonic energy, the initial ultrasound pressure needed for opening the BBB is considerably reduced, leading to the BBB opening with lesser risks of skull bone heating (Burgess et al., 2015).

Focused ultrasound increases the bioavailability of therapeutics in the target area and helps them maintain their bioactivity throughout the delivery processes (Huttunen and Saarma, 2019). In a recent mouse study of Parkinson's disease, FUS was used with two sonication locations in regions that showed severe damage in Parkinson's disease: the caudate-putamen and substantia nigra (Dauer and Przedborski, 2003), and varied pulse lengths of 5,500 cycles (3.3 ms) to 10,000 cycles (6.6 ms) were used. When neurturin, a type of neurotrophic factors, was directly injected, its bioavailability area was limited to an average of $0.20 \pm 0.05\,mm^2$. However, with FUS, the bioavailability of neurturin was $5.07 \pm 0.64\,mm^2$ in the caudate-putamen and $2.25 \pm 1.14\,mm^2$ in the substantia nigra, showing a maximum 25-fold increase due to BBB opening, allowing neurotrophic factors to pass through (Samiotaki et al., 2015). Additionally, FUS causes minimal damage to the nervous system while increasing the delivery rate of therapeutics passing through the BBB. In a study of nonhuman primates in which the short-term (2 days) and long-term (18 days) effects on FUS-mediated BBB opening and the secondary effect on visual-motor cognitive task-related touch accuracy or reaction time were assessed, response accuracy did not decrease in the short term (from 0.76 ± 0.08 to 0.80 ± 0.03) and nor in the long term (from 0.62 ± 0.08 to 0.68 ± 0.05), which suggests that cognitive performance dose not worsen following the FUS-induced BBB opening in nonhuman primates. In addition, no observable damage, microhemorrhage, or necrosis was observed in the histological test after the nonhuman primates were euthanized (Pouliopoulos et al., 2021). The aforementioned results suggest that FUS should be evaluated in healthy human populations to check whether it causes deterioration of cognitive functions or additional damage to the nervous system.

Although FUS has advantages, there are also limitations in applying FUS in clinical practices, especially regarding intensity. HIFU treatment with a frequency of 20 MHz generating a focal intensity ranging of 1,000–10,000 W/cm^2 may induce skin burns and neuronal damage due to thermal injuries caused by the inverse piezoelectric effect, leading to irreversible coagulative necrosis (Fan et al., 2012). In contrast to HIFU, low-intensity focused ultrasound (LIFU) with a peak intensity ranging of 10–500 W/cm^2 can increase the penetration of the therapeutics but may not cause side effects such as microhemorrhage and ischemia (Meng et al., 2018). Regarding the safety margin of FUS, LIFU treatment with a frequency ranging of 220–650 KHz producing a focal intensity of 80 W/cm^2 through an intact cranium induced no significant hemorrhage or necrosis in the necropsic cortex of eight 3–4-month-old swine (Zibly et al., 2014). Therefore, controlling the intensity and establishing clinical evidence is necessary for FUS to be an effective treatment. In authors' personal opinion, the focal peak intensity ranging of 10–80 W/cm^2 is ideal for FUS-based indirect delivery of therapeutics into the CNS in term of safety and efficiency: the stronger intensity, the better permeability but more adverse effects. Nevertheless, if more animal studies can be performed and the results applied to humans, FUS may be an effective way to help deliver therapeutics in a minimally invasive manner.

4.2.2. Light amplification by the stimulated emission of radiation therapy

Light amplification by the stimulated emission of radiation (LASER) therapy has been used in neurosurgery to destroy unhealthy brain tissue by creating heat. However, excess heat can induce damage to neighboring nontarget tissues. Therefore, various studies have been conducted to increase the spatial precision of LASER therapy, leading to the development of CNS-targeted therapy that includes using LASER to change cells into a specific state in which LASER increases the permeability of the BBB and subsequently deliver therapeutics. Currently, LASER interstitial therapy (LITT), PDT, and photobiomodulation therapy (PBM) are three approaches to LASER therapy that are studied for CNS-targeted delivery. LITT is a technique used to increase local BBB permeability by directing a LASER to the target area, transmitting light energy through a thin fiber, which is then converted into thermal energy, and creating a local disruption of the BBB (Melnick et al., 2021). LITT has been applied to the treatment of CNS diseases such as GBM (Patel et al., 2020). LITT-induced hyperthermia disrupts the BBB, with peak permeability for anti-neoplastic drugs happening by 1–2 weeks following ablation and disappearing by 4–6 weeks (Leuthardt et al., 2016). However, there are difficulties in controlling temperature to prevent thermal damage to nearby organs or structures (Salem et al., 2019); specifically, high temperature—close to or above 100°C—at the tissue can cause water to boil, and undesirable air bubbles can be produced (Zhu et al., 2017). To overcome this problem, thermal MRI has been introduced to monitor the heating process in real time and deactivate the system when the temperature reaches a critical level (Salem et al., 2019; Chen et al., 2021). However, well-designed prospective clinical trials and appropriate follow-up time are required to check patient outcomes with using LITT.

Another type of LASER therapy is PDT, which consists of three major elements: photosensitizers, light energy, and tissue oxygen. When a specific wavelength of light activates the photosensitive agent, the photosensitizer generates cytotoxic reactive oxygen species (ROS) such as hydroxyl radicals and singlet oxygen. With the help of photosensitizers such as 5-aminolevulinic acid and phthalocyanines, PDT can site-selectively open the BBB by destroying tight junction proteins and increasing the tight junction gap (Semyachkina-Glushkovskaya et al., 2020). However, although PDT can increase BBB permeability, it cannot utilize near-infrared light, making it difficult to allow deep penetration and low phototoxicity to normal tissues (Lan et al., 2019). Therefore, two-photon excitation and upconversion NPs, such as angiopep-2 conjugated NPs, are being studied to minimize invasiveness (Tsai et al., 2018).

The mechanism of PBM action in cells is the same as that observed in the use of PDT, but the two have apparent differences. PDT requires exogenous photosensitizers, and its high level of ROS generation causes cellular damage, while PBM utilizes endogenous cellular photosensitizers, resulting in low ROS levels that may not deteriorate cellular functions (Lubart and Friedmann, 2011). Furthermore, the combination of PDT and PBM can act as a synergistic therapeutic tool with the help of increased efficacy of anti-neoplastic treatment by increasing ATP production in mitochondria and increasing the production and homogeneity of protoporphyrin X, which is an endogenous photosensitizer required in PDT (Joniová et al., 2021). Additionally, in a study, PDT (660 nm) combined with PBM (850 nm) in which the Ru complex was used as a photosensitizer, increased photocytotoxicity was observed in A375 tumor cells (Negri et al., 2019). However, in the transcranial PBM approach, light cannot penetrates the brain more than 20mm from the cortex, making it difficult to use in delivering sufficient doses to the targeted region (Moro et al., 2014). Further study and clinical tests are required to

fully understand the mechanism of PBM, solve these limitations, and improve the efficacy of PBM.

5. Limitations/challenges

Direct and indirect targeted deliveries have many advantages and a great potential for use in CNS disease treatments, but have some limitations to be overwhelmed. Organic NPs require complicated process in production, and accumulate in the liver and spleen, and have a short half-life, and inorganic NPs have systemic toxicity involving multiple organs to be solved. Exosomes need further studies to figure the dependency of their characteristics on progenitor cells and nonstandardization of isolation and purification out. Hybrid nanomedicine demands the appropriately balanced ratio of the outer shell components, such as ligand/receptor density ratio, for the stability. Also, magnetic field-mediated delivery has difficulty in maintaining magnetic field greater than 2 cm deep within the body and navigational ability properly with increasing distance, MTB may trigger activation of the human immune system, and MRN has the obligation to use pulsatile flow, which disturbs its constant magnetic guidance even in simple pathways, and the tendency of nonspherical microparticles to attach to nontarget tissues surfaces. Regarding challenges of indirect methods, chemical deliveries, such as bradykinin and 1-O pentylglyceol, have numerous disadvantages; a short half-life, extravasation, adverse effects in nontarget organs. FUS has safety issues, intensity-related thermal injury by the inverse piezoelectric effect, and LASER therapy has problems of phototoxicity and generation of local hyperthermia and ROS to be solved.

Meanwhile, many of the delivery methods, especially NPs, described in the current manuscript have been known to reduce libido; for example, silver NPs compromised reproductive activity such as sperm motility 7 days after intravascular injection in rabbits (Castellini et al., 2014). Similarly, treatment of unconjugated titanium, gold, and silver NPs reduced the motility and viability of cryopreserved bovine spermatozoa from post-equilibration to post-thaw period following ejaculation (Pande et al., 2022). Furthermore, gender difference was reported in hepatic toxicity, especially dominant in female sex, after oral exposure of titanium NPs over 90 days in rats (Chen et al., 2019). Also, male sex-dominant differences in histopathology and mortality were noticed after single oral administration of copper NPs at higher dose in rats (Lee et al., 2016). To the contrary, no gender difference was revealed in bone marrow toxicity after oral exposure of silver NPs for 28 days in rats (Kim et al., 2008). Now, there are few clinical studies investigating gender difference of NPs; interestingly, in a randomized controlled clinical trial in which 19 patients with carious teeth were recruited, subgroup analysis showed no gender difference in marginal integrity restoration of resin composites following pretreatment with silver and gold NPs (Nemt-Allah et al., 2021). Hence, it requires further studies prior to discussion about their gender based effect.

6. Future directions and conclusion

In direct CNS-targeted delivery, organic NPs show high biocompatibility and low immunogenicity but are difficult to produce at a large scale, lack stability, and are eliminated too early. Inorganic NPs show a high drug-carrying capacity, surface modifiability, and magnetic field-mediated navigability, but have toxic side effects. To overcome these limitations, efforts have been made to control the components of outer shells for better stability and reduce factors that cause toxicity. Although hybrid NPs, a combination of organic and inorganic NPs, have many advantages, such as tunable size, high stability, and high drug-loading yield, they have side effects, including harmful tissue deposition patterns, unintended activation of the host immune response, and damage to nontarget cells. Among EVs, exosomes show a notable potential for CNS-targeted delivery of therapeutics because of genetically and/or chemically engineered targetability of inherited surface proteins as well as biocompatibility and permeability across the BBB. Therefore, studies are in progress to manufacture NPs, exosomes, and ligands in an appropriate ratio, and contingencies such as PEG stealth technology have evolved, making hybrid nanomedicine, a combination of NPs and EVs, an effective direct delivery method. Another advantageous direct delivery method is magnetic field-mediated delivery, which utilizes magneto-nanobots, MTB, and MRN. However, methods using an external magnetic field have difficulty reaching deep targeted regions, and MTB negatively affect immune system of the human body and have a low production yield. Therefore, MRN was developed to overcome these issues, showing successful targeting efficacy in simple pathways in *in vivo* studies. While further studies are needed to apply MRN in more complex pathways, due to its pulsatile flow-induced navigability weakening in real time, it is one of the most promising direct CNS-targeted delivery methods.

As there are obstacles to overcome in the use of direct CNS-targeted delivery methods, indirect delivery methods have been developed and are used together with direct methods to create a synergistic effect. Chemicals such as mannitol and bradykinin effectively increase the BBB permeability but have a short half-life and show toxicity when injected. Although short-chain alkylglycerols do not have the same drawbacks as mannitol and bradykinin, they lead to complications related to immunogenicity problems and can invade nontarget cells. While FUS, one of the physical targeted delivery methods, increases and maintains the bioavailability of therapeutics and causes minimal damage to the CNS, it has problems related to delivery intensity that need to be solved to make this method more advantageous. LASER therapies, such as LITT, PDT, and PBM, have recently gained prominence and have been increasingly used for disrupting the BBB. However, they still have limitations—thermal damage, shallow penetration, and phototoxicity—to overcome, so thermal MRI is being introduced in LASER therapies, and two-photon excitation and upconversion NPs are being studied. Based on the outcomes, such as anti-neoplastic activity and validity of endogenous photosensitizers, LASER therapy may be one of the most promising indirect CNS-targeted therapy methods. While this article has recommended the most promising direct and indirect targeted therapies, it is important to note that combining the direct and indirect methods, such as hybrid nanomedicine of organic, inorganic NPs, and exosomes via MRN following preconditioning treatment with either PBM or LIFS, will be more effective and focused in the future (Figure 2).

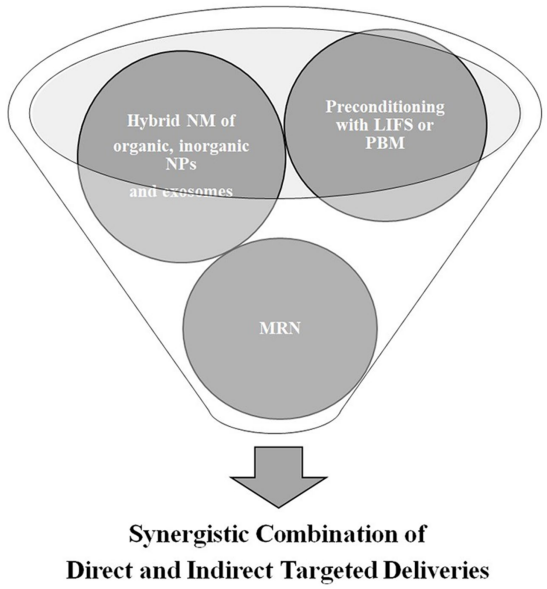

FIGURE 2
Future directions of targeted delivery of therapeutics in central nervous system diseases; low intensity focused ultrasound (LIFS); photobiomodulation therapy (PBM); nanomedicine (NM); nanoparticles (NPs); and magnetic resonance navigation (MRN).

Author contributions

JA, SW, HS, SI, GY, SL, K-iK, and CH substantially contributed to all of the following aspects of this study: (1) study conception and design, acquisition of data, or analysis and interpretation of data, (2) drafting or critical revision of the article for important intellectual content, (3) final approval of the version to be published, and (4) agreement to be accountable for all aspects of the work in ensuring that questions related to the accuracy or integrity of any part of the work are appropriately investigated and resolved. All authors contributed to the article and approved the submitted version.

Funding

This work was supported by the 2022 Research Fund of University of Ulsan, Ulsan, Republic of Korea. The study sponsor had no involvement in the study design; in the collection, analysis, or interpretation of data; in the writing of the manuscript; or in the decision to submit the manuscript for publication.

Conflict of interest

The authors declare that the research was conducted in the absence of any commercial or financial relationships that could be construed as a potential conflict of interest.

Publisher's note

All claims expressed in this article are solely those of the authors and do not necessarily represent those of their affiliated organizations, or those of the publisher, the editors and the reviewers. Any product that may be evaluated in this article, or claim that may be made by its manufacturer, is not guaranteed or endorsed by the publisher.

References

Ahmed, T., Liu, F. F., He, C., Abbasi, A. Z., Cai, P., Rauth, A. M., et al. (2021). Optimizing the Design of Blood-Brain Barrier-Penetrating Polymer-Lipid-Hybrid Nanoparticles for delivering anticancer drugs to Glioblastoma. *Pharm. Res.* 38, 1897–1914. doi: 10.1007/s11095-021-03122-9

Ali-Boucetta, H., Al-Jamal, K. T., Müller, K. H., Li, S., Porter, A. E., Eddaoudi, A., et al. (2011). Cellular uptake and cytotoxic impact of chemically functionalized and polymer-coated carbon nanotubes. *Small* 7, 3230–3238. doi: 10.1002/smll.201101004

Alkilany, A. M., Zhu, L., Weller, H., Mews, A., Parak, W. J., Barz, M., et al. (2019). Ligand density on nanoparticles: a parameter with critical impact on nanomedicine. *Adv. Drug Deliv. Rev.* 143, 22–36. doi: 10.1016/j.addr.2019.05.010

Alphandery, E., Idbaih, A., Adam, C., Delattre, J. Y., Schmitt, C., Guyot, F., et al. (2017). Development of non-pyrogenic magnetosome minerals coated with poly-l-lysine leading to full disappearance of intracranial U87-Luc glioblastoma in 100% of treated mice using magnetic hyperthermia. *Biomaterials* 141, 210–222. doi: 10.1016/j.biomaterials.2017.06.026

Alvarez-Erviti, L., Seow, Y., Yin, H., Betts, C., Lakhal, S., and Wood, M. J. A. (2011). Delivery of siRNA to the mouse brain by systemic injection of targeted exosomes. *Nat. Biotechnol.* 29, 341–345. doi: 10.1038/nbt.1807

Andhari, S. S., Wavhale, R. D., Dhobale, K. D., Tawade, B. V., Chate, G. P., Patil, Y. N., et al. (2020). Self-propelling targeted magneto-Nanobots for deep tumor penetration and pH-responsive intracellular drug delivery. *Sci. Rep.* 10:4703. doi: 10.1038/s41598-020-61586-y

Anraku, Y., Kuwahara, H., Fukusato, Y., Mizoguchi, A., Ishii, T., Nitta, K., et al. (2017). Glycaemic control boosts glucosylated nanocarrier crossing the BBB into the brain. *Nat. Commun.* 8:1001. doi: 10.1038/s41467-017-00952-3

Balasubramanian, S. K., Jittiwat, J., Manikandan, J., Ong, C. N., Yu, L. E., and Ong, W. Y. (2010). Biodistribution of gold nanoparticles and gene expression changes in the liver and spleen after intravenous administration in rats. *Biomaterials* 31, 2034–2042. doi: 10.1016/j.biomaterials.2009.11.079

Bartus, P. E. R. T., Elliott, P., Hayward, N., Dean, R., McEwen, E. L., and Fisher, S. K. (1996). Permeability of the blood brain barrier by the bradykinin agonist, RMP-7: evidence for a sensitive, auto-regulated, receptor-mediated system. *Immunopharmacology* 33, 270–278. doi: 10.1016/0162-3109(96)00070-7

Bertrand, J., Winton, M. J., Rodriguez-Hernandez, N., Campenot, R. B., and McKerracher, L. (2005). Application of rho antagonist to neuronal cell bodies promotes neurite growth in compartmented cultures and regeneration of retinal ganglion cell axons in the optic nerve of adult rats. *J. Neurosci.* 25, 1113–1121. doi: 10.1523/JNEUROSCI.3931-04.2005

Black, K. L. (1995). Biochemical opening of the blood-brain barrier. *Adv. Drug Deliv. Rev.* 15, 37–52. doi: 10.1016/0169-409X(95)00004-Q

Bose, R. J. C., Tharmalingam, N., Choi, Y., Madheswaran, T., Paulmurugan, R., McCarthy, J. R., et al. (2020). Combating intracellular pathogens with Nanohybrid-facilitated antibiotic delivery. *Int. J. Nanomedicine* 15, 8437–8449. doi: 10.2147/IJN.S271850

Burgess, A., Shah, K., Hough, O., and Hynynen, K. (2015). Focused ultrasound-mediated drug delivery through the blood-brain barrier. *Expert. Rev. Neurother.* 15, 477–491. doi: 10.1586/14737175.2015.1028369

Burks, S. R., Kersch, C. N., Witko, J. A., Pagel, M. A., Sundby, M., Muldoon, L. L., et al. (2021). Blood-brain barrier opening by intracarotid artery hyperosmolar mannitol induces sterile inflammatory and innate immune responses. *Proc. Natl. Acad. Sci. U. S. A.* 118: e2021915118. doi: 10.1073/pnas.2021915118

Campbell, F., Bos, F. L., Sieber, S., Arias-Alpizar, G., Koch, B. E., Huwyler, J., et al. (2018). Directing nanoparticle biodistribution through evasion and exploitation of Stab2-dependent nanoparticle uptake. *ACS Nano* 12, 2138–2150. doi: 10.1021/acsnano.7b06995

Castellini, C., Ruggeri, S., Mattioli, S., Bernardini, G., Macchioni, L., Moretti, E., et al. (2014). Long-term effects of silver nanoparticles on reproductive activity of rabbit buck. *Syst Biol Reprod Med* 60, 143–150. doi: 10.3109/19396368.2014.891163

Chacko, A. M., Li, C., Pryma, D. A., Brem, S., Coukos, G., and Muzykantov, V. (2013). Targeted delivery of antibody-based therapeutic and imaging agents to CNS tumors:

crossing the blood-brain barrier divide. *Expert Opin. Drug Deliv.* 10, 907–926. doi: 10.1517/17425247.2013.808184

Chauhan, A. S. (2018). Dendrimers for Drug Delivery. *Molecules* 23:938. doi: 10.3390/molecules23040938

Chen, C., Lee, I., Tatsui, C., Elder, T., and Sloan, A. E. (2021). Laser interstitial thermotherapy (LITT) for the treatment of tumors of the brain and spine: a brief review. *J. Neuro-Oncol.* 151, 429–442. doi: 10.1007/s11060-020-03652-z

Chen, Z., Zhou, D., Zhou, S., and Jia, G. (2019). Gender difference in hepatic toxicity of titanium dioxide nanoparticles after subchronic oral exposure in Sprague-Dawley rats. *J. Appl. Toxicol.* 39, 807–819. doi: 10.1002/jat.3769

Cheng, C. A., Deng, T., Lin, F. C., Cai, Y., and Zink, J. I. (2019). Supramolecular Nanomachines as stimuli-responsive gatekeepers on Mesoporous silica nanoparticles for antibiotic and Cancer drug delivery. *Theranostics* 9, 3341–3364. doi: 10.7150/thno.34576

Cheng, J., Gu, Y. J., Cheng, S. H., and Wong, W. T. (2013). Surface functionalized gold nanoparticles for drug delivery. *J. Biomed. Nanotechnol.* 9, 1362–1369. doi: 10.1166/jbn.2013.1536

Chengyan Chu, G. L., Janowski, M., Bulte, J. W. M., Li, S., Pearl, M., and Walczak, P. (2018). Real-time MRI guidance for reproducible hyperosmolar opening of the blood-brain barrier in mice. *Front. Neurol.*

Chorny, M., Fishbein, I., Forbes, S., and Alferiev, I. (2011). Magnetic nanoparticles for targeted vascular delivery. *IUBMB Life* 63, 613–620. doi: 10.1002/iub.479

Cianfarani, F., Toietta, G., Di Rocco, G., Cesareo, E., Zambruno, G., and Odorisio, T. (2013). Diabetes impairs adipose tissue-derived stem cell function and efficiency in promoting wound healing. *Wound Repair Regen.* 21, 545–553. doi: 10.1111/wrr.12051

Cosolo, W. C., Martinello, P., Louis, W. J., and Christophidis, N. (1989). Blood-brain barrier disruption using mannitol: time course and electron microscopy studies. *Am. J. Phys. Regul. Integr. Comp. Phys.* 256, R443–R447. doi: 10.1152/ajpregu.1989.256.2.R443

Cui, B., and Cho, S. W. (2022). Blood-brain barrier-on-a-chip for brain disease modeling and drug testing. *BMB Rep.* 55, 213–219. doi: 10.5483/BMBRep.2022.55.5.043

Cyr, M., Lepage, Y., Blais, C. Jr., Gervais, N., Cugno, M., Rouleau, J. L., et al. (2001). Bradykinin and des-Arg(9)-bradykinin metabolic pathways and kinetics of activation of human plasma. *Am. J. Physiol. Heart Circ. Physiol.* 281, H275–H283. doi: 10.1152/ajpheart.2001.281.1.H275

Daneman, R., and Prat, A. (2015). The blood-brain barrier. *Cold Spring Harb. Perspect. Biol.* 7:a020412. doi: 10.1101/cshperspect.a020412

Daroff, J. J., Mazziotta, J. C., and Pomeroy, S. L. (2016). "Management of neurological disease" in *Bradley's Neurology in Clinical Practice*. eds. J. J. D. RB, J. C. Mazziotta and S. K. Pomeroy (Philadelphia, PA: Elsevier)

Dauer, W., and Przedborski, S. (2003). Parkinson's disease. *Neuron* 39, 889–909. doi: 10.1016/S0896-6273(03)00568-3

De Vincentiis, S., Falconieri, A., Mickoleit, F., Cappello, V., Schuler, D., and Raffa, V. (2021). Induction of axonal outgrowth in mouse hippocampal neurons via bacterial Magnetosomes. *Int. J. Mol. Sci.* 22:4126. doi: 10.3390/ijms22084126

Dhar, S., Liu, Z., Thomale, J., Dai, H., and Lippard, S. J. (2008). Targeted single-wall carbon nanotube-mediated Pt(IV) prodrug delivery using folate as a homing device. *J. Am. Chem. Soc.* 130, 11467–11476. doi: 10.1021/ja803036e

Dong, X. (2018). Current strategies for brain drug delivery. *Theranostics* 8, 1481–1493. doi: 10.7150/thno.21254

Dorman, H. R., Sondheimer, J. H., and Cadnapaphornchai, P. (1990). Mannitol-induced acute renal failure. *Medicine (Baltimore)* 69, 153–159. doi: 10.1097/00005792-199005000-00003

Elmore, S. (2007). Apoptosis: a review of programmed cell death. *Toxicol. Pathol.* 35, 495–516. doi: 10.1080/01926230701320337

Elsharkasy, O. M., Nordin, J. Z., Hagey, D. W., de Jong, O. G., Schiffelers, R. M., Andaloussi, S. E., et al. (2020). Extracellular vesicles as drug delivery systems: why and how? *Adv. Drug Deliv. Rev.* 159, 332–343. doi: 10.1016/j.addr.2020.04.004

Erdlenbruch, B., Alipour, M., Fricker, G., Miller, D. S., Kugler, W., Eibl, H., et al. (2003). Alkylglycerol opening of the blood-brain barrier to small and large fluorescence markers in normal and C6 glioma-bearing rats and isolated rat brain capillaries. *Br. J. Pharmacol.* 140, 1201–1210. doi: 10.1038/sj.bjp.0705554

Erdlenbruch, B., Kugler, W., Schinkhof, C., Neurath, H., Eibl, H., and Lakomek, M. (2005). Blood-brain barrier opening with alkylglycerols: biodistribution of 1-O-pentylglycerol after intravenous and intracarotid administration in rats. *J. Drug Target.* 13, 143–150. doi: 10.1080/10611860400029085

Fan, Y., Chen, Z., and Zhang, M. (2022). Role of exosomes in the pathogenesis, diagnosis, and treatment of central nervous system diseases. *J. Transl. Med.* 20:291. doi: 10.1186/s12967-022-03493-6

Fan, T.-Y., Zhang, L., Chen, W., Liu, Y., He, M., Huang, X., et al. (2012). Feasibility of MRI-guided high intensity focused ultrasound treatment for adenomyosis. *Eur. J. Radiol.* 81, 3624–3630. doi: 10.1016/j.ejrad.2011.05.036

Ferreira Soares, D. C., Domingues, S. C., Viana, D. B., and Tebaldi, M. L. (2020). Polymer-hybrid nanoparticles: current advances in biomedical applications. *Biomed. Pharmacother.* 131:110695. doi: 10.1016/j.biopha.2020.110695

Folio, D., and Ferreira, A. (2017). Two-dimensional robust magnetic resonance navigation of a ferromagnetic microrobot using Pareto optimality. *IEEE Trans. Robot.* 33, 583–593. doi: 10.1109/TRO.2016.2638446

Forbes, N., Hussain, M. T., Briuglia, M. L., Edwards, D. P., Horst, J. H. T., Szita, N., et al. (2019). Rapid and scale-independent microfluidic manufacture of liposomes entrapping protein incorporating in-line purification and at-line size monitoring. *Int. J. Pharm.* 556, 68–81. doi: 10.1016/j.ijpharm.2018.11.060

Ganz, R. A. (2017). A modern magnetic implant for Gastroesophageal reflux disease. *Clin. Gastroenterol. Hepatol.* 15, 1326–1337. doi: 10.1016/j.cgh.2016.12.019

George, S., Pokhrel, S., Xia, T., Gilbert, B., Ji, Z., Schowalter, M., et al. (2010). Use of a rapid cytotoxicity screening approach to engineer a safer zinc oxide nanoparticle through iron doping. *ACS Nano* 4, 15–29. doi: 10.1021/nn901503q

Ghosh, A., Liu, Y., Artemov, D., and Gracias, D. H. (2021). Magnetic resonance guided navigation of untethered microgrippers. *Adv. Healthc. Mater.* 10:2000869. doi: 10.1002/adhm.202000869

Gu, X., Song, Q., Zhang, Q., Huang, M., Zheng, M., Chen, J., et al. (2020). Clearance of two organic nanoparticles from the brain via the paravascular pathway. *J. Control. Release* 322, 31–41. doi: 10.1016/j.jconrel.2020.03.009

Guimarães, D., Cavaco-Paulo, A., and Nogueira, E. (2021). Design of liposomes as drug delivery system for therapeutic applications. *Int. J. Pharm.* 601:120571. doi: 10.1016/j.ijpharm.2021.120571

Hartl, N., Adams, F., and Merkel, O. M. (2021). From adsorption to covalent bonding: Apolipoprotein E functionalization of polymeric nanoparticles for drug delivery across the blood-brain barrier. *Adv. Ther.* 4:2000092. doi: 10.1002/adtp.202000092

Hendricks, B. K., Cohen-Gadol, A. A., and Miller, J. C. (2015). Novel delivery methods bypassing the blood-brain and blood-tumor barriers. *Neurosurg. Focus.* 38:E10. doi: 10.3171/2015.1.FOCUS14767

Hojun Choi, K. C., Kim, D.-H., Byung-Koo, O., Yim, H., Jo, S., and Choi, C. (2022). Strategies for targeted delivery of Exosomes to the brain: advantages and challenges. *Pharmaceutics*.

Howard, M. D., Hood, E. D., Zern, B., Shuvaev, V. V., Grosser, T., and Muzykantov, V. R. (2014). Nanocarriers for vascular delivery of anti-inflammatory agents. *Annu. Rev. Pharmacol.* 54, 205–226. doi: 10.1146/annurev-pharmtox-011613-140002

Hu, C. M., Kaushal, S., Tran Cao, H. S., Aryal, S., Sartor, M., and Esener, S. (2010). Half-antibody functionalized lipid-polymer hybrid nanoparticles for targeted drug delivery to carcinoembryonic antigen presenting pancreatic cancer cells. *Mol. Pharm.*

Huang, C., Chen, X., Xue, Z., and Wang, T. (2020). Effect of structure: a new insight into nanoparticle assemblies from inanimate to animate. *Sci. Adv.* 6:eaba1321. doi: 10.1126/sciadv.aba1321

Hülper, P., Veszelka, S., Walter, F. R., Wolburg, H., Fallier-Becker, P., Piontek, J., et al. (2013). Acute effects of short-chain alkylglycerols on blood-brain barrier properties of cultured brain endothelial cells. *Br. J. Pharmacol.* 169, 1561–1573. doi: 10.1111/bph.12218

Huttunen, H. J., and Saarma, M. (2019). CDNF protein therapy in Parkinson's disease. *Cell Transplant.* 28, 349–366. doi: 10.1177/0963689719840290

Hwang, C. H. (2020). Targeted delivery of erythropoietin hybridized with magnetic Nanocarriers for the treatment of central nervous system injury: a literature review. *Int. J. Nanomedicine* 15, 9683–9701. doi: 10.2147/IJN.S287456

Ibegbu, D. M., Boussahel, A., Cragg, S. M., Tsibouklis, J., and Barbu, E. (2017). Nanoparticles of alkylglyceryl dextran and poly(ethyl cyanoacrylate) for applications in drug delivery: preparation and characterization. *Int. J. Polym. Mater. Polym. Biomater.* 66, 265–279. doi: 10.1080/00914037.2016.1201827

Jang, S. C., Kim, O. Y., Yoon, C. M., Choi, D. S., Roh, T. Y., Park, J., et al. (2013). Bioinspired exosome-mimetic nanovesicles for targeted delivery of chemotherapeutics to malignant tumors. *ACS Nano* 7, 7698–7710. doi: 10.1021/nn402232g

Joniová, J., Kazemiraad, C., Gerelli, E., and Wagnières, G. (2021). Stimulation and homogenization of the protoporphyrin IX endogenous production by photobiomodulation to increase the potency of photodynamic therapy. *J. Photochem. Photobiol. B Biol.* 225:112347. doi: 10.1016/j.jphotobiol.2021.112347

Kafa, H., Wang, J. T.-W., Rubio, N., Venner, K., Anderson, G., Pach, E., et al. (2015). The interaction of carbon nanotubes with an in vitro blood-brain barrier model and mouse brain in vivo. *Biomaterials* 53, 437–452. doi: 10.1016/j.biomaterials.2015.02.083

Kasinathan, N., Volety, S. M., and Josyula, V. R. (2016). Chondroitinase: a promising therapeutic enzyme. *Crit. Rev. Microbiol.* 42, 474–484.

Khan, M. M., Madni, A., Tahir, N., Parveen, F., Khan, S., Jan, N., et al. (2020). Co-delivery of Curcumin and Cisplatin to enhance cytotoxicity of Cisplatin using lipid-chitosan hybrid nanoparticles. *Int. J. Nanomedicine* 15, 2207–2217. doi: 10.2147/IJN.S247893

Kim, Y. S., Kim, J. S., Cho, H. S., Rha, D. S., Kim, J. M., Park, J. D., et al. (2008). Twenty-eight-day oral toxicity, genotoxicity, and gender-related tissue distribution of silver nanoparticles in Sprague-Dawley rats. *Inhal. Toxicol.* 20, 575–583. doi: 10.1080/08958370701874663

Kostarelos, K., Lacerda, L., Partidos, C. D., Prato, M., and Bianco, A. (2005). Carbon nanotube-mediated delivery of peptides and genes to cells: translating nanobiotechnology to therapeutics. *J. Drug Deliv. Sci. Technol.* 15, 41–47. doi: 10.1016/S1773-2247(05)50005-4

Kou, L., Hou, Y., Yao, Q., Guo, W., Wang, G., Wang, M., et al. (2018). L-Carnitine-conjugated nanoparticles to promote permeation across blood-brain barrier and to target glioma cells for drug delivery via the novel organic cation/carnitine transporter OCTN2. *Artif. Cells Nanomed. Biotechnol.* 46, 1605–1616.

Lan, M., Zhao, S., Liu, W., Lee, C. S., Zhang, W., and Wang, P. (2019). Photosensitizers for photodynamic therapy. *Adv. Healthc. Mater.* 8:1900132. doi: 10.1002/adhm.201900132

Lee, H., Kim, H., Han, H., Lee, M., Lee, S., Yoo, H., et al. (2017). Microbubbles used for contrast enhanced ultrasound and theragnosis: a review of principles to applications. *Biomed. Eng. Lett.* 7, 59–69. doi: 10.1007/s13534-017-0016-5

Lee, I. C., Ko, J. W., Park, S. H., Lim, J. O., Shin, I. S., Moon, C., et al. (2016). Comparative toxicity and biodistribution of copper nanoparticles and cupric ions in rats. *Int. J. Nanomedicine* 11, 2883–2900. doi: 10.2147/IJN.S106346

Leuthardt, E. C., Duan, C., Kim, M. J., Campian, J. L., Kim, A. H., Miller-Thomas, M. M., et al. (2016). Hyperthermic laser ablation of recurrent Glioblastoma leads to temporary disruption of the Peritumoral blood brain barrier. *PLoS One* 11:e0148613. doi: 10.1371/journal.pone.0148613

Li, L., He, D., Guo, Q., Zhang, Z., Ru, D., Wang, L., et al. (2022). Exosome-liposome hybrid nanoparticle codelivery of TP and miR497 conspicuously overcomes chemoresistant ovarian cancer. *J Nanobiotechnol* 20:50. doi: 10.1186/s12951-022-01264-5

Li, N., Jiang, Y., Plantefève, R., Michaud, F., Nosrati, Z., Tremblay, C., et al. (2019). Magnetic resonance navigation for targeted embolization in a two-level bifurcation phantom. *Ann. Biomed. Eng.* 47, 2402–2415. doi: 10.1007/s10439-019-02317-x

Li, M., Liao, L., and Tian, W. (2020). Extracellular vesicles derived from apoptotic cells: an essential link between death and regeneration. *Front. Cell Dev. Biol.* 8:573511. doi: 10.3389/fcell.2020.573511

Liu, W., Bai, X., Zhang, A., Huang, J., Xu, S., and Zhang, J. (2019). Role of Exosomes in central nervous system diseases. *Front. Mol. Neurosci.* 12:240. doi: 10.3389/fnmol.2019.00240

Liu, M. L., Williams, K. J., and Werth, V. P. (2016). Chapter four—Microvesicles in autoimmune diseases. *Advances in Clinical Chemistry*. 125–175. doi: 10.1016/bs.acc.2016.06.005

Lubart, R., and Friedmann, H. (2011). LLLT and PDT. *Laser Ther* 20:233. doi: 10.5978/islsm.20.233

Lueshen, E., Venugopal, I., Soni, T., Alaraj, A., and Linninger, A. (2015). Implant-assisted Intrathecal magnetic drug targeting to aid in therapeutic nanoparticle localization for potential treatment of central nervous system disorders. *J. Biomed. Nanotechnol.* 11, 253–261. doi: 10.1166/jbn.2015.1907

Lv, Q., Cheng, L., Lu, Y., Zhang, X., Wang, Y., Deng, J., et al. (2020). Thermosensitive exosome-liposome hybrid nanoparticle-mediated Chemoimmunotherapy for improved treatment of metastatic peritoneal Cancer. *Adv Sci* 7:2000515. doi: 10.1002/advs.202000515

Macdougall, I. C., Strauss, W. E., Dahl, N. V., Bernard, K., and Li, Z. (2019). Ferumoxytol for iron deficiency anemia in patients undergoing hemodialysis. *Clin. Nephrol.* 91, 237–245. doi: 10.5414/CN109512

Madani, S. Y., Naderi, N., Dissanayake, O., Tan, A., and Seifalian, A. M. (2011). A new era of cancer treatment: carbon nanotubes as drug delivery tools. *Int. J. Nanomedicine* 6, 2963–2979. doi: 10.2147/IJN.S16923

Marcuello, C., Chambel, L., Rodrigues, M. S., Ferreira, L. P., and Cruz, M. M. (2018). Magnetotactic Bacteria: magnetism beyond Magnetosomes. *IEEE Trans. Nanobiosci.* 17, 555–559. doi: 10.1109/TNB.2018.2878085

Marie, C. V., Pauwels, J., and Vandenbroucke, R. E. (2021). Special delEVery: extracellular vesicles as promising delivery platform to the brain. *Biomedicine*

Martel, S. (2010). Microrobotic navigable entities for magnetic resonance targeting. *Annu. Int. Conf. IEEE Eng. Med. Biol. Soc.* 2010, 1942–1945.

Melnick, K., Shin, D., Dastmalchi, F., Kabeer, Z., Rahman, M., Tran, D., et al. (2021). Role of laser interstitial thermal therapy in the Management of Primary and Metastatic Brain Tumors. *Curr. Treat. Options in Oncol.* 22:108. doi: 10.1007/s11864-021-00912-6

Meng, Y., Suppiah, S., Surendrakumar, S., Bigioni, L., and Lipsman, N. (2018). Low-intensity MR-guided focused ultrasound mediated disruption of the blood-brain barrier for intracranial metastatic diseases. *Front. Oncol.* 8:338. doi: 10.3389/fonc.2018.00338

Mitchell, M. J., Billingsley, M. M., Haley, R. M., Wechsler, M. E., Peppas, N. A., and Langer, R. (2021). Engineering precision nanoparticles for drug delivery. *Nat. Rev. Drug Discov.* 20, 101–124. doi: 10.1038/s41573-020-0090-8

Mittal, D., Ali, A., Md, S., Baboota, S., Sahni, J. K., and Ali, J. (2014). Insights into direct nose to brain delivery: current status and future perspective. *Drug Deliv.* 21, 75–86. doi: 10.3109/10717544.2013.838713

Mohammadpour, R., Dobrovolskaia, M. A., Cheney, D. L., Greish, K. F., and Ghandehari, H. (2019). Subchronic and chronic toxicity evaluation of inorganic nanoparticles for delivery applications. *Adv. Drug Deliv. Rev.* 144, 112–132. doi: 10.1016/j.addr.2019.07.006

Moro, C., Massri, N. E., Torres, N., Ratel, D., De Jaeger, X., Chabrol, C., et al. (2014). Photobiomodulation inside the brain: a novel method of applying near-infrared light intracranially and its impact on dopaminergic cell survival in MPTP-treated mice. *J. Neurosurg.* 120, 670–683. doi: 10.3171/2013.9.JNS13423

Mullen, D. G., and Banaszak Holl, M. M. (2011). Heterogeneous ligand-nanoparticle distributions: a major obstacle to scientific understanding and commercial translation. *Acc. Chem. Res.* 44, 1135–1145. doi: 10.1021/ar1001389

Nacev, A., Weinberg, I. N., Stepanov, P. Y., Kupfer, S., Mair, L. O., Urdaneta, M. G., et al. (2015). Dynamic inversion enables external magnets to concentrate ferromagnetic rods to a central target. *Nano Lett.* 15, 359–364. doi: 10.1021/nl503654t

Nan, X., Teng, Y., Tian, J., Hu, Z., and Fang, Q. (2021). A comprehensive assessment of the biocompatibility of *Magnetospirillum gryphiswaldense* MSR-1 bacterial magnetosomes in vitro and in vivo. *Toxicology* 462:152949. doi: 10.1016/j.tox.2021.152949

Nederveen, J. P., Warnier, G., Di Carlo, A., Nilsson, M. I., and Tarnopolsky, M. A. (2021). Extracellular vesicles and Exosomes: insights from exercise science. *Front. Physiol.* 11:604274. doi: 10.3389/fphys.2020.604274

Negri, L. B., Martins, T. J., da Silva, R. S., and Hamblin, M. R. (2019). Photobiomodulation combined with photodynamic therapy using ruthenium phthalocyanine complexes in A375 melanoma cells: effects of nitric oxide generation and ATP production. *J. Photochem. Photobiol. B Biol.* 198:111564. doi: 10.1016/j.jphotobiol.2019.111564

Nemt-Allah, A. A., Ibrahim, S. H., and El-Zoghby, A. F. (2021). Marginal integrity of composite restoration with and without surface pretreatment by gold and silver nanoparticles vs Chlorhexidine: a randomized controlled trial. *J. Contemp. Dent. Pract.* 22, 1087–1097. doi: 10.5005/jp-journals-10024-3200

Owens, D. E. 3rd, and Peppas, N. A. (2006). Opsonization, biodistribution, and pharmacokinetics of polymeric nanoparticles. *Int. J. Pharm.* 307, 93–102. doi: 10.1016/j.ijpharm.2005.10.010

Palmerston Mendes, L., Pan, J., and Torchilin, V. P. (2017). Dendrimers as Nanocarriers for nucleic acid and drug delivery in Cancer therapy. *Molecules* 22:1401. doi: 10.3390/molecules22091401

Pande, M., Tyagi, S., Kumar, S., Soni, Y. K., Chand, N., Sirohi, A. S., et al. (2022). Effects of unconjugated gold, silver and titanium dioxide nanoparticles on bovine spermatozoa at various stages of cryopreservation. *Cryo-Letters* 43, 150–157. doi: 10.54680/fr22310110512

Pardridge, W. M. (2012). Drug transport across the blood-brain barrier. *J. Cereb. Blood Flow Metab.* 32, 1959–1972. doi: 10.1038/jcbfm.2012.126

Pashirova, T. N., Zueva, I. V., Petrov, K. A., Babaev, V. M., Lukashenko, S. S., Rizvanov, I. K., et al. (2017). Nanoparticle-delivered 2-PAM for rat brain protection against Paraoxon central toxicity. *ACS Appl. Mater. Interfaces* 9, 16922–16932. doi: 10.1021/acsami.7b04163

Patel, B., Yang, P. H., and Kim, A. H. (2020). The effect of thermal therapy on the blood-brain barrier and blood-tumor barrier. *Int. J. Hyperth.* 37, 35–43. doi: 10.1080/02656736.2020.1783461

Pentek, T., Newenhouse, E., O'Brien, B., and Chauhan, A. S. (2017). Development of a topical resveratrol formulation for commercial applications using Dendrimer nanotechnology. *Molecules* 22:137. doi: 10.3390/molecules22010137

Perez-Herrero, E., and Fernandez-Medarde, A. (2015). Advanced targeted therapies in cancer: drug nanocarriers, the future of chemotherapy. *Eur. J. Pharm. Biopharm.* 93, 52–79. doi: 10.1016/j.ejpb.2015.03.018

Pouliopoulos, A. N., Kwon, N., Jensen, G., Meaney, A., Niimi, Y., Burgess, M. T., et al. (2021). Safety evaluation of a clinical focused ultrasound system for neuronavigation guided blood-brain barrier opening in non-human primates. *Sci. Rep.* 11:15043. doi: 10.1038/s41598-021-94188-3

Pouponneau, P., Bringout, G., and Martel, S. (2014). Therapeutic magnetic microcarriers guided by magnetic resonance navigation for enhanced liver chemoembilization: a design review. *Ann. Biomed. Eng.* 42, 929–939. doi: 10.1007/s10439-014-0972-1

Qiao, L., Qin, Y., Wang, Y., Liang, Y., Zhu, D., Xiong, W., et al. (2020). A brain glioma gene delivery strategy by angiopep-2 and TAT-modified magnetic lipid-polymer hybrid nanoparticles. *RSC Adv.* 10, 41471–41481. doi: 10.1039/D0RA07161G

Raymond, J., Robertson, D., and Dinsdale, H. (1986). Pharmacological modification of Bradykinin induced breakdown of the blood-brain barrier. *Can. J. Neurol. Sci.* 13, 214–220. doi: 10.1017/S0317167100036301

Roces, C. B., Port, E. C., Daskalakis, N. N., Watts, J. A., Aylott, J. W., Halbert, G. W., et al. (2020). Rapid scale-up and production of active-loaded PEGylated liposomes. *Int. J. Pharm.* 586:119566. doi: 10.1016/j.ijpharm.2020.119566

Rodríguez-Massó, S. R., Erickson, M. A., Banks, W. A., Ulrich, H., and Martins, A. H. (2021). The Bradykinin B2 receptor agonist (NG291) causes rapid onset of transient blood-brain barrier disruption without evidence of early brain injury. *Front. Neurosci.* 15:791709. doi: 10.3389/fnins.2021.791709

Rufino-Ramos, D., Albuquerque, P. R., Carmona, V., Perfeito, R., Nobre, R. J., and Pereira de Almeida, L. (2017). Extracellular vesicles: novel promising delivery systems for therapy of brain diseases. *J. Control. Release* 262, 247–258. doi: 10.1016/j.jconrel.2017.07.001

Salem, U., Kumar, V. A., Madewell, J. E., Schomer, D. F., de Almeida Bastos, D. C., Zinn, P. O., et al. (2019). Neurosurgical applications of MRI guided laser interstitial thermal therapy (LITT). *Cancer Imaging* 19:65. doi: 10.1186/s40644-019-0250-4

Samiotaki, G., Acosta, C., Wang, S., and Konofagou, E. E. (2015). Enhanced delivery and bioactivity of the Neurturin Neurotrophic factor through focused ultrasound—mediated blood—brain barrier Openingin vivo. *J. Cereb. Blood Flow Metab.* 35, 611–622. doi: 10.1038/jcbfm.2014.236

Santavanond, J. P., Rutter, S. F., Atkin-Smith, G. K., and Poon, I. K. H. (2021). Apoptotic bodies: mechanism of formation, isolation and functional relevance. *Subcell. Biochem.* 97, 61–88. doi: 10.1007/978-3-030-67171-6_4

Sela, H., Cohen, H., Elia, P., Zach, R., Karpas, Z., and Zeiri, Y. (2015). Spontaneous penetration of gold nanoparticles through the blood brain barrier (BBB). *J. Nanobiotechnol.* 13:71. doi: 10.1186/s12951-015-0133-1

Semyachkina-Glushkovskaya, O., Borisova, E., Mantareva, V., Angelov, I., Eneva, I., Terskov, A., et al. (2020). Photodynamic opening of the blood–brain barrier using different photosensitizers in mice. *Appl. Sci.* 10:33. doi: 10.3390/app10010033

Seven, E. S., Seven, Y. B., Zhou, Y., Poudel-Sharma, S., Diaz-Rucco, J. J., Kirbas Cilingir, E., et al. (2021). Crossing the blood–brain barrier with carbon dots: uptake mechanism andin vivocargo delivery. *Nanoscale Adv.* 3, 3942–3953. doi: 10.1039/D1NA00145K

Shah, S., Dhawan, V., Holm, R., Nagarsenker, M. S., and Perrie, Y. (2020). Liposomes: advancements and innovation in the manufacturing process. *Adv. Drug Deliv. Rev.* 154-155, 102–122. doi: 10.1016/j.addr.2020.07.002

Shao, H., Im, H., Castro, C. M., Breakefield, X., Weissleder, R., and Lee, H. (2018). New Technologies for Analysis of extracellular vesicles. *Chem. Rev.* 118, 1917–1950. doi: 10.1021/acs.chemrev.7b00534

Soares Martins, T., Marçalo, R., da Cruz e Silva, C. B., Trindade, D., Catita, J., Amado, F., et al. (2022). Novel exosome biomarker candidates for Alzheimer's disease Unravelled through mass spectrometry analysis. *Mol. Neurobiol.* 59, 2838–2854. doi: 10.1007/s12035-022-02762-1

Spuch, C., and Navarro, C. (2011). Liposomes for targeted delivery of active agents against neurodegenerative diseases (Alzheimer's disease and Parkinson's disease). *J. Drug. Deliv.* 2011:469679

Sun, K., Zheng, X., Jin, H., Yu, F., and Zhao, W. (2022). Exosomes as CNS drug delivery tools and their applications. *Pharmaceutics* 14:2252. doi: 10.3390/pharmaceutics14102252

Szabová, J., Mišík, O., Havlíková, M., Lízal, F., and Mravec, F. (2021). Influence of liposomes composition on their stability during the nebulization process by vibrating mesh nebulizer. *Colloids Surf. B: Biointerfaces* 204:111793. doi: 10.1016/j.colsurfb.2021.111793

Tao, J., Fei, W., Tang, H., Li, C., Mu, C., Zheng, H., et al. (2019). Angiopep-2-conjugated "Core-Shell" hybrid Nanovehicles for targeted and pH-triggered delivery of arsenic trioxide into Glioma. *Mol. Pharm.* 16, 786–797. doi: 10.1021/acs.molpharmaceut.8b01056

Tentillier, N., Etzerodt, A., Olesen, M. N., Rizalar, F. S., Jacobsen, J., Bender, D., et al. (2016). Anti-inflammatory modulation of microglia via CD163-targeted glucocorticoids protects dopaminergic neurons in the 6-OHDA Parkinson's disease model. *J. Neurosci.* 36, 9375–9390. doi: 10.1523/JNEUROSCI.1636-16.2016

Tewabe, A., Abate, A., Tamrie, M., Seyfu, A., and Abdela Siraj, E. (2021). Targeted drug delivery—from magic bullet to Nanomedicine: principles, challenges, and future perspectives. *J. Multidiscip. Healthc.* 14, 1711–1724. doi: 10.2147/JMDH.S313968

Tiebosch, I. A., Crielaard, B. J., Bouts, M. J., Zwartbol, R., Salas-Perdomo, A., Lammers, T., et al. (2012). Combined treatment with recombinant tissue plasminogen activator and dexamethasone phosphate-containing liposomes improves neurological outcome and restricts lesion progression after embolic stroke in rats. *J. Neurochem.* 123, 65–74. doi: 10.1111/j.1471-4159.2012.07945.x

Tietze, R., Lyer, S., Dürr, S., Struffert, T., Engelhorn, T., Schwarz, M., et al. (2013). Efficient drug-delivery using magnetic nanoparticles--biodistribution and therapeutic effects in tumour bearing rabbits. *Nanomedicine* 9, 961–971. doi: 10.1016/j.nano.2013.05.001

Timbie, K. F., Mead, B. P., and Price, R. J. (2015). Drug and gene delivery across the blood-brain barrier with focused ultrasound. *J. Control. Release* 219, 61–75. doi: 10.1016/j.jconrel.2015.08.059

Tsai, Y.-C., Vijayaraghavan, P., Chiang, W.-H., Chen, H.-H., Liu, T.-I., Shen, M.-Y., et al. (2018). Targeted delivery of functionalized Upconversion nanoparticles for externally triggered Photothermal/photodynamic therapies of brain Glioblastoma. *Theranostics* 8, 1435–1448. doi: 10.7150/thno.22482

Vanden-Hehir, S., Tipping, W. J., Lee, M., Brunton, V. G., Williams, A., and Hulme, A. N. (2019). Raman imaging of Nanocarriers for drug delivery. *Nano* 9:341. doi: 10.3390/nano9030341

Visweswaran, P., Massin, E. K., and Dubose, T. D. Jr. (1997). Mannitol-induced acute renal failure. *J. Am. Soc. Nephrol.* 8, 1028–1033. doi: 10.1681/ASN.V861028

Vonarbourg, A., Passirani, C., Saulnier, P., and Benoit, J. P. (2006). Parameters influencing the stealthiness of colloidal drug delivery systems. *Biomaterials* 27, 4356–4373. doi: 10.1016/j.biomaterials.2006.03.039

Voronin, D. V., Sindeeva, O. A., Kurochkin, M. A., Mayorova, O., Fedosov, I. V., Semyachkina-Glushkovskaya, O., et al. (2017). In vitro and in vivo visualization and trapping of fluorescent magnetic microcapsules in a bloodstream. *ACS Appl. Mater. Interfaces* 9, 6885–6893. doi: 10.1021/acsami.6b15811

Votteler, J., Ogohara, C., Yi, S., Hsia, Y., Nattermann, U., Belnap, D. M., et al. (2016). Designed proteins induce the formation of nanocage-containing extracellular vesicles. *Nature* 540, 292–295. doi: 10.1038/nature20607

Wahl, M., Görlach, C., Hortobágyi, T., and Benyó, Z. (1999). Effects of bradykinin in the cerebral circulation. *Acta Physiol. Hung.* 86, 155–160.

Walkey, C. D., Olsen, J. B., Guo, H., Emili, A., and Chan, W. C. W. (2012). Nanoparticle size and surface chemistry determine serum protein adsorption and macrophage uptake. *J. Am. Chem. Soc.* 134, 2139–2147. doi: 10.1021/ja2084338

Wang, H., Abdussalam, A., and Xu, G. (2022). The role of doping strategy in nanoparticle-based electrochemiluminescence biosensing. *Bioelectrochemistry* 148:108249. doi: 10.1016/j.bioelechem.2022.108249

Wu, W., Li, R., Bian, X., Zhu, Z., Ding, D., Li, X., et al. (2009). Covalently combining carbon nanotubes with anticancer agent: preparation and antitumor activity. *ACS Nano* 3, 2740–2750. doi: 10.1021/nn9005686

Xie, J., Shen, Z., Anraku, Y., Kataoka, K., and Chen, X. (2019). Nanomaterial-based blood-brain-barrier (BBB) crossing strategies. *Biomaterials* 224:119491. doi: 10.1016/j.biomaterials.2019.119491

Yang, Q., Zhou, Y., Chen, J., Huang, N., Wang, Z., and Cheng, Y. (2021). Gene therapy for drug-resistant Glioblastoma via lipid-polymer hybrid nanoparticles combined with focused ultrasound. *Int. J. Nanomedicine* 16, 185–199. doi: 10.2147/IJN.S286221

Yang, J., Zou, X., Jose, P. A., and Zeng, C. (2021). "Chapter two—extracellular vesicles: potential impact on cardiovascular diseases" in *Advances in Clinical Chemistry*. ed. G. S. Makowski (Dovepress: Elsevier), 49–100.

Yao, Y., Zhou, Y., Liu, L., Xu, Y., Chen, Q., Wang, Y., et al. (2020). Nanoparticle-based drug delivery in cancer therapy and its role in overcoming drug resistance. *Front. Mol. Biosci.* 7:193. doi: 10.3389/fmolb.2020.00193

Yu, M. K., Park, J., and Jon, S. (2012). Targeting strategies for multifunctional nanoparticles in cancer imaging and therapy. *Theranostics* 2, 3–44. doi: 10.7150/thno.3463

Yu, H., Tang, W., Mu, G., Wang, H., Chang, X., Dong, H., et al. (2018). Micro-/Nanorobots propelled by oscillating magnetic fields. *Micromachines* 9:540. doi: 10.3390/mi9110540

Zhang, C., Chen, W., Zhang, T., Jiang, X., and Hu, Y. (2020). Hybrid nanoparticle composites applied to photodynamic therapy: strategies and applications. *J. Mater. Chem. B* 8, 4726–4737. doi: 10.1039/D0TB00093K

Zhou, L., Kodidela, S., Godse, S., Thomas-Gooch, S., Kumar, A., Raji, B., et al. (2022). Targeted drug delivery to the central nervous system using extracellular vesicles. *Pharmaceuticals (Basel)* 15:358. doi: 10.3390/ph15030358

Zhu, M., Sun, Z., and Ng, C. K. (2017). Image-guided thermal ablation with MR-based thermometry. *Quant. Imaging Med. Surg.* 7, 356–368. doi: 10.21037/qims.2017.06.06

Zibly, Z., Graves, C. A., Harnof, S., Hadani, M., and Cohen, Z. R. (2014). Sonoablation and application of MRI guided focused ultrasound in a preclinical model. *J. Clin. Neurosci.* 21, 1808–1814. doi: 10.1016/j.jocn.2014.04.008

Zörner, B., and Schwab, M. E. (2010). Anti-Nogo on the go: from animal models to a clinical trial. *Ann. N. Y. Acad. Sci.* 1198, E22–E34. doi: 10.1111/j.1749-6632.2010.05566.x

Zou, D., Wang, W., Lei, D., Yin, Y., Ren, P., Chen, J., et al. (2017). Penetration of blood-brain barrier and antitumor activity and nerve repair in glioma by doxorubicin-loaded monosialoganglioside micelles system. *Int. J. Nanomedicine*

Frontiers in Neuroscience

Provides a holistic understanding of brain function from genes to behavior

Part of the most cited neuroscience journal series which explores the brain - from the new eras of causation and anatomical neurosciences to neuroeconomics and neuroenergetics.

Discover the latest Research Topics

See more →

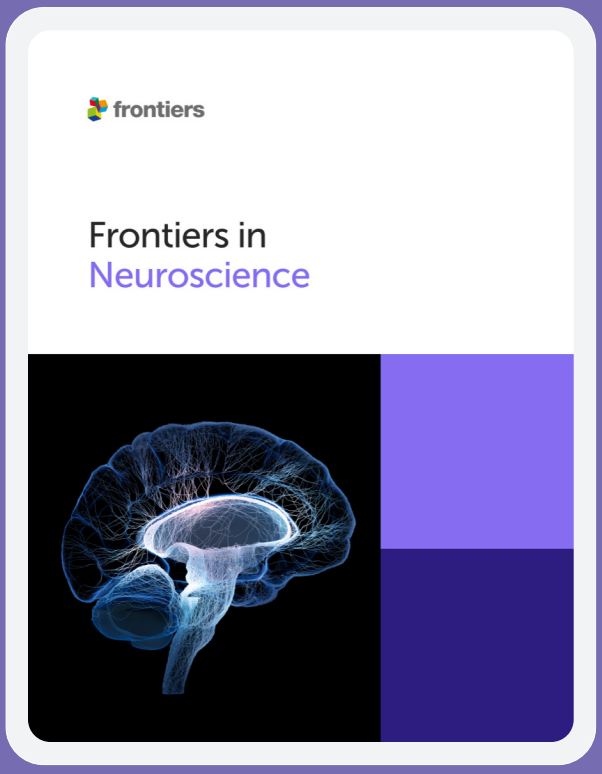

Frontiers

Avenue du Tribunal-Fédéral 34
1005 Lausanne, Switzerland
frontiersin.org

Contact us

+41 (0)21 510 17 00
frontiersin.org/about/contact